

THEORETICAL INVESTIGATIONS FOR PHOTOASSOCIATION AND ION-ATOM SCATTERING EXPERIMENTS IN ULTRACOLD RUBIDIUM GASES

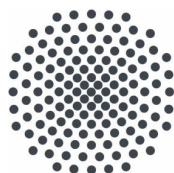
Von der Fakultät Chemie der Universität Stuttgart zur Erlangung der
Würde eines Doktors der Naturwissenschaften (Dr. rer. nat.) genehmigte
Abhandlung

vorgelegt von

Jan Schnabel

geboren am 1. Februar 1992 in Bietigheim-Bissingen

Hauptbericht:	Prof. Dr. Andreas Köhn
Mitbericht:	Prof. Dr. Johannes Kästner
Prüfungsvorsitz:	Prof. Dr. Peer Fischer
Tag der mündlichen Prüfung:	03.11.2021



Institut für Theoretische Chemie
Universität Stuttgart
2021

To Bettina, Harald and Anna – my beloved family.

For their endless love and support

ACKNOWLEDGEMENTS

First and foremost, I would like to express my deep gratitude to Prof. Dr. Andreas Köhn for giving me the opportunity to work on this exciting topic, for providing the perfect ratio between freedom to develop my own ideas and support as well as valuable advice whenever I needed it, and for sharing his great scientific knowledge in numerous fruitful discussions, which were always enlightening and effective. I am also very grateful for his various offers to visit conferences, summer schools, and workshops.

Furthermore, I sincerely thank Prof. Dr. Johannes Kästner for immediately agreeing on becoming the second examiner as well as Prof. Dr. Peer Fischer for unhesitatingly taking the chair in the examination board.

I would also like to offer my special thanks to all cooperation partners, in particular to Prof. Dr. Johannes Hecker-Denschlag and Simon Rupp (University of Ulm). They not only initiated the Rb_3 project, but also significantly contributed to this work through various inspiring and very insightful discussions. Similarly, I am indebted to Dr. Lan Cheng (Johns Hopkins University) for our productive collaboration on Rb_2^+ interaction potentials. Moreover, I want to thank Dr. Jose P. D’Incao (JILA, University of Colorado) for the great exchange of results concerning preliminary computations of $\text{Rb}_2 + \text{Rb}$ collision processes as well as Dr. Florian Meinert and his group (University of Stuttgart) for stimulating the work on Rb_2^+ .

This thesis definitely benefited from the friendly, open and relaxed atmosphere within the institute, wherefore I am very grateful to all colleagues. Here, I would especially like to thank Florian Bauer for being the perfect office colleague, for compensating my lack of chemical knowledge and for taking care of the qpy queuing system. Likewise, my appreciation goes to Dr. Joshua Black for his help with MOLPRO issues and for useful comments on proper English writing. Let me also express my special thanks to Juliane Heitkämper, Julia Netz, Patrik Zielinski and Alexander Waigum for proof-reading important parts of this dissertation. Also, I am very grateful to Dr. Stefan Jagiella for his excellent system administration and for instantaneous support in case of any computer problems.

I am sure that I would not have made it through the five years of physics studies

without my classmates and friends Domenico Paone, Marcel Klett, Michael Schmid and Henri Menke. Not only when I wrote "Mexican hat" in this thesis I wallowed in joyful memories, but also every time I think back to the great time we had - thank you so much, guys! In this respect, I furthermore owe a very important debt to Prof. Dr. Holger Cartarius for his constant support and for amplifying my passion for physics even further.

Beyond that, my deepest heartfelt appreciation goes to all my friends outside the university. Without them I barely would have been able to cope with all the indeterministic and irrational real life problems that appear always cryptically to me. I am truly humbled by your everlasting and unconditional support as well as by the great moments we hitherto could share together. Apparently, the same holds for my parents Bettina and Harald as well as for my sister Anna. They not only enabled my studies both financially and morally but above all, they always believe in me.

CONTENTS

Acknowledgements	v
Contents	vii
List of Abbreviations	xi
Abstract	xv
Kurzzusammenfassung	xvii
Publications	xix
1. Introduction	1
I Theoretical Fundamentals	9
2. From Born-Oppenheimer to Jahn-Teller Theory	11
2.1. Born-Oppenheimer approximation and beyond	11
2.2. Conical intersections	19
2.3. Jahn-Teller effect theory	24
2.4. Coupling effects for linear triatomics	41
3. Wavefunction Methods in Electronic Structure Theory	45
3.1. Many-electron wavefunctions	45
3.2. Hartree-Fock theory	46
3.3. Single-reference correlation methods	54
3.4. Multireference correlation methods	63
3.5. Basis sets	72

II	Investigating Rb₃ for Photoassociation Experiments	77
4.	Towards Photoassociation Processes of Ultracold Rubidium Trimers	79
4.1.	Experimental motivation	79
4.2.	Computational aspects	83
4.3.	General overview of the Rb ₃ system	88
4.4.	Finding appropriate states for photoassociation	108
4.5.	Jahn-Teller analysis of the 1 ⁴ E'' state	115
4.6.	Quadruple interactions in the high-spin manifold	123
5.	Quartet Ground-State Potential Energy Surface for Rubidium Trimer	133
5.1.	RKHS method for constructing potential energy surfaces	133
5.2.	Proof of concept for Rb ₂	140
5.3.	A high-quality Rb ₃ quartet ground state PES	145
III	High-Accuracy <i>ab-initio</i> Calculations for Rb₂⁺	151
6.	Limitations of Coupled-Cluster Approximations for Rb₂⁺	153
6.1.	Computational approach	154
6.2.	Failure of standard coupled-cluster methods	155
6.3.	Symmetry breaking	159
6.4.	Discussion	164
7.	Towards Highly-Accurate Rb₂⁺ Interaction Potentials	167
7.1.	Physical basics and experimental motivation	167
7.2.	Computational aspects and prospects	171
7.3.	Construction procedure	175
7.4.	Results	181
IV	Conclusion	191
8.	Summary and Outlook	193

V	Appendix	199
A.	Point Groups and Selection Rules	201
A.1.	The D_{3h} point group	201
A.2.	The C_{2v} point group	203
A.3.	The C_s point group	205
A.4.	Subduction tables	206
B.	Normal ordering and Wick's theorem	209
C.	Computational Details for Rb_3	213
C.1.	The UET15 basis set family	213
C.2.	MOLPRO input files for Rb_3 investigations	216
D.	Facts and Figures for the Rb_3 System	233
D.1.	Extended overview of Rb_3 states	233
D.2.	More information on spin-orbit coupling effects of Rb_3	240
D.3.	Brief glimpse of 2D ITP surfaces	244
D.4.	Supplementary to the $1 E''$ Jahn-Teller pair	245
D.5.	Supplementary to the analytic Jahn-Teller analysis of the $1^4 E''$ state	246
D.6.	Spin-orbit coupling effects in the Q -manifold	248
D.7.	Nonadditive three-body energy for the quartet ground state of Rb_3	249
E.	Mathematical Details on Kernel Ridge Regression and RKHS Theory	251
E.1.	General descriptions and derivation of the reproducing kernel	251
E.2.	Tikhonov regularization	256
E.3.	Special functions of mathematical physics	257
F.	Computational Details for Rb_2 and Rb_2^+	261
F.1.	The UET17 basis set family	261
F.2.	Basis set extrapolation problems for the aug-cc-p(w)CVnZ-PP family	267
F.3.	Vibrational levels for the $a^3 \Sigma_u$ state of Rb_2	270
F.4.	Excluding possible sources of error for the Rb_2^+ long-range barrier	272
F.5.	Universality of the long-range barrier for alkali-metal dimer cations	277
F.6.	The CCSDT(Q)-PEC for Rb_2^+	278
F.7.	Basis set effects on the $X^2 \Sigma_g^+$ interaction potential of Rb_2^+	279
	Bibliography	281

LIST OF ABBREVIATIONS

The following abbreviations are used, more or less consequently, throughout this thesis:

APES Adiabatic PES. In this thesis APES and PES are used as synonyms

AO Atomic orbital

AU Arbitrary units

AVAS Atomic valence active space. Here this refers to the automated construction of molecular active spaces from atom valence orbitals as reported in *J. Chem. Theory Comput.* **13**, 4063 (2017)

BEC Bose-Einstein condensate

BO Born-Oppenheimer. Here this refers most often to the BO approximation

BSSE Basis set superposition error

CAS Complete active space

CASSCF Complete active space self-consistent field

CBS Complete basis set

CC, CCSD, CCSDT, CCSDTQ Coupled-cluster method with up to singles (S), doubles (D), triples (T) and quadruples (Q) excitations included in the cluster operator

CCSD(T), CCSDT(Q), CCSDT-n Coupled-cluster methods with perturbation-theory based non-iterative treatments of triple and quadruple excitations, respectively. Coupled-cluster methods (with n=1b, 2, 3, 4) with approximate iterative treatment of triple excitations

CI, CISD Configuration-interaction method with up to singly (S) and doubly (D) excited determinants included in the expansion

COIN Conical intersection

CPC Counterpoise correction

CPP Core-polarization potential

CSF Configuration state function

DBOC Diagonal Born-Oppenheimer correction

EA-EOM-CC Electron affinity equation-of-motion coupled-cluster method

ECP Effective core potential. In this work used as lcECP and scECP variant

FCI Full configuration-interaction method

HF Hartree-Fock

IRREP Irreducible representation

ITP Inner turning point

JT/ JTE Jahn-Teller/ Jahn-Teller effect

LR Long-range. Refers to the respective region of a PES

MCSCF Multiconfiguration self-consistent field method

MO Molecular orbital

MRCI (icMRCI and ucMRCI) Multireference configuration-interaction method (internally contracted or uncontracted)

NACME Non-adiabatic coupling matrix element

ONV Occupation number vector

OTP Outer turning point

PA Photoassociation

PEC Potential energy curve, i.e. a one-dimensional PES

PES Potential energy surface

PJT,PJTE Pseudo Jahn-Teller and pseudo Jahn-Teller effect

PP Pseudopotential

RHF Spin-restricted Hartree-Fock

RMSD Root-mean square deviation; can be used to measure the deviation between N *ab-initio* energies $V(R_i)$ given at internuclear distances R_i and the outcome of the RP-RKHS interpolation procedure at the respective geometries $V_{\text{RP-RKHS}}(R_i)$:

$$\text{RMSD} = \sqrt{\frac{\sum_{i=1}^N [V(R_i) - V_{\text{RP-RKHS}}(R_i)]^2}{N}}$$

ROHF spin-restricted open-shell Hartree-Fock

RP-RKHS Reciprocal-power reproducing kernel Hilbert space

RT/ RTE Renner-Teller/ Renner-Teller effect

SCF Self-consistent field method

SOC Spin-orbit coupling

SOPP Spin-orbit coupled pseudopotential

SR Short-range. Refers to the respective region of a PES

SVD Singular value decomposition; A $m \times n$ matrix M can be factorized according to

$$M = U \Sigma V^*,$$

with a $m \times m$ unitary matrix U containing the left-singular vectors u of M as columns, a $m \times n$ rectangular diagonal matrix Σ with the non-negative real singular values σ_i of M on the diagonal and a $n \times n$ unitary matrix V containing the right-singular vectors of M as columns

UET n Uncontracted even-tempered. This acronym is used for denoting the basis sets constructed for this work and n labels the number of exponents included for the description of s orbitals

UHF Spin-unrestricted Hartree-Fock

WMK Werner-Meyer-Knowles (method); see Sec. 3.4.1

ic Internally contracted. For instance: icMRCI

lc Large-core

lt Less tight. Used for the UET17 basis set family in Appendix [F.1](#).

r.k. Reproducing kernel

sc Small-core

uc Uncontracted

ABSTRACT

The increasing level of control attained over ultracold quantum gases provides a platform for studying molecular binding mechanisms on a fundamental level, creating molecules in exactly defined quantum states and paves the way for entering the quantum regime of ion-atom scattering. In ultracold chemistry, photoassociation (PA) is an important spectroscopic technique for producing isolated dimer molecules and it is an encouraging approach to prepare trimer molecules, such as Rb_3 , in precisely defined quantum states. In respect of exploring ion-atom scattering processes on the quantum level, recent experiments demonstrated that a single ionic impurity implanted into a Bose-Einstein condensate (BEC) represents a promising approach for opening this new field.

This thesis is intended to theoretically investigate the prospects for PA of Rb_3 , which includes to provide a broad overview of accessible states and possible transitions. Particular emphasis is placed on the calculation of equilibrium states, the survey of spin-orbit coupling effects and studying selected electronic dipole transition moments. The exploration of the configuration space in terms of special cuts through the potential-energy surfaces (PESs) provides an idea of their topology and gives a first estimate on the expected density of states. In combination with a qualitative discussion of Franck-Condon factors this allows for the identification of concrete and suitable PA transitions to potentially produce long-lived trimer bound states. Further focus is placed on thoroughly discussing symmetries that drive Jahn-Teller (JT) and related effects. In the framework of JT effect theory an analytical representation of the JT manifold with one of its constituting components identified as proper candidate state for use in a PA scheme is derived. Jahn-Teller effect theory is further shown to help in understanding the coupling mechanisms underlying a particular manifold of quadruply interacting excited quartet states. Since these investigations require the computation of a large number of expected states and transitions, a pragmatic but considerably accurate has to be applied. Therefore, the multireference configuration-interaction (MRCI) method together with a large-core effective core potential (ECP) and a core-polarization potential (CPP) with a large uncontracted even-tempered basis set is used.

Another important aspect of this work is the construction of globally smooth and physical meaningful PESs. The applied interpolation method is based on the concept of kernel ridge regression with a specifically adapted kernel function. This is generally described in the mathematical framework of reproducing kernel Hilbert space (RKHS) theory. The generated PESs may then serve as accurate input for subsequent scattering calculations. This might finally lead either to improve the understanding of Rb_2+Rb collision processes or help in making more quantitative statements for conditions needed to identify effects beyond $\text{Rb}+\text{Rb}^+$ Langevin scattering.

The third key subject of this thesis is concerned with high-accuracy *ab-initio* calculations for Rb_2^+ . In doing so, certain limitations of several coupled-cluster methods with perturbative non-iterative or approximate iterative treatments of triple excitations are revealed. It is demonstrated that the use of these methods for X_2^+ systems, with $X = \{\text{Li}, \text{Na}, \text{K}, \text{Rb}, \text{Cs}\}$, lead to a small unphysical repulsive barrier in the long-range region of the respective potential energy curves (PECs). Calculations allowing for charge localization on one of the Rb nuclei show that the unphysical barrier is connected to a symmetry instability of the underlying Hartree-Fock mean-field approach leading to orbitals describing two $+0.5$ -fold charged ions in the long-range limit. This reflects in a leading-order $1/R$ repulsive Coulomb interaction that causes the repulsive barrier. Here it is demonstrated that physically meaningful PECs may be obtained using symmetry-broken triples corrections in the long-range region. This finally motivates a construction procedure following an additive scheme to systematically include results from higher level of theories. A proof of concept is performed at the CCSD(T) level of theory including a modification that allows to correctly reproduce the exchange splitting interaction. This procedure may be systematically extended to higher levels of theory.

KURZZUSAMMENFASSUNG

Die zunehmende Kontrolle, die man über ultrakalte Quantengase erlangt, bietet eine Plattform zur Untersuchung molekularer Bindungsmechanismen auf fundamentaler Ebene, zur Erzeugung von Molekülen in genau definierten Quantenzuständen und ebnet den Weg um Ion-Atom-Streuung auf Quantenebene zu erforschen. In der ultrakalten Chemie ist die Photoassoziation ein wichtiges spektroskopisches Werkzeug um isolierte zweiatomige Moleküle herzustellen und sie ist ein vielversprechender Ansatz um dreiatomige Moleküle, wie Rb_3 , in genau definierten Quantenzuständen zu präparieren. In Bezug auf die Untersuchung von Ion-Atom Streuprozessen auf Quantenebene zeigten jüngste Experimente, dass das Einbauen einer einzelnen ionischen Verunreinigung in ein Bose-Einstein-Kondensat ein vielversprechender Ansatz ist um dieses neue Gebiet zu erschließen.

In dieser Doktorarbeit werden die Möglichkeiten zur Photoassoziation von Rb_3 unter Verwendung der »multireference configuration-interaction« (MRCI) Methode zusammen mit einem »large-core effective core potential« (ECP) und einem »core-polarization potential« (CPP) sowie eines großen unkontrahierten Basissatzes mit äquidistant verteilten Exponenten (even-tempered), theoretisch untersucht. Das umfasst einen umfassenden Überblick der erreichbaren Zustände und möglicher Übergänge. Das Hauptaugenmerk liegt in der Berechnung von Gleichgewichtszuständen, der Analyse von Spin-Bahn Kopplungseffekten und der Untersuchung ausgewählter elektronischer Dipolübergangsmomente. Die Erschließung des Konfigurationsraumes in Form spezieller Schnitte durch die Potentialenergieflächen verleiht ihrer Topologie eine Vorstellung und gibt eine erste Einschätzung über die zu erwartende Zustandsdichte. In Verbindung mit einer qualitativen Diskussion von Franck-Condon Faktoren ermöglicht dies eine Identifizierung konkreter und geeigneter Photoassoziationsübergänge um etwaige langlebige gebundene Trimerzustände zu erzeugen. Ein weiterer Schwerpunkt liegt in der gründlichen Diskussion von Symmetrien die zu Jahn-Teller und verwandten Effekten führen. Im Rahmen der Jahn-Teller-Effekt-Theorie leiten wir eine analytische Darstellung derjenigen Jahn-Teller Mannigfaltigkeit her, die einen Zustand enthält, der als geeigneter Kandidat zur Verwendung in einem Photoassoziationsschema identifiziert wurde. Im Weiteren wird gezeigt, dass diese the-

oretischen Grundbausteine auch dabei helfen den speziellen Kopplungsmechanismus einer Mannigfaltigkeit angeregter Quartett-Zustände mit zugrundeliegender vierfacher Wechselwirkung zu verstehen.

Ein weiterer wichtiger Aspekt dieser Arbeit ist die Konstruktion global glatter und physikalisch sinnvoller Potentialenergieflächen. Die eingesetzte Interpolationsmethode basiert auf dem Konzept der »kernel ridge regression« mit einer speziell angepassten Kernelfunktion. Das wird allgemein im Rahmen der »reproducing kernel Hilbert space (RKHS)« Theorie beschrieben. Die erzeugten Potentialenergieflächen könnten dann als Grundlage für anschließende Streurechnungen dienen. Dies könnte letztendlich entweder dazu führen $\text{Rb}_2 + \text{Rb}$ Stoßprozesse besser zu verstehen oder dabei helfen quantitativere Aussagen zu Bedingungen zu treffen, die bei $\text{Rb} + \text{Rb}^+$ Streuung nötig sind um Effekte über das Langevin-Regime hinaus zu identifizieren.

Der dritte Themenschwerpunkt dieser Doktorarbeit befasst sich mit hochgenauen *ab-initio* Rechnungen zu Rb_2^+ . Hierbei werden bestimmte Anwendungsgrenzen verschiedener coupled-cluster Methoden mit störungstheoretisch nicht-iterativer oder approximativ iterativer Behandlung von dreifach Anregungen aufgedeckt. Es wird gezeigt, dass der Einsatz dieser Methoden für X_2^+ Systeme, mit $X = \{\text{Li}, \text{Na}, \text{K}, \text{Rb}, \text{Cs}\}$, zu einer kleinen unphysikalischen, repulsiven Barriere im langreichweitigen Bereich der jeweiligen Potentialenergiekurve führt. Rechnungen mit einer Ladungslokalisierung an einem der beiden Rb Kerne zeigen, dass die unphysikalische Barriere mit einer Symmetriestabilität der zugrundeliegenden »Mean-Field-Näherung« der Hartree-Fock Theorie einhergeht. Dies führt zu Orbitalen, die im langreichweitigen Limes zwei $+0.5$ -fach geladene Ionen beschreiben. Das schlägt sich wiederum in einer abstoßen Coulomb-Wechselwirkung nieder, die sich wie $1/R$ verhält und letztlich die repulsive Barriere verursacht. Ferner wird dargelegt, dass man physikalisch sinnvolle Potentialenergiekurven dadurch erhalten kann, dass symmetrie-gebrochene Dreifachanregungskorrekturen im langreichweitigen Bereich verwendet werden. Das motiviert schließlich ein Konstruktionsverfahren, das in additiver Weise systematisch Ergebnisse aus höheren Theorieniveaus miteinbezieht. Ein Machbarkeitsnachweis wird auf CCSD(T) Niveau erbracht, das eine Modifikation mit einschließt, die es erlaubt die Austauschwechselwirkung korrekt zu reproduzieren. Dieses Vorgehen kann ebenso auf höhere Theorieniveaus ausgedehnt werden.

PUBLICATIONS

Publications accompanying this thesis:

- *Limitations of perturbative coupled-cluster approximations for highly accurate investigations of Rb_2^+*
J. Schnabel, L. Cheng and A. Köhn
[J. Chem. Phys. 155, 124101 \(2021\)](#).
- *Towards photoassociation processes of ultracold rubidium trimers*
J. Schnabel, T. Kampschulte, S. Rupp, J. Hecker Denschlag and A. Köhn
[Phys. Rev. A 103, 022820 \(2021\)](#) (Editors' Suggestion).

Works published during the course of this PhD or dating back to my pre-PhD era (not covered):

- *Simple models of three coupled \mathcal{PT} -symmetric wave guides allowing for third-order exceptional points*
J. Schnabel, H. Cartarius, J. Main, G. Wunner and W. D. Heiss, [Acta Polytech. 57, 454-461 \(2017\)](#).
- *\mathcal{PT} -symmetric waveguide system with evidence of a third-order exceptional point*
J. Schnabel, H. Cartarius, J. Main, G. Wunner and W. D. Heiss
[Phys. Rev. A 95, 053868 \(2017\)](#).
- *Realizing \mathcal{PT} -symmetric BEC subsystems in closed Hermitian systems*
R. Gutöhrlein, **J. Schnabel**, I. Iskandarov, H. Cartarius, J. Main and G. Wunner
[J. Phys. A: Math. Theor. 48, 335302 \(2015\)](#).

1

INTRODUCTION

The advent of laser cooling techniques for dilute atomic samples [1–3] gradually allowed to enter the field of cold and ultracold matter. This is associated with temperatures above and below 1 mK, respectively. At these low temperatures the de Broglie wavelength becomes large compared to the atom dimensions and new quantum phenomena were discovered. Probably one of the most striking achievement in this regard was the realization of Bose-Einstein condensation in dilute gases of alkali-metal atoms [4, 5] with typical temperatures between 1 nK to 1 μ K. Here, alkali-metal atoms played a fundamental role in the preceding development of laser cooling and magneto-optical trapping techniques [6] as well as in the research of evaporative cooling [7], which is often used as the final stage of cooling to reach sub- μ K temperatures [8]. Alkali atoms have a comparatively simple electronic structure (one valence electron and a polarizable ionic core) and show favorable (hyper)fine splittings that can be conveniently exploited in the respective experiments (e.g. the D₂ line of ⁸⁷Rb has a cycling transition that is used for cooling and trapping [9]).

These experimental milestones clearly opened a door towards an unprecedented level of control gained over quantum systems and established a new intriguing research area. This naturally evolved to the research on cold and ultracold molecules, which succeeded in preparing molecules in precisely defined quantum states and thus led to the realization of the longterm goal to control interactions on the quantum level [10–17]. Ultracold molecules moreover created new opportunities for high-resolution molecular spectroscopy and therewith to highly precise measurements of molecular properties. The level of expected accuracy is such that it may be even used to unravel fundamental questions from high-energy physics, such as the existence of a permanent electric dipole moment of the electron as a probe for the CP violation [13, 18]. Beyond that, the ultracold domain provides prospects to study collisions and chemical reactions in the quantum regime where only a single partial wave contributes. Moreover,

cold molecules have a number of applications, ranging from metrology and quantum sensors, to quantum simulation and computation [15, 17]. The lowest temperatures and the highest control in preparing the molecular quantum state are currently achieved by associating two already ultracold atoms [10–12]. This led to a large number of high-resolution molecular spectroscopy studies and to the production of a variety of different ultracold diatomic molecules. They typically consist of alkali-metal atoms such as the homonuclear dimers Li_2 , Na_2 , K_2 , Rb_2 , Cs_2 or the heteronuclear species NaRb , RbCs , NaK , LiNa , LiK , LiRb , LiCs and NaCs , but also compounds such as LiYb and RbYb have been realized; see, e.g., Refs. [11, 12, 15, 16] and references therein. The approaches to produce these molecules include three-body recombination [19–21], photoassociation (PA) [22–24], and sweeping over a Feshbach resonance [25, 26].

The experimental breakthroughs related to the high-precision spectroscopy of alkali dimers were also driven by a vast amount of theoretical studies; see, e.g., Ref. [13] for a comprehensive overview. In this regard, the detailed theoretical knowledge of the structure of ultracold molecules clearly marked a cornerstone for their formation through association. The simple electronic structure of alkali-atoms with one active valence electron and a polarizable ionic core stimulated a run towards highly accurate *ab-initio* calculations of respective dimer systems. This also holds for the investigation of compounds containing alkaline-earth or ytterbium atoms.

The following examples illustrate the state-of-the-art capabilities of *ab-initio* methods and complement the review of Ref. [13]. Modern quantum chemistry calculations can accurately deal with electron correlation. The standard approaches for computing accurate potential-energy curves (PECs) often involve coupled-cluster (CC) theory [27] in its “gold standard” variant CCSD(T) [28–33] with subsequent inclusion of higher-level correlation contributions via CCSDT [34–37] or CCSDT(Q) [38–41] or CCSDTQ [42–45] or via general CC models [46–48] to render the PECs even more accurate. Systems that reveal a more complex electronic structure or the calculation of electronically excited states can be accurately treated using multireference methods such as multireference configuration-interaction (MRCI) [49, 50] and multireference coupled-cluster (MRCC) theory [51]. Another method for the treatment of excited states is provided by the equation-of-motion coupled-cluster (EOM-CC) theory [52–56]. The effective-core potential (ECP) approach [57, 58] allows for implicitly incorporating major relativistic effects, while at the same time reducing the computational time considerably by modeling the inner core electrons via a scalar-relativistic pseudopotential. This caused further increases in accuracy and significantly contributed to the feasibility of the previ-

ously mentioned higher-level correlation methods for studying larger systems. In this respect, a systematic investigation of all alkali pairs using ECPs and full configuration-interaction (FCI) predicted the value of their permanent electric dipole moment in the ground state to very good accuracy [59]. Furthermore, state-of-the-art *ab-initio* methods are also capable of computing transition dipole moments, static dipole polarizabilities and dynamic polarizabilities. Even hyperfine energy levels and Zeeman splittings of homonuclear and heteronuclear alkali dimers were successfully investigated [60, 61]. It is moreover possible to account for excited electronic states that exhibit strong perturbations; e.g. the well-known $A^1\Sigma^+ - b^3\Pi_u$ spin-orbit coupled manifold, which is dominant when at least one heavy alkali atom (Rb or Cs) is involved. Among others, the Fourier grid Hamiltonian method [62, 63] or the discrete variable representation (DVR) method [64] were used to analyze the corresponding level structure. Recent theoretical work on Mg_2 [65] demonstrated the potential of *ab-initio* PECs to accurately describe weakly bond systems. It was possible to compute 19 vibrational levels of the respective ground-state to an accuracy of $\sim 1 \text{ cm}^{-1}$ compared to 14 experimentally measured term energies, providing thus prospects for the experimental detection of the further so far unresolved levels.

In the spirit of these experimental and theoretical achievements, producing and understanding ultracold alkali-metal triatomics, such as e.g., heteronuclear X_2Y or homonuclear X_3 systems, with $X, Y \in \{\text{Li}, \text{Na}, \text{K}, \text{Rb}, \text{Cs}\}$, would apparently mark a next milestone for the superior goal of controlling the evolution of a complicated quantum system at the quantum level. Alkali-metal trimers are much more complex and challenging as compared to respective dimers, both from the theoretical and experimental perspective. Concerning the latter, a generally reduced lifetime of many trimer levels due to internal relaxation and dissociation processes makes it more complicated to prepare and manipulate those species at the quantum level. Therefore, highly resolved spectroscopy on free trimer molecules is still lacking and ultracold trimers have not been produced yet, apart from extremely weakly bound Efimov states [21, 66]. These are fast-decaying three-body states of resonantly interacting atoms. They also attracted considerable theoretical interest; see, e.g., Refs. [67–72]. In the cold regime, i.e. at mK temperatures, alkali trimers have been produced in experiments using supersonic beam expansion of Ar seeded with, e.g., Na atoms, as in Refs. [73–75], or in experiments with alkali clusters formed on helium nanodroplets [76–79]. Theoretical interest in homonuclear alkali-trimers dates back to the 1980s and 1990s, with some pioneering works in particular on Na_3 (motivated by experimental

results from supersonic beam expansion) [80–90] giving insights into the electronic structure of those systems with special emphasis placed on thoroughly studying the various implications of the intrinsic Jahn-Teller effect (JTE). Already at that time, the large number of low-lying excited electronic states as well as the increased complexity due to the JTE was realized as challenge to accurate electronic structure calculations. Therefore, these early studies were restricted to the light alkali-metals Li, Na, and K. This was certainly also connected with limited capabilities of *ab-initio* methods and computational resources in those days. Later, remarkable progress in *ab-initio* electronic structure theory and the success of the helium nanodroplet method led to a revival of theoretical investigations [91–94], this time, also containing heavier elements such as Rb [95–100]. However, the main focus of these works was again on the analysis of selected JT states and the reproduction of special transitions and spectra measured with the He droplet spectroscopy. Furthermore, emerging experiments studying ultracold collisions between alkali atoms and an alkali dimers motivated calculations of the ground-state potential energy surfaces (PESs) of alkali trimers (in particular for Li₃, Na₃, K₃ and Rb₃), the theoretical analysis of respective scattering processes as well as investigations on nonadditive three-body forces [10, 100–107].

A promising approach for preparing ultracold isolated trimer molecules in precisely defined quantum states is PA. This thesis suggests two possible PA schemes for the production of ultracold rubidium trimers: either photoassociating a previously produced ultracold Rb₂ molecule and a free ground-state Rb atom or photoassociating three colliding free ultracold Rb atoms. In principle both PA schemes can take place at long-range (i.e. for large internuclear distances) or at short-range (i.e. at small internuclear distances). While the former already attracted attention in a number of theoretical works, see, e.g., Refs. [108, 109], the investigations of this thesis rather focus on trimer PA at short-range. The identification of concrete pathways how the trimer PA may explicitly work requires a detailed knowledge of the electronic structure of Rb₃ with expected states and allowed optical transitions between them. While previous theoretical studies on alkali trimers [80–100] were essentially restricted to either the doublet or quartet ground-state or merely analyzed selected JT states, the present study provides a broad overview of electronic states in terms of equilibrium energy levels and reveals the topology of PESs. We are using standard *ab-initio* methods and include spin-orbit effects to estimate their magnitude and explore respective interactions. The PESs are carefully characterized with special emphasis on JT and related effects. We extend the state-of-the-art analytic description to fourth-order and unravel parts of an

unusual coupling mechanism with quadruple interactions. Finally, this work suggests specific PA transitions and identifies a promising candidate state for use in a PA scheme. The results discussed in this thesis could thus provide experimental guidance for the creation of ultracold rubidium trimer molecules and serve as a solid foundation for further more detailed investigations.

Reaching the quantum scattering regime for neutral particles is nowadays well understood and ultracold dimers can routinely be formed. This is in contrast to hybrid ion-atom systems where reaching the s -wave scattering regime is still a non-trivial task due to more stringent temperature requirements [110]. However, reaching the quantum regime for ion-atom mixtures is expected to provide a rich experimental platform with novel phenomena and applications [111]. Among others, those may reach from precision measurements of ion-atom collision parameters and associated molecular potentials [112–114] to ultracold state-resolved quantum chemistry [115], to the ultimate goal of realizing strongly coupled charge-neutral polaron systems [116–118]. A comprehensive overview on both the theoretical and experimental state-of-the-art research on cold hybrid ion-atom systems may be found in Refs. [110, 119]. Novel experimental approaches have been proposed recently [111, 114, 120–122]. These experiments start with an ionic impurity implanted into a ^{87}Rb Bose-Einstein condensate (BEC) through a single precursor Rydberg atom followed by subsequent electric field ionization. In this way, the diffusive transport dynamics of the impurity through the BEC and ion-atom-atom three-body recombination could be observed [121, 122], which was also supported by numerical simulations confirming the inelastic scattering dynamics [123]. In the experimental run described in Ref. [121] it was even possible to estimate the binding energies of some threshold bound states. These experiments can offer a way to probe chemical reaction channels on the quantum level. This so-called state-to-state chemistry will require to resolve the quantized molecular energy levels, which seems in reach for this experimental technique.

This new experimental technique has been used in Ref. [114] for studying $\text{Li}^+\text{-Li}$ scattering processes. Due to the small reduced mass of Li, it was possible to reach the s -wave collision regime. Accompanying highly accurate *ab-initio* calculations based on an additive scheme with CC computations and large basis sets, were for the first time precise enough to yield usable bounds for the ion-atom scattering length. If it may become possible to also reach the quantum regime for Rb-Rb^+ collisions, precise scattering predictions would require *ab-initio* interaction potentials that can compete with the level of accuracy obtained for Li_2^+ . Even if this were experimentally

inaccessible, highly accurate *ab-initio* potentials could support further theoretical investigations to make more quantitative statements for conditions needed to identify effects for the Rb-Rb⁺ scattering that go beyond the classical regime. Recent approaches for studying these collision processes [115, 123, 124] were based on model potentials.

Theoretical investigations of X₂⁺-system (with X = Li, Na, K, Rb) have been reported earlier [125–131]. In respect of approaches aiming at higher precision, the electron affinity equation-of-motion coupled-cluster (EA-EOM-CC) method at EA-EOM-CCSD or EA-EOM-CCSDT level of theory and relativistic effects included via the Douglas-Kroll-Hess method has been used for calculations on Li₂⁺, Na₂⁺, and K₂⁺ [129–131]. The results reported therein yielded satisfactory agreement with available experimental data. However, to the best of our knowledge there are neither examples that can compete with the accuracy obtained for the Li₂⁺ PEC in Ref. [114] nor are there any examples on highly accurate computations of Rb₂⁺. Therefore, another major part of this thesis originally aimed at first high accuracy calculations of Rb₂⁺ ion-atom interaction potentials. In the course of these investigations, corresponding calculations revealed some non-trivial subtleties in CC methods with perturbative noniterative and approximate iterative treatments of triple excitations including the “gold standard” of quantum chemistry: CCSD(T). It is demonstrated that these CC methods lead to unphysical repulsive long-range barriers in the respective PECs, which seem to be undocumented so far. This work explains the origin of the barrier and shows how physically meaningful potentials can be recovered. Finally, we provide PECs that may be subsequently used in scattering calculations and that extent the theoretical literature on benchmark values of spectroscopic constants.

Outline

This thesis is organized as follows. Chapter 2 provides a general introduction into Born-Oppenheimer (BO) theory and effects that go beyond, with particular emphasis on the Jahn-Teller effect (JTE) theory. This includes discussing the breakdown of the BO approximation for degenerate states, motivating the JT theorem and finally focusing on the E ⊗ e JTE of homonuclear triatomic systems. The theory underlying the wavefunction-based *ab-initio* methods used throughout this thesis is summarized in Chap. 3. This covers Hartree-Fock theory, single-reference and multireference correlation methods such as CC theory and the MRCI approach, respectively, and certain aspects of Gaussian basis sets.

Chapter 4 first describes how PA processes work in general and then outlines two possible PA schemes for the realization of trimers. After briefly introducing some computational aspects and convenient coordinate systems for trimers, major topological features of the PESs corresponding to Rb_3 are discussed. This additionally involves providing an overview of expected quartet and doublet equilibrium states of Rb_3 and investigating spin-orbit coupling (SOC) effects to estimate their magnitude. This leads to an analysis of electronically excited states with regard to their applicability in PA processes and it is shown that they can be reached conveniently via the inner turning points (ITPs) on the quartet ground-state PES. In doing so, one component of the $1^4E''$ JT state can be identified as promising candidate for use in PA experiments. Thorough investigations of electronic dipole transition strengths with the quartet ground state, SOC and further mixing effects with other states in its close proximity confirm its suitability as a target state. Hereafter, the $1^4E''$ state is studied analytically yielding a fourth-order JT model of its potential-energy landscape. Finally, the manifold of excited quartet states revealing quadruple interactions is analyzed in detail using tools from JTE theory and computing non-adiabatic coupling matrix elements.

In Chap. 5 it is shown how to construct globally smooth and physically meaningful molecular PESs within a specialized kernel ridge regression framework. A highly accurate PES for the quartet ground-state of Rb_3 is constructed based on ROHF-CCSD(T) *ab-initio* calculations with large uncontracted basis sets.

The computation of Rb_2^+ ion-atom interaction potentials in Chap. 6 reveals certain limitations of standard CC approximations with perturbative noniterative and approximate iterative treatments of triples excitations. It is demonstrated that the use of these methods leads to a small unphysical repulsive long-range barrier in the respective potential energy curve (PEC). This unphysical barrier is shown to be connected with a symmetry instability of the underlying Hartree-Fock mean-field theory.

Chapter 7 presents an appropriate construction procedure towards highly-accurate Rb_2^+ interaction potentials based on CCSD(T) calculations. In addition it is shown how to incorporate a modification that accounts for the correct exchange splitting behavior of the $X^2\Sigma_g^+$ and $(1)^2\Sigma_u^+$ states. The final PEC is constructed based on the method introduced in Chap. 5 and is used to extract spectroscopic constants and to analyze the rovibrational structure.

Finally, the main points and achievements of this work are summarized in Chap. 8. This also includes an outlook to promising subsequent studies with potential for future publications.

Part I

THEORETICAL FUNDAMENTALS

2

FROM BORN-OPPENHEIMER TO JAHN-TELLER THEORY

This chapter provides general insights into the Born-Oppenheimer approximation, reveals its limitations and gives a mathematical explanation for its breakdown. In this regard, general implications such as degenerate states and conical intersections are discussed. This leads to a comparatively broad introduction to the Jahn-Teller effect theory with particular emphasis on homonuclear triatomic systems and ends with outlining coupling effects for linear triatomics.

2.1 | Born-Oppenheimer approximation and beyond

The description of interactions of nuclei and electrons in molecular systems is given, in the non-relativistic limit, by the many-body Hamiltonian

$$\begin{aligned}\mathcal{H} &= \hat{T}_n + \hat{T}_e + \hat{V}_{ne} + \hat{V}_{ee} + \hat{V}_{nn} \\ &= - \sum_{K=1}^M \frac{\hbar^2}{2M_K} \nabla_K^2 - \sum_{i=1}^N \frac{\hbar^2}{2m_e} \nabla_i^2 - \sum_{K=1}^M \sum_{i=1}^N \frac{e^2 Z_K}{4\pi\epsilon_0 |\mathbf{R}_K - \mathbf{r}_i|} \\ &\quad + \sum_{i>j}^N \frac{e^2}{4\pi\epsilon_0 |\mathbf{r}_i - \mathbf{r}_j|} + \sum_{K>L}^M \frac{e^2 Z_K Z_L}{4\pi\epsilon_0 |\mathbf{R}_K - \mathbf{R}_L|},\end{aligned}\tag{2.1}$$

where \hat{T}_n represents the kinetic energy of the nuclei with individual masses M_K , \hat{T}_e the kinetic energy of the electrons and the \hat{V} -terms describe the Coulomb interactions between all pairs of particles, where \mathbf{R}_K and \mathbf{r}_i denote the Cartesian positions of the nuclei and electrons, respectively. It is impossible to solve the stationary molecular Schrödinger equation for the Hamiltonian \mathcal{H} , i.e.

$$\mathcal{H}\Psi_k(\mathbf{x}, \mathbf{R}) = \mathcal{E}_k \Psi_k(\mathbf{x}, \mathbf{R}),\tag{2.2}$$

with $\boldsymbol{x} = (\boldsymbol{r}, \sigma)$ comprising the electrons spatial coordinates \boldsymbol{r} and spin coordinates σ , for any molecular quantum states k exactly. Hence, it is crucial to introduce approximations that reduce the dimensionality of Eq. (2.2). The most fundamental one is the Born-Oppenheimer (BO) approximation that is central to quantum chemistry [132–134] and is thus at the heart of most theoretical methods that generate approximate solutions to Eq. (2.2).

The foundation of Born and Oppenheimer’s work [132] is that the mass of the nuclei is much larger (≈ 2000 times) than the electron mass m_e . Thus, electrons should move on a much faster time scale than the motion of nuclei (*time-scale separation*) and to a good approximation the nuclear motion can be separated from the electronic one. This further implies that for every fixed nuclear coordinate $\bar{\boldsymbol{R}}$, the electronic Schrödinger equation

$$\mathcal{H}_{\text{el}}\psi_n^{\text{el}}(\boldsymbol{x}; \bar{\boldsymbol{R}}) = (\hat{T}_e + \hat{V}_{\text{ne}} + \hat{V}_{\text{ee}})\psi_n^{\text{el}}(\boldsymbol{x}; \bar{\boldsymbol{R}}) = E_n(\bar{\boldsymbol{R}})\psi_n^{\text{el}}(\boldsymbol{x}; \bar{\boldsymbol{R}}) \quad (2.3)$$

can be solved separately. For fixed nuclei, the \hat{V}_{nn} term only contributes a constant and can thus be neglected in the following derivation, but will be added later on. The solution of Eq. (2.3), with the (adiabatic) electronic wavefunctions $\psi_n^{\text{el}}(\boldsymbol{x}; \bar{\boldsymbol{R}})$ and the electronic eigenstates E_n , is the main task of electronic structure theory, which will be discussed in Chap. 3. The quantum number n specifies different electronic states. The notation further indicates that the electronic wavefunctions depend explicitly on the electronic coordinates \boldsymbol{x} and parametrically on the fixed nuclear coordinates $\bar{\boldsymbol{R}}$, while the eigenenergies depend explicitly on $\bar{\boldsymbol{R}}$. For each $\bar{\boldsymbol{R}}$ the electronic eigenfunctions form a complete basis in the space of electronic coordinates \boldsymbol{x} . Therefore, the total molecular wavefunction from Eq. (2.2) can be expanded in this basis for any choice of \boldsymbol{R} , yielding

$$\Psi_k(\boldsymbol{x}, \boldsymbol{R}) = \sum_m \psi_m^{\text{el}}(\boldsymbol{x}; \boldsymbol{R})\chi_{mk}(\boldsymbol{R}), \quad (2.4)$$

which is also known as *Born-Oppenheimer-Huang expansion* [135]. The expansion coefficients $\chi_{mk}(\boldsymbol{R})$ only depend on the nuclear coordinates and the index k labels molecular quantum states that include all electronic and nuclear states. By inserting this ansatz into the molecular Schrödinger equation, considering the nuclear repulsion energy \hat{V}_{nn} to be constant, yields

$$(\hat{T}_{\text{n}} + \mathcal{H}_{\text{el}}) \Psi_k^{\text{tot}} = \sum_m \underbrace{(\hat{T}_{\text{n}} + \mathcal{H}_{\text{el}})}_{\mathcal{H} - \hat{V}_{\text{nn}}} \psi_m^{\text{el}} \chi_{mk}$$

$$\stackrel{(2.2)}{=} \mathcal{E}_k \sum_m \psi_m^{\text{el}} \chi_{mk}. \quad (2.5)$$

Project this onto an electronic wavefunction gives

$$\sum_m \left\langle \psi_n^{\text{el}} \left| \hat{T}_n + \mathcal{H}_{\text{el}} \right| \psi_m^{\text{el}} \chi_{mk} \right\rangle = \mathcal{E}_k \sum_m \left\langle \psi_n^{\text{el}} \left| \psi_m^{\text{el}} \chi_{mk} \right\rangle, \quad (2.6)$$

where orthonormalized electronic wavefunctions $\langle \psi_n^{\text{el}} | \psi_m^{\text{el}} \rangle = \delta_{nm}$ are assumed. Using Eq. (2.3) and integrating over all electronic coordinates \mathbf{x} , this leads to

$$\sum_m \left\langle \psi_n^{\text{el}} \left| \hat{T}_n \right| \psi_m^{\text{el}} \chi_{mk} \right\rangle + E_n(\mathbf{R}) \chi_{nk}(\mathbf{R}) = \mathcal{E}_k \chi_{nk}(\mathbf{R}). \quad (2.7)$$

Since ψ_m^{el} depends parametrically on \mathbf{R} , Eq. (2.7) represents a coupled set of equations, where the corresponding coupling is encoded in the integrals $\langle \psi_n^{\text{el}} | \hat{T}_n | \psi_m^{\text{el}} \chi_{mk} \rangle$. By using $\hat{T}_n \propto \nabla_K^2 = \nabla_k \cdot \nabla_k$ and the product rule, these coupling matrix elements become

$$\sum_m \left\langle \psi_n^{\text{el}} \left| \hat{T}_n \right| \psi_m^{\text{el}} \chi_{mk} \right\rangle = \hat{T}_n \chi_{nk} + \sum_m (\hat{T}'_{nm} + \hat{T}''_{nm}) \chi_{mk}, \quad (2.8)$$

with

$$\hat{T}'_{nm}(\mathbf{R}) = - \sum_K \frac{\hbar^2}{M_K} \left\langle \psi_n^{\text{el}} \left| \nabla_K \right| \psi_m^{\text{el}} \right\rangle \cdot \nabla_K, \quad (2.9a)$$

$$\hat{T}''_{nm}(\mathbf{R}) = - \sum_K \frac{\hbar^2}{2M_K} \left\langle \psi_n^{\text{el}} \left| \nabla_K^2 \right| \psi_m^{\text{el}} \right\rangle, \quad (2.9b)$$

which both act on $\chi_{mk}(\mathbf{R})$ and thus depend on the nuclei coordinates. Since the ψ_n^{el} are orthonormalized it further follows

$$\nabla_K \left\langle \psi_n^{\text{el}} \left| \psi_n^{\text{el}} \right\rangle = 0 = 2 \cdot \text{Re} \left(\left\langle \psi_n^{\text{el}} \left| \nabla_K \right| \psi_n^{\text{el}} \right\rangle \right), \quad (2.10)$$

which implies $T'_{nn} = 0$. With that Eq. (2.7) can be resorted, yielding

$$(\hat{T}_n + E_n(\mathbf{R}) + \hat{T}''_{nn}(\mathbf{R}) - \mathcal{E}_k) \chi_{nk}(\mathbf{R}) = - \sum_{m \neq n} [\hat{T}'_{nm}(\mathbf{R}) + \hat{T}''_{nm}(\mathbf{R})] \chi_{mk}(\mathbf{R}). \quad (2.11)$$

The right hand side of Eq. (2.11) couples the components χ_{mk} for different electronic states n and are therefore referred to as *non-adiabatic coupling terms*. In the *adiabatic approximation* these terms are neglected. Including the diagonal terms $T''_{nn}(\mathbf{R})$ leads to the *diagonal Born-Oppenheimer correction (DBOC)*. However, these terms are usually very small compared to $E_n(\mathbf{R})$. Neglecting them as well defines the BO approximation.

This implies that the total molecular BO wavefunction is, in contrast to the Born-Oppenheimer-Huang expansion of Eq. (2.4), a simple product of the electronic and the nuclear wavefunction

$$\Psi_k^{\text{BO}}(\mathbf{x}, \mathbf{R}) = \psi_m^{\text{el}}(\mathbf{x}; \mathbf{R}) \chi_{mk}(\mathbf{R}). \quad (2.12)$$

Mathematically speaking, this constitutes a separability ansatz, which immediately reflects the physical notion behind the BO approximation; namely the decoupling of electronic and nuclear motion. This leads to an independent eigenvalue equation for each electronic state n : the Schrödinger equation for nuclear motion with nuclear wavefunctions χ_{nk}

$$[\hat{T}_n + E_n(\mathbf{R})] \chi_{nk}(\mathbf{R}) = \mathcal{E}_{nk} \chi_{nk}(\mathbf{R}). \quad (2.13)$$

This shows that within the BO approximation the dynamics of nuclear wavepackets is restricted to a single adiabatic potential energy surface (APES), which serves as an effective potential in which the nuclei move. The APESs $E_n(\mathbf{R})$ are obtained by solving the electronic Schrödinger equation (2.3) for state n , on a grid of fixed nuclear coordinates $\bar{\mathbf{R}}$. Note that due to the decoupling of electronic and nuclear motion the molecular states and energies in Eq. (2.13) are now, in contrast to Eqs. (2.4) and (2.11), specified by the two quantum numbers n and k , where n denotes the electronic state and k labels the eigenstates of the Schrödinger equation for nuclear motion (i.e. vibration and rotation).

The APESs $E_n(\mathbf{R})$ in Eq. (2.13) have to be modified due to the neglect of the constant V_{nn} -term. This gives the Born-Oppenheimer potential V^{BO}

$$E_n(\mathbf{R}) \rightarrow V^{\text{BO}}(\mathbf{R}) = E_n(\mathbf{R}) + V_{\text{nn}}(\mathbf{R}), \quad (2.14)$$

which should be accordingly replaced in Eq. (2.13).

2.1.1 | A paradigm illustrating the limits of the approximation

Neglecting the non-adiabatic coupling matrix elements and the DBOC in Eq. (2.11) is an excellent approximation as long as the energies of electronic states are sufficiently separated. However, in early works by Longuet-Higgings and many others [136–139], it has been shown that the potential energy surfaces of any polyatomic system (including diatomics) can cross, or at least show *avoided crossings*. In these cases, given two electronic states n and m , the corresponding APESs fulfill $E_n(\mathbf{R}_c) \approx E_m(\mathbf{R}_c)$ at

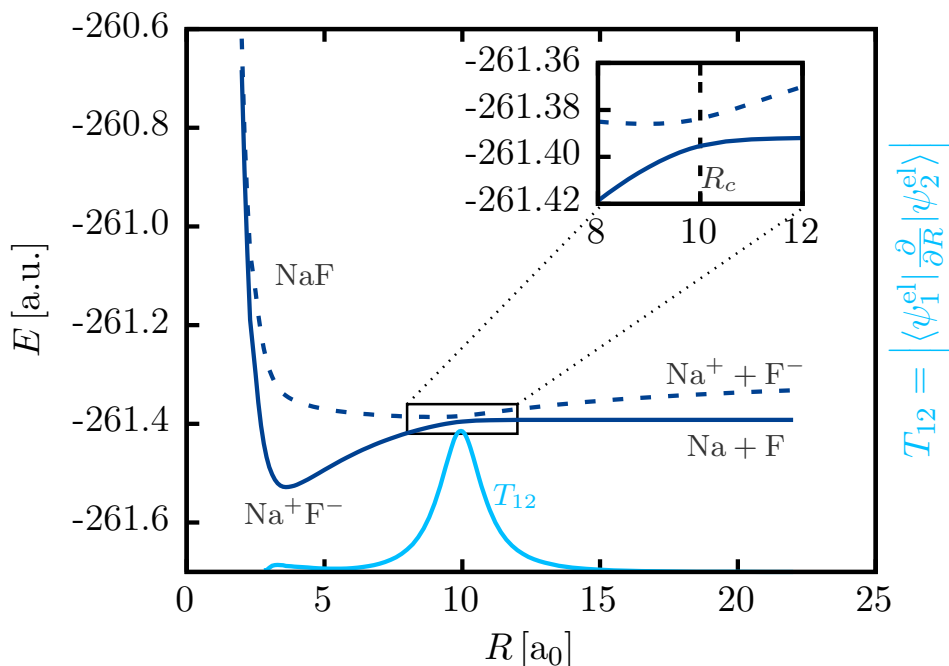


FIGURE 2.1.: The two lowest $^1\Sigma^+$ potential energy curves (PECs) of NaF with the inset showing a close-up of the avoided crossing at $R_c \approx 10 a_0$. The first-order non-adiabatic coupling matrix element (NACME) $T_{12} = \left| \left\langle \psi_1 \left| \frac{\partial}{\partial R} \right| \psi_2 \right\rangle \right|$ is only dominant in close proximity of the avoided crossing at R_c . The calculations were performed at MRCI/aug-cc-pCVQZ level of theory using MOLPRO with corresponding NACMEs obtained from the DDR procedure.

some (near) crossing point \mathbf{R}_c . If this is exact, $E_n(\mathbf{R}_c) = E_m(\mathbf{R}_c)$, we may obtain a so-called *conical intersection* at \mathbf{R}_c (see Sec. 2.2 for an in-depth discussion). In these regions the character of the corresponding (adiabatic) states and thus the corresponding electronic wavefunctions change very rapidly as a function of the nuclear coordinates \mathbf{R} . Therefore, the non-adiabatic coupling matrix elements from Eqs. (2.9) may become large and the underlying assumption of electron-nuclei separability of the BO approach is no longer valid. This results in a breakdown of the approximation. These so-called *non-adiabatic effects* play an important role in the dynamics of these systems and induce, e.g., radiationless transitions between different electronic states.

A prototypical system that reveals APESs with avoided crossings is the NaF molecule, as shown in Fig. 2.1. The avoided crossing occurs between the two lowest $^1\Sigma^+$ states at $R_c \approx 10 a_0$. For short internuclear distances the ground state APES shows ionic character (Na^+F^-), while in the asymptote the neutral state ($\text{Na}+\text{F}$) is energetically more preferable than the ionic one (Na^+F^-). At short internuclear distances this neutral state correlates to the excited state. Consequently, both electronic characters

are mixed and the corresponding electronic wavefunctions change rapidly at $R \approx R_c$ from ionic to covalent for the ground state and vice versa for the excited state [140]. This leads to large derivatives with respect to R and therefore to large non-adiabatic coupling matrix elements, cf. Eqs. (2.9). The matrix element $T_{12} = |\langle \psi_1^{\text{el}} | \frac{\partial}{\partial R} | \psi_2^{\text{el}} \rangle|$ is shown in Fig. 2.1. It is only large in close proximity to the avoided crossing at R_c and negligibly small elsewhere. In other words, the electron transfer from Na to F (for the ground state) can be viewed as a slow electronic motion on the same time-scale as the nuclear motion, which is in contradiction to the basic assumption of the BO approximation and thus leading to its breakdown.

2.1.2 | Formal analysis of the limits of the approximation

The mathematical justification that (nearly) intersecting states cause the failure of the BO approximation can be rigorously derived from the Born-Oppenheimer-Huang set of coupled equations (2.11). Thereto, the non-adiabatic coupling terms, including the DBOC, from Eqs. (2.9) are first summarized to a non-adiabatic coupling matrix [94, 135]

$$\begin{aligned} \Lambda_{nm}(\mathbf{R}) &= -(T'_{nm}(\mathbf{R}) + T''_{nm}(\mathbf{R})) \\ &= \sum_K \frac{\hbar^2}{2M_K} \left(2 \langle \psi_n^{\text{el}} | \nabla_K | \psi_m^{\text{el}} \rangle \cdot \nabla_K + \langle \psi_n^{\text{el}} | \nabla_K^2 | \psi_m^{\text{el}} \rangle \right) \\ &= \sum_K \frac{\hbar^2}{2M_K} \left(2\mathbf{F}_{nm}^K(\mathbf{R}) \cdot \nabla_K + G_{nm}^K(\mathbf{R}) \right), \end{aligned} \quad (2.15)$$

so that Eq. (2.11) takes on the form

$$\mathcal{H}_k^{\text{ad}} \chi_{nk}(\mathbf{R}) = [\hat{T}_n + E_n(\mathbf{R})] \chi_{nk}(\mathbf{R}) - \sum_m \Lambda_{nm}(\mathbf{R}) \chi_{mk}(\mathbf{R}) = \mathcal{E}_k \chi_{nk}(\mathbf{R}), \quad (2.16)$$

where $\mathcal{H}_k^{\text{ad}}$ denotes the *adiabatic* Hamiltonian for state k . This equation can be written in a more compact matrix form using atomic units ($\hbar = 1$) and mass-scaled coordinates as well as the relations

$$\hat{T}_n = -\frac{1}{2M} \nabla_{\mathbf{R}}^2, \quad (2.17a)$$

$$\Lambda_{nm} = \frac{1}{2M} (2\mathbf{F}_{nm} \cdot \nabla_{\mathbf{R}} + G_{nm}), \quad (2.17b)$$

with the total mass of the system M and the elements of the non-adiabatic vector and scalar matrices, respectively

$$\mathbf{F}_{nm} = \langle \psi_n^{\text{el}} | \nabla_{\mathbf{R}} | \psi_m^{\text{el}} \rangle \quad \text{and} \quad G_{nm} = \langle \psi_n^{\text{el}} | \nabla_{\mathbf{R}}^2 | \psi_m^{\text{el}} \rangle. \quad (2.18)$$

For a given sub-Hilbert space the matrices \mathbb{F} and \mathbf{G} are related as [94, 135]

$$\mathbf{G} = \nabla_{\mathbf{R}}\mathbb{F} + \mathbb{F} \cdot \mathbb{F}. \quad (2.19)$$

This leads from Eq. (2.16) to the final form of the *Born-Oppenheimer-Huang equation*

$$\mathcal{H}^{\text{ad}}\chi = \left[-\frac{1}{2M}(\nabla_{\mathbf{R}} + \mathbb{F})^2 + E(\mathbf{R})\mathbb{1} \right] \chi = \mathcal{E}\chi, \quad (2.20)$$

where χ is a column vector that contains the nuclear functions and $E(\mathbf{R})$ represents the APESs. The form of the kinetic part of Eq. (2.20), also denoted as the *dressed* kinetic energy operator

$$\widehat{\mathbf{T}}_{\text{n}} = -\frac{1}{2M}(\nabla_{\mathbf{R}} + \mathbb{F})^2, \quad (2.21)$$

illustrates, due to its non-diagonal nature and dependence on \mathbb{F} , that it couples the nuclear dynamics on multiple electronic PESs. In the BO approximation it is assumed that these couplings are negligible, thus rendering the dressed kinetic energy operator diagonal and recovering Eq. (2.13).

The limitation of this approximation is encoded in the matrix elements \mathbf{F}_{nm} . With some lines of algebra, recalling that the electronic wavefunctions parametrically depend on \mathbf{R} , and diagonalize the electronic Hamiltonian \mathcal{H}_{el} [cf. Eq. (2.3)], which also depends parametrically on \mathbf{R} , it can be shown what is referred to as the *second Hellmann-Feynman theorem* [141, 142] or *adiabatic theorem* [143]

$$\left\langle \psi_n^{\text{el}} \left| \nabla_{\mathbf{R}} \right| \psi_m^{\text{el}} \right\rangle = \mathbf{F}_{nm} = \frac{\left\langle \psi_n^{\text{el}} \left| \nabla_{\mathbf{R}} \mathcal{H}_{\text{el}} \right| \psi_m^{\text{el}} \right\rangle}{E_m(\mathbf{R}) - E_n(\mathbf{R})}. \quad (2.22)$$

This directly reveals that for (near) degeneracies, $E_m \approx E_n$, the matrix elements \mathbf{F}_{nm} become huge or even infinite such that their neglect is no longer justified. In these situations, the singular nature of Eq. (2.20) requires an alternative approach as outlined below.

2.1.3 | Diabatization in a nutshell

The aim in performing what is called diabatization, or adiabatic-to-diabatic transformation, is to get rid of the problematic non-adiabatic coupling matrix Λ_{nm} from Eq. (2.15) that becomes very large or even singular, as shown by Eq. (2.22), for avoided crossings or conical intersections. The underlying idea relies on transforming the kinetic coupling in the adiabatic representation of Eqs. (2.16), (2.20) and (2.21) into a

potential coupling in the diabatic picture. This reduces the electronic-vibronic coupling to an electronic one. Technically, the corresponding diabatic states are obtained from the adiabatic ones, $\psi_n^{\text{ad}}(\mathbf{x}; \mathbf{R}) = \psi_n^{\text{el}}(\mathbf{x}; \mathbf{R})$, through unitary transformation for each nuclear configuration [144, 145]

$$\phi_m^{\text{diab}}(\mathbf{x}; \mathbf{R}) = \sum_n \psi_n^{\text{ad}}(\mathbf{x}; \mathbf{R}) U_{nm}. \quad (2.23)$$

The transformation matrix U is chosen such that the non-adiabatic coupling matrix \mathbb{F} vanishes for all \mathbf{R} which is equivalent to

$$\left\langle \phi_n^{\text{diab}} \left| \nabla_{\mathbf{R}} \right| \phi_m^{\text{diab}} \right\rangle \stackrel{!}{=} 0, \quad (2.24)$$

yielding the condition [94, 135]

$$U^\dagger \mathbb{F} U + U^\dagger \nabla_{\mathbf{R}} U = \mathbf{0}. \quad (2.25)$$

Formally, the same transformation U has to be applied to the nuclear adiabatic basis and thus to the total adiabatic wavefunction. In doing so, Eq. (2.20) finally transforms into the potentially coupled (diabatic) Schrödinger equation

$$\mathcal{H}^{\text{diab}} \chi^{\text{diab}} = \left[-\frac{1}{2M} \nabla_{\mathbf{R}}^2 \mathbb{1} + \mathbf{W} \right] \chi^{\text{diab}} = \mathcal{E} \chi^{\text{diab}}, \quad (2.26)$$

with the *diabatic* Hamiltonian $\mathcal{H}^{\text{diab}}$ and the non-diagonal diabatic potential matrix \mathbf{W} carrying the non-adiabaticity formerly encoded as kinetic coupling.

Note that Eqs. (2.23) and (2.25) are not sufficient to define a diabatic basis unambiguously. However, it can be shown that the matrix elements of W_{nm} must be simple and smooth functions of the nuclear coordinates [145]. If in Eq. (2.23) both the adiabatic and diabatic basis were complete or span the same vector space, the unitary matrix U diagonalizes \mathbf{W}

$$U^\dagger \mathbf{W} U = E(\mathbf{R}) \mathbb{1}, \quad (2.27)$$

and the eigenvalues exactly reproduce the APESs $E(\mathbf{R})$. The matrix U will be called the adiabatic-to-diabatic transformation matrix. Because of Eq. (2.27) the matrix elements of the diabatic potential may be written as

$$W_{mn} = \left\langle \phi_m^{\text{diab}} \left| \mathcal{H}_{\text{el}} \right| \phi_n^{\text{diab}} \right\rangle. \quad (2.28)$$

2.2 | Conical intersections

Conical intersections (COINs), also known as *diabolical points*, represent peculiar cases that lead to a breakdown of the Born-Oppenheimer approximation. They reveal some interesting features and are accompanied with special physical implications, which will be introduced in the following.

2.2.1 | General consideration

From a general point of view, COINs are degeneracies between two energy levels of real symmetric or hermitian, parameter-dependent Hamiltonians $\mathcal{H}(\boldsymbol{\lambda})$, where the set of parameters $\boldsymbol{\lambda}$ is in general a M -dimensional vector [146–148]. Let at some point $\boldsymbol{\lambda}^{(d)}$ in the parameter space the Hamiltonian reveal two degenerate eigenvalues $E_1(\boldsymbol{\lambda}^{(d)}) = E_2(\boldsymbol{\lambda}^{(d)}) \equiv E^{(d)}$ with correlating eigenstates $|\psi_1^{(d)}\rangle$ and $|\psi_2^{(d)}\rangle$, such that [147]

$$\mathcal{H}(\boldsymbol{\lambda}^{(d)}) |\psi_1^{(d)}\rangle = E^{(d)} |\psi_1^{(d)}\rangle, \quad \mathcal{H}(\boldsymbol{\lambda}^{(d)}) |\psi_2^{(d)}\rangle = E^{(d)} |\psi_2^{(d)}\rangle. \quad (2.29)$$

In close proximity to the degeneracy $\boldsymbol{\lambda}^{(d)}$, the behavior of the system can be studied in terms of degenerate perturbation theory. The perturbed states $|\varphi_1(\boldsymbol{\lambda})\rangle$ and $|\varphi_2(\boldsymbol{\lambda})\rangle$ are, to lowest order in $\boldsymbol{\lambda} - \boldsymbol{\lambda}^{(d)}$, given as

$$|\varphi_i(\boldsymbol{\lambda})\rangle = c_{i1}(\boldsymbol{\lambda}) |\psi_1^{(d)}\rangle + c_{i2}(\boldsymbol{\lambda}) |\psi_2^{(d)}\rangle, \quad i = 1, 2, \quad (2.30)$$

whereas finding the coefficients c_{ij} and new energies involves the perturbation matrix elements

$$H'_{ij}(\boldsymbol{\lambda}) = \langle \psi_i^{(d)} | \mathcal{H}(\boldsymbol{\lambda}) - \mathcal{H}(\boldsymbol{\lambda}^{(d)}) | \psi_j^{(d)} \rangle. \quad (2.31)$$

The resulting energies become [146]

$$E_{1,2}(\boldsymbol{\lambda}) = E^{(d)} + \frac{1}{2} \left(H'_{11}(\boldsymbol{\lambda}) + H'_{22}(\boldsymbol{\lambda}) \pm \sqrt{[H'_{11}(\boldsymbol{\lambda}) - H'_{22}(\boldsymbol{\lambda})]^2 + 4|H'_{12}(\boldsymbol{\lambda})|^2} \right), \quad (2.32)$$

such that the corresponding energy splitting reads

$$\Delta E(\boldsymbol{\lambda}) = \sqrt{[H'_{11}(\boldsymbol{\lambda}) - H'_{22}(\boldsymbol{\lambda})]^2 + 4|H'_{12}(\boldsymbol{\lambda})|^2}. \quad (2.33)$$

This defines conditions for systematically searching and adjusting parameters for degeneracies. For general complex hermitian Hamiltonians, i.e., e.g., those representing

quantal systems without time-reversal symmetry, such as a particle bound by a scalar potential and in an external magnetic field [147], there are three independent conditions

$$H'_{11}(\boldsymbol{\lambda}^{(d)}) = H'_{22}(\boldsymbol{\lambda}^{(d)}), \quad \text{Re} \left[H'_{12}(\boldsymbol{\lambda}^{(d)}) \right] = 0 \quad \text{and} \quad \text{Im} \left[H'_{12}(\boldsymbol{\lambda}^{(d)}) \right] = 0, \quad (2.34)$$

showing that at least three parameters are needed to satisfy them. If there are exactly three, the degeneracy $\boldsymbol{\lambda}^{(d)}$ defines an isolated point. For $M > 3$ parameters, the degeneracies describe a $M - 3$ -dimensional manifold. Therefore, degeneracies of complex hermitian Hamiltonians have co-dimension three.

For *real symmetric* Hamiltonians, such as quantum systems with time-reversal symmetry, Eq. (2.34) reduces to two independent conditions to be satisfied for obtaining degeneracies. Hence, degeneracies in real symmetric Hamiltonians have co-dimension two. Analogously, for exactly two parameters they are isolated points, but in a $M > 2$ -dimensional parameter space they describe a $M - 2$ -dimensional manifold.

The original idea behind all this dates back to von Neumann, Wigner and Teller [136, 137] who proved the *non-crossing rule* for electronic states of diatomic molecules of the same symmetry. For real symmetric Hamiltonians, the result in Eq. (2.34) implies that if there is only one parameter, e.g. the internuclear coordinate for diatomic molecules, and if $R^{(d)}$ is a point at which $H'_{11} - H'_{22}$ vanishes, then H'_{12} is most unlikely to vanish at that point too. Hence, crossings between states of the same symmetry are very rare events for diatomic molecules [139]. This is in contrast to the case where electronic states are sufficiently different, i.e. for different spin multiplicities or if the respective wavefunctions belong to different IRREPs of the corresponding point group. Then it is $H'_{12} = 0$ and the corresponding potential energy curves can cross [149]. For every polyatomic system with three or more atoms there are enough free parameters to satisfy Eq. (2.34), independent from symmetry arguments. Equation (2.34) defines general conditions for which *accidental degeneracies*, i.e. those not required by symmetry, can occur. Longuet-Higgins [139] generalized the above conditions and showed that intersections between more than two surfaces are possible and that $1/2r(r + 1) - 1$ conditions are need to be satisfied to obtain r -fold degeneracies for real Hamiltonians.

As follows from perturbation theory, the matrix elements H'_{ij} can be expanded into a Taylor series about the degeneracy $\boldsymbol{\lambda}^{(d)}$. In close proximity to the degeneracy the matrix elements depend linearly on the components of $\boldsymbol{\lambda} - \boldsymbol{\lambda}^{(d)}$. If there are only two parameters (λ_1, λ_2) , the level separation according to Eq. (2.33) takes on the form

$$\Delta E = \sqrt{A \left(\lambda_1 - \lambda_1^{(d)} \right)^2 + B \left(\lambda_2 - \lambda_2^{(d)} \right)^2 + 2C \left(\lambda_1 - \lambda_1^{(d)} \right) \left(\lambda_2 - \lambda_2^{(d)} \right)}. \quad (2.35)$$

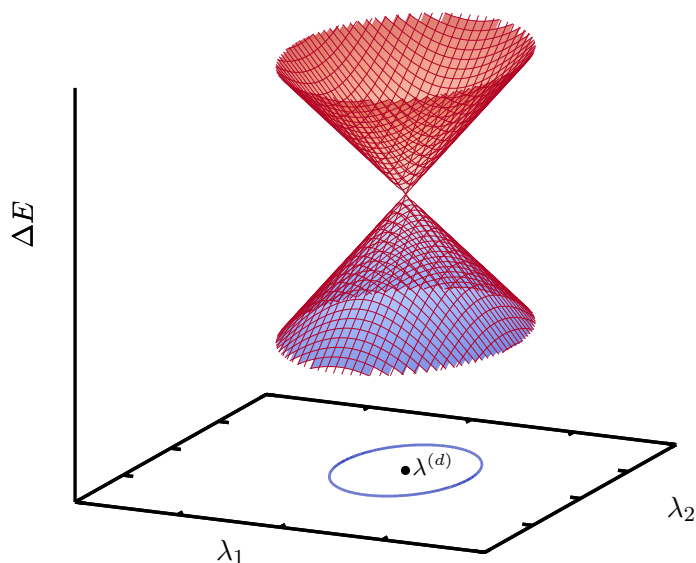


FIGURE 2.2.: Illustration of a conical intersection with diabolical point $\lambda^{(d)}$ for a real symmetric Hamiltonian depending on two parameters λ_1 and λ_2 . The blue circle marks a closed loop in the two-dimensional parameter space around $\lambda^{(d)}$.

This represents a positive definite quadratic form, where A , B and C depend on $\nabla_{\lambda} \mathcal{H}|_{\lambda=\lambda^{(d)}}$, which will be analyzed in more detail in Sec. 2.2.2. Since Eq. (2.35) represents a double cone, i.e. a diabolical geometry, this explains the commonly used expression of a “conical intersection” or a “diabolical point” [146]. An illustration of this characteristic topology is shown in Fig. 2.2. For hermitian Hamiltonians the diabolical structure would generalize to a hyperconical intersection [147] in the four-dimensional $\Delta E, \lambda_1, \lambda_2, \lambda_3$ space, with λ_3 being the third parameter required to satisfy the general three conditions defined by Eq. (2.34).

For a closed path \mathcal{C} in the parameter space around diabolical points, a geometric phase factor occurs resulting in a sign change of both electronic states involved in the degeneracy. Longuet-Higgings [139] pointed out that this sign change is a test for diabolical points of real symmetric Hamiltonians which appears, if and only if \mathcal{C} encloses an odd number of diabolical points – also known as *Longuet-Higgins theorem*. Berry [150] generalized this and showed that eigenstates of parameter-dependent Hamiltonians $\mathcal{H}(\lambda)$ are restored up to a phase factor when λ is varied adiabatically

along a closed loop (not necessarily including degeneracies). In this case, a circuit-dependent geometric phase $e^{i\gamma(\mathcal{C})}$ is accumulated in addition to the familiar dynamical phase $e^{-iE(\lambda)t/\hbar}$. This geometric phase, also called *Berry phase*, is given as the flux of a vector field through a surface \mathcal{A} enclosed by the path \mathcal{C} . The sign change of electronic wavefunctions that occurs for closed loops around degeneracies of real symmetric as well as hermitian Hamiltonians is herein contained as a special case.

2.2.2 | Diabolical points in molecular physics

The following shall unify the general mathematical discussion from above with the analysis of the BO approximation breakdown from Sec. 2.1.2 and Sec. 2.1.3 by means of a typical example from molecular physics. Therefore, let at \mathbf{R}_0 , where \mathbf{R} represents the vector of internuclear distances R_{ij} , be a degeneracy between two adiabatic electronic states $|\psi_1\rangle$ and $|\psi_2\rangle$ with corresponding APESs $E_1(\mathbf{R}_0) = E_2(\mathbf{R}_0) \equiv E_0$. Due to Eq. (2.22), the non-adiabatic coupling matrix becomes singular at this position and a proper system analysis requires to transform to a diabatic basis $\{|\phi_i\rangle\}$, according to Eq. (2.23). In the sense of Eq. (2.28) this yields the diabatic potential matrix

$$\mathbf{W}(\mathbf{R}_0) = \begin{pmatrix} H_{11}^{\text{el}}(\mathbf{R}_0) & H_{12}^{\text{el}}(\mathbf{R}_0) \\ H_{12}^{\text{el}}(\mathbf{R}_0) & H_{22}^{\text{el}}(\mathbf{R}_0) \end{pmatrix}. \quad (2.36)$$

Following the procedure from Sec. 2.2.1, applied to arrive at Eq. (2.35), the topology of the intersecting APESs in close proximity to \mathbf{R}_0 is obtained by expanding \mathbf{W} around it

$$\mathbf{W}(\mathbf{R}) = \mathbf{W}^{(0)}|_{\mathbf{R}_0} + \mathbf{W}^{(1)}|_{\mathbf{R}_0} + \mathbf{W}^{(2)}|_{\mathbf{R}_0} + \dots \quad (2.37)$$

The zeroth-order term just reproduces the degenerate energies at \mathbf{R}_0 , i.e. $\mathbf{W}^{(0)} = E_0 \mathbb{1}_{2 \times 2}$ representing an constant offset, which will be set, without loss of generality, to $E_0 = 0$. The first order term becomes

$$\mathbf{W}^{(1)} = \begin{pmatrix} \nabla_{\mathbf{R}} H_{11}^{\text{el}}|_{\mathbf{R}_0} \cdot \Delta \mathbf{R} & \nabla_{\mathbf{R}} H_{12}^{\text{el}}|_{\mathbf{R}_0} \cdot \Delta \mathbf{R} \\ \nabla_{\mathbf{R}} H_{12}^{\text{el}}|_{\mathbf{R}_0} \cdot \Delta \mathbf{R} & \nabla_{\mathbf{R}} H_{22}^{\text{el}}|_{\mathbf{R}_0} \cdot \Delta \mathbf{R} \end{pmatrix}, \quad (2.38)$$

with $\Delta \mathbf{R} = \mathbf{R} - \mathbf{R}_0$. By introducing the average gradient vector

$$\mathbf{s} \equiv \nabla_{\mathbf{R}} \left(\frac{H_{11}^{\text{el}} + H_{22}^{\text{el}}}{2} \right) \Big|_{\mathbf{R}=\mathbf{R}_0}, \quad (2.39)$$

the gradient difference vector

$$\mathbf{g} \equiv \nabla_{\mathbf{R}} \left(\frac{H_{11}^{\text{el}} - H_{22}^{\text{el}}}{2} \right) \Big|_{\mathbf{R}=\mathbf{R}_0} \quad (2.40)$$

and the derivative coupling vector

$$\mathbf{h} \equiv \nabla_{\mathbf{R}} H_{12}^{\text{el}} \Big|_{\mathbf{R}=\mathbf{R}_0}, \quad (2.41)$$

Eq. (2.38) can be rewritten as

$$\mathbf{W}^{(1)} = \begin{pmatrix} \mathbf{s} \cdot \Delta \mathbf{R} + \mathbf{g} \cdot \Delta \mathbf{R} & \mathbf{h} \cdot \Delta \mathbf{R} \\ \mathbf{h} \cdot \Delta \mathbf{R} & \mathbf{s} \cdot \Delta \mathbf{R} - \mathbf{g} \cdot \Delta \mathbf{R} \end{pmatrix}. \quad (2.42)$$

In close proximity to the intersection, the topology of the APESs $E_1(\Delta \mathbf{R})$ and $E_2(\Delta \mathbf{R})$ follows from diagonalization of $\mathbf{W}^{(1)}$. The resulting energy difference becomes

$$\Delta E(\Delta \mathbf{R}) = E_2(\Delta \mathbf{R}) - E_1(\Delta \mathbf{R}) = \sqrt{(\mathbf{g} \cdot \Delta \mathbf{R})^2 + (\mathbf{h} \cdot \Delta \mathbf{R})^2}, \quad (2.43)$$

which is of the same form as Eq. (2.35) and thus defines a double cone in the so called g - h branching space (see, e.g. Ref. [151] for the basic notion and consequences for introducing this branching space). The physical reason for this lifting of the degeneracy is due to the coupling between electronic and nuclear motion [152]. Moreover, Eq. (2.43) shows how the constants A, B and C from Eq. (2.35) depend on $\nabla_{\mathbf{R}=\mathbf{R}_0}$ through Eqs. (2.39)-(2.41).

If the degeneracy of the two electronic states E_1 and E_2 is accidental, so that E_1 and E_2 each belong to a different irreducible representation (IRREP), a COIN is obtained. If the degeneracy is essential, i.e. required by a high-symmetry nuclear configuration, the COIN is called a Jahn-Teller intersection [153].

Further physical implications of conical intersections are as follows. At COINs nuclear dynamics takes place on more than one adiabatic potential energy surface. This is closely related with the phenomenon that close to a diabolical point in the electron spectrum, an excited electron on the upper sheet of a cone can make a *radiationless transition* to the lower sheet, in which the small energy difference is released not as a photon but into nuclear vibrations [146]. This plays a crucial role in the photochemistry of polyatomic molecules. In this regard, COINs can be also viewed as funnels converting the electronic energy of excited states into nuclear kinetic energy [154]. The geometric or Berry phase effect [138, 150, 155], discussed briefly in Sec. 2.2.1, lets the nuclear wavefunction acquiring an additional nondynamical phase when transported around a closed path that encloses the COIN [156]. This leads to an indirect effect of the diabolical point on the dynamics. Moreover, it is connected with the molecular Aharonov-Bohm effect [157–159]. An in-depth analysis of the occurrences and consequences of diabolical points in molecular systems can be found, e.g., in Ref. [156]. Prominent examples for molecular systems being inherent with this physics are those showing the versatile facets of the Jahn-Teller effect.

2.3 | Jahn-Teller effect theory

Jahn-Teller (JT) systems may lead to the class of symmetry-required conical intersections and arise for highly symmetrical nuclear configurations for which the respective point group reveals degenerate irreducible representations [153]. This causes interesting implications that will be discussed in detail by means of the specific Jahn-Teller effects (JTEs) present in X_3 systems.

2.3.1 | General formulation of the Jahn-Teller theorem

In the original work from 1937 [160], Jahn and Teller showed that stability and (orbital) degeneracy are not possible simultaneously, unless the molecule is a linear one. Here, when disregarding accidental degeneracy, a degenerate electronic state is only possible for symmetrical nuclear configurations. The essential point of their work has been summarized as follows

“All non-linear nuclear configurations are unstable for an orbitally degenerate electronic state.” [... for an electronic state with orbital degeneracy.]

However, nowadays this formulation is not sufficiently rigorous and might be misleading [161]. Also the limitation to linear molecules does not hold either, as will be briefly outlined in Sec. 2.4 and has been analyzed in great detail, e.g., in Refs. [162, 163]. From a rather modern point of view it is more convenient to describe the main effect of electronic degeneracy as producing a special coupling between the nuclear and electronic motion, which in turn results in a series of observable effect: jointly called *Jahn-Teller vibronic coupling effects*. Here, one might also consider to separate the JT effect from the JT theorem. The latter solely refers to the adiabatic potential energy surface (APES) of the system. Although the APES is not an observable, it may serve as an indirect qualitative measure of many observable effects. In a more rigorous framework, the JT theorem formulation according to Bersuker [161] is as follows:

Theorem 2.1–*If the APES of a polyatomic system has two or more branches that intersect in one point (degeneracy point Q_0), then at least one of them has no extremum at this point. Two kinds of cases are exceptions:*

- (i) *Linear molecules*
- (ii) *Twofold spin (Kramers) electronic degeneracy*

This means that if this is the case, there exists at least one direction in the nuclear configuration space for which the first derivative of the APES, with respect to this

coordinate, does not vanish, leaving thus a COIN at the point of degeneracy. The proof of this theorem is based on group theory applied to perturbation calculation. To follow the basic idea of this proof, the Hamiltonian from Eq. (2.1) for a general polyatomic system is rewritten as [164]

$$\mathcal{H} = \hat{T}_n + \hat{H}_r + \hat{V}(\mathbf{x}, \mathbf{Q}), \quad (2.44)$$

with the nuclear kinetic energy \hat{T}_n , the operator \hat{H}_r containing the purely electronic part (i.e. electron kinetic energy and the interelectronic electrostatic interaction), and $\hat{V}(\mathbf{x}, \mathbf{Q})$ including electron-nuclear and nuclear-nuclear interactions. Here, \mathbf{x} is the set of electronic coordinates, and $\mathbf{Q} = \{Q_\alpha\}$ are the N_Q symmetrized nuclear coordinates (normal displacements) chosen to transform according to the IRREPs of the symmetry group \mathcal{G} at the point of degeneracy ($\hat{=}$ JT center; without loss of generality $\mathbf{Q}_0 = \mathbf{0}$), i.e. at the symmetrical configuration. As shown by Wigner [165], this choice is always possible for small (infinitesimal) nuclear displacements $q_\alpha = Q_\alpha - Q_{0\alpha}$ from the point of degeneracy $Q_{0\alpha} = 0$ and one may expand $V(\mathbf{x}, \mathbf{Q})$ as a power series in $q_\alpha = Q_\alpha$, yielding

$$V(\mathbf{x}, \mathbf{Q}) = V(\mathbf{x}, \mathbf{0}) + \sum_\alpha \left(\frac{\partial V}{\partial Q_\alpha} \right)_0 Q_\alpha + \frac{1}{2} \sum_{\alpha, \beta} \left(\frac{\partial^2 V}{\partial Q_\alpha \partial Q_\beta} \right)_0 Q_\alpha Q_\beta + \dots, \quad (2.45)$$

where it is convenient to introduce the terms

$$\begin{aligned} W(\mathbf{x}, \mathbf{Q}) &= V(\mathbf{x}, \mathbf{Q}) - V(\mathbf{x}, \mathbf{0}) \\ &= \sum_\alpha \left(\frac{\partial V}{\partial Q_\alpha} \right)_0 Q_\alpha + \frac{1}{2} \sum_{\alpha, \beta} \left(\frac{\partial^2 V}{\partial Q_\alpha \partial Q_\beta} \right)_0 Q_\alpha Q_\beta + \dots, \end{aligned} \quad (2.46)$$

which are called *vibronic coupling terms*. Although it is the ultimate goal to solve the full molecular Schrödinger equation as given in Eq. (2.2), considerable insight into the physics of the system and the JT effect, is already gained from the form of the corresponding APES. In JT problems the vibronic coupling terms are considered as a perturbation to the electronic Hamiltonian

$$\mathcal{H}^{\text{el}} |\psi_k(\mathbf{x}, \mathbf{0})\rangle = [\hat{H}_r + V(\mathbf{x}, \mathbf{0})] |\psi_k(\mathbf{x}, \mathbf{0})\rangle = E_k |\psi_k(\mathbf{x}, \mathbf{0})\rangle, \quad (2.47)$$

which contains only the zeroth-order term at $Q_{0\alpha} = 0$ [164, 166]. If by solving this equation one obtains a f -fold degenerate electronic term $E_k = E_0 (k = 1, 2, \dots, f)$, the inclusion of linear terms of the vibronic coupling operator after Eq. (2.46) as a perturbation will lead to a splitting of this degeneracy. This represents the same

approach as applied in Secs. 2.2.1 and 2.2.2 for analyzing the topology of conical intersections close to the degeneracy. In analogy to Eq. (2.38), the perturbative inclusion of $W(\mathbf{x}, \mathbf{Q})$ in linear order to Eq. (2.47) will lead to a secular equation of order f to determine the electronic energies. This involves matrix elements of the form $F_{Q_\alpha}^{\Gamma_\gamma \Gamma_{\gamma'}} Q_\alpha$, with the linear vibronic coupling constant

$$F_{Q_\alpha}^{\Gamma_\gamma \Gamma_{\gamma'}} = \left\langle \Gamma_\gamma \left| \left(\frac{\partial V}{\partial Q_\alpha} \right)_0 \right| \Gamma_{\gamma'} \right\rangle, \quad (2.48)$$

where $|\Gamma_\gamma\rangle$ and $|\Gamma_{\gamma'}\rangle$ are the diabatic wave functions of the two electronic states in the degenerate term of representation Γ . The lack of extremum at $Q_{0\alpha} = 0$, as stated by the JT theorem, implies that at least one of the vibronic constants of Eq. (2.48) is nonzero. For this, note that $(\partial V / \partial Q_\alpha)$ transforms as Q_α , which, as mentioned above, can be chosen such that it transforms according to the IRREPs of the symmetry group \mathcal{G} at the JT center. Thus, $F_{Q_\alpha}^{\Gamma_\gamma \Gamma_{\gamma'}} \neq 0$, if there exists a normal displacement of IRREP Γ_α (other than the totally symmetric one) for which $\Gamma_\alpha \otimes \Gamma \otimes \Gamma$ contains the identical representation. Jahn and Teller [160] proved that any nonlinear symmetrical nuclear configuration necessarily possesses non-totally symmetric normal displacements that transform according to Γ_α , such that the previously stated holds. This is equivalent to showing that $[\Gamma^2] = \Gamma \otimes \Gamma$ contains at least one of the IRREPs Γ_α . The proof is based on applying Wigner's method [165] (how to calculate for any given nuclear configuration how many normal displacements of each IRREP occur) to symmetrical nuclear configurations and checking all point groups one by one. Due to the lack of extremum at the point of degeneracy, the APES may have its minimum for distorted nuclear configurations at $Q_\alpha \neq 0$. Moreover, higher-order terms of Eq. (2.45) or Eq. (2.46), respectively, introduce further features into the resulting APES.

In a diabatic basis the vibronic coupling terms of Eq. (2.46) define the diabatic potential matrix $\mathbf{W}(\mathbf{Q})$ yielding the coupled set of equations as given in Eq. (2.26). The eigenvalues obtained from solving Eq. (2.47) with the vibronic coupling terms included as perturbation are functions of the nuclear coordinates Q_α and produce the f branches of APESs with a f -fold degeneracy at $Q_{\alpha 0} = 0$ [161, 164]

$$E_k(\mathbf{Q}) = \frac{1}{2} \sum_\alpha K_\alpha Q_\alpha^2 + E_k^\nu, \quad k = 1, 2, \dots, f, \quad (2.49)$$

where K_α are the primary force constants without vibronic coupling. Finally, with the help of the Hellmann-Feynmann theorem [141, 142], one may define a generalized force at the locus of degeneracy associated to a distortion coordinate Q_α and state $|\Gamma_{\gamma_i}\rangle$,

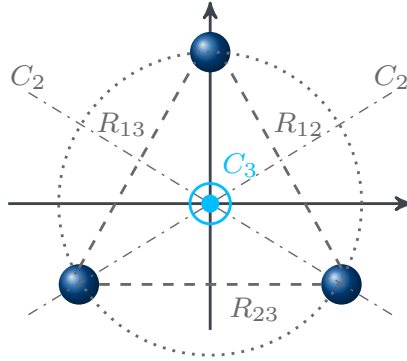


FIGURE 2.3.: Generic representation of a homonuclear triatomic molecule in one plane of the three-dimensional Cartesian coordinate system. Internuclear distances are denoted R_{ij} with $i < j \in \{1, 2, 3\}$. For a equilateral triangular configuration (as depicted), the symmetry of the system is described by the D_{3h} point group. This group contains, besides the trivial identity operator (\hat{E}), symmetry operators for a $2\pi/3$ rotation (\hat{C}_3 , pointing out of the drawing plane), three rotations by $\pi/2$ (\hat{C}_2), where one of them coincides with the ordinate, three reflections on mirror planes oriented along each C_2 axis ($\hat{\sigma}_v$), and the (dotted) plane, the molecular plane, perpendicular to the C_3 axis ($\hat{\sigma}_h$). See also the character table with the corresponding IRREPs in Tab. A.1.

becoming [164]

$$\mathbf{F}_\alpha = - \left\langle \Gamma_{\gamma_i} \left| \frac{\partial V}{\partial Q_\alpha} \right| \Gamma_{\gamma_i} \right\rangle. \quad (2.50)$$

For $\mathbf{F}_\alpha \neq 0$, the system is unstable at the locus of degeneracy, and spontaneously distorts until such a force vanishes at an equilibrium geometry of a lower symmetry.

2.3.2 | The Jahn-Teller effect for X_3 systems

Symmetry-required degenerate states, as a prerequisite for the occurrence of Jahn-Teller vibronic coupling effects, naturally emerge for highly symmetric nuclear configurations [161]. The $E \otimes e$ JTE defines one class of these vibronic coupling effects and describes the splitting of a doubly degenerate electronic E state due to the interaction with a doubly degenerate vibrational e mode (IRREPs for electronic states are labeled by capital letters, while nuclear coordinates correspond to small ones). A doubly degenerate electronic E term arises for all molecules with at least one three-fold axis of symmetry. The simplest systems one may think of are homonuclear triatomics X_3 as illustrated in Fig. 2.3. If the three nuclei define an equilateral triangle, the symmetry of the system is characterized by the point group D_{3h} with a three-fold axis of symmetry (C_3), thus allowing for doubly degenerate electronic E terms (cf. Tab. A.1). Typical

examples are alkali trimers such as Li_3 [80–84], Na_3 [81, 84–91, 93], K_3 [81, 84, 92, 94–97] and Rb_3 [95–97].

Normal coordinates

As indicated above, it is convenient to introduce (symmetrized) normal coordinates Q_α to describe nuclear displacements and to analyze the topology of the APES near the locus of degeneracy. For X_3 systems, given the internuclear distances (R_{12}, R_{23}, R_{13}) , cf. Fig. 2.3, proper (symmetry-adapted) normal coordinates may be defined as [152]

$$\begin{pmatrix} Q_1 \\ Q_2 \\ Q_3 \end{pmatrix} = \begin{pmatrix} \begin{array}{c} \uparrow \\ \swarrow \quad \searrow \\ \downarrow \end{array} \\ \begin{array}{c} \rightarrow \\ \swarrow \quad \searrow \\ \rightarrow \end{array} \\ \begin{array}{c} \uparrow \\ \swarrow \quad \searrow \\ \downarrow \end{array} \end{pmatrix} = \begin{pmatrix} \sqrt{1/3} & \sqrt{1/3} & \sqrt{1/3} \\ -\sqrt{1/2} & \sqrt{1/2} & 0 \\ -\sqrt{1/6} & -\sqrt{1/6} & \sqrt{2/3} \end{pmatrix} \cdot \begin{pmatrix} R_{12} \\ R_{13} \\ R_{23} \end{pmatrix}. \quad (2.51)$$

The totally symmetric, or “breathing” mode Q_1 preserves the D_{3h} symmetry of the system with the associated IRREP a'_1 . The pair (Q_2, Q_3) constitutes the JT active distortion coordinates (corresponding IRREP e') with the asymmetric stretch and bending normal modes, respectively. The former distorts the equilateral triangle into a C_s scalene triangle with only the molecular plane as remaining symmetry element, while the latter takes the system to isosceles triangular conformations of C_{2v} point group symmetry. This differentiation into Q_2 and Q_3 is only of formal nature, since every linear combination of both coordinates yields a proper representation of the e' space. The degeneracy remains for Q_1 vibrations, while the Q_2 and Q_3 modes define the two-dimensional coordinate space referred to as the branching space or g - h plane, introduced in Sec. 2.2.2, in which the degeneracy is lifted.

For the following discussion it is convenient to transform Q_2 and Q_3 into polar coordinates, with

$$Q_2 = \varrho \sin \varphi, \quad Q_3 = \varrho \cos \varphi, \quad \text{with} \quad \varrho^2 = Q_2^2 + Q_3^2, \quad \tan \varphi = \frac{Q_2}{Q_3}. \quad (2.52)$$

Furthermore, it will turn out useful to introduce complex superpositions of these normal modes, via [86, 167]

$$Q_\pm = Q_3 \pm iQ_2 = \varrho e^{\pm i\varphi}. \quad (2.53)$$

The $E \otimes e$ Jahn-Teller effect

The degeneracy of electronic E states for D_{3h} configurations means that there exist two linearly independent eigenvectors to the same eigenvalues of the electronic Hamiltonian, labeled $|\phi_2\rangle$ and $|\phi_3\rangle$, which span a two-dimensional subspace [167]. Within this subspace, every normalized linear combination will be also an eigenvector to the same eigenvalue. This allows to perform arbitrary unitary transformations on such vectors. The same holds for the two-dimensional subspace of the degenerate nuclear e modes, i.e. the pair (Q_2, Q_3) and is finally the mathematical justification for Eq. (2.53). Accordingly, the mapping of the degenerate electronic states to the complex representation is obtained via

$$|\phi_{\pm}\rangle = \frac{1}{\sqrt{2}} (|\phi_3\rangle \pm i |\phi_2\rangle) , \quad (2.54)$$

where the factor $1/\sqrt{2}$ accounts for proper normalization. This approach of the choice of a complex (quasi-)adiabatic basis is based on some pioneering work about the dependence of the electronic wavefunction on the nuclear coordinates [155, 168] and allows for deriving the JT Hamiltonian for a $E \otimes e$ coupled system based on symmetry arguments.

The canonical approach for analyzing JT problems requires to expand the potential energies of the Hamiltonian \mathcal{H} of a given system, which are determined by the eigenvalues of the electronic Hamiltonian \mathcal{H}_{el} at given nuclear geometries, into a Taylor series in the nuclear coordinates, c.f. Eqs. (2.37), (2.45) and (2.46). The following theorem is crucial to determine the non-vanishing terms of this expansion [167]

Theorem 2.2– *The action of any symmetry operator \hat{O} that belongs to the nuclear point group \mathcal{G} does not change the physics of the system described via the total Hamiltonian \mathcal{H} , i.e.*

$$[\mathcal{H}, \hat{O}] = 0, \quad \forall \hat{O} \in \mathcal{G}$$

In the complex representation, the normal coordinates and electronic states according to Eq. (2.53) and Eq. (2.54), respectively, are eigenfunctions of the symmetry operation \hat{C}_3 with eigenvalues $e^{\pm 2\pi i/3}$. This implies

$$\hat{C}_3 Q_{\pm} = e^{\pm 2\pi i/3} Q_{\pm} , \quad (2.55a)$$

$$\hat{C}_3 |\phi_{\pm}\rangle = e^{\pm 2\pi i/3} |\phi_{\pm}\rangle . \quad (2.55b)$$

The electronic Hamiltonian in the $\{|\phi_+\rangle, |\phi_-\rangle\}$ basis becomes

$$\mathbf{W} = \sum_{i,j} |\phi_i\rangle W_{ij} \langle \phi_j| , \quad i, j = \{+, -\} , \quad (2.56)$$

with the matrix elements $W_{ij} = \langle \phi_i | \mathcal{H}_{el} | \phi_j \rangle$ ($i, j = +, -$), defining thus the diabatic potential matrix according to Eq. (2.28). These matrix elements are expanded into a Taylor series in Q_+ , Q_- , yielding, for instance [167, 169]

$$W_{++} = \sum_{p+q}^{\infty} \frac{c_{p,q}^{(++)}}{(p+q)!} Q_+^p Q_-^q, \quad (2.57)$$

with the expansion coefficients $c_{p,q}^{(++)}$. The invariance condition $[\mathcal{H}, \hat{O}]$ has to be fulfilled by each term of Eq. (2.57) and implies for the diabatic potential matrix in the above example

$$\begin{aligned} \hat{C}_3 \mathbf{W}_{++} &= \hat{C}_3 |\phi_+\rangle Q_+^p Q_-^q \langle \phi_+| \stackrel{!}{=} \mathbf{W}_{++} \\ &= e^{-2\pi i/3} e^{+(p)2\pi i/3} e^{-(q)2\pi i/3} e^{2\pi i/3} |\phi_+\rangle Q_+^p Q_-^q \langle \phi_+|. \end{aligned} \quad (2.58)$$

Hence, only contributions with (p, q) combinations that satisfy the condition $(p - q) \bmod(3)$ give non-vanishing expansion coefficients in Eq. (2.57). By repeating the same procedure for the remaining matrix elements and back-transforming to the real presentation $|\phi_{2,3}\rangle$, yields

$$\begin{aligned} \mathbf{W}_r &= \sum_n \frac{1}{n!} \left\{ \begin{pmatrix} \mathcal{V}^{(n)} & 0 \\ 0 & \mathcal{V}^{(n)} \end{pmatrix} + \begin{pmatrix} \mathcal{W}^{(n)} & \mathcal{Z}^{(n)} \\ \mathcal{Z}^{(n)} & -\mathcal{W}^{(n)} \end{pmatrix} \right\}, \\ &= \sum_n \frac{1}{n!} \left[\mathcal{V}^{(n)} \sigma_I + \mathcal{Z}^{(n)} \sigma_x + \mathcal{W}^{(n)} \sigma_z \right], \end{aligned} \quad (2.59)$$

with the 2×2 unit matrix σ_I and the Pauli matrices σ_x and σ_z . The diagonal elements $\mathcal{V}^{(n)}$ correspond to the potential in the absence of the JTE and $\mathcal{W}^{(n)}$ represent the diagonal coupling terms, while $\mathcal{Z}^{(n)}$ describe the off-diagonal coupling elements. All these matrix elements are real functions of the normal coordinates Q_2 and Q_3 , and the so called JT parameters. Their explicit form can be found in Ref. [167]. Consequently, the JT Hamiltonian matrix in diabatic representation is given as

$$\mathcal{H}_{JT}^{\text{diab}} = \hat{T}_n \sigma_I + \mathbf{W}_r. \quad (2.60)$$

The corresponding APESs are obtained by diagonalizing the diabatic potential matrix \mathbf{W}_r . The method used to derive this JT Hamiltonian is called *diabatization by ansatz* [167]. In practice, the JT parameters of the diabatic potential matrix, hidden in the matrix elements $\mathcal{V}^{(n)}$, $\mathcal{W}^{(n)}$ and $\mathcal{Z}^{(n)}$ in Eq. (2.59), are determined by least-square fits to the APESs obtained from *ab-initio* calculations.

The main physical implications of the $E \otimes e$ JT problem can be understood considering up to quadratic terms in Eqs. (2.59) and (2.60), yielding the corresponding JT Hamiltonian

$$\begin{aligned} \mathcal{H}_{\text{JT}2}^{\text{diab}} = & \hat{T}_n \sigma_I + \left[\Delta \varepsilon_0 + V_{2a}(Q_2^2 + Q_3^2) \right] \sigma_I \\ & + \begin{pmatrix} V_{1e}Q_3 + V_{2e}(Q_3^2 - Q_2^2) & V_{1e}Q_2 - 2V_{2e}Q_2Q_3 \\ V_{1e}Q_2 - 2V_{2e}Q_2Q_3 & -V_{1e}Q_3 - V_{2e}(Q_3^2 - Q_2^2) \end{pmatrix}, \end{aligned} \quad (2.61)$$

with the nomenclature taken from Ref. [166], V_{2a} describes the elastic force constant and $V_{ie}, i \in \{1, 2\}$ denote the linear (1) and quadratic (2) coupling constants. The zeroth-order term $\Delta \varepsilon_0$ defines the energetic position of the central COIN at the D_{3h} reference configuration. In general $\Delta \varepsilon_0 \neq 0$, however the zero of energy can always be chosen such that this term vanishes. By diagonalizing the potential part ($\mathcal{H}_{\text{JT}2}^{\text{diab}} - \hat{T}_n \sigma_I$) and using the polar representation of the normal coordinates after Eq. (2.52), the two branches of the APESs are obtained [95]

$$E_{\pm}(\varrho, \varphi) = V_{2a}\varrho^2 \pm \varrho \left[V_{1e}^2 + 2V_{1e}V_{2e} \cos(3\varphi)\varrho + V_{2e}^2\varrho^2 \right]^{\frac{1}{2}}. \quad (2.62)$$

If the quadratic coupling V_{2e} is negligible, the APES becomes a surface of revolution with E_{\pm} independent of the polar angle φ , and the lower surface E_- acquiring a *Mexican hat*-like shape [161]. The point of degeneracy at $\varrho = 0$ reveals a COIN, as can be seen by comparing the square root of Eq. (2.62) to the quadratic form in Eq. (2.35) or by showing the lack of extremum via $(\partial E_{\pm} / \partial \varrho)_{\varrho \rightarrow 0} = \pm V_{1e}$. The topology of the APES is illustrated in Fig. 2.4 (a). For this particular case all pairs (Q_2, Q_3) with

$$\varrho = \varrho_{\min} = \frac{|V_{1e}|}{2V_{2a}} \quad (2.63)$$

correspond to minimum configurations of the APES, where ϱ_{\min} defines the radius of the trough. The movement of the system along the bottom of the trough is called *internal free rotation* or *pseudo-rotation*. Moreover, it is convenient to introduce the JT-stabilization energy E_s that defines the energy difference between the central COIN and the radially symmetric global minimum, cf. Fig. 2.4 (a), yielding

$$E_s = \frac{V_{1e}^2}{4V_{2a}}. \quad (2.64)$$

It is important to note that the system is degenerate for every D_{3h} configuration, i.e. for any triple $(Q_1, 0, 0)$, defining thus an one-dimensional COIN seam in the full 3D configuration space. For nonzero quadratic coupling, as can be seen from

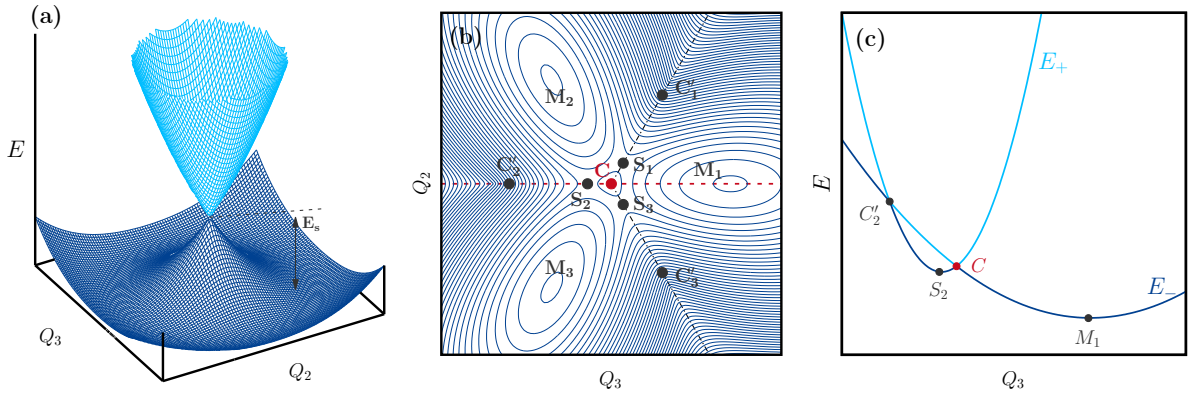


FIGURE 2.4.: (a) Mexican-hat-like APES resulting from the *linear* $E \otimes e$ JT problem. The Jahn-Teller stabilization energy E_s defines the energy difference between the central conical intersection (COIN) and the minimum of E_- (bottom of the trough). (b) Equipotential sections of the lower sheet E_- of the JT APES for *nonzero quadratic coupling*. The APES acquires three equivalent minima ($M_i, i \in \{1, 2, 3\}$) at $\varphi = 0, 2\pi/3$ and $4\pi/3$, divided by three saddle points ($S_i, i \in \{1, 2, 3\}$) at $\varphi = \pi/3, \pi$ and $5\pi/3$. This is also referred to as *tricorn potential*. The points $C'_i, i \in \{1, 2, 3\}$ along the three lines that include the saddle points mark additional COINs, occurring at C_{2v} geometries if the quadratic coupling is sufficiently large. The cross section in (c) shows one of these additional COINs along the red dashed line displayed in (b). There are three equivalent such COINs besides the central one, forming thus three additional COIN seams in the Q_1 - Q_3 space.

Eq. (2.62), a $\cos(3\varphi)$ -warping is introduced to the lower APES sheet, where three equivalent minima occur at $\varphi = 0, 2\pi/3, 4\pi/3$, divided by three saddle points at $\varphi = \pi/3, \pi, 5\pi/3$. The topology is also called *tricorn APES*, where at each of these minima the equilateral triangle is distorted to an isosceles one. This is shown in Fig. 2.4 (b). In this case, instead of free rotations, hindered motions (pulsations) take place, which spectroscopically reflects in a *tunneling splitting* of the vibrational levels in each of the wells [161]. If the barriers between the minima are energetically too high and the system does not have enough energy to cross them, the situation is generally referred to as *static Jahn-Teller effect*. In the cases of free rotation (Mexican-hat potential) and pseudorotation (tricorn APES with sufficiently small barriers), or if pseudorotational motion is conveyed by tunneling, one may speak of the *dynamic Jahn-Teller effect*. In Ref. [170] it was realized that the linear and quadratic coupling terms are described by rather independent constants, which means that the quadratic coupling is not necessarily small compared to the linear one. For sufficiently large quadratic couplings, the topology of the APES changes essentially. In this case, the two branches E_+ and E_- do not only intersect for the central COIN at $q = 0$, but also along the three lines that include the saddle points on the APES, cf. Figs. 2.4 (b)

and (c). Thus, in addition to the symmetry-required D_{3h} crossing seam, there are three symmetry-equivalent C_{2v} COIN seams in the Q_1 - Q_3 subspace in close proximity to the central one. This will significantly affect the tunneling splitting and the general understanding of the problem. This, however, is beyond the scope of this thesis and the reader is referred to Ref. [161] and references therein for more details.

In general, the truncation of the JT expansion according to Eq. (2.59) at quadratic terms is only sufficient for systems showing minima for comparatively small nuclear distortions from the central COIN. For more pronounced anharmonic systems, i.e. when minima occur for larger displacements from the central COIN, higher order terms are needed for an appropriate description. This has been shown, e.g., in Refs. [95, 96] for some doublet and quartet states of K_3 and Rb_3 , where cubic terms turned out relevant. In Sec. 4.5 it will be shown that for a certain JT state of Rb_3 it is necessary to include even fourth- and higher-order terms.

Relativistic $E \otimes e$ Jahn-Teller effect

In a next step, the consequences on Jahn-Teller vibronic coupling effects when additionally including spin-orbit coupling (SOC) are outlined. Since this thesis is concerned with the theoretical investigation of Rb_3 , we restrict ourselves to doublet and quartet states as the only occurring spin multiplicities in this system. For detailed derivations of the following equations it is referred to, e.g., Refs. [171–175] for an in-depth discussion.

With SOC included, the full vibronic Hamiltonian becomes

$$\mathcal{H} = \hat{T}_n + \hat{H}_{el} + \hat{H}_{SO}, \quad (2.65)$$

where in addition to the nuclear kinetic energy operator \hat{T}_n and the electronic Hamiltonian \hat{H}_{el} , the spin-orbit (SO) Hamiltonian is included. Therewith, both the interaction of the electronic motion in a degenerate electronic state with the nuclear motion of degenerate vibrational modes (i.e. nonrelativistic $E \otimes e$ problem) and the interaction of the electron spin angular momentum with the electronic orbital angular momentum is considered [171]. This requires to first construct a proper basis. Considering the doublet case first, it can be shown [171, 172] that the complex representation of the electronic states according to Eq. (2.54) are convenient electronic basis states ($|\Lambda\rangle$)

$$|\Lambda\rangle = |\pm 1\rangle = |\phi_{\pm}\rangle. \quad (2.66)$$

These states have to be augmented with the spin functions of the electron which, for

doublet states, leads the full electronic basis

$$\{|\Lambda\rangle \otimes |\Sigma\rangle = |\Lambda, \Sigma\rangle\} = \left\{ \left| +1, +\frac{1}{2} \right\rangle, \left| -1, +\frac{1}{2} \right\rangle, \left| +1, -\frac{1}{2} \right\rangle, \left| -1, -\frac{1}{2} \right\rangle \right\}. \quad (2.67)$$

As for the nonrelativistic case, the electronic Hamiltonian is expanded in a Taylor series in the normal coordinates. In the basis $|\Lambda, \Sigma\rangle$ this yields, analogous to Eq. (2.61), the diabatic potential matrix [171, 172, 174]

$$\widetilde{\mathbf{W}}_r = \begin{pmatrix} x+y & z \\ z & x-y \end{pmatrix} \otimes \mathbb{1}_{2 \times 2}, \quad (2.68)$$

with

$$x = V_{2a}(Q_2^2 + Q_3^2), \quad (2.69a)$$

$$y = V_{1e}Q_3 + V_{2e}(Q_3^2 - Q_2^2), \quad (2.69b)$$

$$z = V_{1e}Q_2 - 2V_{2e}Q_2Q_3. \quad (2.69c)$$

To a first approximation, the SO Hamiltonian can be represented by diagonal matrix elements $\pm\Delta$ [174]. This leads to the relativistic $E \otimes e$ Hamiltonian with up to second-order vibronic coupling terms included and spin multiplicity $M = 2$

$$\mathcal{H}_{\text{relJT}}^{M=2} = \hat{T}_n \mathbb{1}_{4 \times 4} + \begin{pmatrix} x+y+\Delta & z \\ z & x-y-\Delta \end{pmatrix} \otimes \mathbb{1}_{2 \times 2}. \quad (2.70)$$

Therefrom, the APESs follow from diagonalization of the potential part, again using polar coordinates according to Eq. (2.52), yielding [95, 171]

$$E_{\pm}(\varrho, \varphi) = V_{2a}\varrho^2 \pm \left[\Delta^2 + V_{1e}^2\varrho^2 + 2V_{1e}V_{2e}\cos(3\varphi)\varrho^3 + V_{2e}^2\varrho^4 \right]^{\frac{1}{2}}, \quad (2.71)$$

with the spin-orbit splitting $2\Delta = \alpha\zeta$, where ζ is the projection of the electronic orbital angular momentum onto the C_3 axis, and α is the spin-orbit coupling constant. Apparently, the inclusion of spin-orbit coupling, removes the central COIN for equilateral triangular configurations, while each of the two APES branches are twofold degenerate due to the corresponding Kramers pairs. A characteristic example of this situation is shown in Fig. 2.5 (a).

The quartet case with spin multiplicity $M = 4$ is treated based on the arguments outlined in Refs. [96, 97]. A rigorous derivation for general trigonal systems can be found in Ref. [173]. In this case, a proper basis is defined by

$$\{|\Lambda, \Sigma\rangle\} = \left\{ \left| -1, -\frac{3}{2} \right\rangle, \left| +1, -\frac{3}{2} \right\rangle, \left| -1, -\frac{1}{2} \right\rangle, \left| +1, -\frac{1}{2} \right\rangle \right\},$$

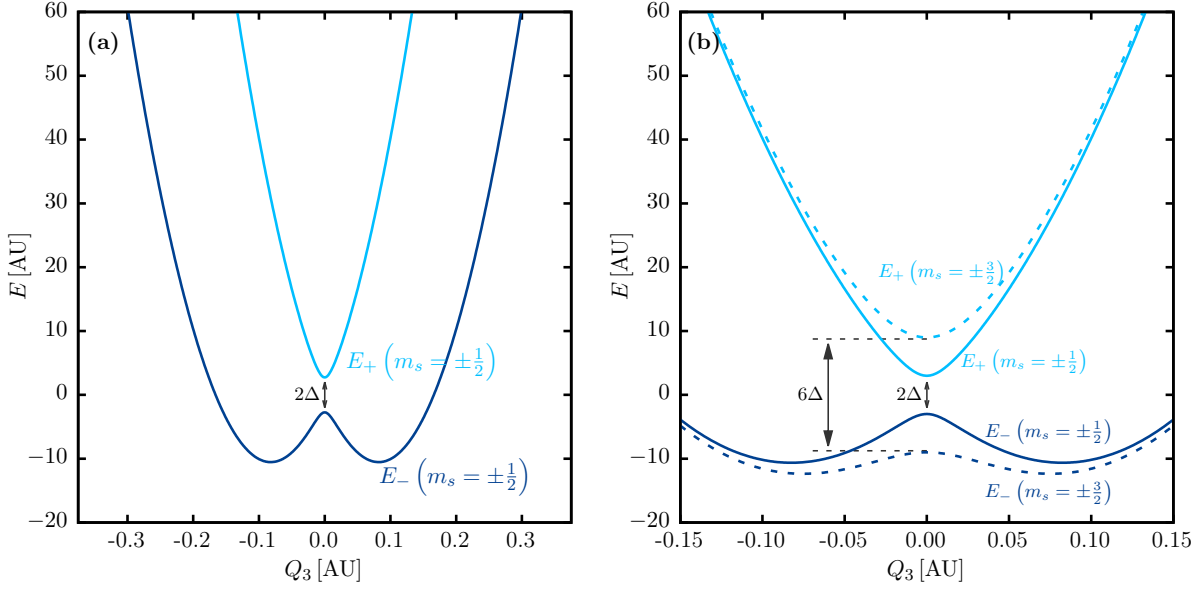


FIGURE 2.5.: Illustration of possible APESs resulting from including spin-orbit coupling to the $E \otimes e$ JT problem. In (a) the spin multiplicity of the degenerate electronic state at D_{3h} configuration corresponds to the doublet case, thus rendering the problem to a relativistic ${}^2E \otimes e$ one. Both branches of the APES remain twofold degenerate due to the corresponding Kramers pairs, but inclusion of spin-orbit coupling lifts the central JT COIN at $Q_3 = 0$ by 2Δ . In (b) the spin multiplicity corresponds to the quartet case, i.e. relativistic ${}^4E \otimes e$ JT problem, where both the upper and lower APES splits twice. Due to the Kramers spin degeneracy each of the four branches is twofold degenerate. Inclusion of spin-orbit coupling leads to a splitting of the central COIN by 2Δ , respectively 6Δ .

$$\left\{ \left| +1, +\frac{1}{2} \right\rangle, \left| -1, +\frac{1}{2} \right\rangle, \left| -1, +\frac{3}{2} \right\rangle, \left| +1, +\frac{3}{2} \right\rangle \right\}, \quad (2.72)$$

with $|\Lambda\rangle$ from Eq. (2.66). Again, the electronic Hamiltonian is expanded in a Taylor series in the normal coordinates. By representing this expansion in the product space defined by Eq. (2.72), the following diabatic potential matrix is obtained

$$\widetilde{\mathbf{W}}_r = \begin{pmatrix} x + y & z \\ z & x - y \end{pmatrix} \otimes \mathbb{1}_{4 \times 4}, \quad (2.73)$$

with the matrix elements given in Eqs. (2.69). The SO Hamiltonian is again assumed to be fully diagonal in the chosen basis set, with the matrix elements

$$[\mathbf{H}_{\text{SO}}]_{ij} = \langle \{\Lambda, \Sigma\}_i | \hat{H}_{\text{SO}} | \{\Lambda, \Sigma\}_j \rangle = 2\Delta \Lambda_i \Sigma_i \delta_{ij}. \quad (2.74)$$

The full 8×8 matrix representation of the resulting JT Hamiltonian $\mathcal{H}_{\text{relJT}}^{M=4}$ can be found in Ref. [97]. The APESs are obtained by diagonalizing the corresponding potential part,

which by using polar coordinates according to Eq. (2.52) leads to [96]

$$E_{1/2\pm}(q, \varphi) = V_{2a}q^2 \pm \left[\Delta^2 + V_{1e}^2q^2 + 2V_{1e}V_{2e} \cos(3\varphi)q^3 + V_{2e}^2q^4 \right]^{\frac{1}{2}}, \quad (2.75a)$$

$$E_{3/2\pm}(q, \varphi) = V_{2a}q^2 \pm \left[(3\Delta)^2 + V_{1e}^2q^2 + 2V_{1e}V_{2e} \cos(3\varphi)q^3 + V_{2e}^2q^4 \right]^{\frac{1}{2}}. \quad (2.75b)$$

Due to the underlying Kramers degeneracy, each branch is twofold degenerate. A prototypical example for the topology of the APESs is shown in Fig. 2.5 (b).

Two remarks to complete the understanding:

1. Only for electronic E states, Λ is related to the electronic angular momentum, since only E states can carry a nonvanishing electronic angular momentum around the molecule-fixed axis: the C_3 axis, with an expectation value $\langle L_z \rangle = \hbar\zeta\Lambda$ [96, 97]
2. The diagonal form of the SO Hamiltonian as assumed here for both doublet and quartet cases, is strictly valid only for systems having a horizontal symmetry plane in addition to the threefold rotational symmetry axis, i.e. for systems showing D_{3h} symmetry [97]

Some further implications

We conclude the discussion of the $E \otimes e$ problem for X_3 systems by briefly mentioning some further physical consequences. All of them are beyond the scope of this thesis, but are good to keep in mind for future studies. Detailed information of the following can be found, e.g., in Ref. [161] and references therein.

- In general, totally symmetric displacements, i.e. those connected with the normal coordinate Q_1 of Eq. (2.51), are also involved in the $E \otimes e$ problem, making it in fact an $E \otimes (e + a)$ one. Whenever a complete three-dimensional description is required it is inevitable to include this additional degree of freedom
- An analytic expression of the resulting three-dimensional APES with the corresponding totally symmetric force constant and linear coupling term can be found in Ref. [161].
- In Ref. [176] the authors discuss the impact of those total symmetric vibrations.
- Due to the central COIN occurring for the $E \otimes e$ JTE of X_3 systems, they are generic for showing the molecular geometric phase [164, 177–179]

- In Ref. [178] it has been shown that experimental data for the $A \leftarrow X$ transition in Na_3 could be only reproduced correctly by *ab-initio* calculations if a geometric phase of π is imposed for the pseudorotation around the equilateral configuration. This can be viewed as an experimental observation of the Berry phase
- It can be generalized that dynamical JT systems, i.e. those showing pseudorotational motion or tunneling between the minima of the tricorner APES, show a nonzero geometric phase [179]
- The existence of this geometric phase effect can have a significant impact on femtosecond pump-probe experiments as demonstrated in Refs. [87, 180]
- For systems with very large quadratic vibrational couplings, the three additional COINs mentioned above approach the central COIN. This provides additional passes for tunneling between the neighbouring minima, eventually changing the whole dynamics. There, instead of one COIN, four COINs are encircled which does not change the sign of the wavefunction, as Berry phase only occurs when an odd number of COINs are encircled [170]

2.3.3 | The pseudo Jahn-Teller effect for X_3 systems

The pseudo Jahn-Teller effect (PJTE) [181] can be viewed as a generalization of the JT problem as reported in the previous section. It is concerned with the vibronic mixing of two or several electronic states under nuclear displacements without the explicit requirement of degeneracy among them [161]. In general, it can be shown that the PJTE is the only source of instability and distortions of high-symmetry configurations of polyatomic systems in nondegenerate states, and it contributes significantly to the instability of degenerate states. The importance of the PJTE, the broad range of its implications, and possible applications cannot be covered in this section. Thereto it is referred to, e.g., Refs. [161, 163, 182, 183] and references therein.

For nonlinear homonuclear triatomics, cases where nearly degenerate (close-in-energy) E and A states emerge are of particular interest. Here, a JT interaction in the electronic E state combined with a PJT coupling that mixes the E and A states may be observed. This is jointly called the $(E + A) \otimes e$ PJT problem. Within this framework, it remains to investigate which of the two coupling mechanisms dominate or if both enter equally. Among the alkali trimers, the Na_3 molecule is probably the most studied one with respect to the JTE; both theoretically and experimentally. It has

been shown that spectroscopic data for the electronic B state could be only sufficiently reproduced within the PJT model [86–91, 161], thus emphasizing its importance. The following discussion is restricted to the $(E + A) \otimes e$ problem, knowing full well that this represents merely one class of PJT problems.

The above treatment for the $E \otimes e$ problem can be extended to account for interactions with a third nondegenerate state nearby in energy. Hereto, the two-dimensional sub-Hilbert space that led to the JT Hamiltonian in Eq. (2.61) is increased by this additional state, hereafter designated $|\phi_0\rangle$, while assuming sufficient separation from all other states. With the states $|\phi_{\pm}\rangle$ from Eq. (2.54), corresponding to the two components of the degenerate E term, this defines a proper basis ($\{|\phi_i\rangle\} = \{|\phi_0\rangle, \{|\phi_+\rangle, |\phi_-\rangle\}$) [152, 168] to set up the Hamiltonian. In analogy to Sec. 2.3.2, the potential part of the Hamiltonian is expanded up to second order in the nuclear displacements to obtain the main physical implications. Couplings to the totally symmetric mode Q_1 are neglected. The back transformation to the real representation yields [184]

$$\mathcal{H}_{\text{PJT2}}^{\text{diab}} = \hat{T}_n \mathbb{1}_{3 \times 3} + \begin{pmatrix} \mathcal{V}_A^{(2)} & \mathcal{W}_{\text{PJT}}^{(2)} & -\mathcal{Z}_{\text{PJT}}^{(2)} \\ \mathcal{W}_{\text{PJT}}^{(2)} & \mathcal{V}_E^{(2)} + \mathcal{W}_{\text{JT}}^{(2)} & \mathcal{Z}_{\text{JT}}^{(2)} \\ -\mathcal{Z}_{\text{PJT}}^{(2)} & \mathcal{Z}_{\text{JT}}^{(2)} & \mathcal{V}_E^{(2)} - \mathcal{W}_{\text{JT}}^{(2)} \end{pmatrix}, \quad (2.76)$$

with the matrix elements $\mathcal{V}_{E/A}^{(2)}$, still using the notation from Ref. [166], representing the potentials in the absence of any coupling

$$\mathcal{V}_A^{(2)} = \Delta\varepsilon_A + V_{2a}^A(Q_2^2 + Q_3^2) \quad \text{and} \quad \mathcal{V}_E^{(2)} = \Delta\varepsilon_0 + V_{2a}^E(Q_2^2 + Q_3^2). \quad (2.77)$$

The off-diagonal matrix elements $\mathcal{W}_{\text{JT/PJT}}^{(2)}$ and $\mathcal{Z}_{\text{JT/PJT}}^{(2)}$ that describe the coupling interactions due to the JTE and PJTE, are defined via

$$\mathcal{W}_{\text{JT}}^{(2)} = V_{1e}^E Q_3 + V_{2e}^E(Q_3^2 - Q_2^2), \quad (2.78a)$$

$$\mathcal{Z}_{\text{JT}}^{(2)} = V_{1e}^E Q_2 - 2V_{2e}^E Q_2 Q_3, \quad (2.78b)$$

$$\mathcal{W}_{\text{PJT}}^{(2)} = V_{1e}^{E/A} Q_3 + V_{2e}^{E/A}(Q_3^2 - Q_2^2), \quad (2.78c)$$

$$\mathcal{Z}_{\text{PJT}}^{(2)} = V_{1e}^{E/A} Q_2 - 2V_{2e}^{E/A} Q_2 Q_3. \quad (2.78d)$$

Here, V_{2a}^Y , $Y = \{E, A\}$ are the elastic force constants for the E and A states, respectively, and V_{ie}^Z , $Z = \{E, E/A\}$ and $i = \{1, 2\}$ are the linear and quadratic vibronic coupling parameters, either describing the “pure” JT interaction (E) or the PJT mixing (E/A). Further, $\Delta\varepsilon_A$ denotes the energy gap between the E and A states at the origin, where in accordance to the treatment in Eq. (2.61) it is $\Delta\varepsilon_0 = 0$. The three branches of the

APES are then obtained from the secular equation $|\mathcal{H}_{\text{PJT}}^{\text{diab}} - [\hat{T}_n + \varepsilon(Q_2, Q_3)]\mathbb{1}_{3 \times 3}| = 0$, and are of the general form

$$E_X(Q_2, Q_3) = V_{2a}^X(Q_2^2 + Q_3^2) + \vartheta_X(Q_2, Q_3), \quad (2.79)$$

where $\vartheta_X(Q_2, Q_3)$ is the vibronic contribution [152]. For C_{2v} configurations ($Q_2 = 0$), these APESs take on a comparatively simple form, as can be directly deduced from Eq. (2.76) with $\Delta\varepsilon_0 = 0$

$$E_0(Q_3) = V_{2a}^E Q_3^2 - V_{1e}^E Q_3 - V_{2e}^E Q_3^2, \quad (2.80a)$$

$$E_{\pm}(Q_3) = \frac{1}{2} \left[V_{2a}^E Q_3^2 + \Delta\varepsilon_A + V_{2a}^A Q_3^2 + V_{1e}^E Q_3 + V_{2e}^E Q_3^2 \right] \\ \pm \frac{1}{2} \left[\left(V_{2a}^E Q_3^2 - \Delta\varepsilon_A - V_{2a}^A Q_3^2 + V_{1e}^E Q_3 + V_{2e}^E Q_3^2 \right)^2 + 4 \left(V_{1e}^{E/A} Q_3 + V_{2e}^{E/A} Q_3^2 \right)^2 \right]^{\frac{1}{2}}. \quad (2.80b)$$

The component of the degenerate E term that transforms according to the B_1 or B_2 IRREP (depending on the choice of axes) for C_{2v} geometries, corresponds to the branch E_0 . The remaining component as well as the near-in-energy third state transform as A_1 or A_2 for isosceles triangular configurations and correlate to the E_{\pm} branches. This form of the APESs displays a variety of minima, saddle points and COINs, which reflect as local minima and curve crossings in the C_{2v} subspace. For D_{3h} configurations at $Q_3 = 0$, there occurs the COIN that is characteristic for the JTE of the E state. This can be seen by proving the discontinuity of E_{\pm} at $Q_3 = 0$, i.e. taking its derivative $(\partial E_{\pm} / \partial Q_3)_{Q_3 \rightarrow 0}$. The presence of this intersections implies a linear splitting for the E-type APESs in close proximity to the degeneracy and a reversal of the energetic ordering of the $A_{1/2}$ and $B_{1/2}$ potential curves when changing the sign of Q_3 [88].

The investigation of the (B, B') system of Na_3 (comprising the 4^2A_1 , 3^2B_2 and 5^2A_1 states) in Refs. [86, 88], revealed that the linear JT coupling parameter V_{1e}^E is vanishingly small. The underlying theoretical model to explain these observations will be outlined in the following.

For vanishing PJT coupling parameters $V_{ie}^{E/A}, i = \{1, 2\}$ the solutions of the ‘‘pure’’ JT problem from Eq. (2.62) are recovered and $E_0 = \Delta\varepsilon_A + V_{2a}^A q^2$. If instead, the PJT coupling dominates the three-state interaction, i.e. if $V_{ie}^E \approx 0, i = \{1, 2\}$, the APESs using polar coordinates from Eq. (2.52) take on the form [86]

$$E_0 = V_{2a}^E q^2, \quad (2.81a)$$

$$E_{\pm} = \frac{1}{2} \left(V_{2a}^E q^2 + \Delta\varepsilon_A + V_{2a}^A q^2 \right)$$

$$\pm \frac{1}{2} \left\{ \left[\varrho^2 \left(V_{2a}^A - V_{2a}^E \right) + \Delta\varepsilon_A \right]^2 + \varrho^2 \left[\left(V_{1e}^{E/A} \right)^2 + \left(V_{2e}^{E/A} \right)^2 \varrho^2 + V_{1e}^{E/A} V_{2e}^{E/A} \varrho \cos(3\varphi) \right] \right\}^{\frac{1}{2}}. \quad (2.81b)$$

This shows that one of the two degenerate states that correlate to the E term remains unperturbed (E_0), while the nondegenerate third A state and the remaining degenerate component of the E term are dispersed about their energy by the discriminant term (E_{\pm}). For large distortions one can show that the mathematical form of E_{\pm} from Eq. (2.81) is equivalent to the one resulting from a “pure” JT treatment in Eq. (2.62), see Ref. [86]. However, despite this formal analogy of the mixing, it now arises due to *accidentally* degenerate states, rather than due to *symmetry* degenerate ones. For $\Delta\varepsilon_A \neq 0$ it further follows that, in contrast to the general case of Eq. (2.80), there is no COIN for $\varrho = 0$ (or $Q_3 = 0$). Because, for $\Delta\varepsilon_A \neq 0$, it follows from Eq. (2.81), $(\partial E_{\pm}/\partial \varrho)_{\varrho \rightarrow 0} = 0$, and thus the discontinuity vanishes. Only if the totally symmetric mode Q_1 equals a certain critical value Q_1^c , with $Q_2 = Q_3 = 0$, the energy gap $\Delta\varepsilon_A$ vanishes and a *triply* degenerate COIN forms. Thus, instead of a COIN seam in the 3D configuration space, as seen for the $E \otimes e$ JT problem, merely one single COIN is observed, whereas the crossing is avoided otherwise. The topology of the resulting coupled APESs (for $\Delta\varepsilon_A \neq 0$) is illustrated in Fig. 2.6 along the C_{2v} symmetry preserving coordinate Q_3 . As a direct consequence of the lack of a COIN for $\varrho = 0$ ($Q_3 = 0$), the energetic ordering of the $A_{1/2}$ and $B_{1/2}$ potentials does not change when changing the sign of Q_3 . Only at the critical value Q_1^c there will be an inversion of the situation leading from the topology shown in Fig. 2.6 (a) to the one in Fig. 2.6 (b).

To obtain better agreement between experiment and theory, concerning the (B, B') system of Na_3 , it might be necessary to include higher-order terms in the expansion of the potential matrix. An expansion up to sixth-order can be found in Ref. [184]. Moreover, considering couplings to the breathing mode Q_1 , which has been neglected here, might turn out relevant as well. A proper treatment that includes Q_1 couplings can be found in Ref. [91]. Furthermore, it remains questionable to what extent the assumption of vanishing linear and quadratic JT coupling parameters remains valid. This means that one has to properly investigate the parameter ranges for V_{1e}^E and V_{2e}^E where the JT coupling supersedes the PJT behaviour. Vice versa, the same should be analyzed for the PJT coupling parameters. A more detailed analysis of this and its connection to the presence or absence of the Berry phase can be found, e.g., in Refs. [88, 180].

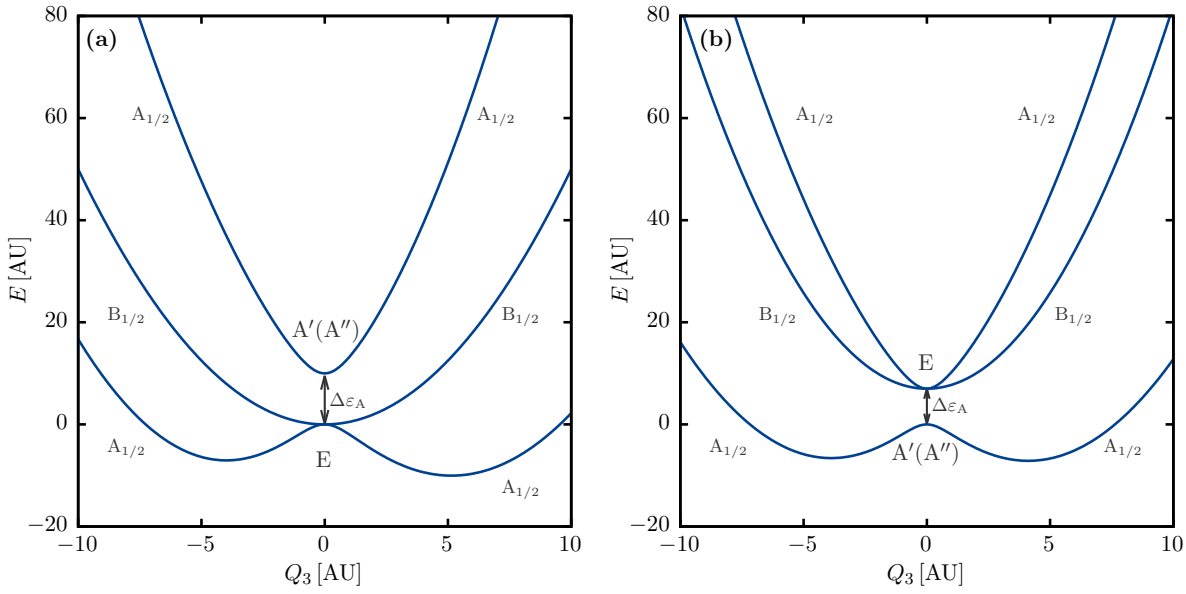
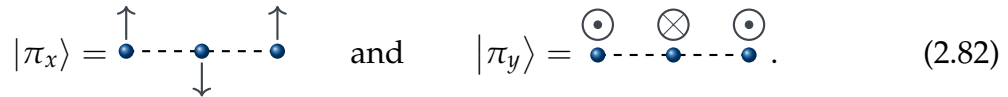


FIGURE 2.6.: Schematic illustration in the one-dimensional cross section along the symmetric distortion coordinate Q_3 of the APEs in case of a E – A pseudo Jahn-Teller effect as it emerges, e.g., in Na_3 [86]. The labeling of states for $Q_3 \neq 0$ correlates to the corresponding IRREPs of the C_{2v} point group (depending on the choice of axes). In (a) one of the two degenerate (E) states remains unperturbed, while the nondegenerate state and the remaining degenerate component dominate the interaction and disperse about their energy minimum. In (b) the situation is inverted, but the interaction is still dominated by the two $A_{1/2}$ states and the $B_{1/2}$ component remains essentially unaffected.

2.4 | Coupling effects for linear triatomics

Electronically degenerate Π states and combined cases of Π – with close-in-energy Σ states are typical scenarios for linear configurations of homonuclear alkali trimers in the energy range investigated in this thesis; see Chap. 4. Historically, it has been first observed by Herzberg and Teller in 1933 [185] that the potential energy curves of linear triatomic molecules split into two branches upon bending. These bending modes of linear triatomics are twofold degenerate and are illustrated as



In 1934, Renner [186] gave a theoretical explanation for these findings by including rovibrational couplings in a perturbative manner to account for the breakdown of the BO approximation – therefore, the splitting of *degenerate* electronic states of linear molecules is jointly called *Renner-Teller effect (RTE)*. In contrast to the JT effects the breakdown of the BO approximation is here caused by the *rotational* kinetic energy

operator instead by the vibrational one. The underlying physical interaction is a strong *Coriolis* coupling.

Since the advent of this theory, it has been a longterm belief that solely the RTE is the driving force in producing bending instabilities of linear molecules in *degenerate* electronic states. While taking into account the PJTE in understanding bending instabilities of *nondegenerate* (Σ) states in, e.g., Ref. [187], was well established, it has been shown only recently, that also for linear molecules in degenerate states the PJTE is the *only* cause of bending instabilities and distortions [163, 182, 188, 189]. Formal insight is attained by applying the same ansatz as already discussed for the treatment of JT problems in Sec. 2.3.1. Therefore, consider a high-symmetry linear configuration in an electronically degenerate Π state with corresponding wavefunctions $|\Pi_x\rangle$ and $|\Pi_y\rangle$ and set up the potential matrix in this basis, including vibronic couplings to one of the twofold degenerate bending modes, cf. Eq. (2.82), described in terms of normal coordinates Q_x and Q_y . The inclusion of only up to quadratic terms in the nuclear displacements and vibronic couplings, yields [163]

$$\mathbf{W}_{\text{RT}} = \frac{1}{2}K_0(Q_x^2 + Q_y^2)\sigma_I + F(Q_x\sigma_z - Q_y\sigma_x) + g \left[(Q_x^2 - Q_y^2)\sigma_z + 2Q_xQ_y\sigma_x \right], \quad (2.83)$$

with the bending primary force constant K_0 (i.e. the force constant without vibronic coupling), the linear vibronic coupling constant F , and the quadratic coupling constant g , calculated analogously as given in Eqs. (2.46) and (2.48), and the well-known 2×2 Pauli matrices σ_i . For a degenerate electronic term $F = 0$ due to symmetry. Thus, RT distortions are always quadratic in the bending coordinates. Solving the resulting secular equation leads to the APESs of the form

$$E_{1,2}(\varrho) = \left(\frac{1}{2}K_0 \pm |g| \right) \varrho^2, \quad (2.84)$$

where, in analogy to Eq. (2.52), cylindrical coordinates $Q_x = \varrho \cos \varphi$ and $Q_y = \varrho \sin \varphi$ were used [163, 182]. In Ref. [190] it has been shown that $K_0 > 0$ for any polyatomic system in a high-symmetry configuration. Thus, it follows that for $|g| < K_0/2$, the two APES branches of the Π term have different but positive curvatures and the degeneracy solely splits upon bending distortions as $\Delta E = |2g|\varrho^2$. Moreover, the average of the two levels $E_{\text{av}} = (1/2)(E_1 + E_2) = (1/2)K_0\varrho^2$ is independent of this effect. For $|g| > K_0/2$, the system would become unstable in the lower branch due to the negative curvature. However, it has been proven in Ref. [189] that in addition to the previous finding $K_0 > 0$, in general, for any molecular system with linear geometry, $(K_0/2 - |g|) > 0$ has to be fulfilled. This implies that *instability induced just by the RTE is not possible* or

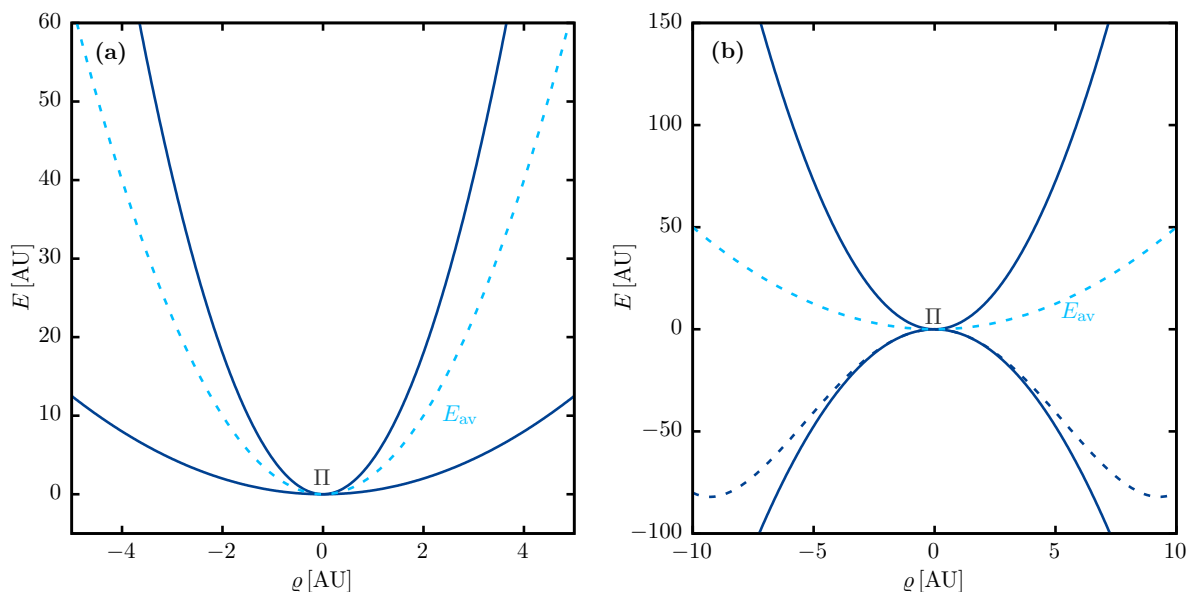


FIGURE 2.7.: Schematic illustration of the essential difference between the “pure” RTE in (a), according to Eq. (2.84), and the combined RTE plus PJTE in (b), according to Eq. (2.87), in application to linear systems in a twofold degenerate Π state. The RTE solely leads to a splitting of the degeneracy, with a softening of the lower curve (and hardening of the upper one). Only in a combined RT plus PJT treatment a bending instability of the lower curve can be explained. The dashed dark blue curve indicates a continuation of the lower state when fourth-order terms are added to Eq. (2.87). In both cases the dashed light blue curves represent the average of the two levels $E_{av} = (1/2)(E_1 + E_2)$ (see text for details).

speaking even more strictly *all instabilities and distortions of linear molecules (in degenerate or nondegenerate states) are due to, and only to the mixing with appropriate excited states in the pseudo Jahn-Teller effect (PJTE)*. This situation is illustrated in Fig. 2.7.

The physical reason for this is that the vibronic coupling with an excited state produces additional covalent bonding that makes the distorted configuration preferable. In contrast, the RTE has no such influence and the splitting of the degenerate term takes place just because the charge distribution in the two states becomes nonequivalent under the bending vibrations [182]. In Ref. [163] it has been demonstrated that simple $(\Pi + \Sigma) \otimes \pi$ or $(\Pi + \Sigma + \Sigma) \otimes \pi$ PJT approaches do not fully solve the problem for the degenerate state and are insufficient for quantitative estimates. This is because not all effective vibronic coupling interactions are included. Accounting for the PJTE along with the RTE by including both interactions in the matrix Eq. (2.83) finally solves the problem and leads to the formulation of the combined RT plus PJT problem. To this end, the PJT interaction \mathcal{P} can be estimated as a second order perturbation correction

to the degenerate term. In the $\{|\Pi_x\rangle, |\Pi_y\rangle\}$ basis the matrix elements are given as

$$\begin{aligned}\mathcal{P}_{xx} &= -\sum_n \frac{|\langle \Pi_x | (\partial H / \partial Q_x)_0 | n \rangle|^2}{\varepsilon_n - \varepsilon_0} Q_x^2 = -p Q_x^2, \\ \mathcal{P}_{yy} &= -p Q_y^2, \\ \mathcal{P}_{xy} &= -p Q_x Q_y,\end{aligned}\tag{2.85}$$

where $|n\rangle$ are the corresponding excited states with energies ε_n for which the PJT vibronic coupling constants $\langle \Pi_x | (\partial H / \partial Q_x)_0 | n \rangle = \langle \Pi_y | (\partial H / \partial Q_y)_0 | n \rangle \neq 0$, and p is positive. This leads to the modified potential matrix

$$\mathbf{W}_{\text{RT+PJT}} = \frac{1}{2}(K_0 - p)(Q_x^2 + Q_y^2)\boldsymbol{\sigma}_I + \left(g - \frac{1}{2}p\right) \left[(Q_x^2 - Q_y^2)\boldsymbol{\sigma}_z + 2Q_x Q_y \boldsymbol{\sigma}_x\right], \tag{2.86}$$

and the corresponding secular equation now gives the following form of the APESs [188]

$$E_{1,2}(\varrho) = \left[\frac{1}{2}(K_0 - p) \pm \left|g - \frac{1}{2}p\right|\right] \varrho^2. \tag{2.87}$$

Apparently, the PJTE, represented by the parameter p , reduces the primary curvature K_0 by p and the RT splitting (represented by the parameter g) by $p/2$ with $\Delta E = |2g - p|\varrho^2$. The average energy $E_{\text{av}} = (1/2)(K_0 - p)\varrho^2$ is only influenced by the PJTE.

This approach does not require any explicit knowledge of excited states or correlating energy gaps; only *ab-initio* calculated energies for the degenerate state as a function of the distortion coordinate ϱ are needed. If all three constants of Eq. (2.87) were known, this would provide a quantitative insight into the coupling mechanism. However, extracting all parameters from least-square fits to *ab-initio* calculated APESs may be insufficient. According to a procedure presented in Refs. [163, 188], it is possible to independently compute g from *ab-initio* calculations such that K_0 and p can be obtained from fitting.

The reverse in understanding this bending mechanism as combined RT plus PJT interaction, also leads to better rationalization and prediction of observables as dipole moments and spectra [189]. Concerning the former, further contributions to permanent dipole moments are possible with the inclusion of the PJTE. Moreover, the PJTE leads to a relaxation of selection rules for optical transitions, which may be important for the identification of the excited states based on spectroscopic observations.

For further reading and more details on coupling effects of polyatomic systems in linear configurations, it is referred to, e.g., Refs. [161, 163, 182, 188, 189] and references therein.

3

WAVEFUNCTION METHODS IN ELECTRONIC STRUCTURE THEORY

Since the electronic Schrödinger equation (2.3) can only be solved exactly for one-electron systems, it is inevitable to introduce approximations to describe many-electron systems. This chapter introduces corresponding *ab-initio* methods used in this work, which are all based on different ansätze for the electronic wavefunction. It will be shown to which extent electron correlation effects are recovered and the concept of basis sets as building blocks of electronic wavefunctions will be outlined.

3.1 | Many-electron wavefunctions

The electronic Hamiltonian in Eq. (2.3) only depends on the spatial coordinates of the electron. However, electrons are endowed with an intrinsic property: their spin. In a nonrelativistic framework, this property is introduced *ad hoc* in terms of two spin functions $\alpha(s)$ and $\beta(s)$, corresponding to spin up ($|\uparrow\rangle$) and spin down ($|\downarrow\rangle$), respectively [191]. The two spin functions form a complete set and are orthonormal

$$\langle\alpha|\alpha\rangle = \langle\beta|\beta\rangle = 1 \quad \text{and} \quad \langle\alpha|\beta\rangle = \langle\beta|\alpha\rangle = 0. \quad (3.1)$$

A general one-electron wavefunction can formally be written in terms of *spin orbitals*, via

$$\psi_i^\alpha(\mathbf{x}) = \varphi_i(\mathbf{r})\alpha(s) \quad \text{or} \quad \psi_i^\beta(\mathbf{x}) = \varphi_i(\mathbf{r})\beta(s), \quad (3.2)$$

where the spatial functions $\varphi_i(\mathbf{r})$ are simply called (*spatial*) *orbitals*. Since the spin- and spatial functions are assumed to be orthonormal, the relation

$$\langle\psi_i^\sigma|\psi_j^{\sigma'}\rangle = \delta_{ij}\delta_{\sigma\sigma'} \quad (3.3)$$

holds for the spin orbitals. In order to build a N -electron wavefunction $\Psi(\mathbf{x}_1, \dots, \mathbf{x}_N)$, one has to regard that the nonrelativistic electronic Hamiltonian in Eq. (2.3) makes no reference to the spin. Hence, it is not sufficient to simply introduce the spin to the wavefunction [191]. It is rather necessary to additionally account for the *Pauli exclusion principle*, generally stating that for identical fermions the wavefunction must be antisymmetric with respect to the permutation of any pairs of coordinates. For identical bosons the wavefunction must be symmetric. Since electrons have half-integer spin they are fermions and thus the wavefunction must be antisymmetric with respect to interchanging the coordinates of two electrons, i.e.

$$\Psi(\mathbf{x}_1, \dots, \mathbf{x}_i, \dots, \mathbf{x}_j, \dots, \mathbf{x}_N) = -\Psi(\mathbf{x}_1, \dots, \mathbf{x}_j, \dots, \mathbf{x}_i, \dots, \mathbf{x}_N). \quad (3.4)$$

The form of the electronic Hamiltonian in Eq. (2.3) suggests an ansatz in terms of a linear combination of products of N one-electron functions. In order to further obey the Pauli principle each orbital product has to be antisymmetrized. A generalization of these requirements is implemented in a *Slater determinant* [192], which represents the simplest N -electron wavefunction ansatz

$$\Phi_{k\ell m\dots r}(\mathbf{x}_1, \mathbf{x}_2, \dots, \mathbf{x}_N) = \frac{1}{\sqrt{N!}} \begin{vmatrix} \psi_k(\mathbf{x}_1) & \psi_\ell(\mathbf{x}_1) & \psi_m(\mathbf{x}_1) & \cdots & \psi_r(\mathbf{x}_1) \\ \psi_k(\mathbf{x}_2) & \psi_\ell(\mathbf{x}_2) & \psi_m(\mathbf{x}_2) & \cdots & \psi_r(\mathbf{x}_2) \\ \vdots & \vdots & \vdots & \ddots & \vdots \\ \psi_k(\mathbf{x}_N) & \psi_\ell(\mathbf{x}_N) & \psi_m(\mathbf{x}_N) & \cdots & \psi_r(\mathbf{x}_N) \end{vmatrix}. \quad (3.5)$$

In this notation, the spin orbitals are labeled by a single index as compared to Eq. (3.2), with $k = \{i, \sigma\}$. The factor $(N!)^{-1/2}$ accounts for proper normalization. Individual spin orbitals are grouped in different columns, while each electron coordinate corresponds to a different row. The mathematical properties of determinants ensure that the physically required antisymmetry principle of Eq. (3.4) is fulfilled. Interchanging two rows ($\hat{=}$ interchanging the coordinates of two electrons) changes the sign of the determinant and if there were two identical columns ($\hat{=}$ two electrons occupying the same spin orbital) the determinant is zero. A specific selection of an ordered set of N different spin orbitals, i.e., e.g., $k < \ell < m < \dots < r$ is called an *electron configuration* and describes a specific distribution of N electrons in these N orbitals [134].

3.2 | Hartree-Fock theory

The Hartree-Fock (HF) method was one of the first methods to solve the electronic Schrödinger equation for a general N -electron problem approximately [193, 194]. It

relies on the clamped-nuclei approximation and uses a *single* Slater determinant $|\Phi_0\rangle$ as an ansatz for the N -electron wavefunction. Consequently, it is computationally efficient and is nowadays routinely used as starting point for many subsequent methods.

3.2.1 | Closed-shell Hartree-Fock equations and the SCF method

Based on the electronic Hamiltonian from Eq. (2.3), with the individual terms according to Eq. (2.1) converted to atomic units, the energy of a system in a single Slater determinant representation, using the Slater-Condon rules, the indistinguishability of electrons, and the symmetry of the Hamiltonian with respect to permutations of electrons, becomes [140]

$$E = \langle \Phi_0 | \mathcal{H}_{\text{el}} | \Phi_0 \rangle = \sum_i h_{ii} + \sum_{i>j} (J_{ij} - K_{ij}) + V_{\text{nn}}, \quad (3.6)$$

where the one-electron integrals

$$h_{ii} = \langle \psi_i | \hat{h} | \psi_i \rangle = -\frac{1}{2} \langle \psi_i(\mathbf{x}_1) | \nabla_1^2 | \psi_i(\mathbf{x}_1) \rangle - \sum_{K=1}^M \left\langle \psi_i(\mathbf{x}_1) \left| \frac{Z_K}{|\mathbf{r}_1 - \mathbf{R}_K|} \right| \psi_i(\mathbf{x}_1) \right\rangle \quad (3.7)$$

represent the kinetic energy of a single electron that moves in the field of all M nuclei. The two-electron integrals J_{ij} and K_{ij} are defined as

$$J_{ij} = \left\langle \psi_i(\mathbf{x}_1) \psi_j(\mathbf{x}_2) \left| r_{12}^{-1} \right| \psi_i(\mathbf{x}_1) \psi_j(\mathbf{x}_2) \right\rangle, \quad (3.8a)$$

$$K_{ij} = \left\langle \psi_i(\mathbf{x}_1) \psi_j(\mathbf{x}_2) \left| r_{12}^{-1} \right| \psi_j(\mathbf{x}_1) \psi_i(\mathbf{x}_2) \right\rangle, \quad (3.8b)$$

where the former describes the classical Coulomb repulsion between two one-electron charge distributions and is therefore also denoted as *Coulomb* integral. The latter arises due to the antisymmetry of the wavefunction and is called *exchange* integral. The nuclear repulsion energy is denoted by V_{nn} . This formal notation makes no assumptions about the form of the spin orbitals ψ_i . If the number of spin-up electrons equals the number of spin-down ones and if each spatial orbital is occupied by one α - and one β -electron, this is called the *closed-shell* case, with the number of occupied orbitals $N_{\text{occ}} = N/2$. The integration over the spin-coordinates in Eq. (3.6) yields the closed-shell HF energy expression

$$E_{\text{HF}} = 2 \sum_{i=1}^{N_{\text{occ}}} h_{ii} + \sum_{i,j}^{N_{\text{occ}}} \left[2 \langle \varphi_i \varphi_j | r_{12}^{-1} | \varphi_i \varphi_j \rangle - \langle \varphi_i \varphi_j | r_{12}^{-1} | \varphi_j \varphi_i \rangle \right] + V_{\text{nn}}. \quad (3.9)$$

The objective of the Hartree-Fock method is to find the set of molecular orbitals (MOs) such that the energy according to Eq. (3.9) represents a minimum or at least a stationary point with respect to changes in these orbitals (*variation principle*). The following outlines the derivation of the corresponding matrix equations required to conveniently solve the problem numerically [195, 196].

The optimization of the MOs must be carried out such that the imposed orthonormality constraint $\langle \varphi_i | \varphi_j \rangle = \delta_{ij}$ is fulfilled at any time. This can be achieved by the method of *Lagrange multipliers*, for which the constrained minimization of the energy becomes equivalent to the unconstrained minimization of the Lagrange functional [140]

$$\min \mathcal{L}[\varphi] = \min \left(E_{\text{HF}} - \sum_{i,j}^{N_{\text{occ}}} \lambda_{ij} (\langle \varphi_i | \varphi_j \rangle - \delta_{ij}) \right), \quad (3.10)$$

which leads to the set of Hartree-Fock equations that define the optimal orbitals φ_i

$$\hat{f} |\varphi_i\rangle = \sum_j^{N_{\text{occ}}} \lambda_{ij} |\varphi_j\rangle. \quad (3.11)$$

The Fock operator \hat{f} is an effective one-electron energy operator describing the motion of one electron in the field of all nuclei via \hat{h} as defined by Eq. (3.7), and the repulsion to all other electrons through \hat{J}_j and \hat{K}_j . It is given as

$$\hat{f} = \hat{h} + \sum_j^{N_{\text{occ}}} (2\hat{J}_j - \hat{K}_j). \quad (3.12)$$

The one-electron character of the Coulomb- and exchange operator in Eq. (3.12), in contrast to Eq. (3.8), is demonstrated by their definitions

$$\hat{J}_j = \langle \varphi_j(\mathbf{r}_2) | r_{12}^{-1} | \varphi_j(\mathbf{r}_2) \rangle = \int |\varphi_j(\mathbf{r}_2)|^2 r_{12}^{-1} d\mathbf{r}_2, \quad (3.13a)$$

$$\hat{K}_j = \langle \varphi_j(\mathbf{r}_2) | r_{12}^{-1} | \varphi_i(\mathbf{r}_2) \rangle = \int \varphi_j^*(\mathbf{r}_2) r_{12}^{-1} \varphi_i(\mathbf{r}_2) d\mathbf{r}_2, \quad (3.13b)$$

which shows that \hat{J}_j describes the average local Coulomb potential at \mathbf{r}_1 arising from an electron in φ_j [191]. The two-electron integrals of Eq. (3.8) represent the corresponding matrix elements, i.e. $J_{ij} = \langle \varphi_i | \hat{J}_i | \varphi_i \rangle$ and $K_{ij} = \langle \varphi_i | \hat{K}_j | \varphi_i \rangle$.

The optimal set of orbitals as defined through Eq. (3.11) is not unique, since the energy expectation value after Eq. (3.6) and the Fock operator according to Eq. (3.12) are invariant with respect to unitary transformations. This provides a certain degree of flexibility for the orbitals: they can be mixed by unitary orbital rotations which will

reflect only in an additional phase factor of the corresponding Slater determinant [191]. In particular, the unitary transformation can be chosen such that the matrix of Lagrange multipliers in Eq. (3.11), and thus the occupied part of the Fock operator, becomes diagonal i.e. $\lambda_{ij} = \varepsilon_i \delta_{ij}$, yielding the *canonical* form of the Hartree-Fock equations

$$\hat{f} |\varphi'_i\rangle = \varepsilon_i |\varphi'_i\rangle, \quad (3.14)$$

with the corresponding MOs $|\varphi'_i\rangle$ commonly denoted as *canonical* (occupied) MOs. In the basis of canonical MOs the diagonal Lagrange multipliers ε_i can be interpreted as MO energies. With that, the Hartree-Fock energy expression after Eq. (3.9) can be rewritten as

$$E_{\text{HF}} = 2 \sum_{i=1}^{N_{\text{occ}}} \varepsilon_i - \sum_{i,j}^{N_{\text{occ}}} [2J_{ij} - K_{ij}] + V_{\text{nn}}, \quad (3.15)$$

which shows that the electronic energy does *not* equal the sum of MO energies. The factor 2 arises because in the closed-shell case each MO is occupied twice.

The MO energy as defined by the Fock operator after Eqs. (3.12) and (3.13) contains the interaction of an electron moving in the average field of all other electrons. The electron-electron repulsion is thus only accounted for in an average fashion. This lives on in the total Hartree-Fock energy as given in Eq. (3.15) and explains why this cannot be exact. Therefore, the Hartree-Fock method is also referred to as a *mean-field approximation*. These consequences are due to the approximation of a single Slater determinant as the trial wavefunction.

The Hartree-Fock equations form a set of integro-differential equations, which is also referred to as pseudo-eigenvalue problem, since the Fock operator depends, through \hat{J} and \hat{K} , on the solutions $\{\varphi_i\}$. This nonlinear structure requires iterative procedures to obtain solutions. To this end, a basis set must be introduced to represent the unknown MOs in terms of known basis functions. In the quantum chemistry context, the *LCAO approximation* is used: the linear combination of atomic orbitals (AOs) [140]. Here, the orthogonal MOs $|i\rangle \equiv |\varphi_i(\mathbf{r})\rangle$ are expanded in terms of a set of N_{AO} non-orthogonal AOs $|\mu\rangle \equiv |\chi_\mu(\mathbf{r})\rangle$, via

$$|i\rangle = \sum_{\mu=1}^{N_{\text{AO}}} C_{\mu i} |\mu\rangle, \quad (3.16)$$

where the expansion coefficients $C_{\mu i}$ are called MO coefficients. Since N_{AO} is always finite, the LCAO approximation of the resulting MO basis is not complete. However,

by increasing the number of AO functions, the accuracy of the LCAO ansatz can be driven to, in principle, any desired accuracy (for more details see Sec. 3.5). As MOs are assumed to be orthonormal it follows

$$\langle i|j\rangle = \sum_{\mu,\nu} C_{\mu i} \langle \mu|\nu\rangle C_{\nu j} = \left[C^\dagger S C \right]_{ij} = \delta_{ij}, \quad (3.17)$$

with the AO overlap matrix $S_{\mu\nu} = \langle \mu|\nu\rangle$.

By inserting the LCAO ansatz (3.16) into the Hartree-Fock equations (3.14) and projecting onto a specific AO, yields

$$\sum_{\nu=1}^{N_{\text{AO}}} \underbrace{\langle \mu | \hat{f} | \nu \rangle}_{F_{\mu\nu}} C_{\nu i} = \sum_{\nu=1}^{N_{\text{AO}}} \underbrace{\langle \mu | \nu \rangle}_{S_{\mu\nu}} C_{\nu i} \varepsilon_i, \quad (3.18)$$

or equivalently in matrix notation

$$FC = SC\varepsilon. \quad (3.19)$$

These are the *Roothaan-Hall equations*, which are nothing but the Hartree-Fock equations in the AO basis [195, 196]. Here, F is the Fock matrix in AO basis, S the overlap matrix, C the coefficient matrix and ε the diagonal matrix with orbital energies ε_i . The Fock matrix in the AO basis, using Eqs. (3.8), (3.12) and (3.16), becomes

$$F_{\mu\nu} = H_{\mu\nu} + G_{\mu\nu}, \quad (3.20a)$$

$$= H_{\mu\nu} + \sum_{\gamma\delta} D_{\gamma\delta} \left[(\mu\nu|\gamma\delta) - \frac{1}{2}(\mu\gamma|\delta\nu) \right], \quad (3.20b)$$

with the one-electron Hamiltonian $H_{\mu\nu}$ in AO basis and the electron interaction matrix $G_{\mu\nu}$ defined in Mulliken notation and in dependence of the density matrix $D_{\gamma\delta}$. The latter is given by

$$D_{\mu\nu} = 2 \sum_{i=1}^{N_{\text{occ}}} C_{\mu i} C_{\nu i} = 2 \left[C_o C_o^\dagger \right]_{\mu\nu}, \quad (3.21)$$

where the subscript “o” denotes the $N_{\text{AO}} \times N_{\text{occ}}$ coefficient matrix describing occupied MOs. The density matrix is related to the charge density $\varrho(\mathbf{r})$ through [191]

$$\varrho(\mathbf{r}) = 2 \sum_{i=1}^{N_{\text{occ}}} |\varphi_i(\mathbf{r})|^2 = \sum_{\mu\nu} D_{\mu\nu} \chi_\mu(\mathbf{r}) \chi_\nu(\mathbf{r}). \quad (3.22)$$

With these quantities we can also rewrite the closed-shell Hartree-Fock energy expression in matrix form, which is nothing but Eq. (3.9) in the AO basis

$$E_{\text{HF}} = \text{tr} \left[\mathbf{D} \cdot \left(\mathbf{H} + \frac{1}{2} \mathbf{G} \right) \right] + V_{\text{nn}}. \quad (3.23)$$

Due to the transformation from the MO- to the AO basis, all relevant equations are now given in matrix form as required for an efficient implementation as a computer program. The Roothaan-Hall equations are still, due to the dependence of the Fock matrix on the MO coefficients, as seen from Eqs. (3.20) and (3.21), nonlinear and require an iterative procedure to be solved. This procedure starts off with an initial guess for the density matrix \mathbf{D} or, according to Eq. (3.22), guessing a charge density. This is then used to compute the Fock matrix according to Eq. (3.20), where for a given basis set the one-electron Hamiltonian and the two-electron integrals are constants and are thus predetermined. Subsequent diagonalization of the Fock matrix yields, according to Eq. (3.19), a new set of optimized MO coefficients \mathbf{C} . This step usually requires to first transform the Fock matrix and thus the Roothaan-Hall equations to an orthogonal basis to solve the eigenvalue problem there and then transform back to the original basis [191]. With the new set \mathbf{C} , a new density and thus Fock matrix is calculated. This procedure is continued until the coefficients used for constructing the Fock matrix equal those resulting from its diagonalization [140]. If the MO coefficients do not change so neither does the density matrix. Therewith, the field that would be calculated from the charge density of Eq. (3.22) is consistent (identical) with the field that produced a particular charge density by solving the Hartree-Fock equations. This is why this procedure is commonly called *self-consistent-field (SCF) method*.

The Roothaan-Hall equations invoke N_{AO} MOs while the Fock matrix resulting from Eq. (3.12) *a priori* only depends on N_{occ} occupied MOs. The corresponding N spin orbitals form the variational Hartree-Fock ground state wavefunction $|\Phi_0\rangle$. The remaining $N_{\text{virt}} = N_{\text{AO}} - N_{\text{occ}}$ orbitals are called *virtual* MOs and are orthogonal to all the occupied ones. The SCF method involves a number of crucial technical details, such as the Brillouin conditions, resulting from the existence of virtual orbitals, used as convergence criterion. A more comprehensive review can be found, e.g., in Refs. [140, 191].

3.2.2 | Open-Shell Hartree-Fock theory

The previous discussion assumed that the spin orbitals are represented by Eq. (3.2), where each spatial orbital is doubly occupied by two electrons with antiparallel spin.

This clearly introduces a restriction to the spatial orbitals and the corresponding Hartree-Fock method, which is usually used for closed-shell systems, is therefore denoted as *restricted Hartree-Fock (RHF)*. However, this restriction is not mandatory and especially for open-shell systems it is important to consider all possibilities on how to describe the spatial part. In the following high-spin coupled systems, in which all open-shell orbitals are occupied by one α -spin electron (e.g. quartets) are considered. These are the only cases for which a single reference wavefunction ansatz provides a sufficient zeroth-order description. For low-spin coupled species, two or even more determinants were required, which will be discussed in Sec. 3.4.

Lifting the restriction that the spatial orbitals are of the same form for both α - and β -spin functions leads to the *unrestricted Hartree-Fock (UHF)* method. Here, the spin orbitals are defined as

$$\psi_i^\alpha(\mathbf{x}) = \varphi_i^\alpha(\mathbf{r})\alpha(s) \quad \text{and} \quad \psi_i^\beta(\mathbf{x}) = \varphi_i^\beta(\mathbf{r})\beta(s), \quad (3.24)$$

with in general (but not always) different spatial orbitals $\varphi_i^\alpha(\mathbf{r})$ and $\varphi_i^\beta(\mathbf{r})$. Maintaining the restriction according Eq. (3.2) for open-shell systems leads to the *restricted open-shell Hartree-Fock (ROHF)* approach. An important consequence of the two different choices is that only the RHF- and ROHF wavefunctions are eigenfunctions of the total N -electron spin operators \hat{S}^2 and \hat{S}_z . UHF wavefunctions are in general not eigenfunctions of \hat{S}^2 , but still of \hat{S}_z , and are thus called *spin contaminated* or *spin-symmetry broken*. In this case spin states of different multiplicities are admixed [140, 191]. The derivation of the UHF and ROHF equations is beyond the scope of this thesis, see, e.g., Refs. [140, 191, 197, 198] for more details.

3.2.3 | Electron correlation effects

The single Slater determinant ansatz, on which the Hartree-Fock method is based, is merely an approximation and results in a mean-field description of the electron movement. The corresponding energy is, due to the underlying variation principle, always an upper bound to the exact energy. It is therefore convenient to introduce the correlation energy

$$E_{\text{corr}} = E_{\text{exact}} - E_{\text{HF}}, \quad (3.25)$$

as a quantity measuring the lacking physics in the Hartree-Fock approach. The term “exact” refers to the solution of the non-relativistic Schrödinger equation as defined in Eq. (2.3) with full correlation and a complete basis set. The correlated movement of

electrons can be categorized by *Fermi correlation* and *Coulomb correlation*. The former is connected with the Pauli principle according to which the probability of finding two electrons with the same spin at the same position must vanish. This is also connected with the *Fermi hole* surrounding a given electron. This is already accounted for in the Hartree-Fock theory through the exchange operator \hat{K}_i and through the inherent antisymmetry of a Slater determinant. However, also electrons with opposite spins tend to avoid each other, which is not accounted for in the Hartree-Fock theory leaving them effectively uncorrelated due to the underlying mean-field character. This evasive motion of electrons is due their repulsive Coulomb interaction through which they interact instantaneously. The correlation energy according to Eq. (3.25) thus refers to Coulomb correlation. Hence, it is at the heart of any theoretical model of quantum chemistry to recover as much of this simultaneous pairwise interactions as possible. The corresponding methods are often called post-Hartree-Fock approaches.

Mathematically, the physical observation of evasive motion can be understood by inspecting the form of the Hamiltonian in Eq. (2.3) for the He atom in its ground state. Here, the electron-electron Coulomb interaction $\propto r_{12}^{-1}$ diverges when their positions coincide [199, 200]. As the stationary Schrödinger equation still needs to be fulfilled, a second infinity with opposite sign is required. This can only be introduced via the kinetic energy operator. Divergent second derivatives occur if there are discontinuities in the first derivative that reflect in a *cusp* in the electronic wavefunction for $r_{12} \rightarrow 0$. This is schematically illustrated in Fig. 3.1.

For any atomic or molecular system there is a decreased probability for finding two electrons at the same position due to the Coulomb interaction, which is referred to as *Coulomb hole*. Consequently, certain cusp conditions for the wavefunction have to be fulfilled in general.

By further subdividing into *dynamic correlation* and *static correlation*, it is accounted for the fact that the Coulomb correlation varies significantly with the bond length. Dynamic correlation effects are present over the whole range of internuclear distances. In the short-range region it is mainly characterized by the Coulomb hole. At intermediate distances, the position of one electron defines the probability of finding other electrons at other positions. In the long-range region dynamic correlation gives rise to dispersion interactions. Dynamic correlation effects can be accounted for by including more Slater determinants into the wavefunction ansatz. These are generated by performing virtual excitations from the Hartree-Fock determinant [199]. This procedure leads to accurate results whenever the Hartree-Fock solution provides a sufficient zeroth-order

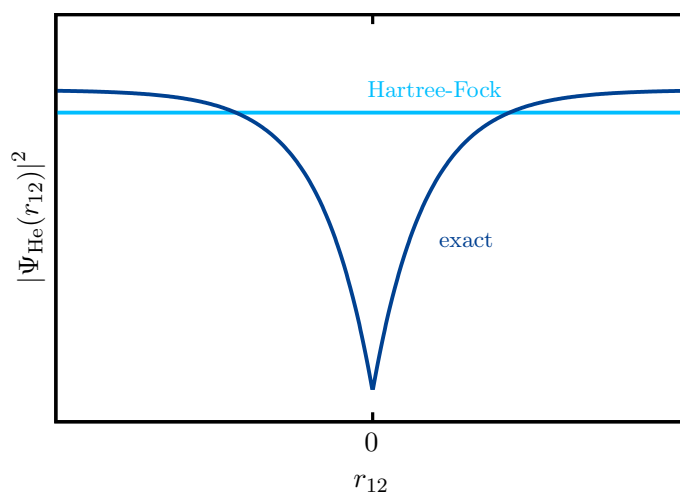


FIGURE 3.1.: Qualitative probability density for the exact helium ground state wavefunction. The probability for finding two electrons with opposite spin at the same position, i.e. $r_{12} \rightarrow 0$ decreases due to their repulsive Coulomb interaction (Coulomb hole). The cusp in the electronic wavefunction results from the singularity of the Coulomb potential for $r_{12} = 0$ (see text). Hartree-Fock theory merely accounts for Coulomb interaction in an averaged fashion leaving the electrons uncorrelated.

description and are thus denoted *single-reference correlation methods*.

Whenever a single Slater determinant does not provide a good description of the system these methods fail. Such situations, referred to as static correlation, arise if a system has several (nearly) degenerate orbitals but less electrons than necessary to fill these orbitals. Typical examples, related to this thesis, are homonuclear alkali-metal triatomics in their doublet ground states as schematically illustrated in the schematic representation in Fig. 3.2. In this case, two or more energetically equivalent (near-degenerate) determinants have to be included to obtain a sufficient zeroth-order wavefunction. Corresponding methods are thus denoted as *multireference correlation methods*.

3.3 | Single-reference correlation methods

Accounting for dynamic correlation effects requires a more flexible ansatz for the trial wavefunction compared to the single Slater determinant approach. Whenever the Hartree-Fock reference provides a sufficient zeroth-order description, this flexibility is obtained by performing virtual excitations from it. This section introduces two of such single-reference correlation methods.

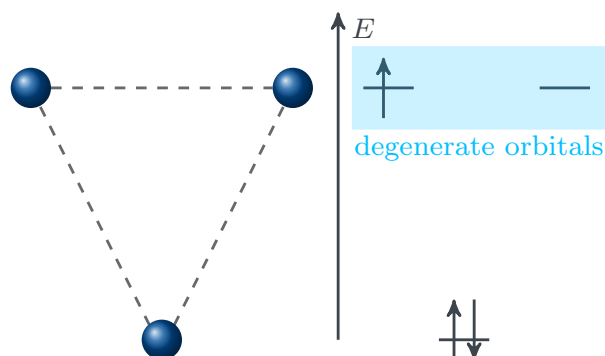


FIGURE 3.2.: Schematic representation of the MO structure of an alkali-metal trimer (e.g. K_3 or Rb_3) in their doublet ground state configuration. There are two energetically degenerate MOs which the third electron can occupy thus representing a case with static correlation. A multireference correlation approach is required.

3.3.1 | Configuration Interaction

The Roothaan-Hall equations (3.19) of Sec. 3.2.1 were derived using N_{AO} atomic basis functions and thus their solution yields the same number of MOs. However, only the energetically lowest N_{occ} occupied orbitals were used to build the resulting HF ground state determinant $|\Phi_0\rangle$. The remaining $N_{\text{virt}} = N_{\text{AO}} - N_{\text{occ}}$ virtual MOs ($\cong 2N_{\text{AO}} - N$ virtual spin orbitals) can be used to construct excited Slater determinants. Starting from the HF reference determinant by replacing one occupied orbital i with a virtual orbital a , leads to a singly excited determinant $|\Phi_i^a\rangle$. Running over all pairs of occupied and virtual orbitals results in the manifold of all possible single excitations. The same procedure can be applied to produce doubly, triply, etc. excited determinants until all N electrons are distributed in all possible ways in the virtual subspace. These determinants can be used as a basis in which to expand the exact N -electron wavefunction, which provides enough flexibility to keep electrons apart. This results in the *configuration interaction (CI) ansatz* [191]

$$|\Psi_{\text{FCI}}\rangle = c_0 |\Phi_0\rangle + \left(\frac{1}{1!}\right)^2 \sum_{i,a} c_i^a |\Phi_i^a\rangle + \left(\frac{1}{2!}\right)^2 \sum_{ij,ab} c_{ij}^{ab} |\Phi_{ij}^{ab}\rangle + \dots = \sum_I c_I |\Phi_I\rangle, \quad (3.26)$$

with intermediate normalization $\langle \Phi_0 | \Psi_{\text{FCI}} \rangle = 1$. The corresponding energies and (generalized) expansion coefficients c_I are determined variationally, which transforms into solving the secular equation

$$\sum_J \langle \Phi_I | \mathcal{H}_{\text{el}} | \Phi_J \rangle c_J = c_I E_{\text{CI}}, \quad (3.27)$$

which is equivalent to diagonalizing the electronic Hamiltonian in the basis $\{|\Phi_I\rangle\}$. The electronic ground state corresponds to the lowest eigenvalue and the n -th eigenvalue to the n -th state.

The $\{|\Phi_I\rangle\}$ basis spans a complete space of all allowed N -electron wavefunctions. If $N_{\text{AO}} \rightarrow \infty$, the wavefunction in Eq. (3.26) would represent the formally exact solution of the nonrelativistic electronic Schrödinger equation. Although, N_{AO} is always finite Eq. (3.26) still provides the best possible solution within the subspace spanned by these basis functions. It is called the *full configuration interaction (FCI)* wavefunction. The total number of n -tuply excited determinants that can be build from N occupied and $2N_{\text{AO}} - N$ virtual spin orbitals is determined by [191]

$$\#_{\text{det}}(n) = \binom{N}{n} \binom{2N_{\text{AO}} - N}{n}. \quad (3.28)$$

In total this amounts to $\binom{2N_{\text{AO}}}{N}$ different N -electron Slater determinants which is, even for small molecules in small basis sets, of the order 10^9 . By exploiting the fact that there is no mixing between wave functions with different spin (provided, e.g. spin-orbit coupling is neglected in the Hamiltonian), the number of determinants can be reduced significantly, i.e. keep only those which are eigenfunctions of \hat{S}_z with the same eigenvalue. In practice one further takes appropriate linear combinations of the remaining determinants such that they are eigenfunctions of \hat{S}^2 . They are called *configuration state functions (CSFs)*. Nevertheless, the factorial growth of the number of determinants limits the application of FCI to small molecules with moderate basis set sizes. Thus, it is necessary to truncate the FCI expansion in Eq. (3.26).

The electronic Hamiltonian describes at most pairwise interactions, therefore twofold excitations should recover most of the physics of correlated electron movement. This defines the CISD method, which only contains the first three terms of Eq. (3.26). However, truncated CI methods are in general no longer size extensive, while FCI is. This means, given a molecule XY it is no longer possible to write the total wavefunction as a product of the separated fragments [201], i.e.

$$\Psi_{\text{CISD}}^{XY} \neq \mathcal{A}\Psi_{\text{CISD}}^X \Psi_{\text{CISD}}^Y, \quad (3.29)$$

where the operator \mathcal{A} accounts for proper antisymmetrization. Therewith, the energy of the supersystem of two infinitely separated molecules X and Y cannot be compared with the sum of both fragments treated separately

$$E_{\text{CISD}}^{XY} \neq E_{\text{CISD}}^X + E_{\text{CISD}}^Y. \quad (3.30)$$

This constitutes a severe problem since experimentally measured energies are relative energies. Thus, truncated CI methods are nowadays barely used.

3.3.2 | Coupled-Cluster theory

The aforementioned problem of size extensivity is resolved by the coupled-cluster wavefunction ansatz. In the following, the fundamental equations are derived and several standard approximations within this theoretical framework are outlined. This leads to methods which are computationally feasible and produce accurate results. In this discussion, the indices i, j, k, \dots shall refer to occupied, a, b, c, \dots to virtual and p, q, r, \dots to any kind of orbitals.

A glimpse on second quantization

Coupled-cluster theory is most efficiently formulated within the formalism of second quantization in which the physics is directly encoded in the inherent algebra. Slater determinants are represented through occupation number vectors (ONVs), which represent the mathematical stage: the Fock space. In ONVs, spin orbitals, as building blocks of Slater determinants, are transformed to a binary encoding, where the occupation numbers “1” denote an occupied spin orbital and “0” an unoccupied one. A HF calculation yields a set of $\{\psi_i\}$ occupied spin-orbitals building the HF ground state wavefunction $|\Phi_0\rangle$. The corresponding ONV representation becomes

$$|\Phi_0\rangle = |\psi_i\psi_j\psi_k\cdots\rangle \equiv |1, 1, 1, \cdots\rangle . \quad (3.31)$$

Excited determinants are generated from this HF reference determinant by applying fermionic creation and annihilation operators. For instance, a singly excited determinant is defined as

$$|\Phi_i^a\rangle = a_a^\dagger a_i |\Phi_0\rangle , \quad (3.32)$$

where an occupied orbital $\psi_i(1 \rightarrow 0)$ is replaced by a virtual one $\psi_a(0 \rightarrow 1)$. The creation and annihilation operators fulfill the following anti-commutation rules

$$\left[a_p^\dagger, a_q^\dagger \right]_+ = [a_p, a_q]_+ = 0 \quad \text{and} \quad \left[a_p, a_q^\dagger \right]_+ = \left[a_q^\dagger, a_p \right]_+ = \delta_{pq} , \quad (3.33)$$

which ensure that the Pauli principle is fulfilled [202]. They may be also used to express the electronic Hamiltonian in second quantization which, neglecting the constant nuclei repulsion term V_{nn} , becomes [27, 201]

$$\hat{H}_{el} = \sum_{pq} \langle \psi_p | \hat{h} | \psi_q \rangle a_p^\dagger a_q + \frac{1}{4} \sum_{pqrs} \langle \psi_p \psi_q | | \psi_r \psi_s \rangle a_p^\dagger a_q^\dagger a_s a_r , \quad (3.34)$$

with the one-electron integrals $\langle \psi_p | \hat{h} | \psi_q \rangle$ and the antisymmetrized two-electron integrals $\langle \psi_p \psi_q || \psi_r \psi_s \rangle \equiv \langle \psi_p \psi_q | r_{12}^{-1} | \psi_r \psi_s \rangle - \langle \psi_p \psi_q | r_{12}^{-1} | \psi_s \psi_r \rangle$.

The subsequent derivation of the coupled-cluster working equations shows that they involve evaluating matrix elements and expectation values. This is simplified by introducing the concept of normal ordering and Wick's theorem [203], which is explained in more detail in the appendix B. Here suffice it to say that normal ordering provides a systematic way of bookkeeping for nonzero contributions and Wick's theorem implies that for expectation values only fully contracted terms give nonvanishing contributions [201]. Moreover, Wick's theorem allows to cast the second-quantized electronic Hamiltonian after Eq. (3.34) into the normal-ordered form (subscripts "N") [27]

$$\hat{H}_{\text{el}} = E_0 + \sum_{pq} f_p^q \{ a_p^\dagger a_q \} + \frac{1}{4} \sum_{pqrs} g_{pq}^{rs} \{ a_p^\dagger a_q^\dagger a_s a_r \}, \quad (3.35a)$$

$$= E_0 + \hat{f}_N + \hat{W}_N, \quad (3.35b)$$

with the HF reference energy $E_0 = \langle \Phi_0 | \hat{H}_{\text{el}} | \Phi_0 \rangle$, the one-particle operator \hat{f}_N , given in terms of the Fock matrix elements f_p^q according to Eq. (3.12), and the two-particle operator \hat{W}_N with the antisymmetrized integrals $g_{pq}^{rs} = \langle \psi_p \psi_q || \psi_r \psi_s \rangle$. In the literature it is also convenient to introduce a correlation Hamiltonian as $\hat{H}_N = \hat{H} - E_0$ [201].

Coupled-cluster ansatz and fundamental equations

To overcome the size extensivity issue resulting from a truncated CI wavefunction after Eq. (3.26), an ansatz for which the product wavefunction recovers the original form is required. This suggests an exponential function acting on the Hartree-Fock reference $|\Phi_0\rangle$ and leads to the coupled-cluster ansatz [204, 205]

$$|\Psi_{\text{CC}}\rangle = e^{\hat{T}} |\Phi_0\rangle = \sum_{k=0}^{\infty} \frac{1}{k!} \hat{T}^k |\Phi_0\rangle. \quad (3.36)$$

For a system of N electrons, the *cluster operator* \hat{T} , generates all kinds of singly, doubly, triply, etc. up to N -fold excited determinants and is defined via

$$\hat{T} = \sum_{n=1}^N \hat{T}_n. \quad (3.37)$$

The n -fold excitation operators \hat{T}_n obey the definition

$$\hat{T}_n = \left(\frac{1}{n!} \right)^2 \sum_{ij\dots ab\dots}^n t_{ij\dots}^{ab\dots} \{ a_a^\dagger a_b^\dagger \dots a_j a_i \dots \}, \quad (3.38)$$

where the coefficients $t_{ij\dots}^{ab\dots}$ are called the cluster *amplitudes*, and normal ordering of the creation and annihilation operators is assumed [206]. By including all operators up to \hat{T}_N , the coupled-cluster and the FCI ansatz according to Eq. (3.26) are equivalent and will produce the same wavefunction. However, due to the exponential parametrization in the CC theory, excitations are introduced in a different manner compared to the linear FCI ansatz. For double excitations, the following relationship between CI and CC may be established

$$\hat{C}_2 = \hat{T}_2 + \frac{1}{2}\hat{T}_1^2. \quad (3.39)$$

This shows that in CC theory, double excitations enter through *connected* terms (\hat{T}_2), describing real two-electron correlations, and *disconnected* terms (\hat{T}_1^2) describing simultaneous single excitations [201]. In general, connected \hat{T}_n operators may be interpreted as accounting for true n -electron correlation effects.

When considering two infinitely separated systems X and Y, the structure of the coupled-cluster ansatz defines a total cluster operator as $\hat{T} = \hat{T}^X + \hat{T}^Y$ and the total wavefunction according to

$$|\Psi_{CC}^{XY}\rangle = e^{\hat{T}} |\Phi_0^{XY}\rangle = e^{\hat{T}^X} e^{\hat{T}^Y} |\Phi_0^{XY}\rangle = \mathcal{A} |\Psi_{CC}^X\rangle |\Psi_{CC}^Y\rangle, \quad (3.40)$$

ensuring thus the separability of the wavefunction and consequently also the size-consistency criterion for the energy: $E_{CC}^{XY} = E_{CC}^X + E_{CC}^Y$ [201].

The CC equations to determine the energy and the cluster amplitudes follow from the stationary Schrödinger equation, with the normal-ordered Hamiltonian (omitting the subscript “el”) according to Eq. (3.35) and the CC ansatz (3.36). The multiplication from the left by $e^{-\hat{T}}$ and subsequently project onto either the reference or onto excited determinants, yields

$$\langle \Phi_0 | e^{-\hat{T}} \hat{H} e^{\hat{T}} | \Phi_0 \rangle = \langle \Phi_0 | \bar{H} | \Phi_0 \rangle = E, \quad (3.41a)$$

$$\langle \Phi_I | e^{-\hat{T}} \hat{H} e^{\hat{T}} | \Phi_0 \rangle = \langle \Phi_I | \bar{H} | \Phi_0 \rangle = 0, \quad (3.41b)$$

using intermediate normalization $\langle \Phi_0 | \Psi_{CC} \rangle = 1$. In Eq. (3.41), the *similarity transformed Hamiltonian* \bar{H} has been introduced, which is evaluated from the Baker-Campbell-Hausdorff (BCH) expansion

$$\bar{H} = \hat{H} + [\hat{H}, \hat{T}] + \frac{1}{2!} [[\hat{H}, \hat{T}], \hat{T}] + \frac{1}{3!} [[[\hat{H}, \hat{T}], \hat{T}], \hat{T}] + \frac{1}{4!} [[[[\hat{H}, \hat{T}], \hat{T}], \hat{T}], \hat{T}]. \quad (3.42)$$

As follows from Wick’s theorem, the termination after fourfold commutators is exact, since the electronic Hamiltonian contains no more than two-electron operators giving

rise to at most four contractions [27]. All higher order terms would only contain commutators with the cluster operators which commute and thus vanish. The projection technique in combination with the BCH expansion lead to decoupled amplitude and energy equations which, due to Eq. (3.42), assume finite expressions. The general CC energy may be derived using the BCH expansion and Wick's theorem from which it follows that only fully contracted terms contribute [201]

$$E_{\text{CC}} = E_0 + \underbrace{\sum_{ia} f_i^a t_i^a + \frac{1}{4} \sum_{ijab} g_{ij}^{ab} t_{ij}^{ab} + \frac{1}{2} \sum_{ijab} g_{ij}^{ab} t_i^a t_j^b}_{E_{\text{corr}}}. \quad (3.43)$$

The CC correlation energy is thus fully determined by singles and doubles amplitudes, but higher excitation operators contribute indirectly through the corresponding t_i^a and t_{ij}^{ab} amplitude equations.

The projection technique comes with one drawback: the similarity transformed Hamiltonian \bar{H} is no longer hermitian and with that the CC energy cannot be determined variationally and will thus not be an upper bound to the exact energy [201].

Approximations

The inclusion of all excitation operators up to \hat{T}_N is, as already stated for the FCI approach, a computationally unsolvable problem for all but very small systems [140]. In practice, the cluster operator after Eq. (3.37) needs to be truncated at a reasonable rank. Thus, neither the derived amplitudes nor the corresponding correlation energy and wavefunction are exact. Including only singles and doubles excitations, i.e. $\hat{T} = \hat{T}_1 + \hat{T}_2$, defines the CCSD method [207–210] where the amplitudes are obtained by projecting onto the manifold of singly and doubly excited determinants $\langle \Phi_I | \in \{ \langle \Phi_i^a |, \langle \Phi_{ij}^{ab} | \}$ in Eq. (3.41). The computational scaling of CCSD is $\mathcal{O}(N_{\text{occ}}^2 N_{\text{virt}}^4) \propto \mathcal{O}(N_{\text{AO}}^6)$ [27]. The next higher level, $\hat{T} = \hat{T}_1 + \hat{T}_2 + \hat{T}_3$, defines the CCSDT method [34–37], which scales as $\mathcal{O}(N_{\text{occ}}^3 N_{\text{virt}}^5) \propto \mathcal{O}(N_{\text{AO}}^8)$. By including also connected fourfold excitations in \hat{T} , gives the CCSDTQ model [42–45] with a scaling of $\mathcal{O}(N_{\text{occ}}^4 N_{\text{virt}}^6) \propto \mathcal{O}(N_{\text{AO}}^{10})$. Nowadays, there are also codes available that can in principle generate any kind of excitation rank which are referred to as general CC models [46–48]. However, the scaling behavior shows that higher excitations are only feasible, if at all, for very small systems rendering the CCSD method to the only generally applicable one.

It has been shown that to produce accurate results often higher excitations, in particular triples, are required [29]. This led to the development of methods that include effects of higher excitations approximately. The proposed methods are either

classified as *iterative* or *non-iterative* approaches. For approximations to CCSDT both approaches reduce the computational costs from $\mathcal{O}(N_{\text{AO}}^8)$ to $\mathcal{O}(N_{\text{AO}}^7)$.

Within the first category Bartlett *et al.* suggested a class of methods, which treat triples excitations perturbatively, but include them systematically into the solution of the amplitude equations: the CCSDT- n methods, with $n = 1b, 2, 3, 4$ [211–215]. In all those approaches, the singles and doubles residuals are identical to those of the full CCSDT method. Hence, the CCSDT- n methods only differ in the way the triples residuals are treated. Here further terms are subsequently included but any N_{AO}^8 -scaling contributions are avoided. For the $n = 1-3$ methods the only contribution from the \hat{T}_3 operator in the triple excitation residual appears via $\langle \Phi_0 | \hat{T}_3^\dagger \hat{f}_N \hat{T}_3 | \Phi_0 \rangle$ defining an equation for determining the corresponding triples amplitudes t_{ijk}^{abc} . This provides an iterative procedure where the triples amplitudes are first computed “on the fly” immediately followed by calculating the resulting contribution of \hat{T}_3 in the projection onto the singles and doubles subspaces. The CCSDT-4 method partially includes N_{AO}^8 terms via the full term $\langle \Phi_{I_3} | [\hat{H}, \hat{T}_3] | \Phi_0 \rangle$ and is thus almost as expensive as CCSDT.

In non-iterative approaches, converged singles and doubles amplitudes from CCSD computations are used to perturbatively formulate energy corrections due to triples excitations. This leads to the CCSD(T) method which is, due to its great success in producing accurate results for many different chemical problems with only $\mathcal{O}(N_{\text{AO}}^7)$ computational scaling, often referred to as the “gold standard” of quantum chemistry [33]. A rigorous derivation of the corresponding equations can be found, e.g., in Refs. [28–32, 201], while the main aspects are outlined in the following.

A perturbative treatment of coupled-cluster theory starts with partitioning the normal-ordered Hamiltonian from Eq. (3.35) by defining $E_0 + \hat{f}_N$ as zeroth-order contribution and considering \hat{W}_N as a perturbation

$$\hat{H} = \hat{H}^{(0)} + \lambda \hat{H}^{(1)}, \quad (3.44)$$

where $\lambda \in [0, 1]$ is a switching parameter. This also requires perturbed wavefunctions and suggests to decompose the cluster operators by orders of perturbation theory

$$\hat{T}_n = \hat{T}_n^{(1)} + \hat{T}_n^{(2)} + \hat{T}_n^{(3)} + \dots \quad (3.45)$$

Moreover, Eqs. (3.44) and (3.45) lead to an expansion of the similarity transformed Hamiltonian after Eq. (3.42) in orders of perturbation theory and thus, after Eq. (3.41), also of the energies

$$\tilde{H} = \tilde{H}^{(0)} + \tilde{H}^{(1)} + \tilde{H}^{(2)} + \dots, \quad (3.46a)$$

$$E = E^{(0)} + E^{(1)} + E^{(2)} + \dots \quad (3.46b)$$

Alternatively, one may cast the CC equations (3.41) into a Lagrange functional and require its stationarity with respect to variations of the cluster amplitudes. In both approaches Wick's theorem is used to derive the corresponding equations for each perturbation order. With this kind of analysis it was shown that CCSD is complete through third order and already contains higher-order contributions through disconnected terms [201]. The triples excitation operator \hat{T}_3 first enters at fourth order perturbation theory defining an corresponding fourth order energy increment to E_{CCSD} . By assuming canonical orbitals, this energy expression is derived to

$$E_{(T)}^{(4)} = \langle \Phi_0 | \hat{T}_2^\dagger \hat{W}_N \hat{T}_3 | \Phi_0 \rangle = - \langle \Phi_0 | \hat{T}_3^\dagger \hat{f}_N \hat{T}_3 | \Phi_0 \rangle = - \frac{1}{36} \sum_{ijk} \sum_{abc} \left(t_{ijk}^{abc} \right)^2 D_{ijk}^{abc}, \quad (3.47)$$

where $D_{ijk}^{abc} = \varepsilon_a + \varepsilon_b + \varepsilon_c - \varepsilon_i - \varepsilon_j - \varepsilon_k$ is the sum of orbital energies that equal the diagonal Fock matrix elements. The triples amplitudes in Eq. (3.47) are determined from the following perturbative expression

$$t_{ijk}^{abc} = - \frac{\langle \Phi_{ijk}^{abc} | [\hat{W}_N, \hat{T}_{2,\text{CCSD}}] | \Phi_0 \rangle}{\varepsilon_a + \varepsilon_b + \varepsilon_c - \varepsilon_i - \varepsilon_j - \varepsilon_k} = - \frac{\mathcal{P}(a|bc)\mathcal{P}(i|jk) \left(\sum_d g_{ab}^{id} t_{dc}^{jk} - \sum_\ell g_{al}^{ij} t_{bc}^{\ell k} \right)}{\varepsilon_a + \varepsilon_b + \varepsilon_c - \varepsilon_i - \varepsilon_j - \varepsilon_k}, \quad (3.48)$$

where $\hat{T}_{2,\text{CCSD}}$ denotes that amplitudes from converged CCSD computations are used. The permutation operators generate the indices $\mathcal{P}(a|bc) = 1 - (bac) - (cba)$, analogously for $\mathcal{P}(i|jk)$, respectively, thus symmetrizing the expression [32]. The last term in Eq. (3.48) is obtained from applying Wick's theorem. Counting the indices in Eq. (3.48), explains why the computational cost is $\mathcal{O}(N_{\text{AO}}^7)$ with explicit contributions from occupied and virtual subspaces according to $\mathcal{O}(N_{\text{occ}}^3 N_{\text{virt}}^4)$. Adding $E_{(T)}^{(4)}$ on top of E_{CCSD} defines the CCSD[T] method, which was originally referred to as CCSD+T(CCSD) [28].

For certain cases, see, e.g., Ref. [216], it was shown that CCSD[T] tends to overestimates the triples effect. It turned out that to properly balance the contribution of singles and doubles excitations to the triples correction an additional term has to be included. To this end, the fifth-order term

$$E_{(T)}^{(5)} = \langle \Phi_0 | \hat{T}_1^\dagger \hat{W}_N \hat{T}_3 | \Phi_0 \rangle = \frac{1}{4} \sum_{ijk} \sum_{abc} g_{jk}^{bc} t_{ijk}^{abc} t_i^a \quad (3.49)$$

was found to properly account for this balance [29–32]. This defines the CCSD(T) method as

$$E_{\text{CCSD(T)}} = E_{\text{CCSD}} + E_{(T)}^{(4)} + E_{(T)}^{(5)}. \quad (3.50)$$

For both CCSD[T] and CCSD(T) there is no need for storing the approximated triples amplitudes. The correction and thus the non-iterative step is carried out after the preceding CCSD calculation has converged.

Perturbative corrections are not only restricted to triples excitations but can be extended, for instance, by including quadruples excitations perturbatively using converged CCSDT amplitudes, which yields the CCSDT[Q] and CCSDT(Q) methods with $\mathcal{O}(N_{\text{AO}}^9)$ scaling [38–41].

A remark on spin factorization and open-shell CC theory

The previous discussion implicitly used spin-orbitals for the definition of determinants and integrals without further referring to the exact form of the reference wavefunction (RHF, UHF or ROHF). In general any set of orbitals may be used assigning α and β spin functions to each occupied and virtual orbital. Thus, the corresponding integrals and operators, and as such also the coupled-cluster energy and amplitude equations, factor into their spin-dependent components. Due to the underlying spin-symmetry, many of them will be zero after subsequent spin integration [201].

For open-shell systems, the situation becomes more challenging. It requires more computational effort and the formulation of a spin-adapted theory is less trivial compared to closed-shell cases. Nowadays, several approaches exist that tackle these problems: spin-unrestricted (UCCSD) and partially spin-restricted (RCCSD) coupled-cluster theories also including (T) corrections, see Refs. [32, 217, 218] and references therein.

3.4 | Multireference correlation methods

As indicated in Sec. 3.2.3 by the doublet ground states of alkali-metal triatomics, in the case of static correlation there are two or more (nearly) degenerate determinants, which show large weights in the FCI expansion of Eq. (3.26). Thus, a HF reference does not provide a sufficient zeroth-order description of the system. A proper reference must include all determinants that may assume a significant weight. The two multireference methods used for calculations in this work will be discussed below.

3.4.1 | The multiconfiguration self-consistent field method

The multiconfiguration self-consistent field (MCSCF) approach can be viewed as an analogue to HF with the key task of generating appropriate orbitals for multireference systems. The corresponding wavefunction ansatz is based on the CI approach of Eq. (3.26) but contains only a selected subset A_0 of configurations considered as important to obtain a sufficient zeroth-order description of the main characteristics of the system. The ansatz for state n becomes [51, 219–221]

$$|\Psi_{\text{MCSCF}}^{(n)}\rangle = \sum_{I \in A_0} c_I^{(n)} |\Phi_I\rangle, \quad \text{with} \quad \sum_I (c_I^{(n)})^2 = 1 \quad \text{and} \quad \langle \Phi_I | \Phi_J \rangle = \delta_{IJ}, \quad (3.51)$$

where $|\Phi_I\rangle$ is either a Slater determinant or a CSF and $c_I^{(n)}$ are the CI coefficients. The basic task of the MCSCF method is related to the CI problem but requires to optimize both the CI coefficients and the MOs $\{\varphi_i\}$, from which the configurations Φ_I are constructed. This is achieved variationally subject to the constraints defined in Eq. (3.51) [222].

The choice of A_0 in Eq. (3.51) is a non-trivial problem, since there is no rigorous mathematical criterion that determines all relevant determinants that have to be considered. A common approach is the *complete active space* (CAS) concept for which A_0 is referred to as *active space* and the method is denoted complete active space self-consistent field (CASSCF). In this, the MO space is divided into inactive orbitals, which are doubly occupied in all configurations, active orbitals being partially occupied and virtual orbitals are unoccupied in all configurations. The CAS ansatz generates all possible configurations resulting from distributing n_e electrons over m active orbitals, which is then denoted as $\text{CAS}(n_e, m)$. This is illustrated in Fig. 3.3. A CAS wavefunction represents a FCI expansion constrained to the subspace spanned by the active orbitals [50]. This leads to an factorial increase of the CAS with the number of active orbitals. Typically, the active orbitals will comprise some of the highest occupied and lowest unoccupied MOs. In general, the selection of which orbitals to include in the active space is still done manually and requires a certain degree of expertise. Reference [140] lists a few rules of thumb that may be helpful. A route toward an automated construction of the active space is described by the AVAS (Automated construction of atomic Valence Active Spaces) technique in Ref. [223].

Due to its formal analogy to the CI problem, the energy expression for state n is given as

$$E_n = \sum_{IJ} c_I^{(n)} \langle \Phi_I | \hat{H} | \Phi_J \rangle c_J^{(n)}, \quad (3.52)$$

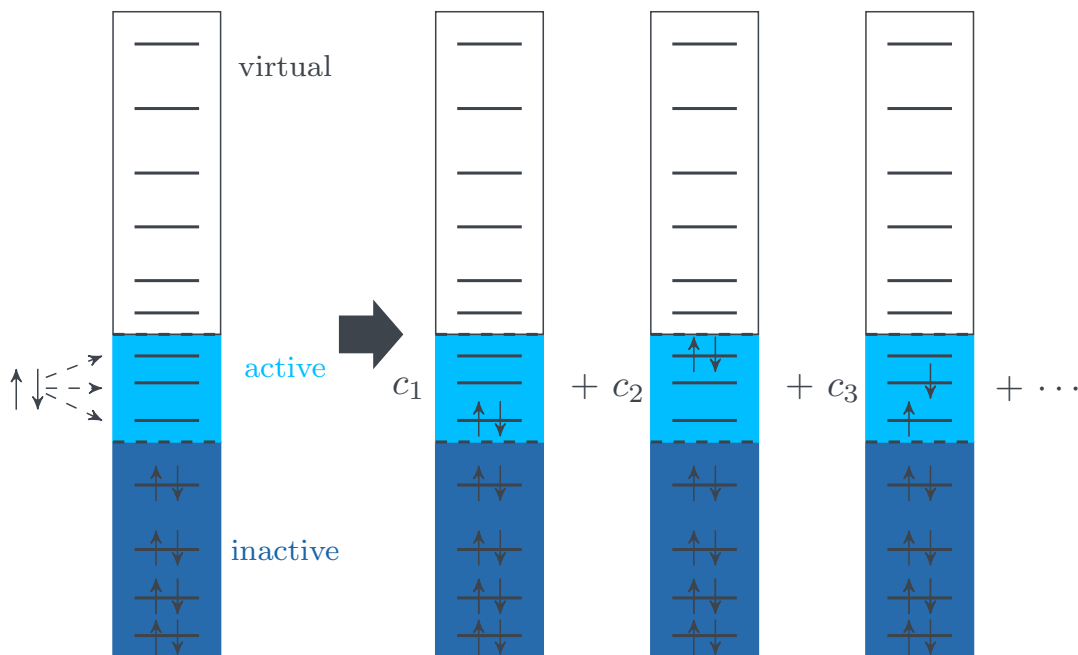


FIGURE 3.3.: Schematic representation of the complete active space (CAS) concept. It describes the distribution of n_ϵ electrons over m active orbitals and the corresponding CAS wavefunction includes all possible configurations (either CSFs or Slater determinants) resulting from this scheme [CAS(n_ϵ, m)].

which shall be optimized with respect to both the CI coefficients and the MOs. To this end, many efficient solutions exist, see, e.g., Ref. [49] for a comprehensive review. The basic ideas underlying the MCSCF implementation in MOLPRO [224, 225] are outlined in the following. The fundamental ideas dating back to some pioneering work of Werner, Meyer and Knowles and therefore the optimization procedure is referred to as the WMK method, which is a second-order algorithm [219, 220, 222, 226].

The orbital optimization is expressed via orbital rotations with an orthogonal transformation U [221]

$$|\tilde{\varphi}_i\rangle = \sum_r |\varphi_r\rangle U_{ri}, \quad (3.53)$$

where the indices r, s, \dots refer to any orbital (inactive + active + virtual), while i, j, \dots denote internal indices (inactive + active). The U matrix is parametrized as proposed by Werner and Meyer [222, 226] via

$$U = e^{\mathbf{R}} = \mathbf{1} + \mathbf{R} + \frac{1}{2}\mathbf{R}^2 + \dots \equiv \mathbf{1} + \mathbf{T}, \quad (3.54)$$

leading to improved convergence as compared to using an expansion in \mathbf{R} . The antisymmetric matrix $\mathbf{R} = -\mathbf{R}^\dagger$ contains the independent orbital rotation parameters.

Working with Eq. (3.52) after inserting Eq. (3.53) would be computationally too expensive due to the involved two-electron integrals ($rs|tu$). Instead, the general way is to define an approximate energy functional that is accurate to second-order with respect to small changes in the CI coefficients c and orbital rotations T .

For fixed CI coefficients, the approximate energy functional $E^{(2)}(T)$ is minimized subject to the orthonormality constraint $\langle \Phi_I | \Phi_J \rangle = \delta_{IJ}$, which reflects in the orthogonality condition $U^\dagger U = 1$. The minimization of the resulting Lagrange functional with respect to the orbital rotation parameters T leads to the non-linear orbital equations of MCSCF, which are iteratively solved.

For given orbitals, i.e. for a $U = 1 + T$, the CI coefficients could be obtained from minimizing Eq. (3.52) subject to the constraint $\sum_I |c_I^{(n)}|^2 = 1$. However, since the orbitals change during the optimization process, the integrals have to be recomputed in each step, which for the two-electron integrals this is very costly. A more efficient way to account for the coupling between the CI coefficients and orbital rotations is to use second order approximations for the one- and two-electron integrals of \hat{H} and thus using a second-order approximate Hamiltonian $H_{IJ}^{(2)}$ with corresponding second-order energy expression $\tilde{E}^{(2)}$. The minimization of the resulting Lagrange functional with respect to c_I subject to the previous constraint leads to an CI eigenvalue problem analogous to Eq. (3.27) for given orbitals.

In each macroiteration, the equations defining the orbitals and the CI coefficients have to be satisfied simultaneously. The solution of these equations constitutes the microiterations. The optimization of the orbitals and CI coefficients is decoupled in the conventional WMK method corresponding to an alternating optimization of the energy $E^{(2)}(T, c)$ with respect to T and c . The main challenge is to converge the microiterations efficiently and reliably. This also involves improved numerical methods and strategies for an coupled optimization of $E^{(2)}(T, c)$. These improvements are described in Ref. [221, 227].

3.4.2 | Multireference Configuration Interaction

The MCSCF method as a zeroth-order description for strongly correlated systems is not well suited to recover dynamic correlation effects to a sufficient degree (in general this depends on the choice of the active space). However, extending the CI method to MCSCF reference wavefunctions provides a powerful tool for calculating accurate potential energy surfaces for systems with strong static and dynamic correlation. The resulting method is referred to as multireference CI (MRCI).

In the sense of the CI method, the MRCI wavefunction ansatz is constructed by orbital excitations, up to a certain excitation limit, for each member of the MCSCF reference wavefunction according to Eq. (3.51). All configurations created in this way constitute the MRCI expansion space. For practical reasons this expansion is truncated after doubles excitations, thus strictly speaking the method should be denoted MRCI(SD). It is useful to distinguish the following orbital subspaces: the entity of inactive and active orbitals, which are occupied in the reference configurations and correlated in the CI wavefunction, cf. Fig. 3.3, are denoted *internal* orbitals and are labeled with i, j, k, ℓ, \dots , and virtual or *external* orbitals are denoted with a, b, c, d, \dots . To label any kind of orbitals the indices r, s, t, u, \dots will be used. This partitioning gives rise to several excitation patterns:

- *Internal* (I): only active \rightarrow active or inactive \rightarrow active excitation, i.e. virtual orbitals remain unoccupied
- *Singly* (S) external: virtual orbitals getting singly occupied
- *Pairwise/Doubly* (P) external: virtual orbitals getting doubly occupied

The wavefunction ansatz can be written as [50, 228]

$$|\Psi_{\text{MRCI}}\rangle = \sum_I c_I |\Phi_I\rangle + \sum_S \sum_a c_S^a |\Phi_S^a\rangle + \sum_P \sum_{ab} c_P^{ab} |\Phi_P^{ab}\rangle, \quad (3.55)$$

with $|\Phi_I\rangle$ representing internal configurations, $|\Phi_S^a\rangle$ describing singly external configurations with $N - 1$ electrons in the internal space and $|\Phi_P^{ab}\rangle$ denoting double excitations into the virtual space, thus representing configurations with $N - 2$ electrons in the internal space. In general, the configurations $\{|\Phi_I\rangle, |\Phi_S^a\rangle, |\Phi_P^{ab}\rangle\}$ are either Slater determinants or CSFs. However, to keep the number of configurations in the MRCI reference space as low as possible it is essential to work with CSFs [229].

Analogous to the single-reference CI problem the MRCI energy as well as the MRCI wavefunction coefficients are determined variationally leading to the already discussed CI eigenvalue problem of the general form as given in Eq. (3.27). Due to the factorial growth of the number of configurations, the solution to this problem is usually performed iteratively using the Davidson subspace method [230]. This method relies on projecting onto a much smaller subspace to solve the eigenvalue problem there, rather than explicitly constructing and storing the full Hamiltonian matrix \mathbf{H} . In each iteration only the product $\mathbf{H} \cdot \mathbf{c}$, where \mathbf{c} is a trial vector representing the coefficients, has to be computed. This method can be efficiently combined with the direct CI

procedure, where the matrix-vector product is computed directly from molecular one- and two-electron integrals [140]. The convergence of this approach is assessed by defining a residual vector $\mathbf{g} = (\mathbf{H} - E\mathbf{1}) \cdot \mathbf{c}$ according to the CI problem. Thus, the most expensive step in a MRCI calculation is the $\mathbf{H} \cdot \mathbf{c}$ product. More technical details may be found, e.g., in Ref. [49].

Even though, the MRCI ansatz according to Eq. (3.55) is truncated after doubles excitations and efficient algorithms for solving the eigenvalue problem exist, for large basis sets and large reference spaces the resulting computational costs are often exceedingly high. To this end, contracted MRCI methods have been developed: *internally* and *externally* contracted versions. The underlying idea of both is to group certain primitive expansion functions together to reduce the number of variational parameters. The external contractions scheme relies on grouping together configurations with the same internal parts and fixing the contraction coefficients after obtaining them by first-order perturbation theory [49]. In the internal contraction scheme singles and doubles excitations are generated by applying single- and double-excitation operators to the MCSCF reference wavefunction $|\Psi_{\text{MCSCF}}\rangle$ of Eq. (3.51) and keep the expansion coefficients as calculated from a preceding MCSCF run fixed [50].

The most successful implementation of the internally contracted MRCI (icMRCI) approach, as claimed in Ref. [49], is the one by Werner and Knowles [228, 229, 231] as implemented in the MOLPRO program package [224, 225]. It is restricted to singles and doubles excitations, where only the latter are contracted, while both the full internal configuration space and the full space of uncontracted singly excited configurations are included in the expansion space. In this implementation the configuration spaces are spanned by CSFs. In the following, the basic aspects of the icMRCI method by Werner and Knowles are outlined.

Let $|\Psi_0\rangle \equiv |\Psi_{\text{MCSCF}}\rangle$, the internally contracted doubly external configurations are defined as [228]

$$|\Phi_{ij,p}^{ab}\rangle = \frac{1}{2}(\hat{E}_{ij}^{ab} + p\hat{E}_{ij}^{ba})|\Psi_0\rangle = \frac{1}{2}(\hat{E}_{ij}^{ab} + p\hat{E}_{ji}^{ab})\sum_{R_\mu}c_{R_\mu}|\Phi_{R_\mu}\rangle, \quad (3.56)$$

where $p = 1$ for external singlet pairs and $p = -1$ for triplet pairs and R_μ denotes the reference configurations. The two-particle spin-summed excitation operators are defined in terms of one-electron creation and annihilation operators $\hat{E}_r^s = \sum_\sigma a_{r\sigma}^\dagger a_{s\sigma}$, with σ accounting for the spin

$$\hat{E}_{rs}^{tu} = \hat{E}_r^s \hat{E}_t^u - \delta_s^u \hat{E}_r^u. \quad (3.57)$$

The contracted configurations $|\Phi_{ij,p}^{ab}\rangle$ can be expanded in terms of the uncontracted doubly external CSFs from Eq. (3.55) to

$$|\Phi_{ij,p}^{ab}\rangle = \sum_P \langle \Phi_{ij,p}^{ab} | \Phi_P^{ab} \rangle |\Phi_P^{ab}\rangle, \quad (3.58)$$

where the contraction coefficients are given by

$$\langle \Phi_{ij,p}^{ab} | \Phi_P^{ab} \rangle = \frac{1}{2} \sum_{R_\mu} c_{R_\mu} \langle \Phi_{R_\mu} | \hat{E}_{ij}^{ab} + p \hat{E}_{ji}^{ab} | \Phi_P^{ab} \rangle, \quad (3.59)$$

showing that these configurations are obtained by contracting different *internal* states $|\Phi_{R_\mu}\rangle$. Moreover, it shows that contracted configurations depend on the expansion coefficients c_{R_μ} of the reference configurations, which are determined from a preceding MCSCF calculation. Since internally contracted configurations are in general not orthogonal, the overlap matrix needs to be computed according to

$$\begin{aligned} \langle \Phi_{ij,p}^{ab} | \Phi_{kl,q}^{cd} \rangle &= \frac{1}{2} \delta_{pq} (\delta_a^c \delta_b^d + p \delta_a^d \delta_b^c) S_{kl,p}^{ij} \\ &= \frac{1}{2} \delta_{pq} (\delta_a^c \delta_b^d + p \delta_a^d \delta_b^c) \langle \Psi_0 | \hat{E}_{kl}^{ij} + p \hat{E}_{lk}^{ij} | \Psi_0 \rangle, \end{aligned} \quad (3.60)$$

with the second-order density matrix $S_{kl,p}^{ij}$. With that, the configurations can be orthogonalized using symmetric Löwdin orthogonalization [191], via

$$|\Phi_{D,p}^{ab}\rangle = \sum_{i>j} T_{D,p}^{ij} |\Phi_{ij,p}^{ab}\rangle, \quad \text{with } \mathbf{T}_p = (\mathbf{S}_p)^{-1/2}. \quad (3.61)$$

In this basis the icMRCI wavefunction is finally given as

$$|\Psi_{\text{icMRCI}}\rangle = \sum_I c_I |\Phi_I\rangle + \sum_S \sum_a c_S^a |\Phi_S^a\rangle + \sum_D \sum_p \sum_{ab} c_{D,p}^{ab} |\Phi_{D,p}^{ab}\rangle. \quad (3.62)$$

This internal contraction scheme comes with the main advantage that the number of configurations in the CI wavefunction is essentially independent of the number of reference configurations and only depends on the number of correlated orbitals in the reference wavefunction [228]. What is more, the error introduced by contractions is only very small. The drawbacks, on the other hand, are the non-orthogonality of the contracted configurations and their complex structure. However, since singly external and internal configurations are not contracted in the Werner-Knowles approach, their orthogonalization is avoided. Otherwise, this could be rather difficult and would constitute a severe bottleneck since rather large sets of nonorthogonal singly external and internal configurations are usually generated. Moreover, matrix elements between

contracted singly and doubly external configurations would become quite difficult and time consuming.

As mentioned above, the CI eigenvalue problem is tackled using the Davidson method combined with the direct CI approach. The required residual vector $\mathbf{g} = (\mathbf{H} - E\mathbb{1}) \cdot \mathbf{c}$ involves calculating Hamiltonian matrix elements, which depend on so-called coupling coefficients. From a strongly simplified point of view, the residual vector is a function $\mathcal{R}(\mathbf{G}_{D,p}, \mathbf{g}_S, g_I, \mathbf{c}_{D,p}, \mathbf{c}_S, c_I)$, where $\mathbf{c}_{D,p}$, \mathbf{c}_S and c_I represent coefficient matrices resulting from the wavefunction expansion according to Eq. (3.62), and the quantities $\mathbf{G}_{D,p}$, \mathbf{g}_S and g_I denote energy expectation values and depend on the coupling coefficients. These coupling coefficients essentially represent integrals and their explicit form is given in Ref. [228]. Werner and Knowles also proposed an efficient way to evaluate them in Ref. [229].

This eventually provides a powerful toolbox to formulate an algorithm to tackle the icMRCI problem. The fundamental steps of the Werner-Knowles implementation are:

- Given the residual vector \mathcal{R} , use the Davidson method [230] combined with the direct CI procedure to obtain eigenvectors and eigenvalues iteratively
- *Macroiterations:*
 1. Update expansion vectors $\mathbf{c}_{D,p}$ and \mathbf{c}_S
 2. Evaluate new quantities $\mathbf{G}_{D,p}$, \mathbf{g}_S and g_I from which matrix elements $\langle \Phi_{\text{ext}}^m | \hat{H} | \Phi_{\text{ext}}^n \rangle$, $\langle \Phi_I | \hat{H} | \Phi_{\text{ext}}^n \rangle$ and $\langle \Phi_{\text{ext}}^m | \Phi_{\text{ext}}^n \rangle$ are evaluated, with external expansion functions

$$|\Phi_{\text{ext}}^n\rangle = \sum_S \sum_a (c_S)_a^n |\Phi_S^a\rangle + \sum_D \sum_p \sum_{ab} (c_{D,p})_{ab}^n |\Phi_{D,p}^{ab}\rangle, \quad (3.63)$$

and the superscript n denoting different expansion vectors describing the external configuration types (i.e. how many holes are generated to singly or doubly occupy the virtual space)

- *Microiterations:* Optimize

$$|\Psi\rangle = \sum_I c_I |\Phi_I\rangle + \sum_n \alpha_n |\Phi_{\text{ext}}^n\rangle \quad (3.64)$$

variationally, with the corresponding eigenvalue problem solved iteratively

1. Simultaneously optimize coefficients c_I of internal configurations and coefficients α_n of sets of external expansion vectors $(c_{D,p})^n$, $(c_S)^n$ for which

residual vectors $(\mathbf{G}_{D,p})^n, (\mathbf{g}_S)^n$ from previous macroiterations are available
 \implies yields also variational energy for present iteration

2. Use new α_n to obtain improved external coefficients $c_{D,p}, c_S$ and corresponding parts of $\mathbf{G}_{D,p}, \mathbf{g}_S$
3. Add contributions from internal part to $\mathbf{G}_{D,p}, \mathbf{g}_S$ using new coefficients c_I
4. Go to next macroiteration

This method can be further extended to a multistate treatment to compute excited states which is briefly outlined below. A detailed description is given in Ref. [231].

The calculation of excited states within the icMRCI framework comes with the difficulty, as shown in Eq. (3.59), that the contraction coefficients depend on the expansion coefficients c_{R_μ} of the reference wavefunction. Hence, different contracted configurations are required for each state. A straightforward approach would include the union of all contracted functions formed from separate reference functions for each state. If one is interested in the k th state, then the first k eigenvectors and eigenvalues of the Hamiltonian matrix must be computed in this basis. In such, the number of external pair functions would increase linear with the number of states and the corresponding total computational effort would even scale quadratic to cubic with the number of states thus limiting its application range.

This unfavourable scaling behaviour could be avoided if there were a state-specific optimization procedure for computing the wavefunction $|\Psi^k\rangle$ for each state k separately. To this end, Werner and Knowles came up with an efficient projection operator approach, which also avoids root flipping problems [231]. In this procedure, a modified Hamiltonian is diagonalized in which the k th state appears as the lowest root with the $k - 1$ states shifted away. The projection operator is defined via

$$\mathbf{P}^{(k)} = \mathbb{1} - \sum_{n=1}^{k-1} \mathbf{c}^{(n)} \mathbf{c}^{(n)\dagger} \quad (3.65)$$

and the projected Hamiltonian is given as

$$\mathbf{H}^{(k)} = \mathbf{P}^{(k)} \mathbf{H} \mathbf{P}^{(k)}. \quad (3.66)$$

The $\mathbf{c}^{(n)}$ represents the eigenvector for the n th state. Since in a state-specific framework different bases are used for each state, a direct construction of the full projector is difficult. However, it has been shown that an approximate projector is sufficient where only such configurations are included in $\mathbf{c}^{(n)}$ that lie in the configuration set for both

the n th and k th state calculations. For the Werner-Knowles icMRCI method, this means that only internal CFSs, which are common to the n th and k th state bases are included implying that the internal space should represent the dominant part of the wavefunction.

After obtaining all desired states in the above manner individually, the resulting $k \times k$ Hamiltonian of this subspace $H_{nm} = \langle \Psi^{(n)} | \hat{H} | \Psi^{(m)} \rangle$ is formed and diagonalized yielding the final states and energies. By using this approach it is also possible (in many cases) to properly describe difficult situations such as avoided crossings [50].

Since the expansion space is usually limited up to doubles excitations, the MRCI method is still lacking of size-consistency. This is, despite its great success in many application, the most serious formal deficiency. However, there are many size-consistency correction schemes available that account for this error. For a comprehensive review on them see, e.g., Ref. [49] and references therein.

3.5 | Basis sets

In the previous sections it was shown that all quantum chemical methods use the LCAO approximation of Eq. (3.16) to represent the unknown MOs $\varphi_i(\mathbf{r})$ as a linear combination of AOs $\chi_\alpha(\mathbf{r})$. Since all *ab-initio* methods scale at least with $\mathcal{O}(N_{\text{AO}}^4)$, this expansion should not become too large. On the other hand, an insufficient expansion would impair the accuracy of the MOs. Therefore, it is very important to choose and to optimize a basis set such that it yields a reasonable accurate expansion of the exact MOs [191].

A reasonable choice to represent AOs might be hydrogen-like functions such as *Slater-type orbitals* (STOs) that approximate the exact Schrödinger solutions very well. In spherical polar coordinates they are defined as [140]

$$\chi_\alpha^{\text{STO}}(\mathbf{r}) = \mathcal{N}_\alpha^{\text{STO}} Y_{\ell_\alpha, m_\alpha}(\theta, \phi) r^{n_\alpha - 1} e^{-\zeta_\alpha r}, \quad (3.67)$$

where $\mathcal{N}_\alpha^{\text{STO}}$ are normalization factors, $Y_{\ell_\alpha, m_\alpha}$ are the spherical harmonics, the integers n, ℓ, m determine the type of orbital (s,p,d, etc.) and ζ_α are known as the exponents. This form ensures fast convergence with increasing number of functions but the one- and two electron integrals $\langle \alpha | \hat{h} | \beta \rangle$ and $\langle \alpha \beta | \gamma \delta \rangle$ cannot be computed analytically. Therefore, *Gaussian-type orbitals* (GTOs) are used almost exclusively in practice. In Cartesian coordinates, the *Gaussian primitives* are defined via

$$\chi_\alpha^{\text{GTO}}(\mathbf{r}) = \mathcal{N}_\alpha^{\text{GTO}} S_{\ell_\alpha, m_\alpha}(\mathbf{r} - \mathbf{R}_K) e^{-\zeta_\alpha |\mathbf{r} - \mathbf{R}_K|^2}, \quad (3.68)$$

where $\mathcal{N}_\alpha^{\text{GTO}}$ are normalization factors, ℓ, m determine the type of orbital, and \mathbf{R}_K denotes the position of the nucleus K . The latter accounts for the fact that AOs have to be placed on every atom. The functions $S_{\ell_\alpha, m_\alpha}$ are the real solid harmonics. This choice allows for efficiently computing the integrals due to the *Gaussian product theorem*, which drastically reduces the complexity of the expressions. For the remaining tasks fast and stable algorithms exist. This comes at the cost of physical meaningfulness, since the radial part of GTOs do not show a cusp at the nuclei and GTOs decay too quickly at long range. However, the correct physical behavior can be fitted to a very good approximation by a linear combination of a sufficiently large number of GTOs with different exponents. Therefore, more GTOs are needed for reaching a good accuracy for representing MOs compared to using STOs. This deficiency is compensated by the outperforming computational scaling.

It can be shown that a large amount of basis functions serve to model the energetically important, but chemically unimportant core electrons [140]. As these core orbitals change very little depending on the chemical bonding situation, the corresponding MO coefficients ($C_{\alpha i}$) in front of these inner basis functions also change very little. This motivates to reduce the number of basis functions by combining certain primitive Gaussians with the same ℓ and m quantum numbers but different exponents in pre-defined superpositions. The resulting functions are called *contracted GTOs* (CGTOs) [232, 233]

$$\chi_{\alpha, \text{CGTO}}(\mathbf{r}) = \sum_{q=1}^P w_{\alpha q} \chi_q(\mathbf{r}), \quad (3.69)$$

with the contraction coefficients $w_{\alpha q}$. In quantum chemical calculations ζ_α and $w_{\alpha q}$ are kept fix; only the MO coefficients $c_{i, \mu}$ are varied. The exponents and contraction coefficients are optimized in laborious atomic calculations. This is a highly non-trivial task and also depends on the intended use of the basis set. The construction and optimization of basis sets is therefore still object of current research and several classifications exist, see, e.g., Ref. [232] for a comprehensive review. The following outlines only such aspects which are important for this work.

Due to the cusp problem discussed in Sec. 3.2.3, correlated wavefunction methods require large basis sets to obtain meaningful results. The singularity of the electronic Coulomb operator $\propto r_{12}^{-1}$ requires the exact wavefunction to fulfill certain cusp conditions [199, 200], as exemplarily illustrated in Fig. 3.1 for $r_{12} \rightarrow 0$. Approximate wavefunctions that are represented as linear combinations of Slater determinants never show this cusp behavior making it impossible to exactly reproduce the discontinuity.

However, by increasing the basis set size it is possible to slowly approach the exact wavefunction. This is the underlying reason for the slow convergence of the correlation energy with respect to the basis set size and due to the $\geq \mathcal{O}(N_{\text{AO}})$ scaling, this makes it difficult to estimate the exact correlation energy.

In this regard Dunning *et al.* invented a very important family of basis sets: the *correlation consistent (cc) basis sets* [234]. They are designed to systematically improve the correlation energy of the valence electrons when primitives corresponding to higher ℓ quantum numbers are added. This is based on the hierarchical construction principle that functions which contribute to similar amounts to the correlation energy are included at the same stage, independent of the function type [140]. The naming convention of this basis set is: cc-pVnZ, where n is the *cardinal number* corresponding to the highest angular momentum quantum number included in the basis set (e.g. $n = 2$ for double-zeta includes up to d functions) [235]. The “p” denotes that polarization functions (also denoted as correlation functions) are included. These functions correspond to higher angular momentum quantum numbers than required for the neutral atom (e.g. d functions and higher for Ne). They allow for higher flexibility of the basis set and account for deviations from the spherical shape of AOs due to the environment. The “V” denotes that the basis set corresponding to the valence electrons of a given element is increased since inner-shell electrons are less sensitive to the environment.

The main advantage of correlation consistent basis sets comes with empirical observations that energies and also other properties converge smoothly toward the complete basis set (CBS) limit when the cardinal number of the basis set is increased [232]. This allows for a systematic improvement of *ab-initio* calculations toward the exact solution. This improvement is not unique and a vast variety of (semi-) empirical extrapolation formulas exist, see, e.g., Refs. [236, 237] and references therein for a comprehensive review. One of the most popular formulas employed for the correlation energy was proposed by Helgaker *et al.* [238, 239] and states that the error for a given basis set size n with respect to the CBS limit scales as n^{-3} .

Beyond that, cc basis sets provide great flexibility for a number of “extensions”:

- Augmentation with *diffuse* functions with small exponents which are necessary to describe loosely bound electrons, e.g. in anions or excited states. Those diffuse exponents are optimized and added to their parent set (e.g. **aug-cc-pVDZ**)
- Augmentation with *tight* functions with large exponents if the interest is in recovering core-core and core-valence correlation (e.g. cc-pCVnZ)

- For heavier elements relativistic effects become more important, while the number of electrons grows drastically such that correlating all electrons becomes impossible. A computationally efficient approach to treat such elements are relativistic pseudopotentials (PPs). They come either in a small-core (an extra core-valence shell of electrons remain) or in a large-core (replacing all but the valence electrons) variant to model the electrons with a relativistic PP, see, e.g., Refs. [57, 58] for more details. Correlation consistent basis sets can be designed such that they accompany these PPs for yielding an accurate description, see, e.g., Ref. [240]

Another particular useful approach for extending given basis set with additional diffuse functions relies on even-tempered schemes [232]. Even-tempered basis set are very powerful when extremely large basis sets are necessary and optimization of individual Gaussian primitives is rather difficult [241]. In this regard it was shown in Ref. [242] that these basis sets span the Hilbert space evenly and provide a way for accurately simulate fully optimized exponents without optimizing any of them.

Part II

INVESTIGATING Rb_3 FOR PHOTOASSOCIATION EXPERIMENTS

4

TOWARDS PHOTOASSOCIATION PROCESSES OF ULTRACOLD RUBIDIUM TRIMERS

The main aspects of this chapter have been published previously in

[245] J. Schnabel, T. Kampschulte, S. Rupp, J. Hecker Denschlag, and A. Köhn, *Phys. Rev. A* **103**, 022820 (2021).

This part of the thesis is intended to provide experimental guidance for the creation of ultracold rubidium trimer molecules. After briefly outlining the experimental motivation behind this work, the prospects for photoassociation (PA) processes of Rb_3 are theoretically investigated. This includes a broad overview of expected states and transitions and involves special cuts through the potential-energy landscapes. Major focus is placed on the calculation of equilibrium states, electronic dipole transition moments, and a survey of spin-orbit coupling effects. In connection with a qualitative discussion of Franck-Condon overlaps, concrete and suitable PA transitions to produce long-lived trimer bound states are identified.

Further emphasis is placed on symmetries that drive Jahn-Teller and related effects. It is demonstrated that the identified PA candidate state forming one component of a Jahn-Teller manifold, requires an analytical JT analysis that goes beyond the standard approach. In conclusion, the understanding of underlying coupling mechanisms of a special manifold of quadruply interacting excited quartet states is broadened.

4.1 | Experimental motivation

Experiments in the regime of ultracold controlled chemistry provide the ability to study molecular binding mechanisms on a fundamental level and to create molecules in

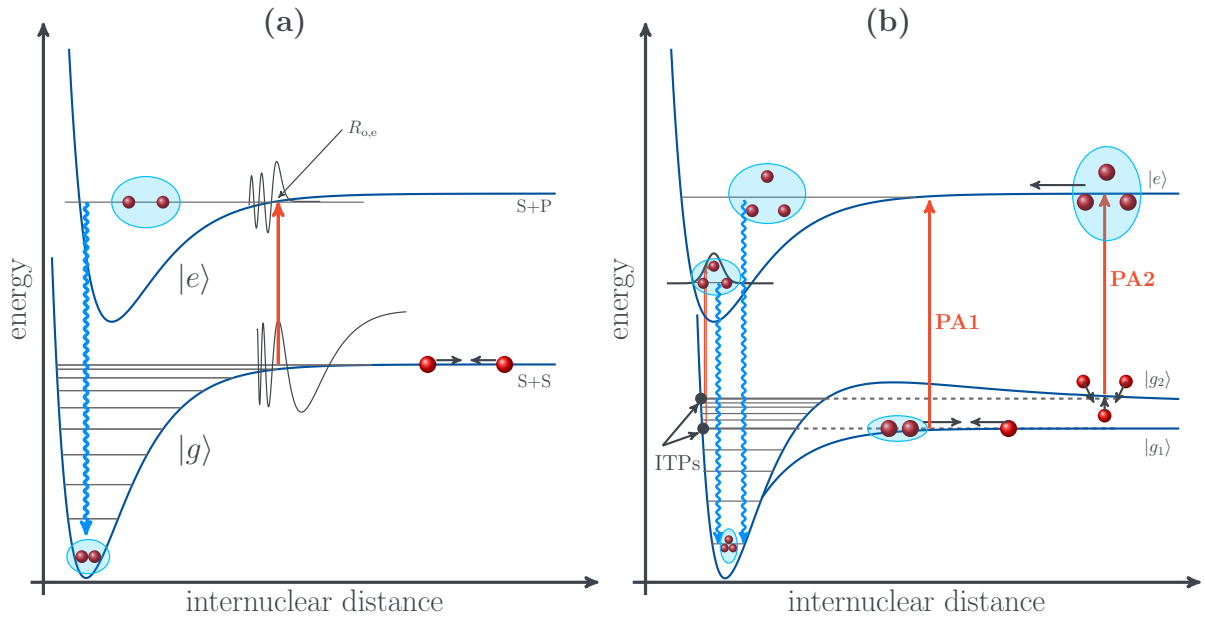


FIGURE 4.1.: **(a)** Schematic illustration of a PA process for the formation of diatomic molecules. The PA laser (solid orange arrow) couples a continuum state of free colliding atoms (S+S asymptote) in an ultracold quantum gas to a weakly bound excited molecular state $|e\rangle$ (S+P asymptote) at large internuclear distance. The excited dimer state can radiatively (curly blue arrow) decay to a number of long-lived rovibrational states of the ground state manifold $|g\rangle$. The PA transition can be considered as occurring at the outer turning point $R_{0,e}$ of the vibrational level of $|e\rangle$ (see text). **(b)** Strongly simplified representation of two different PA schemes for the production of X_3 species. PA1 photoassociates a previously formed X_2 dimer with a free ground state X atom from the asymptote $|g_1\rangle$. PA2 photoassociates three X atoms from the asymptote $|g_2\rangle$. Both PA processes can be also realized, in principle, starting from an inner turning point (ITP), which produces more deeply bound excited trimers. This is discussed in detail in Sec. 4.4 and indicated on the very left. In both cases the excited trimer (more weakly bound for PA starting from $|g_1\rangle$ or $|g_2\rangle$) can spontaneously decay to the ground state.

precisely defined quantum states. An important method to produce ultracold molecules is photoassociation (PA), which so far has been successfully used for creating diatomic molecules [22–24]. In PA processes a laser photon resonantly excites an unbound scattering state of two atoms into a often weakly bound, but well-defined, rovibrational level of the electronically excited state $|e\rangle$. Under favorable circumstances the short-lived excited molecule may be subsequently stabilized by spontaneous decay into a stable rovibrational level of the ground-state manifold $|g\rangle$. This is schematically illustrated in Fig. 4.1 (a). The efficiency of a PA process depends on the density of atomic pairs at a internuclear distance R , which scales with R^2 [13]. Hence, it preferably probes rovibrational levels of the excited state that are close to the corresponding

dissociation limit, i.e. at large internuclear separations.

In general, the basic prerequisite of PA is a non-vanishing electric dipole transition between the free scattering state and a molecular state with well-defined electronic symmetries. Thus, PA processes follow certain selection rules representing necessary conditions for PA transitions. The sufficient condition to drive PA transitions is determined by the *Franck-Condon factor*: the squared overlap between the initial and final vibrational wavefunctions as indicated in Fig. 4.1 (a). For diatomic molecules, favorable Franck-Condon factors are, in many cases, usually obtained near the classical outer turning points $R_{o,e}$ of the rovibrational level of the excited state. Indeed, the probability for making PA transitions is directly proportional to the square of the ground state wavefunction at $R_{o,e}$ [23]. However, this also implies that PA to an excited state whose outer turning point lies over a node in the ground state wavefunction will be suppressed.

Photoassociation was originally proposed for the production of homonuclear alkali-metal dimers. But with the successful formation of these species, PA has been furthermore employed to a more general class of dimers such as NaRb, RbCs, RbK, NaK, LiNa, LiCs, NaCs, but also to other compounds, such as LiYb and RbYb, see, e.g. Refs. [11, 12, 15, 16] and references therein. A general feature of homonuclear alkali dimers is that the leading-order long-range interaction of excited states, for instance those correlating to the S+P asymptote, scales as R^{-3} . This leads to potentials that can support vibrational levels with classical outer turning points at large internuclear distances where the atomic pair density is high [24]. In contrast, the long-range interaction of excited states of heteronuclear dimers, e.g., Rb(5S) + Cs(6P), scales as R^{-6} [243]. Thus, corresponding outer turning points are located at smaller distances. Therefore, PA rates of homonuclear dimers typically exceed those of the heteronuclear species. The long-range part of the ground state potentials scales, for both homo- and heteronuclear dimers, with R^{-6} . For heteronuclear dimers, the ground and excited potentials are thus of the same form, generally leading to large overlap integrals between the vibrational wavefunctions of the photoassociated state and those of the ground-state levels. However, in regard to formation processes both effects can compensate each other so that the total molecule formation rate is often similar for homo- and heteronuclear dimers.

Besides creating ultracold molecules from ultracold atoms, PA is a powerful tool for high-resolution molecular spectroscopy and provides the ability to directly measure absolute binding energies. Furthermore, PA spectra were widely used to measure

scattering lengths and other aspects of cold atomic collisions [23]. To control the spontaneous emission and to selectively enhance the population of a pre-determined final state, the use of optical cavities has been proposed in Ref. [244] as promising experimental improvement.

Due to previously discussed achievements, producing ultracold alkali-metal trimers, such as X_2Y or X_3 , with $(X,Y) \in \{\text{Li, Na, K, Rb, Cs}\}$, apparently marks a next milestone. However, alkali-metal trimers are much more complicated as compared to respective dimers, both from the experimental and theoretical perspective. The experimental challenge in preparing and manipulating trimer species on the quantum level is related to a generally reduced lifetime of many of its levels due to internal relaxation and dissociation mechanisms. Nevertheless, a promising approach for preparing isolated trimer molecules in precisely defined quantum states is PA. In analogy to PA processes for the creation of dimer molecules, one may think of two possible PA schemes for the realization of trimers [245]:

1. A dimer molecule and a free ground-state atom are photoassociated (\equiv PA1). This is shown in Fig. 4.1 (b). The laser photon PA1 drives a transition from the asymptote $|g_1\rangle$ to an electronically excited bound state $|e\rangle$ of the trimer complex. From there it can spontaneously relax to a stable level of the ground state.
2. Three colliding free atoms are photoassociated (\equiv PA2). As shown in Fig. 4.1 (b) the photon PA2 couples the asymptote $|g_2\rangle$ to the excited trimer state $|e\rangle$.

Both PA processes can in principle take place at long-range or at short-range. Since PA in the long-range regime was recently discussed theoretically in Ref. [109], the following explorations rather focus on trimer PA in the short-range region. However, recent theoretical work in Ref. [70] suggests that the simultaneous collision of three atoms is strongly suppressed due to an effective barrier in the short-range of the three-body potential, rendering the realization of PA2 at short-range less likely. So far, this barrier has only been studied in a single-channel approach but considering the more realistic multi-channel structure could turn out important. Thus, an approach similar to what was shown recently in Refs. [246, 247] may be applied to obtain a more comprehensive understanding. Nevertheless, it can be expected that the multi-channel calculations will qualitatively reveal the same findings [248] concerning the short-range barrier for PA2. In general, such a restriction is not expected for PA1.

This shows that PA processes depend on the detailed knowledge of the interaction properties of the colliding atoms and of the electronic structure of the involved molec-

ular states. The identification of efficient pathways for the production of ultracold trimer species thus requires profound theoretical investigations.

4.2 | Computational aspects

In order to theoretically investigate the prospects for PA of Rb₃, an extensive survey of a large number of expected states is required. Therefore, a pragmatic but sufficiently accurate computational approach has to be applied. The calculations in this chapter are based on using a large-core (lc) effective core potential (ECP) in combination with a core-polarization potential (CPP) as it has been developed in Ref. [249]. In doing so, merely the 5s valence electron of Rb is treated explicitly while the remaining 36 electrons are described by the ECP. Simply speaking, ECPs modify the one-electron operator \hat{h} in the Fock operator by replacing the \hat{V}_{ne} contribution, cf. Eqs. (2.1), (3.7) and (3.12), by a pseudopotential (PP), leading thus to an effective valence-only Hamiltonian [58]. This allows for significant computational savings in integral calculations. The large-core PP takes on the explicit form [249]

$$\begin{aligned} V_{\text{lcECP}} &= -\frac{Z}{r} + \sum_{\ell,j} B_{\ell,j} \exp(-\beta_{\ell,j} r^2) \mathbb{P}_{\ell,j} + V_{\text{CPP}}, \\ &= -\frac{Z}{r} + \sum_{\ell,j} B_{\ell,j} \exp(-\beta_{\ell,j} r^2) \sum_{m_j=-j}^j |\ell, j, m_j\rangle \langle \ell, j, m_j| + V_{\text{CPP}}, \end{aligned} \quad (4.1)$$

with Z the core charge (for lcECP: $Z = 1$) and the projection operator $\mathbb{P}_{\ell,j}$ projecting a given one-electron spin orbital into the subspace of orbital momentum ℓ and total angular momentum j . The parameters $B_{\ell,j}$ and $\beta_{\ell,j}$ are in general adjusted to reproduce all-electron relativistic atomic calculations (e.g. at four-component level using the Dirac-Coulomb Hamiltonian with Breit interaction). In case of the lcECP of Ref. [249], they are fitted so that the experimental ionization energies of the two lowest states of the one-valence-electron atom are reproduced as orbital energies of the two lowest states of the pseudo-Hamiltonian. This shows that ECPs are constructed such that (quasi-)relativistic effects are implicitly incorporated in their parameterization. The CPP (V_{CPP}) accounts for dynamic polarization of the core electrons by the valence electron and may be written as [250]

$$\begin{aligned} V_{\text{CPP}} &= -\frac{1}{2} \alpha_{\text{d}} \mathbf{f}^2, \\ &= -\frac{1}{2} \alpha_{\text{d}} \left(-\sum_i \left[1 - \exp(-\delta r_i^2) \right]^2 \frac{\mathbf{r}_i}{r_i^3} \right)^2, \end{aligned} \quad (4.2)$$

where α_d is the static dipole polarizability of the atomic core without valence electrons and f is the instantaneous field produced by the valence electron at the site of the core. Since the multipole expansion breaks down for positions near and inside the core, a cut-off function with the damping parameter $\delta \propto r_{\text{ion}}^{-2}$, i.e. correlated to the ion radius, was introduced. Comprehensive reviews on the construction of ECPs and CPPs as well as their parameterization and their adjustment can be found in Refs. [57, 58].

Rubidium trimers occur either as doublet or quartet states. The corresponding high-spin states are often reasonably well described by single-reference approaches, while the low-spin states have (nearly) degenerate configurations and are thus prototypical systems showing multireference character, as discussed in Sec. 3.2.3. The doublet and quartet states of Rb_3 , in the energy range considered in this work, were therefore computed using the internally contracted multireference configuration-interaction (icMRCI) method [228, 229, 231], cf. Sec. 3.4.2. Due to the lcECP approach, the system reduces to an effective three-electron problem and thus the MRCI method does not show size extensivity issues. This means that the PESs are entirely well defined and dissociate correctly into three noninteracting Rb atoms.

The orbitals for the MRCI calculation were generated by a preceding MCSCF calculation with a corresponding CASSCF reference space. The active space, unless otherwise stated, was chosen such that it comprises the $5s$ and $5p$ (p_x, p_y, p_z) orbitals of Rb. As shown in Sec. 4.3.1, the coordinate system is chosen such that the molecular plane of Rb_3 coincides with the xz plane. According to the internal orbital ordering of MOLPRO ($A_1/B_1/B_2/A_2$) for the C_{2v} point group, the active space for this coordinate system corresponds to an $5/4/2/1$ occupation pattern. For the C_s point group (A'/A'') this transforms into $9/3$. Hence, the active space describes three electrons in 12 orbitals which covers an energy spectrum of $> 20000 \text{ cm}^{-1}$. The calculations in this chapter were performed using the MOLPRO program package in its versions 2018.2, 2019.2 or 2020.1 [224, 225, 251–253].

The corresponding basis set for these calculations was constructed in an uncontracted even-tempered (UET) manner. As mentioned in Sec. 3.5, this approach can be used when large basis sets are required, which is the case here, since basis set superposition errors (BSSEs) shall be kept as small as possible. The construction started with the [13s10p5d3f] basis set from Ref. [250] designed for the ECP28MDF small-core (sc) ECP by first changing the tightest d exponent to 1.75067, as suggested by Soldán in Ref. [100]. Since this basis set was originally optimized with respect to atomic polarizabilities it does not provide enough diffuse functions for a proper description

of higher electronic states [254], cf. Sec. 3.5. Therefore, a $(2s, 2p, 2d, 2f)$ set of diffuse functions was added, analogously to the approach in Ref. [100] for the quartet ground state of Rb_3 . The corresponding ratios to obtain the diffuse functions were determined from the original lowest two exponents in each orbital set. Within this resulting span of functions, defined by the largest exponents of the original set and the new most diffuse function, new exponents were calculated in an even-tempered manner as implemented in MOLPRO. Here, the exponents in each orbital set are explicitly given by

$$\log e_i = \log c + [(n+1)/2 - i] \log r + \frac{1}{2} [(n+1)/2 - i]^2 \log d, \quad i = 1, 2, \dots, n, \quad (4.3)$$

with the number of exponents n , their geometric mean c , the mean ratio of successive exponents r , and the variation of this ratio d , which is set to $d = 1$ in all cases. The number of exponents for each orbital set followed from systematically increasing the basis set size such that calculated atomic energy levels of Rb are as close as possible at the basis set limit while, at the same time, the corresponding trimer calculations do not suffer from linear dependencies in the basis set. Having identified the “optimal” basis set size in this way, additional g -exponents were generated according to [255–257]

$$\zeta^{\ell'} = \zeta^{\ell} \frac{\ell' + 3}{\ell + 3}, \quad (4.4)$$

with the angular momentum quantum number ℓ' of the new exponents (i.e. $\ell' = 4$ for g -functions) generated from existing exponents with quantum number ℓ ($\ell = 3$ for f -exponents). This procedure resulted in a $[15s12p7d5f3g]$ uncontracted even-tempered basis set (\equiv UET15), where the g -functions were added to provide more flexibility and to account for additional polarization effects. The corresponding exponents are listed in Tab. C.1.

As shown in the following, the pragmatic lcECP+CPP approach is sufficient for gaining a reliable understanding of the physics of the system, while saving tremendously on computational costs. As mentioned above, the lcECP is by construction designed so to reproduce the experimentally determined atomic energy levels up to the ^2F state to a certain accuracy [249]. This is further demonstrated by the results listed in Tab. 4.1. The mean differences $\bar{\Delta}$ show that both absolute energy levels and SO splittings are reproduced to very good accuracy.

Benchmark calculations on spectroscopic constants for selected singlet and triplet states of Rb_2 reveal the expected accuracy for molecular systems. The results are reported in Tab. 4.2 and the corresponding potential energy curves are shown in Fig. 4.2. In contrast to atomic Rb, these calculations do not account for SOC effects.

TABLE 4.1.: Comparison of calculated (calc.) Rb energy levels and spin-orbit (SO) splittings with experimental data from the NIST [258] database. Calculations were performed at MRCI(lcECP+CPP)/UET15 (see text) level of theory using the ECP-LS technique to account for SOC effects. Differences Δ between theory and experiment as well as the mean difference $\bar{\Delta}$ and the absolute mean difference $\bar{\Delta}_{\text{abs}}$ for the given set of states are also reported.

Term	J	absolute levels [cm^{-1}]			SO splitting [cm^{-1}]		
		calc.	NIST	Δ	calc.	NIST	Δ
^2S	1/2	0	0	0	0	0	0
^2P	1/2	12 577.76	12 578.95	-1.19	12 577.76	12 578.95	-1.19
	3/2	12 811.80	12 816.55	-4.75	234.04	237.60	-3.56
^2D	5/2	19 356.95	19 355.20	1.75	6545.15	6538.66	6.49
	3/2	19 357.15	19 355.65	1.50	0.20	0.45	-0.25
		$\bar{\Delta}$:		-0.67	$\bar{\Delta}$:		0.38
		$\bar{\Delta}_{\text{abs}}$:		2.30	$\bar{\Delta}_{\text{abs}}$:		2.87

TABLE 4.2.: Comparison of experimental (references given in square brackets) and calculated values (calc.) of some spectroscopic constants of a few Rb_2 states (see Fig. 4.2 for assignment). The dissociation energy is denoted by D_e , R_e is the equilibrium distance, and T_e the electronic term energy. Calculations were performed at MRCI(lcECP+CPP)/UET15 level of theory. Differences Δ between theory and experiment as well as the mean difference $\bar{\Delta}$ and the absolute mean difference $\bar{\Delta}_{\text{abs}}$ for the given set of states are also reported.

State	D_e [cm^{-1}]			R_e [\AA]			T_e [cm^{-1}]		
	calc.	exp.	Δ	calc.	exp.	Δ	calc.	exp.	Δ
$X\ ^1\Sigma_g$ [259]	4116	3993.593	122	4.1689	4.2099	-0.0410	0	0	0
$a\ ^3\Sigma_u$ [259]	250	241.503	8	6.0065	6.0940	-0.0875	3866	-	-
$b\ ^3\Pi_u$ [260]	7218	7039	179	4.1537	4.1329	0.0208	9632	9601	31
$A\ ^1\Sigma_u$ [260]	6071	5981	90	4.8637	4.8737	-0.0100	10778	10750	28
$(2)\ ^1\Sigma_g$ [261, 262]	3140	2963	177	5.4081	5.4399	-0.0318	13709	13602	107
$(1)\ ^1\Pi_u$ [263]	2150	1907	243	4.5203	-	-	14700	14666	34
$(1)\ ^1\Pi_g$ [264]	1246	1290	-44	5.4225	5.4188	0.0037	15604	15510	94
		$\bar{\Delta}$:		111	$\bar{\Delta}$:		-0.0243	59	
		$\bar{\Delta}_{\text{abs}}$:		123	$\bar{\Delta}_{\text{abs}}$:		0.0325	59	

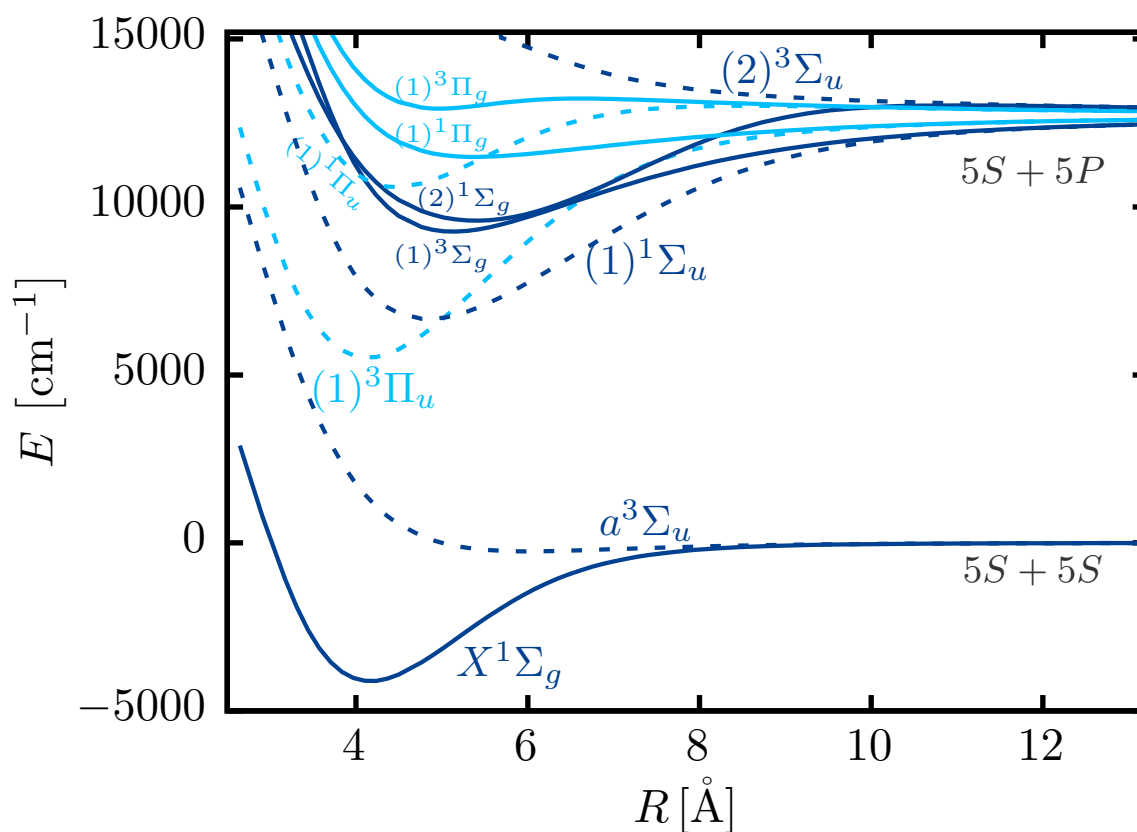


FIGURE 4.2.: Overview of Rb_2 potential energy curves up to the $5S + 5P$ asymptote calculated at MRCI(lcECP+CPP)/UET15 level of theory. Σ -states are plotted in dark blue, while Π states are given in light blue. Solid curves represent electronic states of “gerade” (g) symmetry, while dashed lines correspond to states of “ungerade” (u) symmetry. All energies are given as interaction energies with respect to the $5S + 5S$ asymptote.

This is the default setting (unless otherwise noted) for the following discussions of this chapter. In Sec. 4.3.5 it is shown that in most cases, SOC effects for Rb_3 are only rather small perturbations. The mean differences given in Tab. 4.2 show that binding energies are systematically overestimated by 100 to 250 cm^{-1} , while equilibrium distances are typically underestimated by 0.01 to 0.04 \AA . This over- and underestimation is a well-known bias introduced by the lcECP due to its approximative and insufficient description of the repulsive interaction of core electrons [265–267]. The electronic term energies usually show errors on the order of 30 to 100 cm^{-1} . Since the Rb_3 molecule forms three Rb-Rb bonds, the above mean errors suggest a corresponding estimated accuracy of the *ab-initio* method of $\approx \pm 300\text{ cm}^{-1}$ for equilibrium energies. For bond lengths the same accuracy as for Rb_2 is expected, i.e. about 1% of the total predicted distance. According to the previous findings, energies are probably again overestimated while bond lengths are underestimated. Although these errors seem rather large in the context of ultracold chemistry, the deviations are already in the regime of accurate quantum chemical calculations, defined by the “chemical accuracy” level of $\approx \pm 1\text{ kcal/mol} \approx 350\text{ cm}^{-1}$ for energies.

Increasing this accuracy is possible but requires steeply increasing computational resources. The present approach only requires approximately 40 minutes on eight cores to compute 27 states for a given Rb_3 geometry, thus allowing to explore the configuration space efficiently [245]. An approach toward higher accuracy is shown in Chap. 5 in connection with the construction of a global potential energy surface for the quartet ground state. However, this approach is still insufficient for doublet states, which would ultimately require, e.g., a multireference coupled-cluster approach with a reasonable basis set.

4.3 | General overview of the Rb_3 system

The following discussion gives broad insights into the physics of the Rb_3 system, ranging from proper coordinate systems to exploring occurring coupling and crossing effects by special cuts through the PESs, to a detailed study of equilibrium states and a survey of spin-orbit coupling effects.

4.3.1 | Coordinates

The generic representation of homonuclear triatomic systems was already shown in Fig. 2.3 to motivate the symmetry operations of the D_{3h} point group. The results

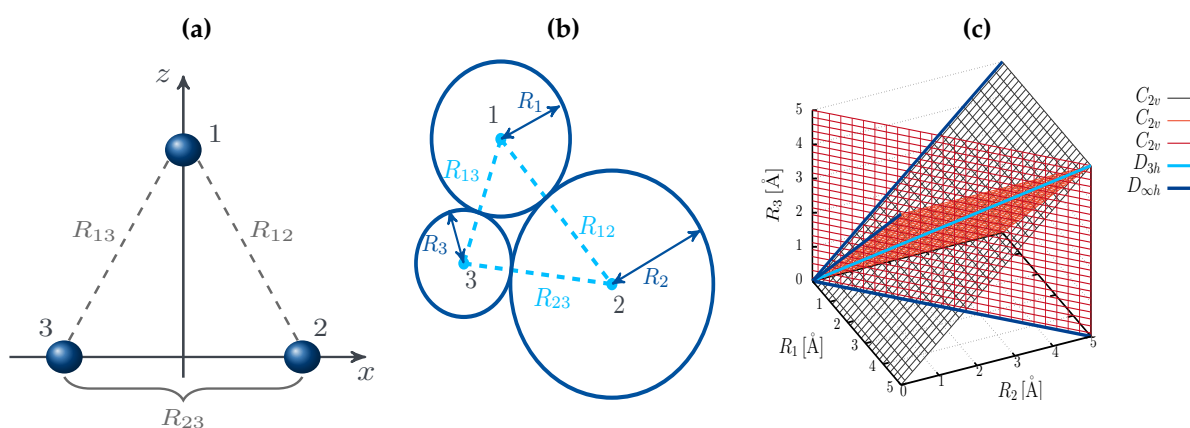


FIGURE 4.3.: (a) The Rb_3 system in the xz plane with *internuclear distances* R_{12}, R_{23}, R_{13} . (b) Sketch of the geometric interpretation of the *perimetric coordinates* for triatomic molecules. They represent the radii of three mutual tangent circles centered on the nuclei. Internuclear distances satisfying the triangular inequality may be recovered using Eq. (4.5). (c) The positive octant in perimetric coordinates to show special configuration subspaces of triatomic systems (i.e. $D_{\infty h}$, D_{3h} and C_{2v}). *Freely adapted from J. Schnabel et al., Phys. Rev. A* **103**, 022820 (2021).

presented below are based on calculations in which the Cartesian coordinate system was chosen, without loss of generality, such that the molecular plane coincides with the xz plane; see Fig. 4.3 (a). Apart from internal use, e.g., in MOLPRO to assign electronic states to their corresponding IRREP, Cartesian coordinates are barely used to study the physics of trimers. Triatomic systems have three internal degrees of freedom, except for linear configurations for which they have a fourth degree of freedom. There are many coordinate systems available to study three-body problems and in general each of them has its strengths and weaknesses and the choice strongly depends on what one wants to analyze. For the investigation of three-body collision processes, Jacobi and hyperspherical coordinates are commonly used; see, e.g., Refs. [268–270] and references therein. The findings reported in this thesis make use of three different coordinate systems.

Two of these coordinate systems were already introduced in Eq. (2.51): the (*symmetry-adapted*) *JT coordinates* and the *internuclear distances*, which can be used to define the former. As shown in Sec. 2.3.2, JT coordinates are powerful to characterize the main topological features of PESs near D_{3h} equilateral triangular configurations, wherefore JT theory is most efficiently formulated using these coordinates. It is straightforward to use internuclear distances as illustrated in Fig. 4.3 (a). However, not every triple (R_{12}, R_{23}, R_{13}) obeys the triangular inequality and thus defines a possible molecular conformation. Therefore, it is convenient to employ *perimetric coordinates* [271–277] as

used by Davidson in his analysis of H_3 [278]. This coordinate system follows from mapping each set $\{R_{12}, R_{23}, R_{13}\}$ that satisfies the triangular inequality to the positive octant and becomes

$$R_1 = \frac{1}{2}(R_{12} + R_{13} - R_{23}) , \quad (4.5a)$$

$$R_2 = \frac{1}{2}(R_{12} + R_{23} - R_{13}) , \quad (4.5b)$$

$$R_3 = \frac{1}{2}(R_{13} + R_{23} - R_{12}) . \quad (4.5c)$$

These are the radii of three mutually tangent circles centered on the nuclei, as shown in Fig. 4.3 (b). The perimetric coordinates reveal some general properties [245]:

1. Every triple of numbers (R_1, R_2, R_3) in the positive octant, cf. Fig. 4.3 (c), gives a unique molecular conformation (modulo permutational inversion; it is symmetric in the three atoms), i.e. the coordinates fulfill the triangular inequality by definition.
2. Internuclear distances are given as the sum of these coordinates, e.g. $R_{12} = R_1 + R_2$.
3. Linear arrangements, in general of $C_{\infty v}$ symmetry, are defined by one of the perimetric coordinates being zero, this being the coordinate related to the central atom (e.g. for $R_1 = 0$, $R_2 = R_{12}$ and $R_3 = R_{13}$). In the positive octant this corresponds to the three equivalent boundary planes.
4. The dissociation limit atom + dimer corresponds to the respective atom coordinate being large (e.g. $\text{atom}_1 + \text{dimer}_{23} \Leftrightarrow R_1 \rightarrow \infty$).

Fig. 4.3 (c) summarizes further special positions in the positive octant, i.e. all such showing higher point group symmetry than C_s . Linear molecules of $D_{\infty h}$ symmetry are found on three equivalent diagonals of the boundary planes. Equilateral triangular configurations are defined by the space diagonal and isosceles triangular conformations are, due to the permutational symmetry, represented by one of the three space diagonal surfaces. Since it is not defined if the atoms are labeled clockwise or counterclockwise, strictly speaking there are six such C_{2v} surfaces. All configurations which are not described by one of the above subspaces are of C_s point group symmetry.

In the following it is shown that the use of perimetric coordinates provides a powerful tool to efficiently explore the configuration space of Rb_3 .

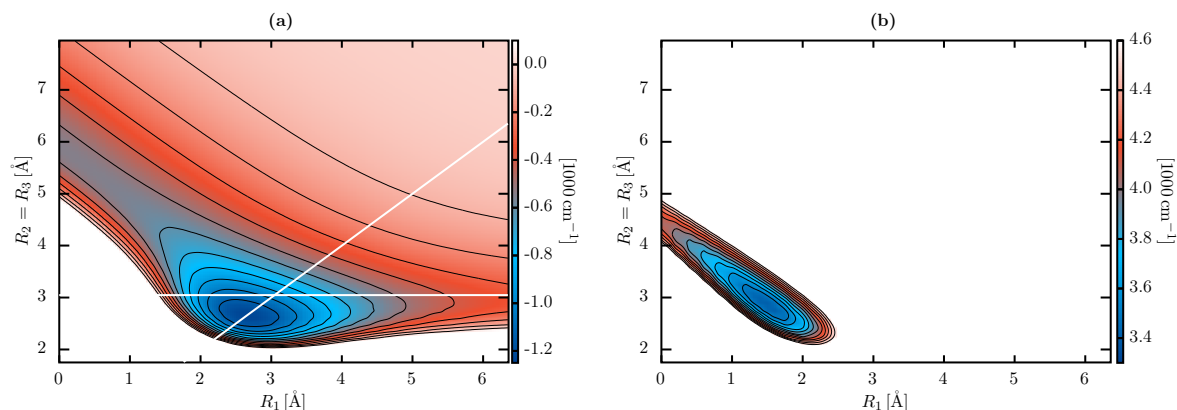


FIGURE 4.4.: Two-dimensional contour plots of the PESs of the quartet ground state 1^4B_1 in (a) and the first excited quartet state 1^4A_2 in (b). The R_1 and $R_2 = R_3$ subspace of perimetric coordinates corresponds to one of the space diagonal surfaces in Fig. 4.3 (c). In (a), the diagonal line shown in white represents the space diagonal along D_{3h} configurations, while the horizontal line represents a special one-dimensional C_{2v} -cut for $R_{23} = 6.094 \text{\AA}$ drawn for later reference. The wavy character in (b) is due to the underlying spline interpolation of the corresponding *ab-initio* data. Energies are given with respect to the free atom-atom-atom limit and were computed at MRCI(lcECP+CPP)/UET15 level of theory. *Freely adapted from J. Schnabel et al., Phys. Rev. A 103, 022820 (2021).*

4.3.2 | Exploring the system by special cuts through the PESs

The identification of appropriate states for PA first requires a basic understanding of occurring coupling and crossing effects. Hence, the following investigations start with special cuts through the potential energy surfaces of both doublet and quartet manifolds.

Two-dimensional cuts in the C_{2v} subspace

To obtain a first insight it is sufficient to restrict the investigations to the C_{2v} subspace, since all equilibrium structures show at least isosceles triangular configurations, which is further discussed in Sec. 4.3.3. This is moreover the reason that in the following all electronic states are labeled according to the IRREPs of the C_{2v} point group. With the definition of coordinates as illustrated in Fig. 4.3 (a), A_1 and B_1 states are symmetric, and B_2 and A_2 states are antisymmetric with respect to reflections of the electronic coordinates at the molecular plane. The topology of the two-dimensional potential-energy landscapes of the quartet ground state 1^4B_1 and the first excited quartet state 1^4A_2 is shown in Fig. 4.4. This corresponds to a two-dimensional scan of C_{2v} nuclear configurations, i.e. to one of the space diagonal surfaces shown in Fig. 4.3 (c). As

depicted in Fig. 4.4 (a), the global minimum of the quartet ground state occurs at equilateral triangular (D_{3h}) symmetry and the PES is rather shallow. Linear geometries correspond in this cut to $R_1 = 0$, where the 1^4B_1 state reveals a saddle point marking the transition to the inverted structure. These findings are in perfect agreement with Soldán's previous work [100] on the quartet ground state PES of Rb_3 . Moreover, it turns out that the quartet ground state is well isolated from excited quartet states, with crossings occurring only high above the dissociation limits and thus high above the global minimum. From Fig. 4.4 (b) it is apparent that the global minimum on the PES of the first excited quartet state 1^4A_2 occurs at C_{2v} symmetry. This distortion from the high-symmetry configuration is considered in detail in Secs. 4.4 and 4.5 and is due to the JT effect forming a twofold degenerate $1^4E''$ state at D_{3h} geometries. The PES of the 1^4A_2 state rises significantly steeper than the shallow quartet ground-state PES.

One-dimensional D_{3h} and C_{2v} cuts

The presence of $E \otimes e$ and $(E + A) \otimes e$ (pseudo) Jahn-Teller vibronic coupling effects, as discussed in detail in Sec. 2.3, are generic for homonuclear trimers. Equilateral triangular configurations of X_3 systems display D_{3h} symmetry and allow for twofold degenerate E terms. Since MOLPRO can only use Abelian point group symmetries, the degenerate E terms have to be identified by hand from Fig. 4.5 using Tab. A.1. The JT theorem states [152, 161, 164, 183] that the PES of at least one of the degenerate states has no extremum at the high-symmetry point. According to Eq. (2.50) this implies a non-vanishing generalized force at the point of degeneracy leading to a stabilization of the system by symmetry-lowering. In the present case, E' states branch off into $A_1 + B_1$, and E'' states branch off into $B_2 + A_2$ states, each with the formation of a COIN at the D_{3h} reference point. These (pseudo) Jahn-Teller interactions can be already deduced from one-dimensional scans along the D_{3h} subspace indicated by the diagonal shown in white in Fig. 4.4 (a). The resulting PECs are shown in Fig. 4.5 in the space of internal coordinates ($R_{12} = R_{23} = R_{13}$). The JT-induced energy lowering with respect to distortions to C_{2v} configurations is indicated by the insets in Fig. 4.5. Potential energy curves which are degenerate over the whole range shown in Fig. 4.5 correspond to Jahn-Teller E states and are thus actually one-dimensional COIN seams in the full three-dimensional configuration space.

The doublet ground states of alkali trimers are well known to undergo JT distortions with respective global minima occurring at obtuse triangular C_{2v} geometries [80–84, 86–97]. This is also illustrated in Fig. 4.5 (a) by the correlating inset. Moreover, the

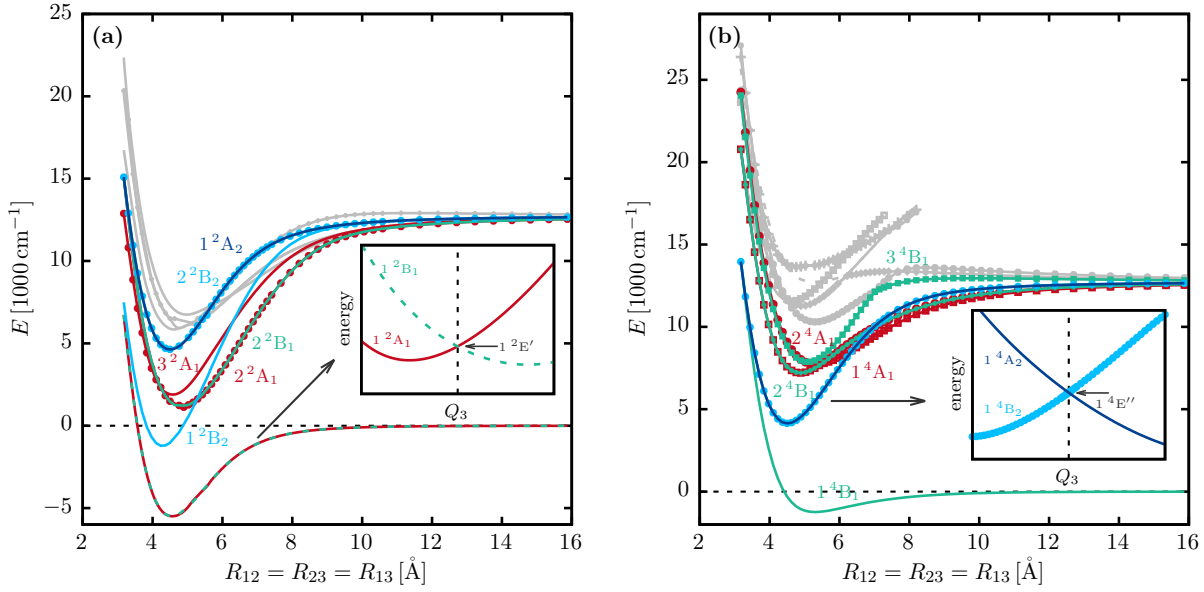


FIGURE 4.5.: One-dimensional D_{3h} cut through the PESs along the space diagonal in the perimetric coordinate space shown Fig. 4.3 (c) or along the diagonal shown in white in Fig. 4.4 (a) (equilateral triangular configuration maintained). Doublet states are shown in (a) and quartet states in (b), respectively. Only states discussed in the text are colored, while remaining states are indicated by the gray lines. Energies are given with respect to the free atom-atom-atom limit and were computed at MRCI(lcECP+CPP)/UET15 level of theory. *Freely adapted from J. Schnabel et al., Phys. Rev. A* **103**, 022820 (2021).

presence of combined JT and PJT coupling, cf. e.g., Ref. [86] for Na_3 , is also indicated in Fig. 4.5. The 2^2A_1 and 2^2B_1 states are degenerate components of the $2^2E'$ term and the 3^2A_1 states is nearby in energy. Hence, as outlined in Sec. 2.3.3, the triple of states $\{2^2A_1, 2^2B_1, 3^2A_1\}$ constitutes a typical scenario for combined JT plus PJT interactions [182].

In contrast to the doublet ground state, the quartet ground state is free of JT distortions, with its global minimum occurring at D_{3h} configurations. The first two excited quartet states are degenerate along a one-dimensional COIN seam in the D_{3h} subspace forming the $1^4E''$ term. This term splits into the 1^4A_2 and 1^4B_2 states when the symmetry is lowered. A further peculiarity is made up of the subset of quadruple interactions of quartet states:

$$\mathcal{Q} = \{1^4A_1, 2^4B_1, 2^4A_1, 3^4B_1\}. \quad (4.6)$$

As illustrated in Fig. 4.5 (b), these states are nearly degenerate in the region from $\approx 5.0 - 7.0 \text{ \AA}$. Section 4.6 attempts to unravel the underlying coupling mechanisms.

The horizontal line in Fig. 4.4 (a) indicates a special one-dimensional cut along C_{2v}

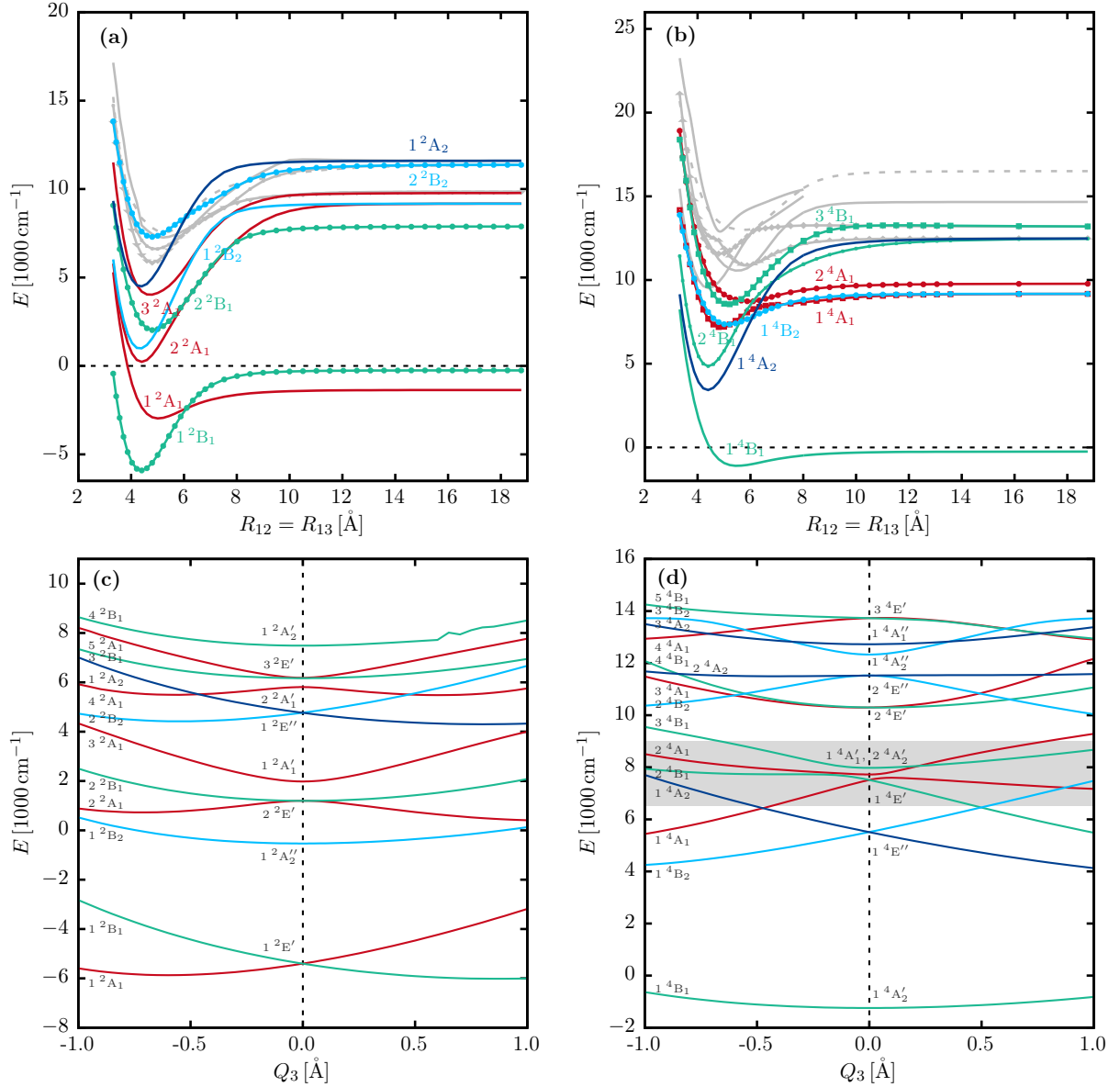


FIGURE 4.6.: **Upper panel:** One-dimensional C_{2v} cut through the PESs along one special direction on one of the space diagonal surfaces shown in Fig. 4.3 (c). This C_{2v} scan corresponds to $R_{23} = R_e(a^3\Sigma_u) = 6.094 \text{ \AA}$ and thus to the horizontal white line shown in Fig. 4.4 (a). Doublets are shown in (a) and quartets in (b), respectively. **Lower panel:** One-dimensional scans along the JT active bending mode Q_3 of Eq. (2.51), with $Q_2 = 0.0 \text{ \AA}$, distorting equilateral triangular configurations to C_{2v} geometries. For $Q_3 \neq 0$ the states are labeled according to the IRREPs of the C_{2v} point group while the corresponding D_{3h} IRREPs are given at $Q_3 = 0$. Doublet states are depicted in (c) for $Q_1 = 8.1701 \text{ \AA}$ while quartet states are shown in (d) for $Q_1 = 9.1989 \text{ \AA}$. The area highlighted in gray represents the manifold \mathcal{Q} of excited quartet states where a complicated interplay between avoided crossings, conical intersections and JT interactions is present (see text and Sec. 4.6 for details). Energies are given with respect to the $3 \cdot \text{Rb}$ limit and were computed at MRCI(lcECP+CPP)/UET15 level of theory. *Freely adapted from J. Schnabel et al., Phys. Rev. A 103, 022820 (2021).*

configurations and corresponds to a collision trajectory between a Rb₂ molecule and a Rb atom. For this cut, the distance R_{23} was fixed to the equilibrium distance of the lowest triplet state $a^3\Sigma_u$ of Rb₂. The resulting potential energy curves in the space of internal coordinates $R_{12} = R_{13}$ in Fig. 4.6 (a) and (b) give a first impression of the expected states possibly involved in a PA1 scheme. The density of states increases for higher energies for both doublet and quartet states and thus decreases the chance to find sufficiently long-lived target states for PA experiments [245].

Inspired by Refs. [92, 95, 96, 99], a better understanding of present JT and PJT coupling effects in Rb₃ may be obtained from one-dimensional scans along the symmetric distortion coordinate Q_3 according to Eq. (2.51) preserving at least C_{2v} symmetry. This represents one dimension of the 2D branching space formally spanned by Q_2 and Q_3 and thus gives an improved notion of the topology of the full 3D potential-energy-landscape near the central degeneracy at $Q_2 = Q_3 = 0.0 \text{ \AA}$. The resulting cuts are shown in Fig. 4.6 (c) and (d). In this regard it is worth mentioning that the D_{3h} scans in Fig. 4.5 can be viewed as cuts along the totally symmetric breathing mode Q_1 with $Q_2 = Q_3 = 0.0 \text{ \AA}$, cf. Eq. (2.51).

In general, the doublet states in Fig. 4.6 (c) may be divided in three classes of interactions: non-interacting states, JT states and PJT states. The first class is made up of states that are free of strong JT interactions and which show minima near equilateral configurations. Merely the 1^2B_2 and 4^2B_1 states belong to this class. Jahn-Teller interacting states are those which cross at $Q_3 = 0.0 \text{ \AA}$ and lift the degeneracy for $Q_3 \neq 0.0 \text{ \AA}$. These JT states form a one-dimensional COIN seam in the subspace of D_{3h} configurations as indicated in Fig. 4.5 (a). The third class is made up of near-in-energy E and A states (in terms of D_{3h} IRREPs, cf. Tabs. A.1 and A.7): the $(E + A) \otimes e$ PJTE as outlined in Sec. 2.3.3. Due to the interaction with the third state, the doubly degenerate E terms may not always show COINs rather than glancing intersections at $Q_3 = 0.0 \text{ \AA}$. If this is the case, only at a single point in the D_{3h} subspace all three states become degenerate and form a triple COIN. This intersection is analogous to the JT one, but it is not required by symmetry. This observation may be modeled by Eq. (2.81), which is based on the assumption that the PJT interaction supersedes the JT one justifying thus the approximation $V_{ie}^E \approx 0, i = \{1, 2\}$, which then moreover implies that the central COIN vanishes. This seems to reproduce the topology shown in Fig. 4.6 (c) and is in agreement with what have been reported for the doublet states of Na₃ in Ref. [86]. However, as insinuated, the absence of a central COIN for triply interacting states is not generally implied by the PJT theory for X_3 systems. In particular, as also pointed out

for Na_3 in Sec. 2.3.3 and in Ref. [88], it remains to properly investigate the parameter range for which vanishing JT coupling parameters (i.e. $V_{ie}^E \approx 0, i = \{1, 2\}$), i.e. a pure PJT model, is a good approximation. Vice versa, it shall be investigated if there is a parameter range for which the JT interaction supersedes the PJT one. In contrast to what is reported here, Rocha and Varandas [152] found central COINs in their PJT model for C_3 . Furthermore, to obtain a full three-dimensional picture, couplings to the Q_1 mode should be considered as well [91].

The quartet states as shown in Fig. 4.6 (d) may be classified accordingly with a fourth class made up by the area highlighted in gray marking the peculiar sub-manifold of quadruple interactions \mathcal{Q} after Eq. (4.6). This complicated coupling situation describes an interplay of JT couplings and avoided crossings and is analyzed in more detail in Sec. 4.6.

More information on the JT and PJT states shown in Fig. 4.6 (c) and (d) are summarized in Tab. 4.3. The lowest COIN corresponds to the respective minimum on the one-dimensional D_{3h} PEC and can be used to define a stabilization energy of the global minimum on the respective JT PES [86]. Table 4.3 reveals that the lowest COINs on the quartet $1^4E''$ and doublet $1^2E''$ JT manifolds occur at the exact same position. This is due to the underlying orbital degeneracies, which are the same for both states. A notion of the topology of the resulting JT-PESs in the 2D branching space according to Fig. 2.4 can be deduced from the specification of the kind of extrema obtained for the components forming the JT pairs. Explicit values of the extremal points are given in Tabs. 4.4, D.1 and D.3. The energetically high-lying doublet and quartet JT states $3^2E'$ and $3^4E'$ as shown in Figs. 4.6 (c) and (d), respectively, correspond to cases where the MRCI approach reaches its limits. The corresponding geometry optimization did not properly converge and thus these states are not listed in Tab. 4.3. Figure 4.6 (c) suggests that the $3^2E'$ state shows PJT interaction with the close-in-energy 4^2A_1 state. A final classification of the PJT interaction, possibly present between the $2^4E''$ JT pair and either the 3^4A_2 or the 3^4B_2 state, requires to model the *ab-initio* data through a PJT Hamiltonian of the form given in Eq. (2.76).

Linear configurations and corresponding coupling effects

One-dimensional cuts along the $D_{\infty h}$ subspace for $R_1 = 0$ [cf. Fig. 4.3 (c)] are shown in Fig. 4.7. In the case of the Li trimer it has been shown [83, 100, 104, 106] that the $1^4\Sigma_u^+$ and $1^4\Pi_g$ state intersect and form a secondary $D_{\infty h}$ minimum on the quartet ground state PES. Moreover, the states cross on a COIN seam that lies below the

TABLE 4.3.: Overview on (pseudo) Jahn-Teller pairs of the doublet and quartet states of Rb_3 as shown in Fig. 4.6 (c) and (d). Calculations were performed at MRCI(lcECP+CPP)/UET15 level of theory and energies are given relative to the $3 \cdot \text{Rb}$ asymptote. At D_{3h} geometries there are degenerate states which branch off into their correlating components when lowering the symmetry to C_{2v} . The reported geometries and energies $E[\text{min}(\text{COIN})]$ refer to the minima on the one-dimensional D_{3h} PECs shown in Fig. 4.5. The classification denotes if the interaction is due to a pure JT coupling, a PJT coupling or if it is part of \mathcal{Q} after Eq. (4.6). The kind of extrema corresponding to the components gives a notion of the topology of the JT-PES in the 2D branching space, cf. Fig. 2.4.

State (D_{3h})	Components (C_{2v})	R_{12}, R_{23}, R_{13} [\AA] (R_1, R_2, R_3)	$E[\text{min}(\text{COIN})]$ [cm^{-1}]	Classification
$1^4\text{E}'$	$1^4\text{A}_1 + 2^4\text{B}_1$	4.879, 4.879, 4.879 (2.440, 2.440, 2.440)	7202	part of \mathcal{Q} manifold
$2^4\text{E}'$	$3^4\text{A}_1 + 4^4\text{B}_1$	5.305, 5.305, 5.305 (2.653, 2.653, 2.653)	10302	JT pair 3^4A_1 saddle point, 4^4B_1 minimum
$1^4\text{E}''$	$1^4\text{B}_2 + 1^4\text{A}_2$	4.500, 4.500, 4.500 (2.250, 2.250, 2.250)	4146	JT pair 1^4B_2 saddle point, 1^4A_2 minimum
$2^4\text{E}''$	$2^4\text{B}_2 + 2^4\text{A}_2$	4.916, 4.916, 4.916 (2.458, 2.458, 2.458)	11271	possibly PJT with 3^4A_2 or 3^4B_2
$1^2\text{E}'$	$1^2\text{A}_1 + 1^2\text{B}_1$	4.546, 4.546, 4.546 (2.273, 2.273, 2.273)	-5494	JT pair 1^2A_1 saddle point, 1^2B_1 minimum
$2^2\text{E}'$	$2^2\text{A}_1 + 2^2\text{B}_1$	4.824, 4.824, 4.824 (2.412, 2.412, 2.412)	1167	PJT with 3^2A_1
$1^2\text{E}''$	$2^2\text{B}_2 + 1^2\text{A}_2$	4.500, 4.500, 4.500 (2.250, 2.250, 2.250)	4624	JT pair 2^2B_2 saddle point, 1^2A_2 minimum

three-atom dissociation limit and due to its proximity to the atom-diatom dissociation limit it could potentially influence the low-energy atom-diatom collisions. The cut in Fig. 4.7 (b) shows that for Rb_3 no secondary minimum is formed on the quartet ground state PES since the crossing occurs high above the three-atom limit and thus also high above the atom-diatom dissociation limit. This was also demonstrated by Soldán in Ref. [100].

In general, linear configurations of homonuclear trimers have four degrees of freedom and usually occur at $D_{\infty h}$ symmetry. This point group allows for twofold degenerate Π terms, which have to be identified by hand (calculations were performed using the C_{2v} symmetry group) from Fig. 4.7 using Tab. A.8. Again, degenerate states give rise to rovibrational coupling effects. The corresponding theoretical basics were outlined in Sec. 2.4 and are mainly based on the findings from Ref. [163]. The longstanding belief that linear molecules in degenerate states are only affected by the Renner-Teller

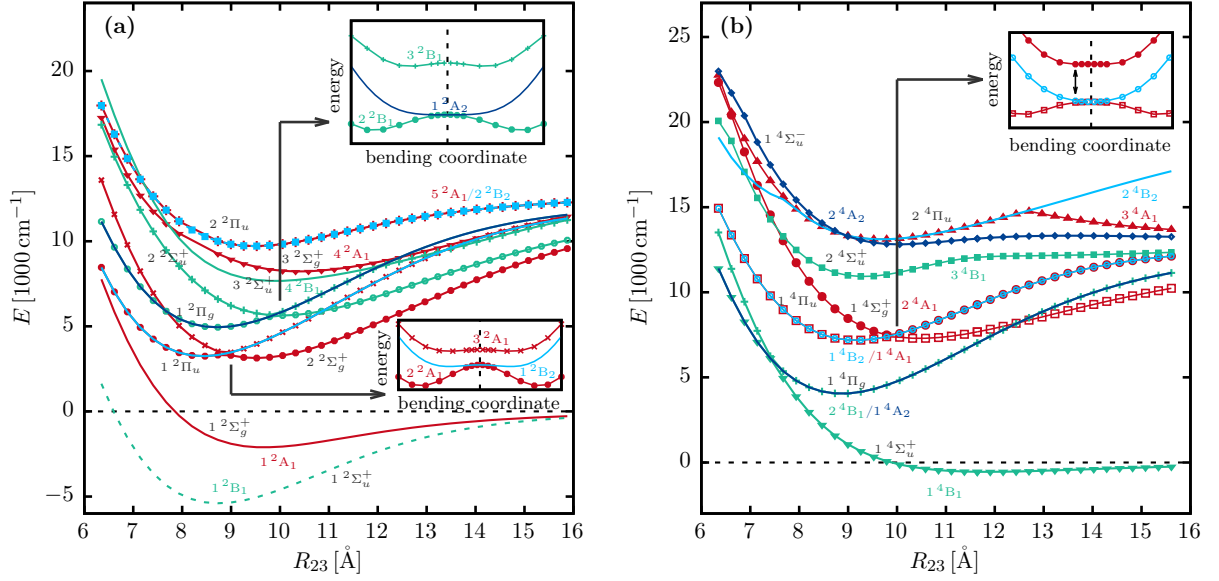


FIGURE 4.7.: One-dimensional $D_{\infty h}$ cut through the PESs along the diagonal of the boundary plane for $R_1 = 0$ as shown in Fig. 4.3 (c). The central atom (1) in Fig. 4.3 (a) is fixed at the origin so that the linear molecule is oriented along the x-axis. Doublet states are shown in (a) and quartet states in (b). The states are labeled according to their corresponding C_{2v} IRREPs and are assigned to their correlating $D_{\infty h}$ IRREPs after Tab. A.8. Doubly degenerate states form Π states. The insets illustrate the bending instabilities of linear configurations with respect to triangular distortions due to a combined RTE plus PJTE (see text). These calculations are based on an insertion scan of the central atom [cf. Fig. 4.3 (a)] along the z-axis, while fixing the R_{23} coordinate. All energies are given with respect to the $3 \cdot \text{Rb}$ limit and were computed at MRCI(lcECP+CPP)/UET15 level of theory. *Freely adapted from J. Schnabel et al., Phys. Rev. A 103, 022820 (2021).*

effect has been reversed in this work and it was shown that bending instabilities are only due to the PJTE. This led to the formulation of a combined RTE plus PJTE theory. For homonuclear trimers close-in-energy Π and Σ states are of particular interest. As a consequence of this combined pseudo Jahn-Teller and Renner-Teller interaction, two A_1 states, one of them arising from a Π_u state, can mix for greater displacements along $D_{\infty h}$ geometries. This can be seen for both doublet and quartet states in Fig. 4.7. For the energy range shown in Fig. 4.7, typical scenarios of bending instabilities due to a combined RT plus PJT interaction are illustrated in the insets.

A deeper investigation of coupling mechanisms for linear configurations of Rb_3 in terms of the RTE or combined RTE plus PJTE theory is beyond the scope of this thesis. This might be part of future investigations to fully understand occurring bending instabilities on the one hand and stable linear configurations on the other hand.

4.3.3 | Equilibrium states

Useful information towards the realization of PA processes may be provided by the electronic energies at the respective equilibrium geometries. A systematic overview of these equilibrium energy levels of all doublet and quartet states of Rb₃ within the energy range investigated in this work is given in Fig. 4.8. The geometry optimizations for finding the equilibrium states started from D_{3h} configurations followed by lowering the symmetry to C_{2v} geometries. Further decreasing the symmetry to C_s allows for searching equilibrium structures of even lower symmetry. The topological implications of the JT effect onto the potential-energy landscapes do not predict C_s minima and neither revealed our analysis in this low-symmetry space. The explored energy range contains all equilibrium states and corresponding term energies up to the $5s + 2 \cdot 5p$ asymptote. The energies of the Rb₂+Rb or Rb+Rb+Rb dissociation asymptotes are given in the middle panel. A unique assignment of the trimer states to the Rb₂+Rb asymptotes is only possible for the quartet ground state dissociating into $a^3\Sigma_u + 5s$. For cuts along one-dimensional C_{2v} subspaces, as shown in Figs. 4.6 (a) and (b), such assignments are also possible for the remaining trimer states both of quartet and doublet spin multiplicity. In the general case, however, all Rb₂+Rb asymptotes correlating with the respective trimer state symmetry are possible dissociation channels [245]. The lowest doublet JT manifold $1^2E'$ dissociates either to $X^1\Sigma_g + 5s$ or to $a^3\Sigma_u + 5s$. All excited doublet and quartet states given in Fig. 4.8 correlate to the $2 \cdot 5s + 5p$ asymptote and thus to Rb₂+Rb dissociation limits below that. So do most of the states shown in Figs. 4.6 (c) and (d). For doublet states, both singlet and triplet Rb₂ states are possible. Merely the highly excited quartet states 2^4B_2 , 3^4B_2 and 4^4A_1 correspond to the $5s + 2 \cdot 5p$ asymptote and thus to the $(1)^3\Pi_u + 5p$ dissociation limit. The top panel of Fig. 4.8 shows the ionized trimer states, which appear either in singlet or triplet configuration. These Rb₃⁺ states could be useful if a resonance-enhanced multi-photon ionization [279] scheme is used for the detection of previously generated Rb₃ species. All these findings, together with the corresponding harmonic vibrational frequencies $\tilde{\nu}$, are listed in Tab. 4.4 for triangular geometries and in Tab. 4.5 for $D_{\infty h}$ linear configurations.

These results are in good agreement with previous works on Rb₃. Concerning the quartet ground state PES of Rb₃, Soldán [100] found the global minimum at equilateral bond distances b with $b = 5.450 \text{ \AA}$ and corresponding minimum energy $E_{\min} = -1071 \text{ cm}^{-1}$. These findings were based on a RHF-RCCSD(T) approach with a [16s13p8d5f3g] basis set and the small-core pseudopotential ECP28MDF from Ref. [250].

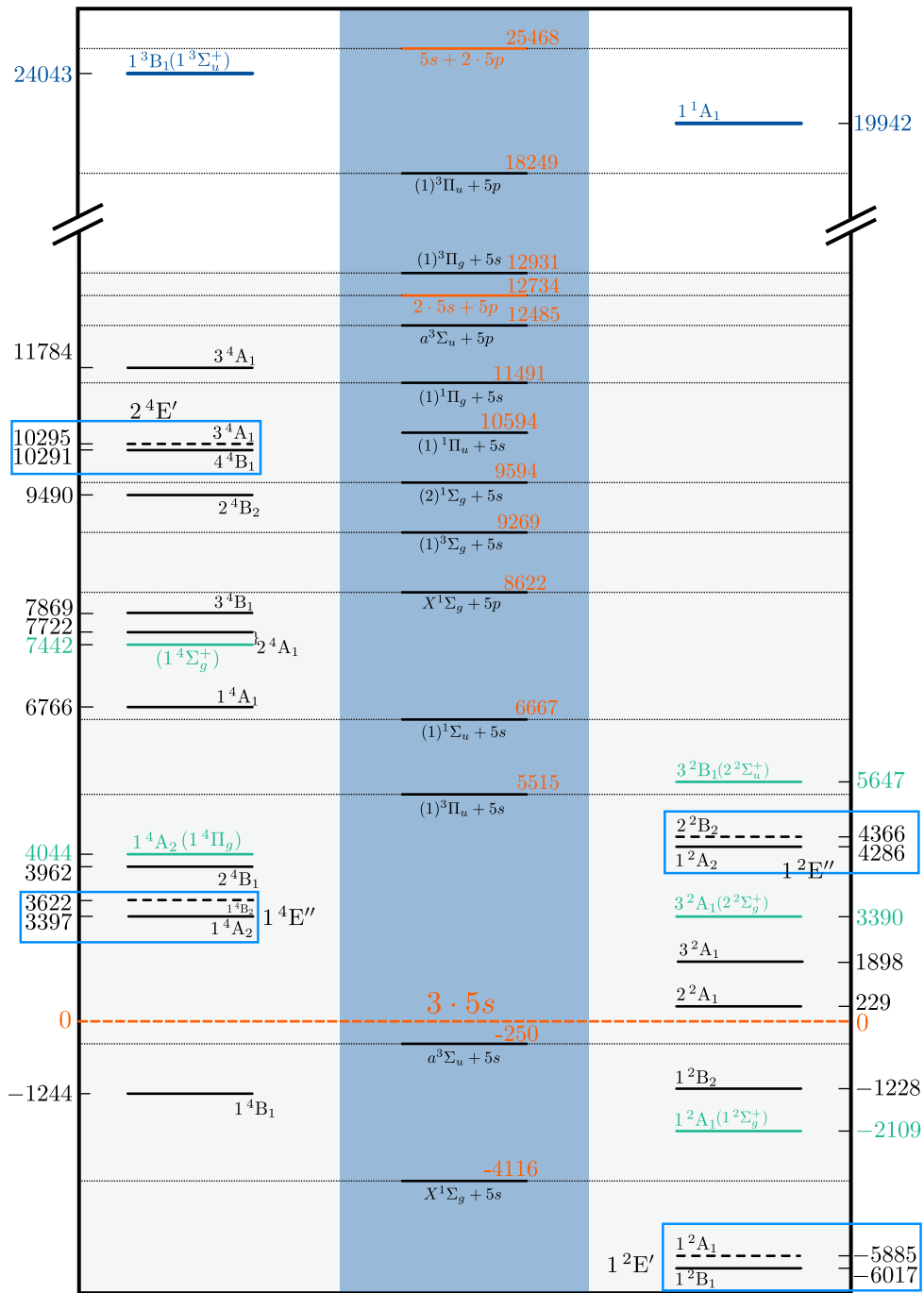


FIGURE 4.8.: Energy level diagram of the extremal points of **doublet (right)** and **quartet (left)** states of Rb_3 optimized at MRCI(lcECP+CPP)/UET15 level of theory. The dissociation asymptotes into Rb_2+Rb (with the corresponding equilibrium energies of the Rb_2 states) or $Rb+Rb+Rb$ are shown in the area highlighted in blue. Levels given in **black** belong to **triangular** equilibrium configurations (i.e. D_{3h} or C_{2v} symmetry) while levels given in **green** represent **linear** equilibrium configurations (all of them $D_{\infty h}$ symmetry). **Light blue boxes** mark selected Jahn-Teller pairs from Tab. 4.3, where the respective dashed lines correspond to saddle points showing isosceles triangular geometry. Ionized Rb_3^+ states are shown at the top in terms of blue energy levels. All energies are given relative to the $3 \cdot Rb [5s]$ limit. *Freely adapted from J. Schnabel et al., Phys. Rev. A 103, 022820 (2021).*

TABLE 4.4.: Synopsis of **triangular** (C_{2v} and D_{3h}) doublet and quartet states of Rb₃ as well as the singlet state of Rb₃⁺ computed at MRCI(lcECP+CPP)/UET15 level of theory. Equilibrium structures are given in terms of the internal coordinates (perimetric coordinates) introduced in Fig. 4.3 and all corresponding energies (E_{rel}) are given relative to the ($3 \cdot 5s$)–asymptote. The states are labeled according to the C_{2v} IRREPs while the corresponding assignment to D_{3h} symmetry is given in parenthesis. This complements the results of the energy level diagram of Fig. 4.8.

State (D_{3h})	R_{12}, R_{23}, R_{13} [Å] (R_1, R_2, R_3)	Geometry	E_{rel} [cm ⁻¹]	$\tilde{\nu}_{D_{3h}}$ [cm ⁻¹] ^a	$\tilde{\nu}_{C_{2v}}$ [cm ⁻¹] ^a	$\tilde{\nu}_{C_s}$ [cm ⁻¹] ^a
1 ⁴ B ₁ (1 ⁴ A ₂)	5.311, 5.311, 5.311 (2.656, 2.656, 2.656)	D_{3h}	-1244	23.8	23.6	23.6
1 ⁴ A ₂ (1 ⁴ E'')	4.368, 5.700, 4.368 (1.518, 2.850, 2.850)	C_{2v}	3397	50.2	17.2	35.8
2 ⁴ B ₁ (1 ⁴ E')	4.442, 8.179, 4.442 (0.352, 4.090, 4.090)	C_{2v}	3962	40.3	9.6	40.4
1 ⁴ A ₁ (1 ⁴ E')	4.993, 8.076, 4.993 (0.955, 4.038, 4.038)	C_{2v}	6766	32.8	9.8	50.7
2 ⁴ A ₁ (1 ⁴ A ₁ ')	5.325, 5.325, 5.325 (2.663, 2.663, 2.663)	D_{3h}	7722	32.0	83.9	83.9
3 ⁴ B ₁ (2 ⁴ A ₂)	5.084, 5.084, 5.084 (2.542, 2.542, 2.542)	D_{3h}	7869	43.0	58.2	58.2
2 ⁴ B ₂ (2 ⁴ E'')	4.443, 6.217, 4.443 (1.335, 3.109, 3.109)	C_{2v}	9490	52.0	42.7	41.3
4 ⁴ B ₁ (2 ⁴ E')	5.283, 5.337, 5.283 (2.615, 2.669, 2.669)	C_{2v}	10291	31.5	37.7	39.0
3 ⁴ A ₁ (upper) (2 ⁴ E')	4.687, 7.226, 4.687 (1.074, 3.613, 3.613)	C_{2v}	11784	41.5	28.2	27.5
1 ² B ₁ (1 ² E')	4.379, 5.393, 4.379 (1.682, 2.697, 2.697)	C_{2v}	-6017	53.1	20.6	33.3
1 ² B ₂ (1 ² A ₂ '')	4.276, 4.285, 4.276 (2.134, 2.143, 2.143)	C_{2v}	-1228	60.9	43.9	44.1
2 ² A ₁ (2 ² E')	4.398, 6.073, 4.398 (1.361, 3.037, 3.037)	C_{2v}	229	50.4	26.7	42.1
3 ² A ₁ (1 ² A ₁ ')	4.557, 4.557, 4.557 (2.279, 2.279, 2.279)	D_{3h}	1898	51.9	100.6	100.6
1 ² A ₂ (1 ² E'')	4.337, 5.132, 4.337 (1.771, 2.566, 2.566)	C_{2v}	4286	52.9	23.7	30.2
1 ¹ A ₁ (1 ¹ A ₁ ')	4.610, 4.610, 4.610 (2.305, 2.305, 2.305)	D_{3h}	19942	53.2	36.6	36.5

^a In general the assignment is not unique but usually $\tilde{\nu}_{D_{3h}}$ is Q₁-like, $\tilde{\nu}_{C_{2v}}$ is Q₃-like and $\tilde{\nu}_{C_s}$ is Q₂-like.

TABLE 4.5.: Synopsis of **linear** ($D_{\infty h}$) doublet and quartet states of Rb_3 as well as the triplet state of Rb_3^+ computed at MRCI(lcECP+CPP)/UET15 level of theory. Equilibrium structures are given in terms of the internal coordinates (perimetric coordinates) introduced in Fig. 4.3 and all corresponding energies (E_{rel}) are given relative to the $(3 \cdot 5s)$ -asymptote. The states are labeled according to the C_{2v} IRREPs while the corresponding assignment to $D_{\infty h}$ symmetry is given in parenthesis. This complements the results of the energy level diagram of Fig. 4.8.

State ($D_{\infty h}$)	R_{12}, R_{23}, R_{13} [\AA] (R_1, R_2, R_3)	E_{rel} [cm^{-1}]	$\tilde{\nu}_{\text{symm}}$ [cm^{-1}]	$\tilde{\nu}_{\text{asymm}}$ [cm^{-1}]	$\tilde{\nu}_{\text{bending}_1}$ [cm^{-1}]	$\tilde{\nu}_{\text{bending}_2}$ [cm^{-1}]
$1^4A_2 + 2^4B_1$ ($1^4\Pi_g$) ^a	4.435, 8.869, 4.435 (0.000, 4.435, 4.435)	4044	33.7	41.7	236.8	84.7
2^4A_1 ($1^4\Sigma_g^+$) ^b	4.937, 9.874, 4.937 (0.000, 4.937, 4.937)	7442	398.2	48.9	282.6	282.6
1^2A_1 ($1^2\Sigma_g^+$)	4.795, 9.590, 4.795 (0.000, 4.795, 4.795)	-2109	24.9	60.8	4.1	4.1
3^2A_1 ($2^2\Sigma_g^+$) ^b	4.440, 8.880, 4.440 (0.000, 4.440, 4.440)	3390	405.9	46.9	313.8	350.3
3^2B_1 ($2^2\Sigma_u^+$)	4.930, 9.860, 4.930 (0.000, 4.930, 4.930)	5647	27.7	48.4	169.6	169.6
1^3B_1 ($3^3\Sigma_u^+$)	4.875, 9.749, 4.875 (0.000, 4.875, 4.875)	24043	30.3	49.7	6.3	6.3

^a Renner-Teller pair with the 4B_1 state turning out as saddle point at this linear configuration

^b As a consequence of a combined pseudo Jahn-Teller and Renner-Teller interaction two A_1 states, one of them arising from a Π_u state, can mix for greater displacements along $D_{\infty h}$ geometries. This is also the reason for non-degenerate frequencies $\tilde{\nu}_{\text{bending}_{1,2}}$

Hauser *et al.* [78, 96] reported bond distances $b = 5.500 \text{ \AA}$ with a corresponding energy $E_{\text{min}} = -939 \text{ cm}^{-1}$ and harmonic frequencies $\{\tilde{\nu}_{D_{3h}}, \tilde{\nu}_{C_{2v}}, \tilde{\nu}_{C_s}\} = \{18, 21, 21\} \text{ cm}^{-1}$ resulting from calculations at RHF-RCCSD(T) level of theory with the ECP28MDF pseudopotential and the corresponding basis set augmented by a $(1s, 1p, 1d)$ set of diffuse functions. The present results, as listed in Tab. 4.4, reveal the global minimum of the quartet ground state at a binding energy of -1244 cm^{-1} , equilateral bond distances of 5.311 \AA , and harmonic frequencies of $\{\tilde{\nu}_{D_{3h}}, \tilde{\nu}_{C_{2v}}, \tilde{\nu}_{C_s}\} = \{23.8, 23.6, 23.6\} \text{ cm}^{-1}$.

The underlying JT interactions of the doublet ground state manifold lead to the a $1^2E'$ potential-energy landscape with characteristics according to Fig. 2.4 (b). For the global minimum on this lower PES sheet, Hauser *et al.* [95, 96] found bond distances of $R_{12} = R_{13} = 4.387 \text{ \AA}$, $R_{23} = 5.575 \text{ \AA}$, and an equilibrium energy of $E_{\text{min}} = -5321 \text{ cm}^{-1}$. The respective saddle point on the $1^2E'$ PES was found at $R_{12} = R_{13} = 4.951 \text{ \AA}$, $R_{23} = 4.220 \text{ \AA}$ with corresponding energy $E_{\text{sp}} = -5165 \text{ cm}^{-1}$. Finally, the lowest COIN was reported at equilateral bond distances $b = 4.589 \text{ \AA}$ with a stabilization energy of the global minimum from this COIN of $E_s[\text{min}(\text{COIN})] = 591 \text{ cm}^{-1}$. All these

findings were based on RHF-UCCSD(T) calculations with the ECP28MDF and a [14s11p6d3f1g] uncontracted even-tempered basis set derived from the scECP basis. The corresponding numbers of this work can be deduced from Tabs. 4.3, 4.4 and D.3. This results in a global minimum at bond distances $R_{12} = R_{13} = 4.379 \text{ \AA}$, $R_{23} = 5.393 \text{ \AA}$ with a corresponding binding energy of -6017 cm^{-1} . The saddle point appears at $R_{12} = R_{13} = 4.863 \text{ \AA}$, $R_{23} = 4.197 \text{ \AA}$ with energy -5885 cm^{-1} . The lowest COIN is found at equilateral bond distances $R_{12} = R_{23} = R_{13} = 4.546 \text{ \AA}$ leading to a stabilization energy of 523 cm^{-1} .

Hauser *et al.* [78, 96] moreover computed the vertical transition energy from the quartet ground state to the high-spin $2^4E'$ JT manifold. The calculations were based on a modified version of the CASPT2 method (referred to as RS2C in MOLPRO) with the ECP28MDF and the same basis set as described at last. In doing so, they found $E_{2^4E' \leftarrow 1^4A'_2} = 11530 \text{ cm}^{-1}$. From Fig. 4.8 and Tab. 4.4 we obtain $E_{2^4E' \leftarrow 1^4A'_2} = 11535 \text{ cm}^{-1}$. The corresponding experimental value [76, 79] is 11510 cm^{-1} referring to the lowest-energy maximum band of the measured band spectra applying laser-induced fluorescence (LIF) spectroscopy to Rb₃ clusters formed on helium nanodroplets.

A more detailed overview on all states including saddle points obtained within the energy range up to the $5s + 2 \cdot 5p$ asymptote is given in Tabs. D.1 to D.4 as well as in Fig. D.1 of the Appendix D. Some of these saddle points define the barrier heights between minima on the JT manifolds. In combination with Tab. 4.3 this provides important information to get a notion of the topology of corresponding potential-energy landscapes and serves as a starting point for subsequent JT analyses.

Technical remarks

Some peculiarities have to be considered carrying out the calculations corresponding to the states listed in Tabs. 4.3, 4.4 and 4.5 and Tabs. D.1 to D.4 using MOLPRO:

- *MRCI calculations performed with different computational point group symmetries generally lead to different results*
- *Exact degeneracy of the $2^4E'$ state at D_{3h} configurations is only obtained for C_s calculations using the AVAS scheme [223] for generating an appropriate active space. A short note may be found in the Appendix C.2.2 with an example input in C.3. This also accounts for the fact that the degeneracy is nearly symmetrically lifted when lowering the symmetry to C_{2v} ; cf. Fig. 4.6 (d). These calculations were performed*

using the MOLPRO 2019.2 program package [252]

- An example input for a MRCI geometry optimization (using C_{2v} symmetry) corresponding to Tabs. 4.4 and 4.5 as well as Tabs. D.1 to D.4 is given in C.1
- Subsequent MRCI frequency calculations to characterize the obtained extremal points are only possible without symmetry: see example input C.2.

4.3.4 | Rotational constants

Besides equilibrium geometries and energies, rotational constants are important spectroscopic magnitudes. Within the rigid rotor approximation, the rotational constants $A_i, i \in \{x, y, z\}$ of a polyatomic molecule define the rotational term energies and are given by

$$A_x = \frac{\hbar}{4\pi c \Theta_x} \quad (4.7a)$$

$$A_y = \frac{\hbar}{4\pi c \Theta_y} \quad (4.7b)$$

$$A_z = \frac{\hbar}{4\pi c \Theta_z}, \quad (4.7c)$$

with $\Theta_i, i \in \{x, y, z\}$ the principal moments of inertia. They are obtained as the eigenvalues of the inertia tensor

$$\Theta_{ij} = \sum_{k=1}^N m_k \left(\|\mathbf{r}\|^2 \delta_{ij} - x_i x_j \right), \quad (4.8)$$

which is a real symmetric rank-2 tensor and can thus be always diagonalized.

In general, it is only useful to calculate the inertia tensor with respect to the center of mass. However, the molecule fixed coordinate system K' according to Fig. 4.3 (a) does not coincide with the center of mass system K . For obtaining the »correct« principal moments of inertia to calculate the rotational constants after Eqs. (4.7), one has to either account for the parallel axis theorem or transform to the center of mass system first. In the center of mass system K , the inertia tensor is diagonal with

$$\Theta_x = \frac{2}{3}m \left(R_{12}^2 - \frac{R_{23}^2}{4} \right) = \frac{2}{3}m \left(R_{13}^2 - \frac{R_{23}^2}{4} \right) \quad (4.9a)$$

$$\Theta_y = \frac{1}{3}m \left(R_{12}^2 + R_{23}^2 \right) = \frac{1}{3}m \left(R_{13}^2 + R_{23}^2 \right) \quad (4.9b)$$

$$\Theta_z = \frac{1}{2}m R_{23}^2, \quad (4.9c)$$

TABLE 4.6.: Overview of rotational constants for doublet and quartet states of Rb₃ in **triangular** configurations. The last row shows the rotational constants for the singlet state of Rb₃⁺. Numbers refer to triatomic systems made up of the ⁸⁷Rb isotope.

State (D_{3h})	R_{12}, R_{23}, R_{13} [Å]	Geometry	A_x [cm ⁻¹]	A_y [cm ⁻¹]	A_z [cm ⁻¹]	Classification
1 ⁴ B ₁ (1 ⁴ A' ₂)	5.311, 5.311, 5.311	D_{3h}	1.38	0.69	1.38	symmetric rotor
1 ⁴ A ₂ (1 ⁴ E'')	4.368, 5.700, 4.368	C_{2v}	2.66	0.82	1.19	asymmetric rotor
2 ⁴ B ₁ (1 ⁴ E')	4.442, 8.179, 4.442	C_{2v}	9.68	0.55	0.58	asymmetric rotor
1 ⁴ A ₁ (1 ⁴ E')	4.993, 8.076, 4.993	C_{2v}	3.38	0.51	0.59	asymmetric rotor
2 ⁴ A ₁ (1 ⁴ A' ₁)	5.325, 5.325, 5.325	D_{3h}	1.37	0.68	1.37	symmetric rotor
3 ⁴ B ₁ (2 ⁴ A' ₂)	5.084, 5.084, 5.084	D_{3h}	1.50	0.75	1.50	symmetric rotor
2 ⁴ B ₂ (2 ⁴ E'')	4.443, 6.217, 4.443	C_{2v}	2.89	0.74	1.00	asymmetric rotor
4 ⁴ B ₁ (2 ⁴ E')	5.283, 5.337, 5.283	C_{2v}	1.40	0.69	1.36	asymmetric rotor
3 ⁴ A ₁ (upper) (2 ⁴ E')	4.687, 7.226, 4.687	C_{2v}	3.27	0.61	0.74	asymmetric rotor
1 ² B ₁ (1 ² E')	4.379, 5.393, 4.379	C_{2v}	2.44	0.86	1.33	asymmetric rotor
1 ² B ₂ (1 ² A' ₂)	4.276, 4.285, 4.276	C_{2v}	2.12	1.06	2.11	asymmetric rotor
2 ² A ₁ (2 ² E')	4.398, 6.073, 4.398	C_{2v}	2.87	0.77	1.05	asymmetric rotor
3 ² A ₁ (1 ² A' ₁)	4.557, 4.557, 4.557	D_{3h}	1.87	0.93	1.87	symmetric rotor
1 ² A ₂ (1 ² E'')	4.337, 5.132, 4.337	C_{2v}	2.38	0.91	1.47	asymmetric rotor
1 ¹ A ₁ (1 ¹ A' ₁)	4.610, 4.610, 4.610	D_{3h}	1.82	0.91	1.82	symmetric rotor

where the mass m refers to the ⁸⁷Rb isotope. For equilateral triangular configurations it immediately follows $\Theta_x = \Theta_z$ and corresponding molecules are usually denoted as *symmetric top* ones. In the case of linear $D_{\infty h}$ geometries it can be seen $\Theta_x = 0$ and $\Theta_y = \Theta_z$, which leaves the rotational constant A_x undefined. The rotational constants corresponding to the equilibrium states listed in Tabs. 4.4 and 4.5 are given in Tab. 4.6 for triangular configurations and in Tab. 4.7 for linear geometries.

4.3.5 | Spin-orbit coupling effects

A survey of expected SOC effects in the Rb₃ system marks a further building block for exploring the prospects of PA processes. As demonstrated in Tab. 4.1, the SOC induced splitting of the atomic ²P state is ≈ 240 cm⁻¹ and thus SOC is still a comparatively weak effect. *A posteriori*, this justifies the labeling of states in terms of their total spin as in the previous sections [245]. Nevertheless, as outlined in Sec. 2.3 and shown in Fig. 2.5, SOC changes the topology of $E \otimes e$ JT-PESs as they remove the central COIN. Moreover, in particular for near-in-energy states, SOC may lead to a mixing of states

TABLE 4.7.: Overview of rotational constants for doublet and quartet states of Rb_3 in **linear** configurations. The last row shows the rotational constants for the triplet state of Rb_3^+ . Numbers refer to triatomic systems made up of the ^{87}Rb isotope.

State ($D_{\infty h}$)	R_{12}, R_{23}, R_{13} [\AA]	A_x [cm^{-1}]	A_y [cm^{-1}]	A_z [cm^{-1}]	Classification
$1^4A_2 + 2^4B_1(1^4\Pi_g)$	4.435, 8.869, 4.435	–	0.493	0.493	symmetric rotor
$2^4A_1(1^4\Sigma_g^+)$	4.937, 9.874, 4.937	–	0.398	0.398	symmetric rotor
$1^2A_1(1^2\Sigma_g^+)$	4.795, 9.590, 4.795	–	0.422	0.422	symmetric rotor
$3^2A_1(2^2\Sigma_g^+)$	4.440, 8.880, 4.440	–	0.492	0.492	symmetric rotor
$3^2B_1(2^2\Sigma_u^+)$	4.930, 9.860, 4.930	–	0.399	0.399	symmetric rotor
$1^3B_1(3^3\Sigma_u^+)$	4.875, 9.749, 4.875	–	0.408	0.408	symmetric rotor

of the same or of different spin. By computing the SO-matrix for selected nuclear configuration one may get an estimate on the actual size of these couplings. Correlating calculations were performed at the MRCI(lcECP+CPP)/UET15 level of theory using the ECP-LS technique. In this approach, the spin-orbit coupling is obtained from the ECP. The computations included 15 quartet (4/5/3/3) and 12 doublet (5/4/2/1) states, according to the MOLPRO specific ordering of the IRREPs ($A_1/B_1/B_2/A_2$). That is, in total a 84×84 SO-matrix was set up and diagonalized.

A heat-map representation of the absolute values of the SO-matrix $|\hat{H}_{ij}^{\text{SO}}|$ is given in Fig. 4.9 at the equilibrium geometry of the first excited quartet state 1^4A_2 . This provides a qualitative overview, since it should look similar for comparable geometrical configurations. The SO interactions are dominated by doublet-doublet ($D \leftrightarrow D$), respectively quartet-quartet ($Q \leftrightarrow Q$) couplings. The corresponding selection rules for C_{2v} configurations obtained from group theoretical arguments allow for $\Delta S = 0, \pm 1$ (a detailed derivation is given in the Appendix A). Hence, there are also non-vanishing doublet-quartet ($D \leftrightarrow Q$ and vice versa) couplings.

As shown in Fig. 4.9, the typical magnitude of the coupling strengths amounts to 20 to 70 cm^{-1} , while the resulting energy shifts and zero-field splittings are much smaller. Explicit values for these energy shifts and zero-field splittings corresponding to the equilibrium states listed in Tabs. 4.4 and 4.5 are summarized in the Appendix in Tabs. D.6 to D.9. For instance, the quartet ground state splits into the two states $E_{1/2}$ and $E_{3/2}$ of the D_{3h} spin double group [96], but the corresponding zero-field splitting is less than 0.1 cm^{-1} and the energy lowering induced by the SOC is less than 0.2 cm^{-1} . This small splitting is due to most dominant couplings to the 1^4B_2

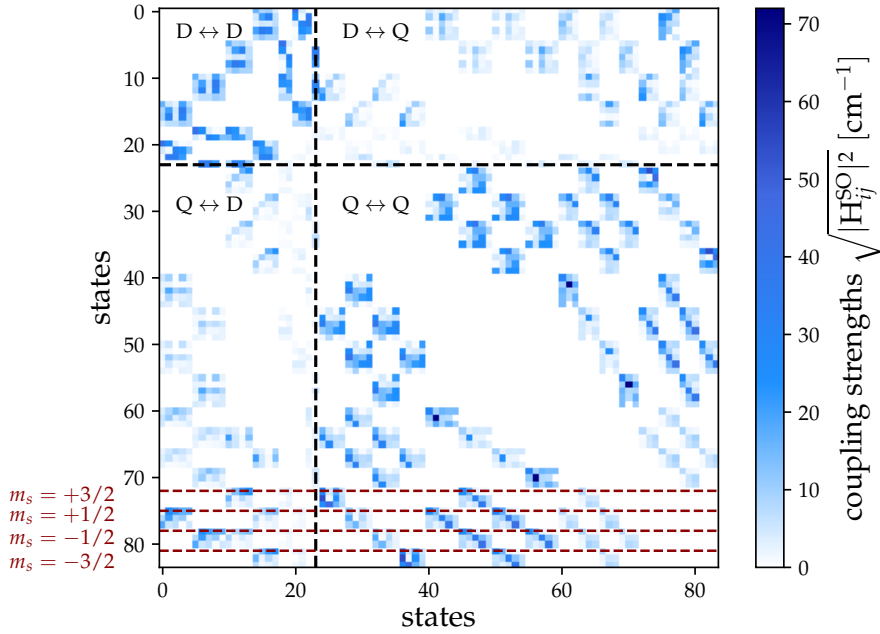


FIGURE 4.9.: Heat-map representation of the absolute values of the spin-orbit matrix $\sqrt{|\hat{H}_{ij}^{\text{SO}}|^2}$ (without diagonal elements) for the Rb_3 geometry fixed to the equilibrium configuration of the first excited quartet state 1^4A_2 (see Tab. 4.4). Dashed black lines separate doublet-doublet ($\text{D} \leftrightarrow \text{D}$), quartet-quartet ($\text{Q} \leftrightarrow \text{Q}$) and quartet-doublet ($\text{Q} \leftrightarrow \text{D}$) couplings. Dashed dark red lines mark the rows where the four components corresponding to the 1^4A_2 state are found in the SO-matrix. The SO matrix is sorted according to C_{2v} IRREPs in the sequence ($\text{A}_1/\text{B}_1/\text{B}_2/\text{A}_2$), where each of them (in zeroth-order basis) are ordered with respect to increasing energy and are accordingly combined with the m_s spin function starting from $m_s = +1/2$ to $m_s = -1/2$ for doublets and $m_s = +3/2$ to $m_s = -3/2$ for quartets. This representation is complete with respect to the energetically lowest 12 doublet (5/4/2/1) and 15 quartet states (4/5/3/3) leading to the 84×84 SO-matrix. *Freely adapted from J. Schnabel et al., Phys. Rev. A 103, 022820 (2021).*

and 1^4A_2 states. For the latter, the SOC effects are again smaller than 1 cm^{-1} at its respective equilibrium geometry. These small values are due to an effective quenching of the orbital angular momentum in triangular geometries and due to a large energy separation to other states. In general, SOC effects are expected to become larger for highly symmetric configurations, in particular for linear geometries and in the presence of spatial degeneracies. For instance, for the $1^4\Pi_g$ state, splittings and energy shifts up to 200 cm^{-1} are computed.

The strength of SOC between the quartet ground state 1^4B_1 and the first excited quartet state 1^4A_2 , decays with respect to distortions from equilateral triangular

geometries. Thus, only in the dissociation limits Rb_2+Rb or $3 \cdot \text{Rb}$, SOC effects become larger. This is because Rb_2 always has a well-defined C_∞ axis. In conclusion, it can be pointed out that SOC induced mixing of states near their equilibrium geometries are not expected. This holds in particular for the quartet ground state and the first excited quartet state.

Example input

The SO calculation corresponding to Fig. 4.9 is based on a calculation as defined by input C.4.

4.4 | Finding appropriate states for photoassociation

This section qualitatively discusses Franck-Condon overlaps and investigates electronic transition dipole moments. In combination with the previous findings, this finally allows for the identification of concrete and suitable PA transitions to potentially produce long-lived trimer bound states.

4.4.1 | Configuration space and electronic dipole transitions

The realization of PA processes necessarily requires non-vanishing electronic dipole transition moments between the initial state and the corresponding excited state. However, only if the correlating Franck-Condon factors are nonzero as well, this is sufficient to drive PA transitions. In regard to trimer PA, this means that significant overlap of the nuclear scattering wavefunction of Rb_2+Rb or $3 \cdot \text{Rb}$ collisions and the molecular trimer vibrational wavefunction of the excited state is required. In an initial approach it may be convenient to first explore the prospects for producing deeply bound excited trimers near the vibrational ground state for reasons of increased stability, lifetime and simplicity. The configuration space survey in Fig. 4.10 (a) shows that a number of excited doublet and quartet equilibrium structures are in close proximity to the inner turning points (ITPs) of the scattering wavefunction. Since the scattering wavefunction typically exhibits a local maximum at the ITP, this suggests that favorable Franck-Condon factors might be found for photoassociating excited trimer states in their equilibrium geometry [245]; cf. Fig. 4.1 (b) for visual guidance. For triatomic molecules, the ITPs are 2D surfaces in the complete 3D configuration space, as indicated in Fig. D.2. They represent points on the quartet ground state PES that equal a certain energy of the scattering state. For the case of PA1, i.e. Rb_2+Rb ,

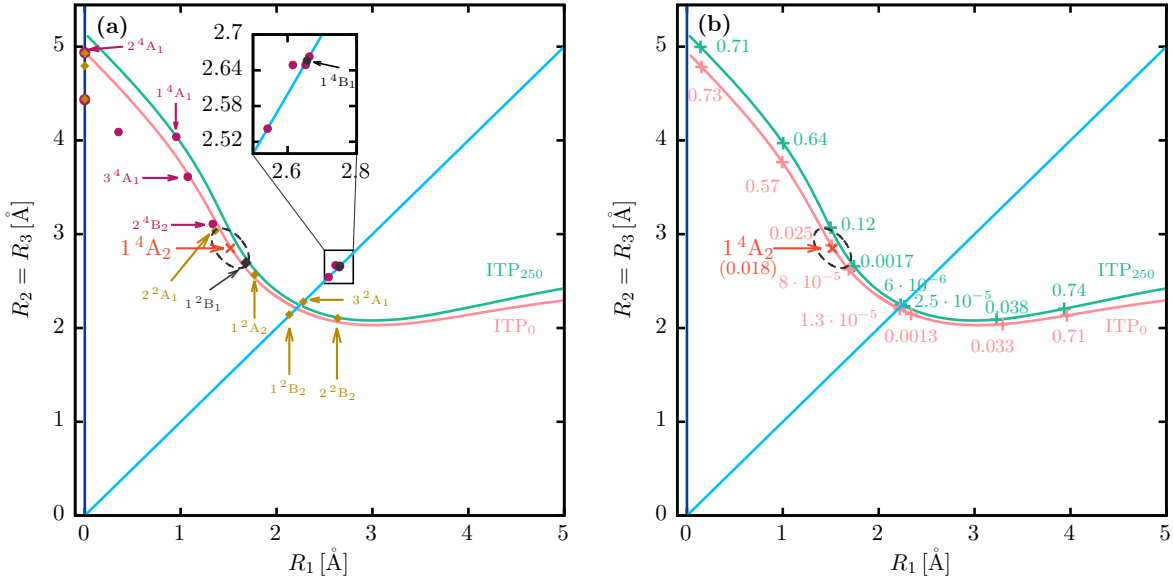


FIGURE 4.10.: Inner-turning points (ITPs) and locations of equilibrium geometries in the configuration space of perimetric coordinates. **(a)** As all equilibrium geometries show at least C_{2v} symmetry the configuration space survey can be restricted to one of the space diagonal surfaces shown in Fig. 4.3 (c), where the diagonal light blue line marks D_{3h} configurations. ITPs on the quartet ground-state PES with respect to either the $Rb_2 + Rb$ (ITP_{250}) or $3 \cdot Rb$ (ITP_0) dissociation scenarios are given in green and pink, respectively. States lying close to this lines are promising candidates for showing good Franck-Condon factors. Section 4.4 focuses on the 1^4A_2 state highlighted in orange. The numbers given in **(b)** along both ITP lines represent the electronic dipole transition strengths (in units of $[D^2]$) between the quartet ground state and this 1^4A_2 state at the corresponding ITP locations. The numbers given in (b) do not correlate with the equilibrium geometries depicted in (a). The transition dipole strength at the equilibrium geometry of the first excited quartet state amounts to $0.018 D^2$. The ellipses shown in (a) and (b) give an estimate of the size of the vibrational ground state wavefunction for the 1^4A_2 state. Freely adapted from J. Schnabel et al., *Phys. Rev. A* **103**, 022820 (2021).

this energy is given by the negative binding energy of the $a^3\Sigma_u$ state with $\approx 250 \text{ cm}^{-1}$. For $3 \cdot Rb$ collisions, i.e. PA2, the energy is approximately zero. Both ITP locations, i.e. ITP_{250} and ITP_0 are given in Fig. 4.10. Since all equilibrium geometries show at least C_{2v} symmetry, this view corresponds to one of the three equivalent space diagonal surfaces as shown in Fig. 4.3 (c).

As mentioned in Sec. 4.1, PA2 at short distances, i.e. at ITP locations, is expected to be rather unlikely due to the effective repulsive short-range barrier reported in Ref. [70]. But in the long-range PA2 should be possible. The feasibility of PA1 at large distances has been shown in Ref. [109].

The identification of appropriate excited states to drive PA transitions is finally determined by the electronic dipole transition moment. In C_{2v} symmetry electronic

dipole transitions with $\Delta S = 0$ are allowed between all states except transitions between A_1 and A_2 as well as B_1 and B_2 . The corresponding selection rules are derived in the Appendix A.2. From a theoretical point of view, due to the more complicated electronic structure (multireference character) of the doublet ground state and the more complex character due to the underlying JT effect, it is simpler to confine oneself to the quartet manifold of states. In fact, in realistic experimental setups there is often a magnetic field present [107]. This restricts collisions of molecules and atoms to high-spin PESs and provides, to some degree, more control. Since the density of states increases with increasing energy, the chance for finding sufficiently long-lived target states for PA experiments decreases. Therefore, low-lying states shall be considered. Combining this with the findings that the transition between the quartet ground state and the first excited quartet state (1^4A_2) is symmetry-allowed and in close proximity to the ITP lines, the following discussion will focus on this state.

The specific dipole transition strengths (in units of $[D^2]$) between the quartet ground state and the 1^4A_2 state at ITP configurations are shown in Fig. 4.10 (b) in the subspace of C_{2v} geometries. The magnitudes along the two ITP lines are approximately the same and in both cases no considerable changes are obtained in C_s direction. Explicit values for scans in C_s direction may be found in Fig D.2, which moreover indicates the actual topology of the 2D ITP₂₅₀ surface. Close to the D_{3h} subspace (diagonal light blue line), the transition strengths become vanishingly small. This is due to the fact that for D_{3h} geometries the 1^4A_2 state forms one component of the twofold degenerate $1^4E''$ JT state and the quartet ground state is described by the A_2' IRREP of the D_{3h} point group. In Appendix A.1, it is shown that electronic dipole transitions between these two states are zero by symmetry. For C_{2v} configurations admixture of further components makes the transition non-vanishing, but it remains rather small.

The extent of the vibrational ground-state wavefunction of the 1^4A_2 state can be estimated from the harmonic frequencies in Tab. 4.4 and from the topology of the 2D PES in Fig. 4.4 (b). To zeroth-order, the size associated with each normal mode i can be approximated by the harmonic oscillator length. It can be derived from the one-dimensional Schrödinger equation for a particle of reduced mass μ (for homonuclear triatomics $\mu = m/\sqrt{3}$) moving in a harmonic potential, yielding for ^{87}Rb

$$x_i = \sqrt{\frac{\hbar}{\mu\omega_i}} = \sqrt{\frac{\sqrt{3}\hbar}{100 \cdot m(^{87}\text{Rb}) \cdot c\tilde{\nu}_i}}, \quad (4.10)$$

with the speed of light c and the mass m of ^{87}Rb . As already seen in Fig. 4.4 (b), the PES in this region takes on the form of a rotated ellipse. Equation (4.10) yields

$a = 0.495 \text{ \AA}$ for the semi-major axis and $b = 0.290 \text{ \AA}$ for the semi-minor axis using the corresponding values for $\tilde{\nu}_{D_{3h}}$ and $\tilde{\nu}_{C_{2v}}$ from Tab. 4.4. This ellipse is indicated in Fig. 4.10. Since it shows good overlap with the ITPs, a sizeable Franck-Condon factor can be expected.

4.4.2 | The $1^4E''$ Jahn-Teller pair and surrounding interactions

As repeatedly outlined in the previous sections and listed in Tab. 4.3 the first excited quartet state 1^4A_2 forms, together with the 1^4B_2 state, the $1^4E''$ JT manifold. The two states are degenerate for every equilateral triangular geometry (D_{3h} point group) and are thus paradigmatic for the $E \otimes e$ JT effect of homonuclear trimer systems that produces a one-dimensional COIN seam in the D_{3h} subspace embedded in the full 3D configuration space. A detailed discussion of the foundations of JT theory was given in Sec. 2.3.2. In the context of PA processes it is important to note that due to underlying JT interactions the 1^4A_2 and 1^4B_2 states cannot be viewed separately as one would be tempted by the incomplete view from the C_{2v} symmetry subspace. Here, both states are of different symmetry and their corresponding PESs can intersect. However, in general the Rb_3 system is characterized by the C_s point group, where both states fall into the same IRREP A'' and thus the associated PESs avoid each other. This is illustrated in Fig. 4.11 (a) and reveals the origin of discontinuities. These facts are further supported by the following topological implications of JT potential-energy-landscapes.

When lowering the symmetry, by scanning along the asymmetric stretch mode Q_2 and/or the bending mode Q_3 , the central symmetry-required COIN is lifted and both states branch off forming a lower PES sheet E_- and a upper PES E_+ . The former shows the tricorn topology with three equivalent minima (of 1^4A_2 character) alternating regularly with three equivalent saddle points (of 1^4B_2 character). This lower PES sheet in the $Q_2 - Q_3$ -branching space is illustrated by the lower inset in Fig. 4.11 (a). The upper surface E_+ is a paraboloid of revolution about the center at $Q_2 = Q_3 = 0$ [86], as shown in Fig. 2.4 (a). The inset on the upper left of Fig. 4.11 (a) indicates, in accordance with the underlying theory from Sec. 2.3.2, that including SOC removes the central COIN [171–175] and leads to an energy splitting of $\Delta \approx 10 - 20 \text{ cm}^{-1}$ between the corresponding Kramers pairs of E_- and E_+ . The sizes of these splittings again confirm that SOC is a comparatively weak effect.

The one-dimensional COIN seam occurs for $Q_2 = Q_3 = 0$ and is illustrated in Fig. 4.11 (b) in the D_{3h} - C_{2v} subspace of Q_1 and Q_3 . It also shows a contour plot of the E_- surface. The energetically lowest COIN is found for $R_1 = R_2 = R_3 = 2.250 \text{ \AA}$

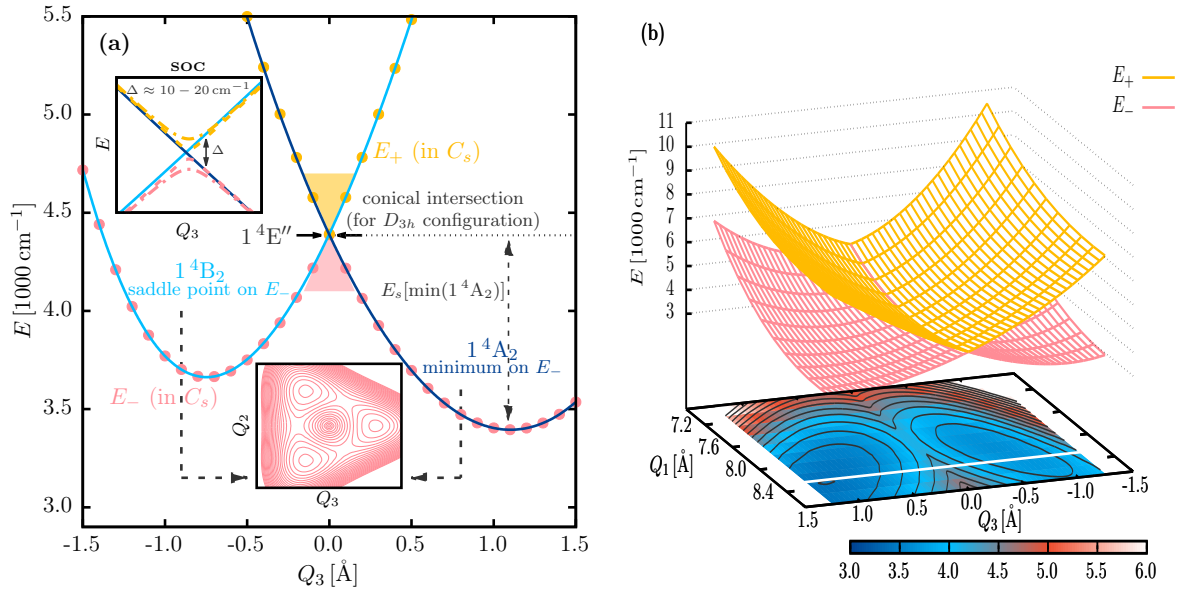


FIGURE 4.11.: The first two excited quartet states 1^4B_2 and 1^4A_2 (according to the simplified C_{2v} nomenclature) are degenerate for D_{3h} configurations forming the $1^4E''$ Jahn-Teller pair. A complete picture of the underlying physics can only be obtained from a consideration in terms of the C_s point group. For each D_{3h} configuration the two states reveal a conical intersection (COIN) leading to a one-dimensional COIN seam in the full 3D configuration space. By scanning along a symmetry-lowering coordinate, e.g. along the C_{2v} preserving Q_3 -mode, the two states split; see (a) for $Q_1 = 8.335 \text{ \AA}$ and $Q_2 = 0.0 \text{ \AA}$. Since both states undergo the Jahn-Teller effect they cannot be viewed separately, as suggested by the general description in C_s symmetry (1^4B_2 and 1^4A_2 both fall into the IRREP A''). This leads to the formation of a lower PES sheet E_- showing tricorn topology and a parabolically shaped upper surface E_+ . The former shows three equivalent minima alternating regularly with three saddle points, separated by the localization energy $E_{loc} = 225 \text{ cm}^{-1}$. The global minimum on E_- is of 1^4A_2 character while the saddle point is of 1^4B_2 character as seen in (a) for $Q_1 = 8.335 \text{ \AA}$. Spin-orbit coupling (SOC) removes the COIN and splits both parts of the JT surface by Δ as shown by the inset on the top left in (a). The topology of the PESs in the two-dimensional subspace of Q_1 and Q_3 is shown in (b). The discontinuities at $Q_3 = 0.0 \text{ \AA}$ correspond to D_{3h} geometries and represent the one-dimensional COIN seam. The horizontal white line at the bottom indicates the one-dimensional cut shown in (a). Energies are given with respect to the $3 \cdot \text{Rb}$ limit and were computed at MRCI(1cECP+CPP)/UET15 level of theory. *Freely adapted from J. Schnabel et al., Phys. Rev. A 103, 022820 (2021).*

with an energy $E_{\min(\text{COIN})} = 4146 \text{ cm}^{-1}$, as listed in Tab. 4.3. As mentioned above, it is convenient to specify a stabilization energy E_s of the global minima on E_- from the central COINs. Another useful quantity is the localization energy E_{loc} defining the barrier height in the tricorn potential. In the lower inset of Fig. 4.11 (a) this defines the energy barrier for transitions between the three equivalent minima on E_- separated by three saddle points. Relative to the energetically lowest COIN the stabilization energy becomes $E_s[\min(\text{COIN})] = 749 \text{ cm}^{-1}$ while for a cut through the 1^4A_2 minimum it yields $E_s[\min(1^4A_2)] = 991 \text{ cm}^{-1}$ as indicated in Fig. 4.11 (a). The localization energy is $E_{\text{loc}} = 225 \text{ cm}^{-1}$ (obtained from Tab. D.1). The ambiguity in defining the stabilization energy as well as the graphical definition of E_{loc} is illustrated in Fig. D.3.

Due to the small electronic dipole transition moments between the quartet ground state and the first excited quartet state, cf. Fig. 4.10 (b), one might doubt the applicability of the 1^4A_2 state for use in PA experiments. Nevertheless, it is suggested, as in Ref. [245], for use as a promising candidate for realizing PA processes of Rb_3 . This is explained by the reasons given below.

First, the global minimum of the 1^4A_2 state is sufficiently isolated from surrounding intersections with either doublet or quartet states due to the low density of states. A corresponding study in close proximity to the global minimum is shown in Fig. 4.12 for scans along the perimetric coordinate R_1 with R_2 and R_3 adjusted such that either C_{2v} or nearby C_s configurations are realized. Only the 2^2B_1 and 3^2A_1 states show intersections close to the 1^4A_2 minimum. The energetically closest intersection is illustrated in Fig. 4.12 (b) and emerges at C_{2v} symmetry with the 3^2A_1 state for $R_2 = R_3 = 2.65 \text{ \AA}$ and $R_1 \approx 1.7 \text{ \AA}$. Figure 4.12 (a) shows that for C_s geometries intersections with the 2^2B_1 state move slightly closer to the minimum of the first excited quartet state, while the 3^2A_1 intersections approximately remain at the same position. But all intersections occur $\gtrsim 60 \text{ cm}^{-1}$ away from the 1^4A_2 minimum. Since realistic experiments often apply magnetic fields to obtain only spin-polarized states, the near doublet intersections might actually not be problematic at all. Furthermore, as mentioned above, the 1^4A_2 minimum is stabilized from COINs by $E_s[\min(\text{COIN})]$ or $E_s[\min(1^4A_2)]$.

In the presence of SOC the JT potential-energy landscapes are locally described by Eqs. (2.75) showing that for large $\varrho = \sqrt{Q_2^2 + Q_3^2}$, which measures distortions from D_{3h} symmetry to acute C_{2v} triangular geometries, the SO contribution vanishes as $1/\varrho$ [96, 171]. By scanning the configuration space around the 1^4A_2 equilibrium geometry, strongest SOC are found to the quartet ground state 1^4B_1 and to the 1^4A_1 state with

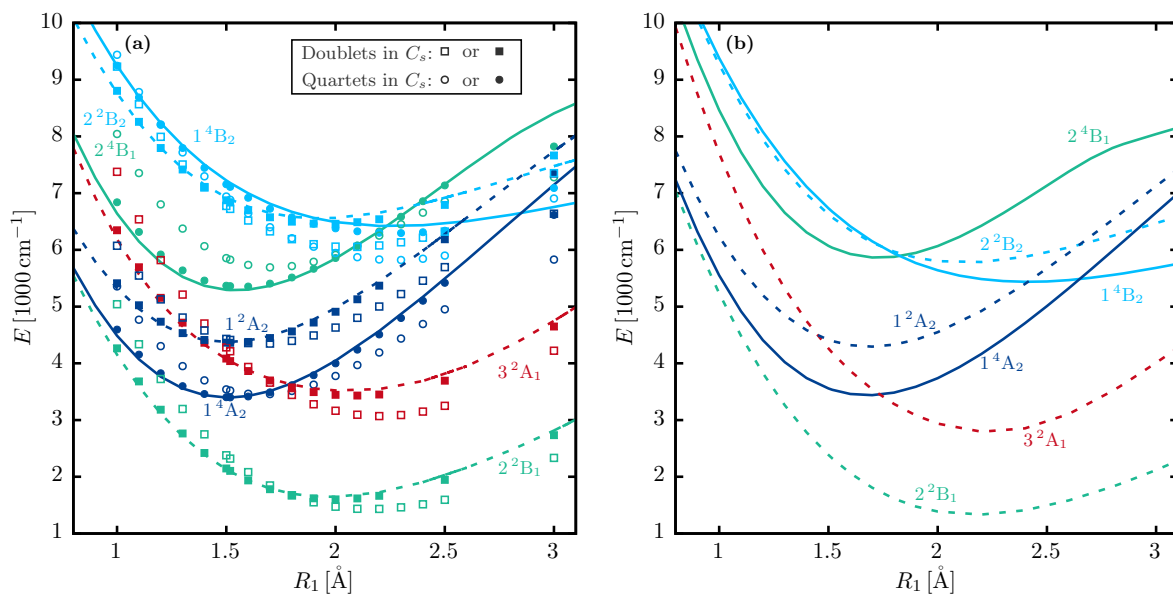


FIGURE 4.12.: One-dimensional scans along the perimetric coordinate R_1 for different settings of R_2 and R_3 to study intersections in proximity to the 1^4A_2 global minimum. (a) Solid and dashed lines represent quartet and doublet states, respectively for C_{2v} scans with $R_2 = R_3 = 2.85 \text{ \AA}$ (1^4A_2 global minimum at $R_1 = 1.518 \text{ \AA}$; cf. Tab. 4.4). Symbols represent geometries which are slightly C_s distorted, with circles and squares corresponding to quartet and doublet states, respectively. Filled symbols represent configurations with $R_2 = 2.85 \text{ \AA}$ and $R_3 = 2.8 \text{ \AA}$ while open symbols correspond to $R_2 = 2.85 \text{ \AA}$ and $R_3 = 2.55 \text{ \AA}$ [cf. Fig. 4.3 (c)]. (b) C_{2v} scan with $R_2 = R_3 = 2.65 \text{ \AA}$ where solid and dashed lines represent quartet and doublet states, respectively. Energies are given with respect to the $3 \cdot \text{Rb}$ limit and were computed at MRCI(lcECP+CPP)/UET15 level of theory. *Freely adapted from J. Schnabel et al., Phys. Rev. A 103, 022820 (2021).*

typical magnitudes between 30 and 50 cm^{-1} . According to Tab. 4.4, the 1^4A_1 state shows its global minimum at $E_{\min}(1^4A_1) = 6766 \text{ cm}^{-1}$ and is thus well separated from the first excited quartet state. The same scans reveal that spin-orbit couplings to doublet states are slightly weaker with interactions between 1^4A_2 and the 2^2A_1 , 3^2A_1 , 4^2A_1 , 5^2A_1 , 3^2B_1 , and 4^2B_1 states in the order of 10 to 25 cm^{-1} . Those equilibrium states are found either well below the minimum of the 1^4A_2 state at 229 cm^{-1} or 1898 cm^{-1} , respectively, or well above, starting from 5431 cm^{-1} as obtained from Tab. D.3.

Example input for a Q_3 scan including SOC

The example input C.5 shows how to perform a calculation corresponding to the upper left inset of Fig. 4.11 (a), i.e. including SOC to Q_3 scans to remove the central COIN.

4.5 | Jahn-Teller analysis of the $1^4E''$ state

The topology of the $1^4E''$ PES, as illustrated in the lower inset of Fig. 4.11 (a), can be further analyzed and eventually analytically modeled by means of the (non-relativistic) $E \otimes e$ Jahn-Teller theory as presented in Sec. 2.3.2. This involves diagonalizing the potential part of the JT Hamiltonian according to Eq. (2.60) to obtain an analytic representation of the potential-energy landscape in the two-dimensional branching space spanned by the JT active modes Q_2 and Q_3 . The inclusion of quadratic JT coupling parameters leads to the form given in Eq. (2.62). These JT parameters are obtained from fits to *ab-initio* data and can be used to generate theoretical predictions for vibrational spectra [96]. As mentioned in Sec. 2.3.2 including up to quadratic terms is only a good approximation for matching the *ab-initio* data if the extrema (minium and saddle points) occur near the central COIN. In this regard, the analysis of some doublet and quartet JT manifolds in Refs. [95, 96] revealed that cubic terms were necessary to sufficiently reproduce the *ab-initio* data. The resulting PES manifold $E_{\pm}^{\text{JT}3}$ follows from Eq. (2.59) using polar coordinates according to Eq. (2.52) and becomes

$$E_{\pm}^{\text{JT}3}(\varrho, \varphi) = V_{2a}\varrho^2 + V_{3a} \cos(3\varphi)\varrho^3 \pm \varrho [V_{1e}^2 + 2V_{1e}V_{2e} \cos(3\varphi)\varrho + (2V_{1e}V_{3e} + V_{2e}^2)\varrho^2 + 2V_{2e}V_{3e} \cos(3\varphi)\varrho^3 + V_{3e}^2\varrho^4]^{\frac{1}{2}}, \quad (4.11)$$

with $V_{\ell a}, \ell \in \{2, 3\}$ the elastic and cubic, respectively, force constants and $V_{ie}, i \in \{1, 2, 3\}$ the linear/quadratic/cubic coupling parameters.

Equation (4.11) demonstrates that the V_{3a} and V_{2e} terms produce the same kind of $\cos(3\varphi)$ warping. However, there is no reason to prefer one term over the other in the subsequent fitting procedure to obtain the JT parameters [95]. To this end, it has been shown in Ref. [166] that the two contributions to the PES can be separated by analyzing the oscillatory behavior of both branches $E_-(\varrho, \varphi)$ and $E_+(\varrho, \varphi)$ individually. Therefore, Eq. (4.11) is first expanded up to third order in ϱ , yielding

$$E_{\pm}^{\text{JT}3}(\varrho, \varphi) \approx V_{2a}\varrho^2 + V_{3a} \cos(3\varphi)\varrho^3 \pm \left[\varrho V_{1e} + V_{2e} \cos(3\varphi)\varrho^2 + \frac{V_{2e}^2}{2V_{1e}} \sin^2(3\varphi)\varrho^3 + V_{3e}\varrho^3 \right]. \quad (4.12)$$

Since $\sin^2(3\varphi) = (1 - \cos(6\varphi))/2$, this term would lead to a $\cos(6\varphi)$ -warping of the PES. However, as indicated by the lower inset of Fig. 4.11 (a), no significant higher-order warping contributions are observed for the $1^4E''$ state of Rb_3 . This suggests

$V_{2e} \ll V_{1e}$ and leads to the approximation

$$E_{\pm}^{\text{JT}3}(\varrho, \varphi) \approx V_{2a}\varrho^2 + V_{3a} \cos(3\varphi)\varrho^3 \pm \left[\varrho V_{1e} + V_{2e} \cos(3\varphi)\varrho^2 + V_{3e}\varrho^3 \right], \quad (4.13)$$

where in a first approximation V_{3e} may be neglected as well [95]. Rewriting Eq. (4.13) to the form

$$E_{\pm}^{\text{JT}3}(\varrho, \varphi) = c_{\pm} + A_{\pm} \cos(3\varphi), \quad (4.14)$$

with the amplitudes of the $\cos(3\varphi)$ -warping term given as

$$A_{\pm} = V_{3a}\varrho^3 \pm V_{2e}\varrho^2, \quad (4.15)$$

shows that both branches of $E_{\pm}^{\text{JT}3}$ have different dependence on $\cos(3\varphi)$. Thus, the amplitudes A_{\pm} convey information about the actual weight of the two contributions V_{3a} and V_{2e} . The remaining parameters V_{2a} , V_{1e} and V_{3e} are obtained from Eq. (4.13) by defining [95]

$$\mathcal{F}_1(\varrho, \varphi) = \frac{E_{+}^{\text{JT}3}(\varrho, \varphi) + E_{-}^{\text{JT}3}(\varrho, \varphi)}{2} = V_{2a}\varrho^2 + V_{3a} \cos(3\varphi)\varrho^3 + E_s[\min(1^4A_2)], \quad (4.16a)$$

$$\mathcal{F}_2(\varrho, \varphi) = \frac{E_{+}^{\text{JT}3}(\varrho, \varphi) - E_{-}^{\text{JT}3}(\varrho, \varphi)}{2} = V_{1e}\varrho + V_{2e} \cos(3\varphi)\varrho^2 + V_{3e}\varrho^3, \quad (4.16b)$$

where $E_s[\min(1^4A_2)] = 991 \text{ cm}^{-1}$ is the JT-stabilization energy accounting for the fact that in the following the zero of energy is chosen such that it coincides with the 1^4A_2 global minimum. This method can be applied to a cut of the PES at $\varphi = 0$, which corresponds to a one-dimensional scan along the C_{2v} symmetry preserving mode Q_3 with $Q_2 = 0$ and $Q_1 = 8.335 \text{ \AA}$, i.e. to the *ab-initio* data shown in Fig. 4.11 (a). The corresponding fitting procedure is illustrated in Fig. 4.13 (a). The method according to Eq. (4.16) would also allow for extracting the parameters V_{3a} and V_{2e} , however the more sophisticated approach uses Eqs. (4.14) and (4.15) describing the $\cos(3\varphi)$ oscillations explicitly. Thereto, *ab-initio* data are calculated for $\varrho = \varrho_{\min} = 1.0876 \text{ \AA}$ in the range $\varphi \in \{0, 2\pi/3\}$ utilizing the symmetry of the PES. The data are fitted using $\cos(3\varphi)$ functions to extract the unknowns c_+, c_-, A_+, A_- . For constant ϱ the two branches of Eq. (4.15) form a system of linear equations, which can be solved for V_{3a} and V_{2e} . This fitting procedure is illustrated in Fig. 4.13 (b).

The resulting JT parameters are listed in Tab. 4.8 for both cases: neglecting V_{3e} in Eq. (4.13) and including it. The inclusion of the cubic coupling parameter changes V_{1e} by only about 4%. However, the obtained size of V_{3e} shows that neglecting it is not a good approximation, which is also displayed by the RMSD results. This is further

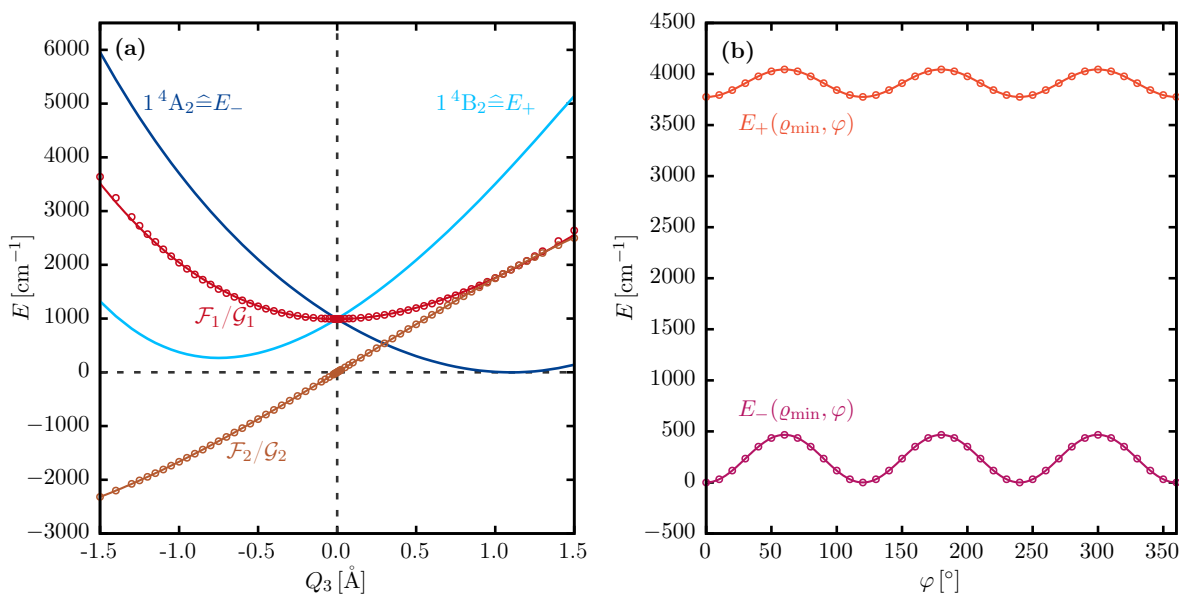


FIGURE 4.13.: Illustration of the two fitting procedures applied for the extraction of JT parameters. **(a)** Shows the approach according to Eqs. (4.16) with V_{3e} included in \mathcal{F}_2 and the 1^4B_2 and 1^4A_2 states as a function of $\varrho = Q_3$, i.e. $\varphi = 0$ (calculated in C_{2v} symmetry). Dots represent *ab-initio* data while solid lines correspond to the respective polynomial fits from which the JT parameters V_{2a} , V_{1e} and V_{3e} (as well as V_{4a} and \tilde{V}'_{4e} , for the fourth order expansion) are extracted. **(b)** The fitting procedure based on Eqs. (4.14) and (4.15) with the two branches of the $1^4E''$ JT manifold given as a function of the polar angle φ with $\varrho = \varrho_{\min} = 1.0876 \text{\AA}$ (calculated in C_s symmetry). This corresponds to a circle with fixed radius ϱ_{\min} in the Q_2 - Q_3 branching plane. Both branches are fitted with trigonometric functions according to Eq. (4.14) or Eq. (4.23) to extract the JT parameters V_{3a} and V_{2e} (as well as V_{4e} and V'_{4e} for the fourth order expansion). Note that both branches are in phase, indicating the dominance of the cubic anharmonicity parameter in Eqs. (4.11), (4.24) or (4.19). All *ab-initio* calculations were performed at MRCI(lcECP+CPP)/UET15 level of theory with the zero of energy chosen so to coincide with the 1^4A_2 minimum ($Q_1 = 8.335 \text{\AA}$). The fitting procedures for the fourth order cases (JT4) are qualitatively indistinguishable from the depicted ones in (a) and (b).

demonstrated by Fig. 4.14 (a) showing that the obtained topology of the lower PES sheet $E_-^{\text{JT}3}$ according to Eq. (4.11) with $V_{3e} \rightarrow 0$ clearly does not match the *ab-initio* data sufficiently. As shown in Fig. 4.14 (b), including the V_{3e} parameter improves the agreement between *ab-initio* data and analytic PES, but still fails in accurately reproducing the shape around the global minima. These findings are also reflected in the RMSD values of Tab. 4.8. Hence, considering even higher anharmonicities and JT coupling parameters in the potential part of the JT Hamiltonian in Eqs. (2.59) and (2.60) becomes inevitable.

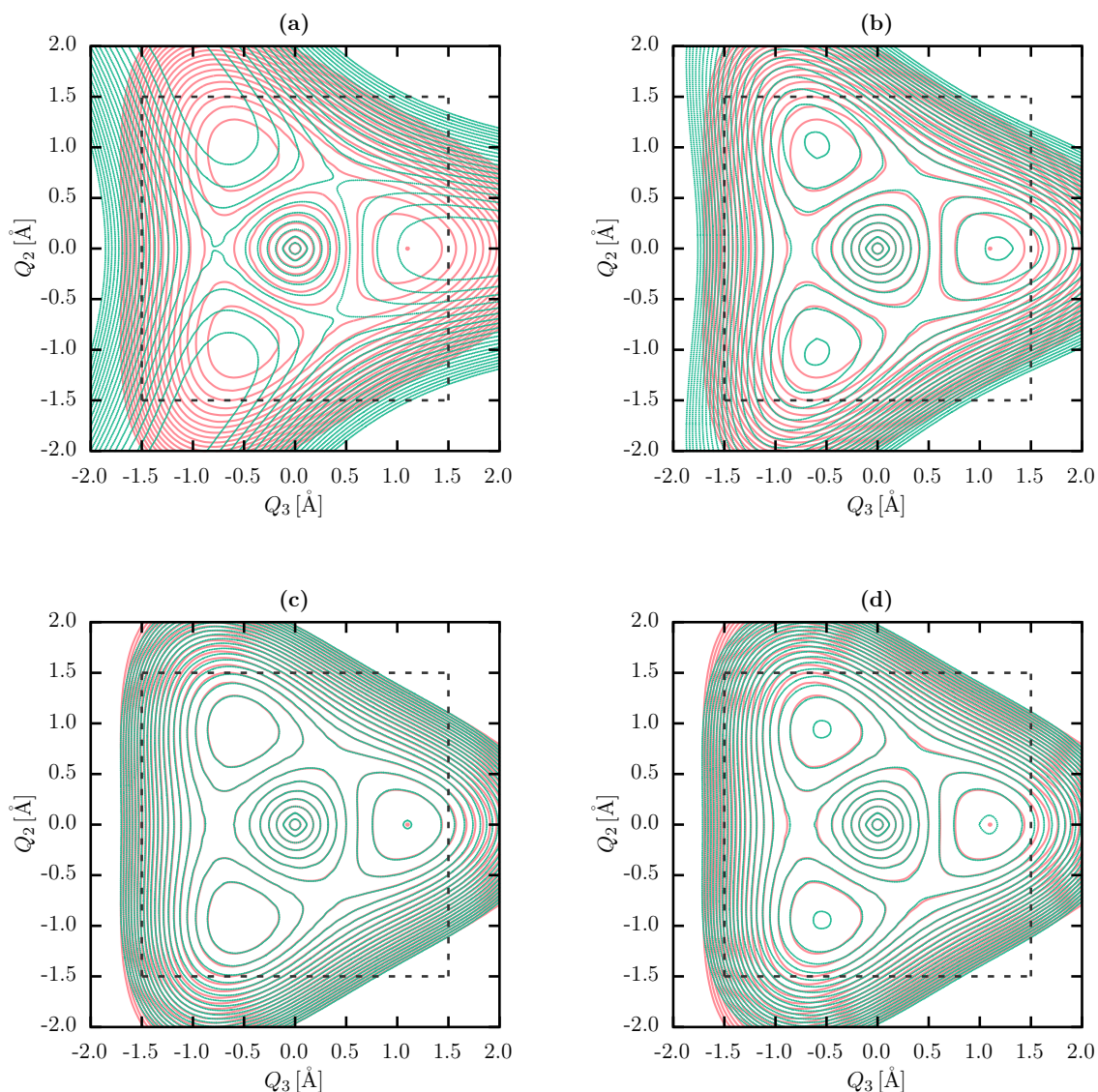


FIGURE 4.14.: Comparison of the $1^4E''$ lower branch JT-PES E_- (light green crosses) obtained analytically at different model levels with the corresponding *ab-initio* data (pink solid lines). The third-order JT expansion after Eq. (4.11) is shown in the upper panel, where in (a) the cubic vibronic coupling parameter V_{3e} is neglected. In (b) this parameter is included. The lower panel corresponds to the case where the potential part of the JT Hamiltonian is expanded up to the fourth order. The “simplified” fourth-order model after Eq. (4.22) is shown in (c), while the “complete” fourth-order PES according to Eq. (4.17) is displayed in (d). In each figure the dashed squares indicate the area within which the restricted RMSD values $\text{RMSD}_{\text{restr}}$ were calculated. The zero of energy is chosen to coincide with the 1^4A_2 minimum; i.e. the global minimum on E_- . The contour lines are given equidistantly with respective energy differences of 100 cm^{-1} covering a range from 0 to 2000 cm^{-1} . All *ab-initio* data were computed at MRCI(lcECP+CPP)/UET15 level of theory.

Including all terms up to fourth order (JT4) yields

$$\begin{aligned}
 E_{\pm}^{\text{JT4}} = & V_{2a}q^2 + V_{3a} \cos(3\varphi)q^3 + V_{4a}q^4 \pm q \left[V_{1e}^2 + 2V_{1e}V_{2e} \cos(3\varphi)q + (2V_{1e}V_{3e} + V_{2e}^2)q^2 \right. \\
 & + 2(V_{1e}V_{4e} + V_{1e}V'_{4e} + V_{2e}V_{3e}) \cos(3\varphi)q^3 + (2V_{2e}V'_{4e} + V_{3e}^2)q^4 + 2V_{2e}V_{4e} \cos(6\varphi)q^4 \\
 & \left. + 2V_{3e}(V_{4e} + V'_{4e}) \cos(3\varphi)q^5 + (V_{4e}^2 + (V'_{4e})^2)q^6 + 2V_{4e}V'_{4e} \cos(6\varphi)q^6 \right]^{\frac{1}{2}}, \quad (4.17)
 \end{aligned}$$

with the quartic force constant V_{4a} and the two fourth-order coupling parameters V_{4e} and V'_{4e} entering the theory as compared to Eq. (4.11). In analogy to the JT3 model, the cubic anharmonicity V_{3a} , the quadratic coupling V_{2e} , and the two quartic coupling parameters V_{4e} and V'_{4e} produce the same kind of $\cos(3\varphi)$ -warping of the PES. Again, there is no reason to prefer one of the terms over the others in the corresponding expansions. To derive a fitting procedure, analogous to Eq. (4.14) that allows for the separation of these contributions, one may first expand Eq. (4.17) to fifth order in q , yielding

$$\begin{aligned}
 E_{\pm}^{\text{JT4}}(q, \varphi) \approx & V_{2a}q^2 + V_{3a}q^3 \cos(3\varphi) + V_{4a}q^4 \pm \left[V_{1e}q + V_{2e} \cos(3\varphi)q^2 + V_{3e}q^3 \right. \\
 & - \frac{V_{2e}^2}{4V_{1e}} \cos(6\varphi)q^3 + \frac{V_{2e}^2}{4V_{1e}} q^3 + (V_{4e} + V'_{4e}) \cos(3\varphi)q^4 + \frac{3V_{2e}^3}{8V_{1e}^2} \cos(3\varphi)q^4 \\
 & + \frac{V_{2e}^3}{8V_{1e}^2} \cos(9\varphi)q^4 - \frac{V_{2e}^3}{2V_{1e}^2} q^4 + \frac{V_{2e}(V_{4e} - V'_{4e})}{2V_{1e}} \cos(6\varphi)q^5 - \frac{V_{2e}^2 V_{3e}}{2V_{1e}^2} \cos(6\varphi)q^5 \\
 & + \frac{V_{2e}(V'_{4e} - V_{4e})}{2V_{1e}} q^5 - \frac{V_{2e}^2 V_{3e}}{V_{1e}^2} q^5 - \frac{V_{2e}^4}{8V_{1e}^3} q^5 + q^5 \left(\frac{3V_{2e}^2 V_{3e}}{2V_{1e}^2} + \frac{V_{2e}^4}{8V_{1e}^3} \right) \cos(6\varphi) \\
 & \left. - \frac{5V_{2e}^4}{32V_{1e}^3} \cos(12\varphi)q^5 + \left(\frac{3V_{2e}^2 V_{3e}}{2V_{1e}^2} + \frac{9V_{2e}^4}{32V_{1e}^3} \right) q^5 \right]. \quad (4.18)
 \end{aligned}$$

Since the *ab-initio* results for the $1^4E''$ state show no significant warping contributions higher than $\cos(3\varphi)$, all those terms are neglected in Eq. (4.18). Assuming that the quartic couplings only enter via $\tilde{V}_{4e} = V_{4e} + V'_{4e}$, with $\tilde{V}_{4e} \ll V_{3a}$ and $\tilde{V}_{4e} \ll V_{2e}$, one may further neglect this contribution to the $\cos(3\varphi)$ oscillations. These two assumptions give rise to rewriting Eq. (4.18) into the form of Eq. (4.14), where the amplitudes now become

$$A'_{\pm} = V_{3a}q^3 \pm V_{2e}q^2 \mp \frac{3V_{2e}^3}{8V_{1e}^2} q^4. \quad (4.19)$$

By fitting the *ab-initio* data corresponding to $q = q_{\min} = 1.0876 \text{ \AA}$ with a $\cos(3\varphi)$ function, the two branches of Eq. (4.19) can be directly solved for V_{3a} . The quadratic

coupling V_{2e} follows from finding the proper root of the residual function

$$\mathcal{R}(V_{2e}) = 8V_{1e}^2 \varrho^2 \cdot V_{2e} - 3\varrho^4 \cdot V_{2e}^3 - 4V_{1e}^2 (A'_+ - A'_-), \quad (4.20)$$

with V_{1e} predetermined from polynomial fits defined analogously to Eq. (4.18), via

$$\mathcal{G}_1(\varrho, 0) = \frac{E_+^{\text{JT4}}(\varrho, 0) + E_-^{\text{JT4}}(\varrho, 0)}{2} = V_{2a}\varrho^2 + V_{3a}\varrho^3 + V_{4a}\varrho^4 + E_s[\min(1^4A_2)], \quad (4.21a)$$

$$\begin{aligned} \mathcal{G}_2(\varrho, 0) &= \frac{E_+^{\text{JT4}}(\varrho, 0) - E_-^{\text{JT4}}(\varrho, 0)}{2} \\ &= V_{1e}\varrho + V_{2e}\varrho^2 + V_{3e}\varrho^3 + \underbrace{(V_{4e} + V'_{4e})}_{\tilde{V}_{4e}}\varrho^4 + \sigma\varrho^5, \end{aligned} \quad (4.21b)$$

from which V_{2a} , V_{3e} , and \tilde{V}_{4e} follow as well. Here, σ is a tiny correction summarizing all terms $\propto \varrho^5$ and leads to small changes of less than 2% for V_{1e} and V_{3e} . This is due to the respective curvature which is mainly linear as shown in Fig. 4.13 (a). The constant shift $E_s[\min(1^4A_2)]$ again denotes the JT-stabilization energy as introduced above. As for the cubic case \mathcal{G}_1 and \mathcal{G}_2 are fitted to *ab-initio* data corresponding to a one-dimensional scan along Q_3 with $Q_2 = 0$ and $Q_1 = 8.335 \text{ \AA}$. Since the modifications introduced by the amplitudes after Eq. (4.19) and by the polynomial fits $\mathcal{G}_{1,2}$ according to Eq. (4.21) are rather small, the fitting procedures qualitatively look as already illustrated in Fig. 4.13.

The assumptions that the quartic coupling only enters via $\tilde{V}_{4e} = V_{4e} + V'_{4e}$ and can be extracted from \mathcal{G}_2 , furthermore allows for approximations in the exact expression for the fourth-order JT-PES of Eq. (4.17), yielding

$$\begin{aligned} E_{\pm}^{\text{JT4,simpl}}(\varrho, \varphi) &= V_{2a}\varrho^2 + V_{3a} \cos(3\varphi)\varrho^3 + V_{4a}\varrho^4 \pm \varrho \left[V_{1e}^2 + 2V_{1e}V_{2e} \cos(3\varphi) \right. \\ &\quad \left. + (2V_{1e}V_{3e} + V_{2e}^2)\varrho^2 + 2V_{1e}\tilde{V}_{4e} \cos(3\varphi)\varrho^3 + V_{2e}V_{3e} \cos(3\varphi) \right] \varrho^3 \\ &\quad \left. + V_{3e}^2\varrho^4 + 2V_{3e}\tilde{V}_{4e} \cos(3\varphi)\varrho^5 + \tilde{V}_{4e}^2 \cos(6\varphi)\varrho^6 \right]^{\frac{1}{2}}, \end{aligned} \quad (4.22)$$

where $2V_{4e}V'_{4e} \approx (V_{4e} + V'_{4e})^2 = \tilde{V}_{4e}^2$ was used. This form accounts for quartic couplings on an equal footing and does not require to determine V_{4e} and V'_{4e} individually. The resulting JT parameters obtained from this “simplified” quartic approach are summarized in Tab. 4.8. Including the fourth-order anharmonicity considerably changes the elastic force constant V_{2a} , while V_{3a} does not change per definition. The linear and quadratic coupling parameters show only minor changes due to the small size of \tilde{V}_{4e} . The resulting topology of the analytical JT-PES $E_-^{\text{JT4,simpl}}$ after Eq. (4.22) is

depicted in Fig. 4.14 (c) and shows excellent agreement with the corresponding *ab-initio* data. This is also demonstrated by the respective values for the RMSD as given in Tab. 4.8 showing that quartic terms are necessary to match the analytic JT model with respective *ab-initio* data. This reflects the fact that the extrema on the $1^4E''$ PES occur comparatively far away from the central COIN.

Nevertheless, the exact fourth-order form according to Eq. (4.17) suggests that $\cos(6\varphi)$ contributions are relevant and the above approximations might turn out insufficient. In an “complete” approach the quartic couplings V_{4e} and V'_{4e} should be treated independently. To this end, one may merely neglect the $\cos(12\varphi)$ term in Eq. (4.18) and rewrite it as

$$E_{\pm}^{\text{JT}4}(\varrho, \varphi) = \tilde{c}_{\pm} + \tilde{A}_{\pm} \cos(3\varphi) + \tilde{B}_{\pm} \cos(6\varphi) + \tilde{C}_{\pm} \cos(9\varphi), \quad (4.23)$$

with the amplitudes of the corresponding oscillations given via

$$\tilde{A}_{\pm} = V_{3a}\varrho^3 \pm V_{2e}\varrho^2 \pm (V_{4e} + V'_{4e})\varrho^4 \mp \frac{3V_{2e}^3}{8V_{1e}^2}\varrho^4, \quad (4.24a)$$

$$\tilde{B}_{\pm} = \mp \frac{V_{2e}^2}{4V_{1e}}\varrho^3 \pm \frac{V_{2e}(V_{4e} - V'_{4e})}{2V_{1e}}\varrho^5 \mp \frac{V_{2e}^2 V_{3e}}{2V_{1e}^2}\varrho^5 \pm \left(\frac{3V_{2e}^2 V_{3e}}{2V_{1e}^2} + \frac{V_{2e}^4}{8V_{1e}^3} \right) \varrho^5, \quad (4.24b)$$

$$\tilde{C}_{\pm} = \mp \frac{V_{2e}^3}{8V_{1e}^2}\varrho^4. \quad (4.24c)$$

For $\varrho = \varrho_{\min} = 1.0876 \text{ \AA}$, Eqs. (4.23) and (4.24) define unique conditions to extract the parameters V_{3a} , V_{2e} , V_{4e} , and V'_{4e} through fits of the corresponding *ab-initio* data. Again, the remaining parameters are obtained from polynomial fits according to Eq. (4.21), where V_{1e} needs to be determined beforehand for use in Eqs. (4.24). The illustration of this fitting procedure still qualitatively coincides with what is shown in Fig. 4.13.

The resulting JT parameters of this “complete” fourth order treatment are summarized in Tab. 4.8 and the corresponding lower branch PES $E_{-}^{\text{JT}4}$ is illustrated in Fig. 4.14 (d) showing that the “simplified” and “complete” fourth order approach are qualitatively indistinguishable. The fitting procedure according to Eq. (4.24) causes negligibly changes for V_{3a} but significantly modifies the quadratic coupling V_{2e} . Table 4.8 reveals that the quartic couplings V_{4e} and V'_{4e} clearly contribute to the obtained topology of the $1^4E''$ JT manifold. However, this also indicates that, despite the success of the simplified JT4 approach to locally describe the correct topology, the corresponding approximations concerning \tilde{V}_{4e} may be in general invalid. The RMSD values indicate that the simplified JT4 model is perfectly suited to describe the PES in

TABLE 4.8.: Synopsis of the JT parameters extracted for the analytical PESs of the $1^4E''$ state of Rb_3 according to Eq. (4.11) for the third order model JT3 as well as Eqs. (4.22) and (4.17) for the simplified and complete fourth-order models JT4, respectively. The root-mean-square deviation (RMSD) values provide a quantitative measure for the quality of the respective analytical JT model. The subscript “full” refers to deviations with respect to the complete range of *ab-initio* data shown in Figs. 4.14 and D.4, while the subscript “restr.” denotes deviations with respect to the constrained area indicated by dashed squares in Fig. 4.14. These areas represent the most relevant region of the potential-energy landscape and accounts for the fact that for $|Q_2|, |Q_3| \geq 1.5 \text{ \AA}$ the upper branch PES E_+ starts to intersect with higher-lying states. The corresponding “restr.,2” area is defined by $Q_2, Q_3 \in [-1.3, 1.3] \text{ \AA}$ as shown in Fig. D.4.

Parameter	Unit	3rd order model JT3		4th order model JT4	
		V_{3e} neglected	V_{3e} included	simplified	complete
V_{2a}	$\text{cm}^{-1}/\text{\AA}^2$	909.652	909.652	866.772	866.772
V_{1e}	$\text{cm}^{-1}/\text{\AA}$	1714.319	1784.133	1783.466	1783.446
V_{2e}	$\text{cm}^{-1}/\text{\AA}^2$	41.755	41.755	41.765	59.232
V_{3a}	$\text{cm}^{-1}/\text{\AA}^3$	-142.832	-142.832	-142.832	-142.827
V_{3e}	$\text{cm}^{-1}/\text{\AA}^3$	-	-77.658	-75.571	-75.571
V_{4a}	$\text{cm}^{-1}/\text{\AA}^4$	-	-	40.066	40.066
\tilde{V}_{4e}	$\text{cm}^{-1}/\text{\AA}^4$	-	-	0.116	-
V_{4e}	$\text{cm}^{-1}/\text{\AA}^4$	-	-	-	16.164
V'_{4e}	$\text{cm}^{-1}/\text{\AA}^4$	-	-	-	-27.171
$\text{RMSD}_{\text{full}}(E_-)$	cm^{-1}	832.200	386.024	143.782	120.942
$\text{RMSD}_{\text{restr.}}(E_-)$	cm^{-1}	290.492	130.018	13.262	30.370
$\text{RMSD}_{\text{restr.,2}}(E_+)$	cm^{-1}	46.063	56.757	30.715	26.465

an restricted area whereas the complete JT4 model should be used for a more global representation.

In general, since the quadratic couplings V_{2e} for both third-order and fourth-order approaches are about 50 times smaller than the linear couplings, no additional COINs near the central one are expected [161].

It should be noted that the approach outlined in this section with the analytical description of the JT-PES according to Eqs. (4.11), (4.22) or (4.17) does not account for couplings to the totally symmetric mode Q_1 . In general, cutting the seam of an E state at a slightly altered Q_1 coordinate would result in different curvatures of

the branches E_{\pm} . However, as shown in Fig. 4.11 (b) the region around the global minimum (cut indicated by the horizontal white line at the bottom) does not suggest major changes in the curvature. Thus, this effect might be negligible and the main physical implication may be already obtained from the two-dimensional approach. Nevertheless, an analytical expression for a three-dimensional APES including the totally symmetric force and the corresponding linear coupling term can be found in Refs. [91, 161]. This approach would be necessary to accurately reproduce experimental spectra.

Furthermore, the analysis presented here, neglects SOC effects which removes the central COIN at $Q_2 = Q_3 = 0$. The analytic form of the corresponding PES as given in Eqs. (2.75) assumes only a constant SO-induced shift Δ of the corresponding PESs. The investigation of Hauser *et al.* [95] concerning the impact of SOC onto the JT-parameters of the $1^2E'$ manifold of Rb_3 revealed that its effect is negligibly small for a corresponding energy splitting of $\Delta = 30.2 \text{ cm}^{-1}$. The same holds for the $2^4E'$ state of Rb_3 , for which Hauser *et al.* [96] found $\Delta = 15.1 \text{ cm}^{-1}$. Since the SO-splitting for the $1^4E''$ state amounts to $\Delta \approx 10 \text{ cm}^{-1}$ (cf. Sec. 4.4.2) no major effects on the JT-parameters caused by SOC are expected as well.

The results of the above fitting procedures concerning the higher branch PES E_+ are shown in Fig. D.4 in the appendix D.5.

4.6 | Quadruple interactions in the high-spin manifold

The following discussion attempts to provide a qualitative understanding of the physics underlying the quadruple interactions in the high-spin Q -manifold of Eq. (4.6). The complex interplay of avoided crossings, COINs and JT interactions was already mentioned above related to Fig. 4.6 (d). Since the four states ($1^4A_1, 2^4A_1, 2^4B_1, 3^4B_1$) are close in energy, a PJT-like interaction pattern may be expected. However, due to the fourth state this cannot be readily compared to the well-known $(E + A) \otimes e$ PJTE occurring, for instance, in the doublet manifold of homonuclear alkali-metal trimers, as it has been extensively studied for Na_3 in, e.g., Refs. [86–91, 93]. Nevertheless, as suggested by PJT theory to detect triple degeneracies, the coupling mechanism of the Q -manifold may be first analyzed by a one-dimensional cut along the totally symmetric breathing mode Q_1 preserving D_{3h} symmetry. The resulting PESs are shown in Fig. 4.15 where, for later reference, the area highlighted in gray marks the region left to the triple COIN. Potential-energy curves which are degenerate over a certain range

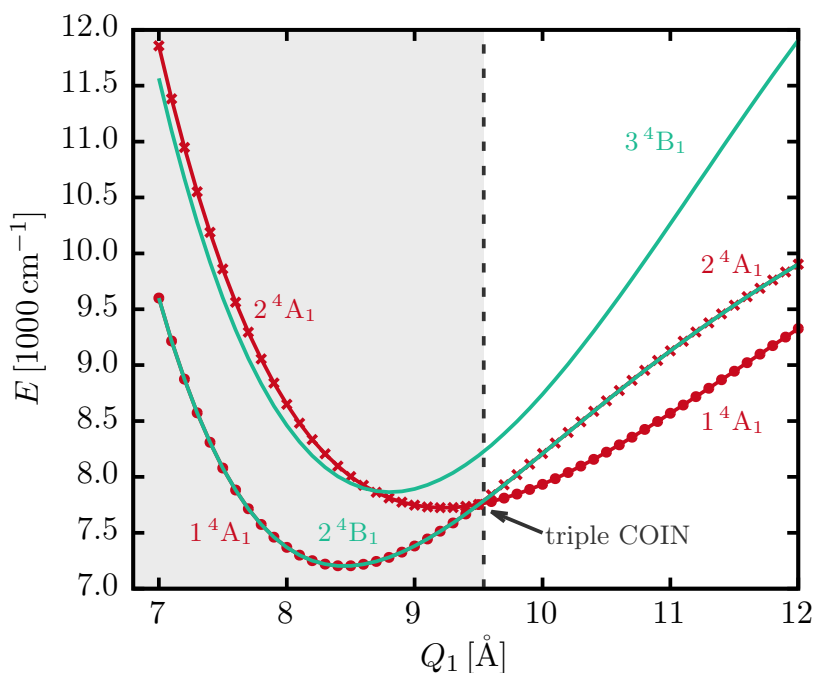


FIGURE 4.15.: One-dimensional cut through the \mathcal{Q} manifold of Eq. (4.6) along the totally symmetric breathing mode Q_1 computed at MRCI(lcECP+CPP)/UET15 level of theory ($Q_2 = Q_3 = 0$). The D_{3h} preserving scan shows that the 1^4A_1 and 2^4B_1 states are degenerate forming the $1^4E'$ JT state. At $Q_1^{\text{COIN}} \approx 9.5 \text{ \AA}$ this JT pair additionally coalesces with the 2^4A_1 state leaving a triply degenerate COIN in the configuration space. Beyond the triple COIN the degeneracy with the 1^4A_1 state is lifted suggesting a change of the JT interaction to $1^4E' = 2^4A_1 + 2^4B_1$. The intersection between the 2^4A_1 and 3^4B_1 states at $Q_1 \approx 8.8 \text{ \AA}$ seems to be accidental. For later reference, the area highlighted in gray marks Q_1 values left to Q_1^{COIN} . Energies are given relative to the $3 \cdot \text{Rb}$ asymptote.

(i.e. not only at a single point) may indicate JT interactions; whereas the presence of a triply degenerate COIN between the 1^4A_1 , 2^4A_1 and 2^4B_1 states may suggest a combined JT and PJT interaction as, e.g., observed for the (B, B') system of Na_3 [86] and discussed in Sec. 2.3.3. Moreover, the triple COIN points to a change of components forming the twofold degenerate $1^4E'$ state: from $1^4A_1 + 2^4B_1$ to $2^4B_1 + 2^4A_1$. The 3^4B_1 state shows merely one accidental degeneracy at $Q_1 \approx 8.8 \text{ \AA}$ with the 2^4A_1 state thus excluding conventional JT interaction between these two states. An avoided crossing between the 3^4B_1 and 2^4B_1 states can be observed at around $Q_1 \approx 10.0 \text{ \AA}$ suggesting mixing between them. Hence, the 3^4B_1 state may also contribute in a PJT-like interaction scenario with the other states.

In order to better understand the effects of the triple COIN on the topology of the PESs and on the respective coupling behavior among the states, scans along the C_{2v} symmetry preserving Q_3 JT coordinate are performed. The resulting potential-

energy curves together with the corresponding non-adiabatic coupling matrix elements (NACMEs) are shown in Fig. 4.16. Since the Rb_3 system is in general characterized by the C_s point group, general investigations require the use of this symmetry. Therefore, the left-hand side of Fig. 4.16 shows both C_{2v} results (solid lines) and C_s data (dots), wherefrom one may deduce a first notion of the full 3D topology. This is due to the fact that the A_1 and B_1 IRREPs of the C_{2v} point group fall both into the A' IRREP in the adjacent low symmetry subspace (cf. Tab. A.9) and thus mix and avoid each other. Moreover, the use of C_s symmetry allows for computing NACMEs among all states involved in the \mathcal{Q} manifold since all of them are of A' character (here: $2^4A'$, $3^4A'$, $4^4A'$ and $5^4A'$). The NACMEs were obtained using the DDR method in MOLPRO 2019.2 [252] embedded in a MRCI(lcECP+CPP)/UET15 approach. In the DDR-procedure, the matrix elements are assembled from the underlying wavefunctions and transition densities by using finite differences. In its current implementation, this is only possible among states of the same symmetry. The non-adiabatic coupling matrix is already known from the Born-Oppenheimer-Huang equation (2.20) with its definition from Eqs. (2.18) and (2.19). In general, NACMEs between two electronic states i, j are defined with respect to all nuclear coordinates Q_k of a given system. Usually they are given componentwise as $\tau_{Q_k}^{ij} = (\mathbf{F}_{ij})_k = \langle \psi_i | \partial / \partial Q_k | \psi_j \rangle$, with $Q_k = \{Q_1, Q_2, Q_3\}$ for the case of Rb_3 . Thus, non-vanishing contributions are obtained if $\Gamma(i) \otimes \Gamma(Q_k) \otimes \Gamma(j)$ contains the identical representation. The results on the right-hand side of Fig. 4.16 display the Q_3 component of NACMEs between all pairs of states given in C_s symmetry, i.e., e.g., $\tau_{23} = \langle 2^4A' | \partial / \partial Q_3 | 3^4A' \rangle$. Since all calculations were performed in C_s symmetry, it follows that $\Gamma(Q_1) = \Gamma(Q_2) = \Gamma(Q_3) = a'$ and thus all components of the NACMEs between the states of the \mathcal{Q} manifold as depicted in Fig. 4.16 allow for non-vanishing contributions.

The coupling left to the triple COIN [Fig. 4.16 (a)] is dominated by the δ -function-like behavior of τ_{23} at $Q_2 = Q_3 = 0.0 \text{ \AA}$. This represents the JT interaction at the point of degeneracy among the $2^4A'$ and $3^4A'$ components of the $1^4E'$ term (in C_{2v} described by the 1^4A_1 and 2^4B_1 states). The vanishingly small NACME τ_{45} between the $4^4A'$ and $5^4A'$ states (i.e. the 2^4A_1 and 3^4B_1 states in C_{2v}) once more suggests the lack of JT interaction between both states. Preliminary results indicate that major contributions to the Q_3 component of the τ_{45} NACME occur for C_s scalene triangular configurations of Rb_3 , i.e. in subspaces with $Q_2 \neq 0$. It remains to investigate the behavior of the Q_1 and Q_2 components of the respective NACME. The situation depicted in Fig. 4.16 (a) implies that the size of the couplings of the $4^4A'$ and $5^4A'$ states to the components of

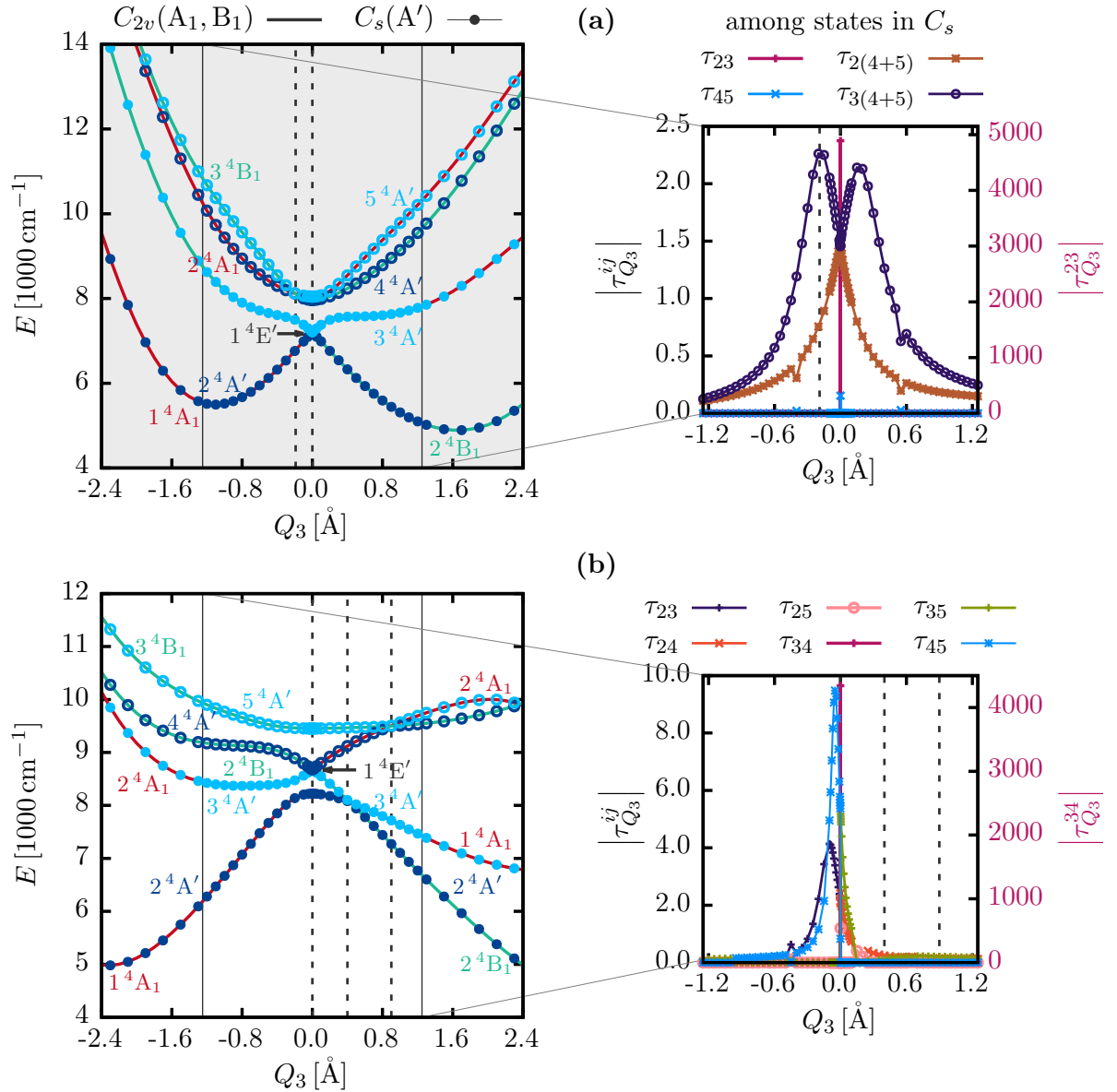


FIGURE 4.16.: Cuts through the Q -manifold of Eq. (4.6) along the C_{2v} preserving distortion coordinate Q_3 are given on the left-hand side of both panels for different Q_1 and $Q_2 = 0.0$ Å. Solid lines represent C_{2v} results, with IRREPs A₁ and B₁, while dots correspond to C_s data where all states fall into the IRREP A'. At the central COIN (D_{3h} symmetry) the twofold degenerate $1^4E'$ JT state is formed. The right-hand side of each panel displays the Q_3 component of NACMEs between all pairs of states given in C_s symmetry, i.e., e.g., $\tau_{23} = \langle 2^4A' | \partial/\partial Q_3 | 3^4A' \rangle$. (a) Cut left to the triple COIN Q_1^{tCOIN} [cf. Fig. 4.15] at $Q_1 \approx 8.451$ Å which is the D_{3h} minimum of the $1^4E'$ state as shown in Fig. 4.15 and reported in Tab. 4.3 (lower horizontal white lines in Fig. 4.17). A cut right to the triple COIN for $Q_1 = 10.5$ Å (upper horizontal white lines in Fig. 4.17) is shown in (b). A direct consequence of the triple COIN is an inversion of components forming the $1^4E'$ JT pair (see text for details). Vertical dashed lines highlight the positions of COINs occurring both at D_{3h} and C_{2v} configurations. The NACMEs τ_{23} in (a) and τ_{34} in (b) scale with respect to the right axis. Calculations were performed at MRCI(lcECP+CPP)/UET15 level of theory and energies are given relative to the $3 \cdot \text{Rb}$ asymptote.

the JT manifold ($\cong 2^4A' + 3^4A'$) exceeds the coupling between these states themselves. Therefore, one may consider the $4^4A'$ and $5^4A'$ states together and define combined NACMEs $\tau_{2(4+5)}$ and $\tau_{3(4+5)}$ describing the couplings of this sub-manifold of states to each of the two components of the $1^4E'$ JT state separately. These two NACMEs give sizable contributions at the positions of avoided crossings and at the high-symmetry point $Q_3 = 0.0 \text{ \AA}$. This may indicate the presence of a PJT coupling behavior besides the dominant JT interaction. Thus, to reach comprehensive understanding an approach within the PJT theory may be required (see below).

The topology right to the triple COIN [Fig. 4.16 (b)] occurs more complex with the $1^4E'$ JT term now formed by the $3^4A'$ and $4^4A'$ states. The $2^4A'$ and $5^4A'$ state disperse below and above the $1^4E'$ JT-manifold with additional COINs occurring close to the central one at C_{2v} configurations. In contrast to Fig. 4.16 (a), the NACMEs are now explicitly given among all pairs of states individually, since it is not straightforwardly possible to define a joint sub-manifold as before. Again, the δ -function-like NACME at $Q_2 = Q_3 = 0.0 \text{ \AA}$ representing the JT interaction, here τ_{34} , dominates the coupling scenario. Besides, it is worth mentioning that the couplings at the additional C_{2v} COINs (for $Q_3 > 0.0 \text{ \AA}$) are almost zero while they show significant contributions at the avoided crossings for $Q_3 < 0.0 \text{ \AA}$.

Note that for further use of the NACMEs, e.g. in an adiabatic-to-diabatic transformation, they have to be symmetry-adapted by the corresponding molecular symmetry group as shown for K_3 in Ref. [94].

Example input for the DDR procedure

The NACME scan according to Fig. 4.16 can be reproduced with the example input C.6.

Deeper understanding of the discussed effects may be attained by investigating the potential-energy landscapes in two-dimensional subspaces. The D_{3h} COIN seams (for $Q_2 = Q_3 = 0.0 \text{ \AA}$) occur in cuts through the Q_1 - Q_3 subspace. This is shown in Fig. 4.17. The $2^4A'$ state shown in Fig 4.17 (a) reveals an one-dimensional COIN seam up to $Q_1 = Q_1^{\text{tCOIN}} \approx 9.5 \text{ \AA}$. Beyond this point the COINs are removed due to the inversion of components forming the $1^4E'$ JT pair as a consequence of the triple COIN. The $3^4A'$ states always forms one component of the $1^4E'$ JT-manifold and thus shows a one-dimensional COIN seam over the full Q_1 -range considered here. This is illustrated in Fig. 4.17 (b). Since the $4^4A'$ and $2^4A'$ states change their role at the triple COIN, the former shows a COIN seam for $Q_1 > Q_1^{\text{tCOIN}} \approx 9.5 \text{ \AA}$ as indicated in Fig. 4.17 (c). There are further COINs occurring at C_{2v} configurations for both $Q_3 < 0.0 \text{ \AA}$ and $Q_3 > 0.0 \text{ \AA}$

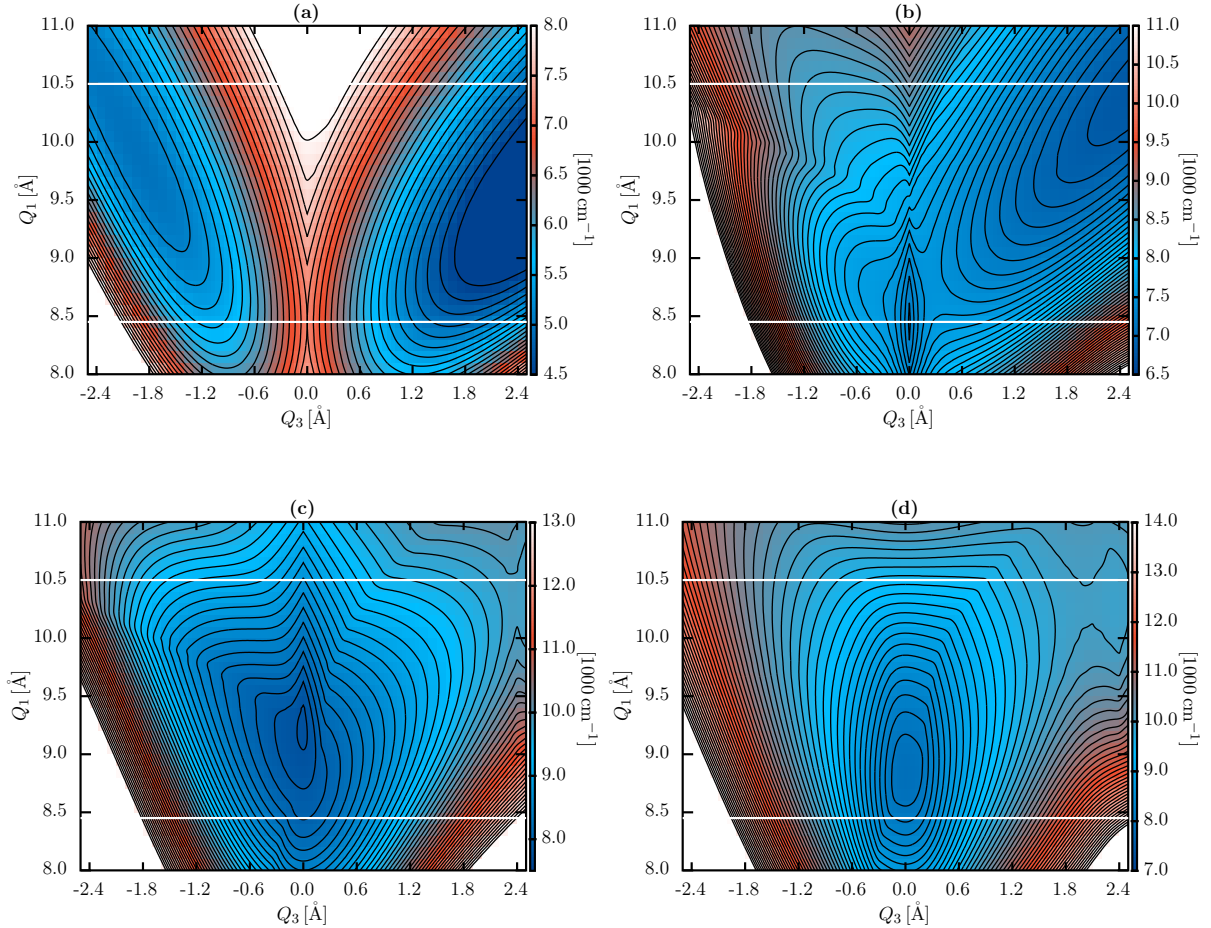


FIGURE 4.17.: Contour plots of the PESs of the Q -manifold according to Eq. (4.6) in the two-dimensional subspace of Q_1 and Q_3 preserving at least C_{2v} symmetry (i.e. $Q_2 = 0.0 \text{ \AA}$). To obtain the correct topology with respect to the full 3D configuration space the computational point group was chosen to be C_s . The $2^4A'$ state is shown in (a), the $3^4A'$ state in (b), the $4^4A'$ state in (c) and the $5^4A'$ state is illustrated in (d). Discontinuities in the contour lines at $Q_3 = 0.0 \text{ \AA}$ correspond to the D_{3h} COIN seam occurring due to JT interactions among the respective states. Additional COINs are found for C_{2v} geometries at $Q_3 < 0.0 \text{ \AA}$ and $Q_3 > 0.0 \text{ \AA}$. See text for more details. The lower and upper horizontal white lines represent the respective cuts left and right to the triple COIN as shown in Figs. 4.16 and 4.18. Calculations were performed at MRCI(lcECP+CPP)/UET15 level of theory and energies are given relative to the $3 \cdot \text{Rb}$ asymptote.

due to accidental degeneracies with the $5^4A'$ state as already shown in Fig. 4.16 (this corresponds to accidental intersections between the 2^4A_1 and 3^4B_1 states mentioned at the beginning). This finding is further demonstrated in Fig. 4.17 (d) where it is moreover shown that the $5^4A'$ state is free of COINs at D_{3h} configurations.

The topology of the PESs in the two-dimensional branching space spanned by the Q_2 and Q_3 modes is shown in Fig. 4.18. The tricorn surface clearly indicates the presence of the $E \otimes e$ JT effect dominating over the PJT coupling, as discussed in Sec. 2.3.3. The inversion of the states forming the $1^4E'$ JT manifold is shown in Figs. 4.18 (a), (b) and (c). The lower panels in each subframe demonstrate the situation right to the triple COIN with additional C_{2v} COIN seams near the central D_{3h} one. These C_{2v} COIN seams are formed between the $2^4A'$ and $3^4A'$ states as well as between the $4^4A'$ and $5^4A'$ states. The similarity of the $4^4A'$ and $5^4A'$ surfaces left to the triple COIN and of the $2^4A'$ and $5^4A'$ PESs right to the triple COIN may further indicate the presence of combined JT and PJT couplings.

The minima on the $3^4A'$ PES [lower panel of Fig. 4.18 (b)] are, for $Q_1 = 10.5 \text{ \AA}$, of 1^4A_1 character in the adjacent C_{2v} subspace as indicated by Fig. 4.16 (b). This explains the occurrence of a minimum of the 1^4A_1 state as reported in Tab. 4.4 at $(Q_1, Q_2, Q_3) \approx (10.428, 0.0, 2.517) \text{ \AA}$, although it is found to form saddle points on the lower PES branch of the $1^4E'$ manifold left to the triple COIN. This proves the non-static nature of the states forming the $1^4E'$ JT pair and can be viewed as a direct consequence of its inversion. This is also seen in Fig. 4.17 (b). In this regard, the 2^4B_1 minimum found at $Q_1 \approx 9.85 \text{ \AA}$ in Tab. 4.4 may now be understood from a broader perspective as occurring in close proximity to the triple COIN as illustrated in Fig. 4.17 (a). The formation of this minimum at C_{2v} symmetry is explained by the underlying JT effect as shown in Fig. 4.18 (a). Moreover, the equilateral triangular configurations of the 2^4A_1 and 3^4B_1 states occurring at $(Q_1, Q_2, Q_3) \approx (9.22, 0.0, 0.0) \text{ \AA}$ and $(Q_1, Q_2, Q_3) \approx (8.81, 0.0, 0.0) \text{ \AA}$, respectively, as reported in Tab. 4.4, are also confirmed by Figs. 4.17 (c) and (d).

In order to properly describe the quadruple interactions in the Q -manifold and to quantitatively understand the topology and properties of the corresponding PESs, a combined JT and PJT approach including all four states is required. The PJT treatment is suggested by the occurrence of a triple COIN beyond which the characteristics of the $1^4E'$ manifold is inverted, cf. Figs. 4.16 to 4.18. However, in contrast to the PJTE in the 2E - 2A systems of homonuclear alkali-metal trimers, the JT coupling in the $1^4E'$ state strongly dominates the four-state interaction. This is the case both left and right to

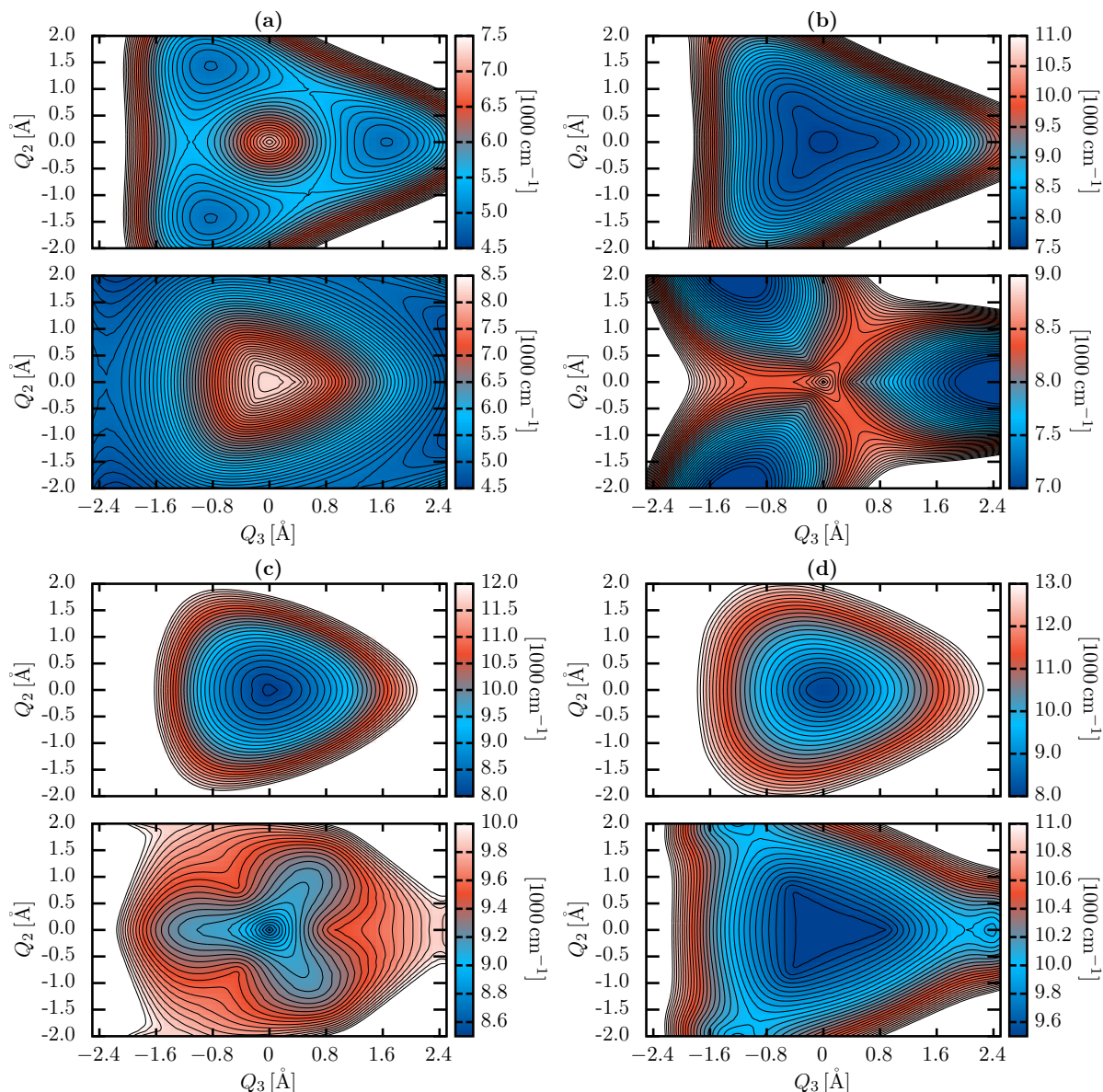


FIGURE 4.18.: Contour plots of the PESs of the Q -manifold according to Eq. (4.6) in the two-dimensional branching space spanned by the JT-active modes Q_2 and Q_3 . The upper panel of each subframe corresponds to a cut left to the triple COIN for $Q_1 \approx 8.451 \text{ \AA}$ (lower horizontal white lines in Fig. 4.17), while the lower panel represents a cut right to Q_1^{COIN} for $Q_1 = 10.5 \text{ \AA}$ (upper horizontal white line in Fig. 4.17). The computational point group is C_s . (a) displays the $2^4A'$ state, (b) the $3^4A'$ state, (c) the $4^4A'$ and (d) depicts the $5^4A'$ state. The plots demonstrate the increasing complexity of the topology right to the triple COIN (lower panel) and show the inversion of states forming the $1^4E'$ JT manifold. The tricorner topology of the lower branch is illustrated in (a) and (b) indicating the dominance of JT interactions over PJT couplings. See text for a detailed discussion. Calculations were performed at MRCI(lcECP+CPP)/UET15 level of theory and energies are given relative to the $3 \cdot \text{Rb}$ asymptote.

Q_1^{tCOIN} as demonstrated by the respective NACMEs scans in Fig. 4.16. Left to the triple COIN the interaction between the $2^4A'$, $3^4A'$ and $4^4A'$ states may be first modeled by a 3×3 PJT-Hamiltonian according to Eq. (2.76). The resulting analytical PESs after Eqs. (2.80) should reveal $V_{1e}^{E/A} \rightarrow 0$. This might at least serve as zeroth-order approximation to gain a basic understanding of the problem. Including the remaining $5^4A'$ state into the description and map the problem to a 4×4 PJT Hamiltonian should then lead to improved coincidence with *ab-initio* results. However, right to the triple COIN a complete effective 4×4 PJT-Hamiltonian would probably be needed right from the start. The PJT-Hamiltonian should account for all states of the Q -manifold and the respective interactions among them to properly model the underlying physics. A first idea on how to extent a 3×3 PJT-Hamiltonian after Eq. (2.76) to a 4×4 one, might be deduced from the NACMEs of Fig. 4.16 (b). It seems that both the $2^4A'$ and the $5^4A'$ states take a similar role as the $4^4A'$ state left to Q_1^{tCOIN} . In general, a 4×4 -approach is required in both cases since a proper treatment of vibronic coupling effects needs to consider all excited states that show sufficient couplings [161, 182, 183]. This would finally also reveal which coupling mechanism dominates over the other and if there is a smooth transition between both.

The quantitative approach outlined above only considers couplings to the JT active modes Q_2 and Q_3 . For a full three-dimensional treatment and to entirely understand all topological properties of the corresponding PESs one also needs to consider couplings to the totally symmetric breathing mode Q_1 . The correlating form of a 3×3 PJT-Hamiltonian can be found, e.g., in Ref. [91], which may further serve as an inspiration for the 4×4 case.

Once a suitable 4×4 PJT-Hamiltonian $\mathcal{H}_{\text{PJT}}^Q$ is set up, the analytical form of the corresponding PESs is found by diagonalization, where the JT- and PJT-parameters are obtained from proper fits to the *ab-initio* data. The positions of the extrema, as displayed in Figs. 4.16 to 4.18, indicate that higher anharmonicities may become relevant. This was shown in the previous discussion of Sec. 4.5, where fourth-order terms turned out relevant for a sufficient agreement with *ab-initio* results.

Including spin-orbit coupling in the above analysis removes the central symmetry-required COIN of the $1^4E'$ JT state with rather small splittings between the respective Kramers pairs of $\Delta \approx \mathcal{O}(10 \text{ cm}^{-1})$. Moreover, the additional C_{2v} COINs resulting from interactions with the remaining states are also lifted. Two generic situations are shown in Fig. D.5 in appendix D.6. In general, it has been shown that the presence of SOC reduces the dimension of the COIN seam to $N_{\text{int}} - 3$ (when C_s symmetry can be

imposed); with N_{int} the number of internal degrees of freedom [280–282]. This means that there is merely one COIN point in the full 3D configuration space.

The set of states according to Eq. (4.6) with occurring quadruple interactions are expected for all high-spin alkali metal trimers [99]. However, in contrast to what has been mentioned therein, it was shown that the coupling mechanism of the \mathcal{Q} manifold is not only due to pairs of E' states but rather reveals a more complex interaction behavior. In the course of the present discussion possible approaches for a more quantitative analysis were outlined which may be part of future works.

Technical remark

The ab-initio data shown in Figs. 4.17 and 4.18 were generated using the MOLPRO 2020.1 program package [225, 253] with corresponding calculations performed on the JUSTUS 2 cluster.

5

QUARTET GROUND-STATE POTENTIAL ENERGY SURFACE FOR RUBIDIUM TRIMER

This chapter provides a concise introduction into a particular *kernel ridge regression* technique proposed for use as an effective tool for the construction of globally smooth molecular potential energy surfaces. The respective technique is related (but mathematically not equivalent) to the well-known and widespread machine learning procedure of Gaussian process regression but is designed such that the underlying physics of molecules can be readily incorporated. By using this ansatz it is shown that highly accurate potential-energy landscapes for both Rb_2 and Rb_3 can be constructed which may be subsequently used in quantum dynamics calculations.

The following merely motivates the basics of the interpolation method used for subsequent investigations of this chapter, rather than deriving them rigorously. The mathematical interested reader is referred to Appendix E for a detailed and formal discussion in the framework of reproducing kernel Hilbert space (RKHS) theory.

5.1 | RKHS method for constructing potential energy surfaces

The reproducing kernel Hilbert space (RKHS) theory [283–286] is a general concept embedded in the field of functional analysis. With the formulation of the *representer theorem* [284–287], it became particularly important in the field of statistical learning theory. The representer theorem states that any function f of a RKHS \mathcal{H}_k that minimizes an arbitrary regularized empirical risk functional (required by any data interpolation problem) can be represented as a *finite* linear combination of a reproducing symmetric

kernel function k evaluated on the training data x_i

$$f(\cdot) = \sum_{i=1}^N c_i k(\cdot, x_i), \quad (5.1)$$

with expansion coefficients $c_i \in \mathbb{R}$ (see Appendix E.1 for more details). This reduces any general infinite dimensional machine learning problem to the solution of a finite dimensional linear system. For instance, assuming squared-error loss and regularization based on Tikhonov's method [284, 285, 288–292], the minimization problem for n training data y_i given at positions x_i becomes

$$f^* = \min_{f \in \mathcal{H}_k} \left[\sum_{i=1}^n (y_i - f(x_i))^2 + \lambda \|f\|^2 \right], \quad (5.2)$$

with $\|\cdot\|$ the L_2 norm. The representer theorem defines the minimizer to be of the form (5.1) so that Eq. (5.2) reduces to solve for the vector of expansion coefficients \mathbf{c} , yielding [284, 285]

$$\mathbf{c}^* = \min_{\mathbf{c} \in \mathbb{R}^n} \left[\|\mathbf{y} - \mathbf{K} \cdot \mathbf{c}\|^2 + \lambda \mathbf{c}^T \mathbf{K} \mathbf{c} \right], \quad (5.3)$$

with the vector of training data \mathbf{y} and the symmetric and positive (semi-) definite $n \times n$ kernel matrix \mathbf{K} with the ij -th entry $k(x_i, x_j)$. The solution vector $\hat{\mathbf{c}}$ of Eq. (5.3) results from solving the linear system

$$(\mathbf{K} + \lambda \mathbb{1}_{n \times n}) \cdot \hat{\mathbf{c}} = \mathbf{y}, \quad (5.4)$$

for which classical numerical procedures such as LU decomposition or Cholesky factorization can be efficiently used [291]. More details on reproducing kernels may be found in Appendix E.1.

The regularization used above ($= \lambda \mathbb{1}_{n \times n}$) is a special case of Tikhonov's method, which is also referred to as L_2 regularization and defines the class of (kernel) ridge regression methods. The rationale of applying regularization is to account for ill-conditioning in inverse problems such as Eq. (5.4). Ill-conditioning may arise due to large or densely clustered training data sets rendering the matrix \mathbf{K} nearly rank deficient. In this case the solutions of the unregularized ($\lambda = 0$) linear system (5.4) may become very sensitive to arbitrarily small perturbations such as machine roundoff errors. Another origin of ill-posed problems may be data errors. Here, regularization operates as a penalty function filtering out destabilizing high frequency components corresponding to small singular values of the linear system under study [291]. More details are outlined in the Appendix E.2.

Although the representer theorem is a powerful tool to map general data interpolation problems to the solution of finite-dimensional linear systems, it does not further specify the form (apart from being symmetric and positive (semi-) definite) of the reproducing kernel function and thus introduces a certain degree of ambiguity. From a simplified viewpoint the kernel function can be considered as measuring the similarity between a pair of input data whereof it learns how to predict data that are not in the training set. This illustrates that for certain problems some kernels are more suited than others. One may either choose from a set of “standard” kernels (rational quadratic, Matérn, periodic, RBF; see Ref. [286] for a comprehensive overview) or explicitly derive a kernel function for a given problem. The latter approach was chosen by Ho and Rabitz [291, 293, 294] who constructed a reciprocal power (RP) reproducing kernel (r.k.) to obtain globally smooth molecular PESs as a function of distancelike variables in the semi-infinite interval $[0, \infty)$. This approach ensures that the resulting PESs show the physical correct asymptotic form, which is especially important in the context of scattering calculations. The construction is based on using the fundamental properties of RKHSs and the fact that molecular PESs are asymptotically constant. A detailed derivation is given in Appendix E.1, while the following merely shows its final form, reading

$$q_1^{n,m}(x, x') = n^2 x_{>}^{-(m+1)} B(m+1, n) {}_2F_1 \left(-n+1, m+1; n+m+1; \frac{x_{<}}{x_{>}} \right). \quad (5.5)$$

Here $x_{>}$ and $x_{<}$ are, respectively the larger and smaller of x and x' , $B(a, b)$ is the beta function and ${}_2F_1(a, b; c; z)$ is the Gaussian hypergeometric function (see Appendix E.3 for their explicit form). The parameters n and m dictate, respectively, the number of terms and the leading asymptotical reciprocal power behavior of the RP-r.k. function. The latter may be also found from Eq. (5.5) with the help of Appendix E.3.3, yielding

$$\lim_{x' \rightarrow \infty} q_1^{n,m}(x, x') \propto x'^{-(m+1)}, \quad m \geq 1. \quad (5.6)$$

A generic example of the behavior of the RP-r.k. for $n = 3$ and $m = 2$ (cf. Sec. 5.2) is shown in Fig. 5.1 as a function of R^s (for later reference) with $R_i \approx 4.5 \text{ \AA}$.

The RP-r.k. according to Eq. (5.5) was used in several applications for the construction of alkali-metal diatomic and triatomic PESs [100, 103, 105, 107, 295–297]. Here, the PES construction procedure for, e.g., the weakly interacting species K_3 and Rb_3 is based on decomposing the total potential energy function into a sum of the pairwise additive contributions and the three-body nonadditive part V_3

$$V_{X_3} = \sum_{i < j} V_{X_2}(R_{ij}) + V_3(R_{12}, R_{23}, R_{13}), \quad (5.7)$$

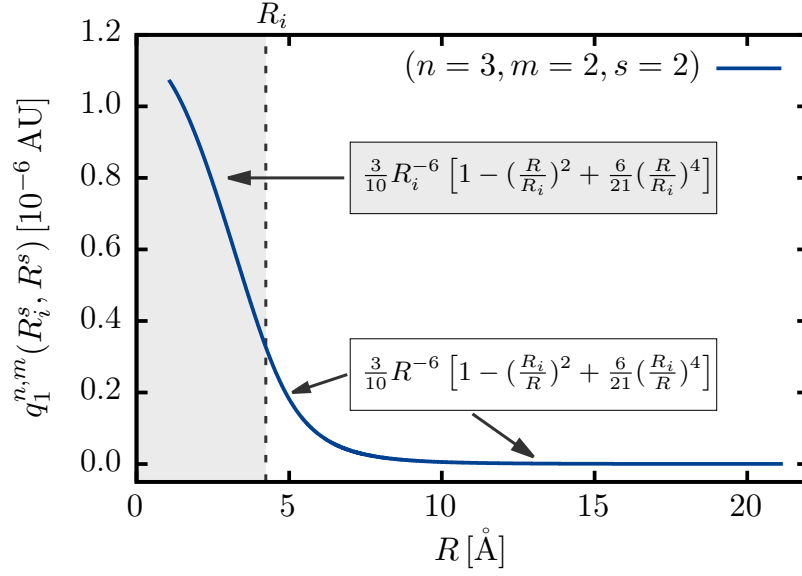


FIGURE 5.1.: Generic example of the one-dimensional RP-r.k. $q_1^{n,m}(R_i^s, R^s)$ according to Eq. (5.5) for $R_i \approx 4.5 \text{ \AA}$. The RP-RKHS hyperparameters n , m and s where chosen to represent the case discussed in Sec. 5.2 with $n = 3$ and $m = 2$, while the power $s = 2$ is introduced for later reference. The functional behavior for $R \geq R_i$ was deduced from the beta function $B(a, b)$ and the special case of the Gaussian hypergeometric function ${}_2F_1$ given in Appendix E.3. The interpolation behavior for $R < R_i$ (area highlighted in gray) is merely polynomial $\propto R^4$, while for $R > R_i$ it shows the correct reciprocal power decay.

with $R_{ij}; (i, j) \in \{1, 2, 3\}$ denoting the internuclear distances. The dimer and trimer interaction energies V_{X_2} and V_{X_3} , respectively, are obtained from *ab-initio* calculations relative to the non-interacting limits (i.e. $2 \cdot X$ or $3 \cdot X$) and are used to extract the nonadditive energies V_3 . The following outlines how the individual terms of Eq. (5.7) are efficiently interpolated using the RP-RKHS method based on Eq. (5.5).

5.1.1 | Additive two-body part

The subsequent derivation follows Ref. [294]

Motivated by the representer theorem (cf. Eq. (5.1)) the optimal interpolation ansatz for the diatomic PEC V_{X_2} given N internuclear distances R_i may be

$$V_{X_2}(R) = \sum_{i=1}^N \alpha_i q_1^{n,m}(R_i^s, R^s), \quad (5.8)$$

where $s > 0$ is a power introduced for later reference. From Eq. (5.5) and (5.8) one may

obtain the behavior at large distances

$$V(R) = - \sum_{k=0}^{n-1} \frac{C_{s(k+m+1)}}{R^{s(k+m+1)}}, \quad R > R_N > R_{N-1} > \dots > R_2 > R_1. \quad (5.9)$$

Here, the individual n leading inverse power dispersion interactions $V_{s(k+m+1)}^{\text{disp}}(R)$ at an asymptotic distance beyond the last *ab-initio* point $R > R_N$ take on the form

$$\begin{aligned} V_{s(k+m+1)}^{\text{disp}} &= - \frac{C_{s(k+m+1)}}{R^{s(k+m+1)}} \\ &= \frac{A_{nmk}}{R^{s(k+m+1)}} \sum_{i=1}^N \alpha_i R_i^{sk}, \quad k = 0, 1, \dots, n-1, \end{aligned} \quad (5.10)$$

where the constant A_{nmk} is given as

$$A_{nmk} = n^2 B(n, m+1) \frac{(-n+1)_k (m+1)_k}{(n+m+1)_k k!}, \quad (5.11)$$

and the notation $(a)_k$ denotes the (rising) Pochhammer's symbol (see Appendix E.3). This allows for the formulation of a constrained construction procedure that provides accurate long-range interactions by incorporating (high-level) theoretically calculated or experimentally determined values of dispersion coefficients into the interpolation protocol to obtain the expansion coefficients α_i of Eq. (5.8).

Given $N - n$ *ab-initio* energies $V(R_i)$ at distances R_1, \dots, R_{N-n} and n leading dispersion coefficients $C_{s(m+1)}, \dots, C_{s(m+n)}$ one may derive, using Eqs. (5.8) and (5.10), the linear system

$$\sum_{j=1}^N (\Gamma_{ij}^{(s)} + \lambda_{1D} \delta_{ij}) \alpha_j = \beta_i, \quad i = 1, \dots, N. \quad (5.12)$$

Here, $\Gamma_{ij}^{(s)}$ denote the matrix elements of the $N \times N$ positive (semi-) definite symmetric kernel matrix $\Gamma^{(s)}$ defined as

$$\Gamma_{ij}^{(s)} = \begin{cases} q_1^{n,m}(R_i^s, R_j^s) & \text{for } i = 1, \dots, N' = N - n \\ \frac{A_{nmk} R_j^{sk}}{R_a^{s(k+m+1)}} & \text{for } i = N' + 1 + k, k = 0, \dots, n-1 \end{cases} \quad (5.13)$$

and β_i are the elements of the training vector β , given as

$$\beta_i = \begin{cases} V(R_i) & \text{for } i = 1, \dots, N' = N - n \\ V_{s(k+m+1)}^{\text{disp}}(R_a) & \text{for } i = N' + 1 + k, k = 0, \dots, n-1. \end{cases} \quad (5.14)$$

The fixed value R_a should be chosen such that all dispersion terms are within two or three orders-of-magnitude of each other to ensure that they enter in a balanced fashion; i.e. R_a is not necessarily at large distance. The solution of Eq. (5.12) yields the expansion coefficients α_i and requires $R_1 < \dots < R_{N-n} < R_{N-n+1} < \dots < R_N$ internuclear distances. The last n distances are required to delimit the asymptotic region and to provide the same number of input values and unknown expansion coefficients α_i . Furthermore, due to potential data and machine roundoff errors the solution of Eq. (5.12) is subject to Tikhonov's regularization procedure as given in Eq. (5.4) with the corresponding regularization parameter λ_{1D} .

Apparently, this approach effectively alleviates the dependence of the long-range tail of the PEC on *ab-initio* data, while simultaneously retaining the globally smooth interpolatory quality at the short- and intermediate-range of internuclear distances R . As such, this method imposes by construction the correct long-range physics.

5.1.2 | Nonadditive three-body part

The subsequent derivation follows Refs. [100, 103, 105, 107, 296]

The construction of a proper three-dimensional kernel function for the nonadditive three-body part of Eq. (5.7) is based on the property of RKHSs that a product of reproducing kernels is still a r.k. (cf. Appendix E.1). Hence, the 3D (symmetric) r.k. $Q(\mathbf{R}, \mathbf{R}')$ can be written as a product of the one-dimensional (symmetric) kernels $q_1^{n,m}$ according to Eq. (5.5), yielding

$$Q^{n,m}(\mathbf{R}, \mathbf{R}') = q_1^{n,m}(x, x')q_1^{n,m}(y, y')q_1^{n,m}(z, z'). \quad (5.15)$$

Furthermore, for X_3 systems one needs to account for the underlying permutational symmetry of the three identical nuclei X . Given M configurations of the X_3 system, the interpolation ansatz for the nonadditive three-body term may be expressed as

$$V_3(\mathbf{R}) = \sum_{i=1}^M \gamma_i \left\{ \frac{1}{3!} \sum_{\{123\}} \mathcal{P}_{\{123\}}^i Q^{n,m}(\mathbf{R}_i, \mathbf{R}) \right\}, \quad (5.16)$$

as suggested by the representer theorem (5.1). For numerical reasons it is convenient to introduce reduced internuclear distances

$$x = (R_{12}/S)^s, \quad y = (R_{23}/S)^s, \quad z = (R_{13}/S)^s, \quad (5.17)$$

with an arbitrary scaling factor S and a power $s > 0$, to keep the expansion coefficients γ_i small. The permutation operator $\mathcal{P}_{\{123\}}^i$ renders V_3 symmetric with respect to the

exchange of any two atoms, while the summation over the subscript $\{123\}$ is performed over all $3!$ symmetry permutations of the trimer bond lengths associated with the ij -th data point on the PES. Given M nonadditive energies $V_3(\mathbf{R}_i)$ at configurations $\mathbf{R}_i = (R_{12}^i, R_{23}^i, R_{13}^i)^T$ obtained from *ab-initio* calculations, the expansion coefficients γ_i are obtained by solving the linear system

$$V_3(\mathbf{R}_i) = \sum_{j=1}^M \underbrace{\left[\frac{1}{3!} \sum_{\{123\}} \mathcal{P}_{\{123\}}^i Q^{n,m}(\mathbf{R}_i, \mathbf{R}_j) \right]}_{\Xi_{ij}} \gamma_j + \lambda_{3D} \delta_{ij} \gamma_j. \quad (5.18)$$

Due to large and densely clustered or numerically noisy data sets, the (symmetric) kernel matrix Ξ might be ill-conditioned. Therefore, the solution of Eq. (5.18) is subject to Tikhonov's regularization method according to Eq. (5.4), with corresponding parameter λ_{3D} .

To use the resulting PES after Eq. (5.7) in low-energy scattering calculations it has to show the physically correct long-range behavior. By construction this is always fulfilled for the one-dimensional interaction potentials V_{X_2} . From Eqs. (5.15) and (5.6) it follows that the V_3 potential extrapolates as $R_{12}^{-(m+1)} R_{23}^{-(m+1)} R_{13}^{-(m+1)}$ in the long-range region. However, the leading contributions in the asymptotic expansion of the nonadditive energy are the third-order dipole-dipole-dipole (DDD) and dipole-dipole-quadrupole (DDQ) terms given by [100, 103, 105]

$$V_3^{\text{DDD}} = 3Z_{111}^{(3)} \frac{1 + 3 \cos \phi_3 \cos \phi_1 \cos \phi_2}{R_{12}^3 R_{23}^3 R_{13}^3}, \quad (5.19)$$

which is also known as the Axilrod-Teller potential [298], and

$$V_3^{\text{DDQ}} = Z_{112}^{(3)} \left(W^{123} + W^{231} + W^{312} \right), \quad (5.20)$$

where

$$W^{ijk} = \frac{3}{16R_{jk}^4 R_{ik}^4 R_{ij}^3} \left[9 \cos \phi_k - 25 \cos 3\phi_k + 6 \cos(\phi_i - \phi_j) \cdot (3 + 5 \cos 2\phi_k) \right], \quad (5.21)$$

and ϕ_i is the bond angle at atom i [299]. This shows that an isotropic interpolation approach according to Eq. (5.18) is clearly incorrect in the long-range. Therefore, it is best to first transform V_3 to a form that behaves as a simple product of inverse powers at large internuclear distances and then interpolate in that form [105]. This starts with first subtracting out V_3^{DDD} and V_3^{DDQ} according to

$$V_3' = V_3 - f_{\text{damp}} \left[V_3^{\text{DDD}} + V_3^{\text{DDQ}} \right], \quad (5.22)$$

with the damping function $f_{\text{damp}}(R_{12}, R_{23}, R_{13}) = f(R_{12})f(R_{23})f(R_{13})$ preventing the nonadditive energy from diverging at short-range, where

$$f(R) = \begin{cases} \exp [-(k_3/R - 1)^2] & 0 < R < k_3 \\ 1 & r \geq k_3 \end{cases}, \quad (5.23)$$

with the cut-off parameter k_3 . The dispersion coefficients $Z_{111}^{(3)}$ and $Z_{112}^{(3)}$ are known for all homonuclear alkali-metal atom systems and may be found in Refs. [100, 300, 301]. The leading term of the asymptotic multipole expansion of V_3' is the fourth-order dipole-dipole-dipole-dipole (DDDD) term [100, 302]

$$V_3^{\text{DDDD}} = -\frac{45}{64} Z_{111}^{(3)} \left[\frac{1 + \cos^2 \phi_1}{R_{12}^6 R_{13}^6} + \frac{1 + \cos^2 \phi_2}{R_{12}^6 R_{23}^6} + \frac{1 + \cos^2 \phi_3}{R_{13}^6 R_{23}^6} \right], \quad (5.24)$$

which is apparently unfactorizable. If $Z_{111}^{(3)}$ were known, this contribution could be subtracted out as well. Since V_3^{DDDD} is negative at all geometries a sufficient approach is to simply modify it for isotropic interpolation by defining $V_3'' = g \cdot V_3'$, with

$$g(\mathbf{R}) = \frac{R_{12}^3 R_{23}^3 R_{13}^3}{(1 + \cos^2 \phi_1) R_{23}^6 + (1 + \cos^2 \phi_2) R_{13}^6 + (1 + \cos^2 \phi_3) R_{12}^6}. \quad (5.25)$$

The resulting V_3'' term now reveals the simple asymptotic form $\propto R_{12}^{-3} R_{23}^{-3} R_{13}^{-3}$ and is thus suitable for using the fully symmetrized 3D RP-RKHS interpolation procedure according to Eq. (5.18). The original three-body nonadditive part is rebuilt afterwards as

$$V_3^{\text{mult}} = \frac{1}{g(\mathbf{R})} V_3'' + f_{\text{damp}} \left[V_3^{\text{DDD}} + V_3^{\text{DDQ}} \right]. \quad (5.26)$$

5.2 | Proof of concept for Rb₂

The power of the RP-RKHS method may be revealed by first studying the additive contributions to Eq. (5.7). To obtain a highly accurate quartet ground state PES of Rb₃, the corresponding dimer potential V_{Rb_2} has to be the $a^3\Sigma_u$ state. The leading long-range behavior of this state is given by [105, 259]

$$V_{\text{LR}}(R) = -\frac{C_6}{R^6} - \frac{C_8}{R^8} - \frac{C_{10}}{R^{10}}, \quad (5.27)$$

with the dispersion coefficients $C_6 = 0.227003 \cdot 10^8 \text{ cm}^{-1} \text{ \AA}^6$, $C_8 = 0.778289 \cdot 10^9 \text{ cm}^{-1} \text{ \AA}^8$ and $C_{10} = 0.286887 \cdot 10^{11} \text{ cm}^{-1} \text{ \AA}^{10}$ from Ref. [259]. This functional form requires the free RP-RKHS parameters n, m, s in Eqs. (5.8) to (5.14) to become

$$n_{1D} = 3 \quad \text{and} \quad m_{1D} = 2 \quad \text{and} \quad s_{1D} = 2, \quad (5.28)$$

and defines how the dimer potential energy is extrapolated beyond the last *ab-initio* point included into the RP-RKHS procedure. The PEC construction for the $a^3\Sigma_u$ state of Rb₂ first uses *ab-initio* data obtained at the MRCI(lcECP+CPP)/UET15 level of theory (cf. Chap. 4). It is important to include a sufficient amount of *ab-initio* data at small internuclear distances to avoid extrapolation in this region [294, 303] due to the merely polynomial behavior of the RP-r.k. $q_1^{n,m}(R_i^s, R^s)$ in the short-range, as indicated in Fig. 5.1. The interpolation procedure performed best if it was based on $N - n_{1D} = 29$ *ab-initio* interaction energies (training data); cf. Sec. 5.1.1. Since the kernel matrix $\Gamma^{(s)}$ is low-dimensional and the underlying training data were carefully selected it is sufficient to assume that the main source of error comes from machine roundoff errors. Hence, the regularization parameter in Eq. (5.12) is set to $\lambda_{1D} = \varepsilon \cdot \sigma_1$, with ε and σ_1 being the unit machine roundoff ($\propto 10^{-16}$ for double precision) and the largest singular value of the kernel matrix $\Gamma^{(s)}$ [291, 294]. The resulting order of magnitude is $\mathcal{O}(10^{-21})$ and thus the interpolation is effectively exact. Furthermore, the parameter R_a entering Eqs. (5.13) and (5.14) was chosen such that the RP-RKHS dispersion coefficients obtained after Eq. (5.10) show optimal agreement with the ones following from experiment after Ref. [259], yielding $R_a = 18.0 a_0$. The quality of the RP-RKHS interpolated/extrapolated PEC V_{Rb_2} according to Eq. (5.8) is illustrated in Fig. 5.2. Due to the vanishingly small regularization parameter λ_{1D} of order 10^{-21} , the RP-RKHS potential V_{Rb_2} reproduces the training data virtually exact. This can be also observed from the respective energy differences in Fig. 5.2 (b). Beyond the last *ab-initio* point the potential energy is extrapolated to the form of Eq. (5.27) yielding the physically correct long-range behavior V_{LR} , which is also illustrated in Fig. 5.2 (b). The above mentioned importance of including a sufficient amount of *ab-initio* data in the short-range is indicated in Fig. 5.2 (b). As the RP-r.k. is not designed for extrapolation in the short-range region, the differences corresponding to data not included in the training set become larger. Nevertheless, measuring the interpolative quality in terms of the root-mean square deviation (RMSD) with respect to those *ab-initio* data shown in Fig. 5.2 (a) that yield relative energies $< 0.0 \text{ cm}^{-1}$ give $\text{RMSD}_{<0} = 0.00345 \text{ cm}^{-1}$, while those with interaction energies $< 15000.0 \text{ cm}^{-1}$ lead to $\text{RMSD}_{<15000} = 1.909 \text{ cm}^{-1}$. This demonstrates that the major error contribution comes from the short-range. A close-up

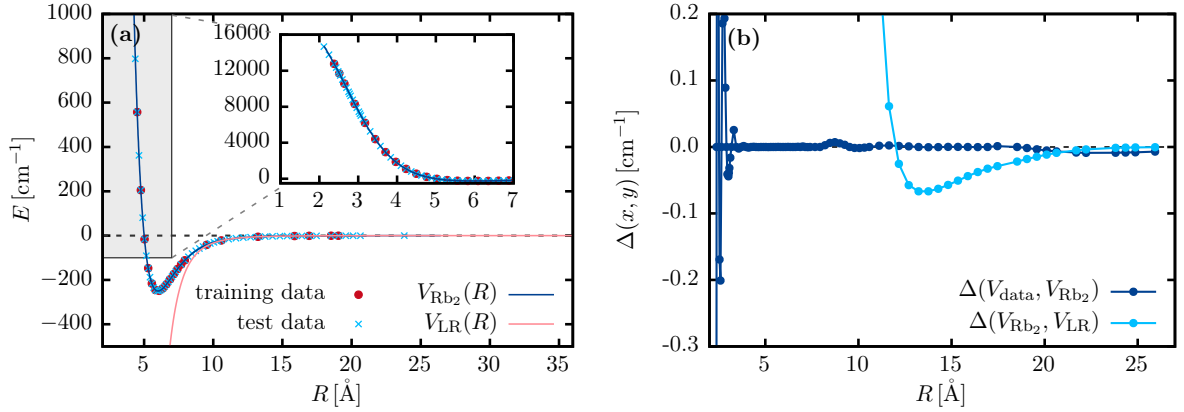


FIGURE 5.2.: Demonstration of the interpolatory quality of the RP-RKHS method for the $a^3\Sigma_u$ PEC of Rb_2 . The underlying *ab-initio* (training) data were calculated at MRCI(lcECP+CPP)/UET15 level of theory. **(a)** The RP-RKHS PEC $V_{\text{Rb}_2}(R)$ according to Eq. (5.8) based on 29 training data (see text for details). Beyond the last *ab-initio* point the PEC is extrapolated to the long-range form of Eq. (5.10). The inset shows a close-up of the short-range wall and reveals the limitations of the lcECP+CPP approach (see text). **(b)** The full *ab-initio* set V_{data} is very well reproduced as shown by the respective differences (dark blue line). Computing the root-mean square deviation with respect to those *ab-initio* data yielding relative energies $< 0.0 \text{ cm}^{-1}$ give $\text{RMSD}_{<0} = 0.00345 \text{ cm}^{-1}$, while those with interaction energies $< 15000.0 \text{ cm}^{-1}$ lead to $\text{RMSD}_{<15000} = 1.909 \text{ cm}^{-1}$. Only in the short-range region the deviations become larger as the RP-r.k. scales only polynomially in this area. The light blue curve displays the deviation of the RP-RKHS PEC from the true long-range potential according to Eq. (5.27).

view of the short-range region as displayed by the inset of Fig. 5.2 (a) reveals that the *ab-initio* data fail to describe the physically expected repulsive $1/R$ Coulomb wall caused by the nuclei. The saturation behavior which would lead to the transition to a short-range plateau is clearly unphysical and might be caused by the underlying lcECP+CPP approach which reaches its limits due to an insufficient description of the repulsion of the core electrons and the repulsion between the nuclei in general.

The following discussion will thus use the small-core ECP developed in Ref. [250], which widely accounts for the repulsive interaction of the core electrons. Furthermore, studying scattering events in the ultracold regime requires very precise PESs suggesting to improve the level of theory. Therefore, the UET15 basis set has been enlarged according to the approach as described in Sec. 4.2. The resulting uncontracted even-tempered basis set UET17 allows to systematically increase the cardinality from $X = 4$ to $X = 6$; see Appendix F.1 and Tab. F.1. Moreover, the computational method was changed to the RHF-UCCSD(T) approach. Highly precise results usually also require to estimate the complete basis set (CBS) limit. It was found that using the largest basis set [UET17($X = 6$)] for the Hartree-Fock reference energy and for the singles

TABLE 5.1.: Overview on the spectroscopic constants D_e and R_e of the $a^3\Sigma_u$ state of Rb₂ obtained from the 1D RP-RKHS interpolation based on *ab-initio* dimer interaction energies calculated at RHF-UCCSD(T)/ECP28MDF/UET17 level of theory with increasing basis set size. The CBS values were obtained from Eq. (5.29) with the pair energy and triples energy correlation contributions extrapolated according to the conventional two-point extrapolation formula (5.30). The CBS $_{\zeta}$ values used an approach based on the Riemann- ζ function, which has been recently proposed in Ref. [304]. Results based on the MRCI(lcECP+CPP)/UET15 approach, with UET15 from Tab. C.1, are given for comparison. The experimental values are $D_e^{\text{exp}} = 241.5045 \text{ cm}^{-1}$ and $R_e^{\text{exp}} = 6.0650 \text{ \AA}$ and were taken from Ref. [305].

basis set size	$D_e [\text{cm}^{-1}]$	$R_e [\text{\AA}]$
UET17($X = 4$)	239.0766	6.0809
UET17($X = 5$)	241.0339	6.0689
UET17($X = 6$)	241.8987	6.0661
UET17(CBS)	242.2874	6.0624
UET17(CBS $_{\zeta}$)	242.3365	6.0619
MRCI(lcECP+CPP)/UET15	249.9099	6.0063

contribution to the UCCSD(T) correlation energy, while extrapolating the remaining contributions to their respective CBS limit, provides the most promising results. The total RHF-UCCSD(T) energy at the CBS limit is thus approximated via

$$E_{\text{UCCSD(T)}}^{\infty} \approx E_{\text{RHF}}(X = 6) + E_{\text{singles}}(X = 6) + E_{\text{pair}}^{\infty} + E_{\text{(T)}}^{\infty}. \quad (5.29)$$

The CBS values (E_i^{∞}) for the pair and perturbative triples contribution to the correlation energy were either obtained from the conventional two-point extrapolation formula [238, 239]

$$E_i(X) = E_i^{\infty} + \frac{A}{X^3}, \quad (5.30)$$

or by applying an approach based on the Riemann- ζ function (CBS $_{\zeta}$), as proposed recently in Ref. [304].

Table 5.1 gives an overview on the spectroscopic constants D_e and R_e following from PECs obtained using the RP-RKHS method with underlying dimer interaction energies calculated at the RHF-UCCSD(T)/ECP28MDF/UET17 level of theory with increasing basis set size. The corresponding interpolative quality was again assessed by RMSDs which are of the same magnitude as the $\text{RMSD}_{<0}$ and $\text{RMSD}_{<15000}$ values as given above. Again, major error contributions can be assigned to the region with $R < 4.5 \text{ \AA}$, which is already high-up the repulsive short-range wall. In addition, the

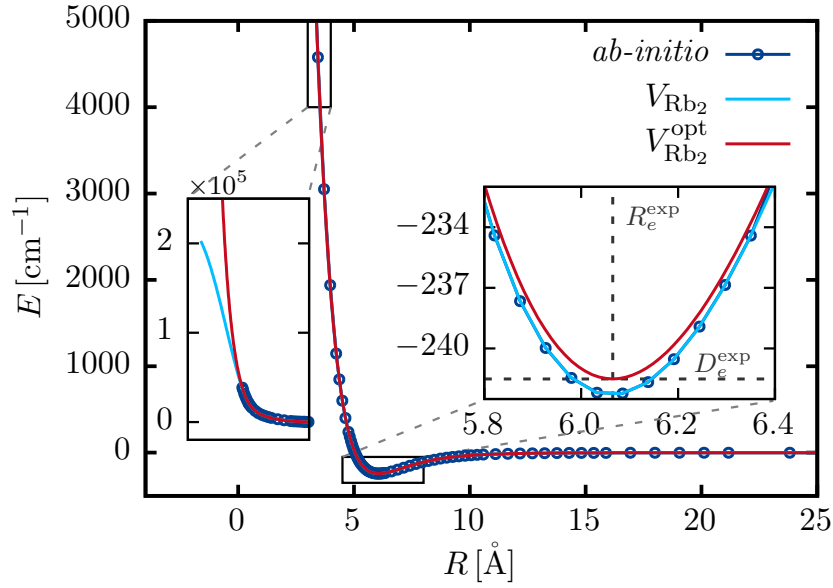


FIGURE 5.3.: Illustration of the modified RP-RKHS construction procedure according to Eq. (5.32) to obtain a highly accurate PEC for the $a^3\Sigma_u$ state of Rb_2 . The underlying *ab-initio* data were generated at RHF-UCCSD(T)/ECP28MDF/UET17(CBS) level of theory with extrapolation to the CBS limit after Eq. (5.29). The inset shown on the left reveals that the resulting RP-RKHS interpolated PEC becomes defective high-up the repulsive short-range wall due to the insufficient extrapolation behavior of the RP-r.k. for small internuclear distances [102]. The introduction of a short-range correction according to Eq. (5.31) with the *ab-initio* data shifted and scaled so that the experimentally derived values for D_e and R_e from Ref. [305] are reproduced yields a highly accurate and physically meaningful PEC.

CBS *ab-initio* data and the resulting interpolated PEC V_{Rb_2} are visualized in Fig. 5.3. The *ab-initio* data do not show a saturation behavior in the short-range as observed for the MRCI(lcECP+CPP) approach but the corresponding RP-RKHS interpolated PEC still becomes defective high up the repulsive short-range wall. This is indicated by the left inset in Fig. 5.3 and can be assigned to the insufficient extrapolation behavior of the RP-RKHS method in the short-range region [303]. To ensure a correct description of the repulsive part, which is also important for scattering calculations, one may employ a short-range correction according to

$$V_{\text{SR}}(R) = \frac{a}{R} e^{-bR}, \quad (5.31)$$

with the parameters a and b obtained from least-squares fits to the CBS *ab-initio* data in the range $[4.5, 5.25] a_0$, yielding $a = 31.8214$ and $b = 0.89515$. Inspired by the approach of Soldán [100], one may furthermore scale and shift the *ab-initio* interaction energies and internuclear distances so that the resulting PEC yields the experimentally derived values for D_e and R_e from Ref. [305]. These spectroscopic constants were in other

works [306, 307] referred to as the most accurate ones. To this end, one may first transform the *ab-initio* data according to

$$\tilde{V}_{\text{Rb}_2}^{ab-initio} = \kappa_e V_{\text{Rb}_2}^{ab-initio}(R - R_s) - V_{\text{SR}}(R - R_s), \quad (5.32)$$

with κ_e and R_s derived from the UET17(CBS) values of Tab. 5.1 to yield $D_e^{\text{exp}} = 241.5041 \text{ cm}^{-1}$ and $R_e^{\text{exp}} = 6.0650 \text{ \AA}$, respectively

$$\kappa_e = \frac{241.5041 \text{ cm}^{-1}}{242.2874 \text{ cm}^{-1}} = 0.99677 \quad \text{and} \quad R_s = \frac{(6.0650 - 6.0624) \text{ \AA}}{0.529177} = 0.00491 a_0. \quad (5.33)$$

The transformed *ab-initio* interaction energies $\tilde{V}_{\text{Rb}_2}^{ab-initio}$ are then interpolated using the RP-RKHS method with the parameters from Eq. (5.28), yielding \tilde{V}_{Rb_2} . Finally, the optimized dimer potential $V_{\text{Rb}_2}^{\text{opt}}$ is rebuilt via

$$V_{\text{Rb}_2}^{\text{opt}} = \tilde{V}_{\text{Rb}_2}(R) + V_{\text{SR}}(R), \quad (5.34)$$

where shifted internuclear distances $R_{i,s} = R_i + R_s$ have to be used in $\tilde{V}_{\text{Rb}_2}(R)$ as defined via Eq. (5.8). This shifted, scaled and short-range-corrected PEC $V_{\text{Rb}_2}^{\text{opt}}$ is illustrated in Fig. 5.3 and serves as foundation for the high-accuracy PES construction for the quartet ground state of Rb₃ as discussed below. A more detailed insight to its accuracy is outlined in Appendix F.3 by a comparison of computed vibrational energy levels with experimentally measured term values. Appendix F.3 further shows the effect of shifting and scaling the *ab-initio* data as compared to merely applying the short-range correction.

5.3 | A high-quality Rb₃ quartet ground state PES

The previously discussed problems connected with the MRCI(lcECP+CPP) approach suggest to also use the RHF-UCCSD(T)/ECP28MDF method for highly accurate calculations of quartet ground state energies of Rb₃. However, using the previously introduced UET17 basis set causes linear dependencies in the corresponding trimer calculations. Therefore, a slightly modified version of the UET15 basis set introduced in Sec. 4.2 is used. Here, the existing exponents are augmented by one additional *g* function; *h*- and *i*-functions are generated according to Eq. (4.4), thus allowing to systematically increase the cardinality from UET15($X = 4$) to UET15($X = 6$). The corresponding exponents are listed in Tab. C.2. In this way, 759 trimer interaction energies V_{Rb_3} of the 1^4B_1 quartet ground state manifold of Rb₃ (using the C_{2v} nomenclature from Chap. 4) were calculated on a 3D grid of perimetric coordinates to ensure

that each generated configuration satisfies the triangular inequality. The resulting configurations cover a range of internuclear distances from 4.5 to 36.0 a_0 where R_{23} was pruned to $R_{23} \leq 30.0 a_0$.

From the trimer interaction energies at RHF-UCCSD(T)/ECP28MDF/UET15 level of theory, the nonadditive energies V_3 were extracted from the many-body decomposition according to Eq. (5.7). Note that this approach is only valid if the nonadditive forces do not dwarf the additive ones [102, 107], which is fulfilled for the quartet ground state of Rb_3 , as shown in Appendix D.7. In general, for spin-polarized alkali-metal trimers, the nonadditive terms make substantial contributions to the PESs and are most important in the vicinity of the D_{3h} minimum where they are attractive; cf. Figs. 5.4 and D.6. Thus, the corresponding bond lengths are significantly shorter as compared to the respective triplet dimers and trimer potentials are all deeper than pairwise sums of dimer potentials. The physical explanation for this behavior may be found in Refs. [102, 107]. Here suffice it to say that accounting for V_3 is important if the resulting trimer potential is to be capable of representing all the properties of experimental interest (atom-atom scattering lengths, dimer and trimer bound states, atom-diatom collisions and three-body recombination). This moreover requires that the potential should dissociate properly into all possible sets of products (atom+diatom and three separated atoms) with the correct long-range behavior. In this regard, the nonadditive dispersion forces are important at long-range but show comparatively small contributions around the trimer potential minimum.

After manipulating the extracted nonadditive energies to obtain the correct long-range behavior according to the procedure described in Sec. 5.1.2, the resulting V_3'' points were then interpolated using the 3D RP-RKHS method with respect to the reduced internuclear distances of Eq. (5.17), suggesting the parameters in Eqs. (5.15) to (5.18)

$$n_{3D} = 2 \quad \text{and} \quad m_{3D} = 0 \quad \text{and} \quad s_{3D} = 3 \quad \text{and} \quad S = 10.0 a_0. \quad (5.35)$$

The cutoff parameter entering the damping function in Eq. (5.23) was chosen as $k_3 = 18.0 a_0$. The three-body dispersion coefficients corresponding to the triple-dipole V_3^{DDD} [cf. Eq. (5.19)] and dipole-dipole-quadrupole V_3^{DDQ} [cf. Eq. (5.20)] terms were taken from Refs. [100, 300, 301] with $Z_{111}^{(3)} = 3.543 \cdot 10^5 E_h a_0^9$ and $Z_{112}^{(3)} = 7.750 \cdot 10^6 E_h a_0^{11}$. Again, assuming that the main source of instability comes from machine roundoff errors (which may be a good approximation for data resulting from *ab-initio* calculations) the regularization parameter in Eq. (5.18) was set to $\lambda_{3D} = 10^{-16} \cdot \tilde{\sigma}_1$, with $\tilde{\sigma}_1$ the largest singular value of the kernel matrix Ξ , yielding $\lambda_{3D} \propto 10^{-12}$.

TABLE 5.2.: Overview of the Rb₃ quartet ground state equilibrium configuration and energy obtained from the RP-RKHS approach using different UET15 basis set sizes (cf. Tab. C.2) for the RHF-UCCSD(T)/-ECP28MDF calculations of respective *ab-initio* trimer interaction energies yielding the nonadditive energies V_3 according to Eq. (5.7). The corresponding dimer interaction potential was constructed based on RHF-UCCSD(T)/ECP28MDF/UET17(CBS) *ab-initio* data employing short-range extrapolation but no scaling and shifting to match experimental results as outlined previously. The results following from Chap. 4 are given for comparison as well as the values reported by Soldán.

basis set size (V_3)	$\mathbf{R}_{\text{eq}} = (R_{12}^{\text{eq}}, R_{23}^{\text{eq}}, R_{13}^{\text{eq}})$ [Å]	$V_{\text{trimer}}(\mathbf{R}_{\text{eq}})$ [cm ⁻¹]
UET15($X = 5$)	5.4048,5.4048,5.4048	-1141.7070
UET15($X = 6$)	5.4047,5.4047,5.4047	-1141.9265
UET15(CBS)	5.4046,5.4046,5.4046	-1141.9265
MRCI(lcECP+CPP)/UET15 [cf. Tab. 4.4]	5.3110,5.3110,5.3110	-1244
Soldán [100]	5.5000,5.5000,5.5000	-1105

The dependence of the outlined approach on the UET15 basis set size used for the calculation of trimer interaction energies is summarized in Tab. 5.2. The CBS extrapolation follows the ansatz given in Eqs. (5.29) and (5.30) and thus only the UET15($X = 5$) and UET15($X = 6$) results were considered. A detailed insight into this basis set dependence of V_3 is provided by Fig. 5.4 (a) in terms of a one-dimensional scan along D_{3h} geometries. The cuts of the nonadditive energy functions V_3 show the expected attractive behavior around the equilibrium geometry of the quartet ground state (≈ 5.0 Å; cf. Tab. 4.4) as discussed previously. For larger bond distances one obtains a small repulsive barrier due to the character of the Axilrod-Teller triple-dipole potential after Eq. (5.19) defining the leading long-range behavior (together with the V_3^{DDQ} term). However, a close-up of this region shows that due to intersections of the UET15($X = 5$) and UET15($X = 6$) curves, the CBS extrapolation leads to unphysical oscillations in the corresponding curve. This would be clearly undesirable for quantum dynamics calculations, which require smooth potential-energy functions without oscillations between *ab-initio* data. The negligible changes obtained for the equilibrium energies and geometries of the Rb₃ quartet ground state when using a UET15($X = 6$) or UET15(CBS) approach (cf. Tab. 5.2), thus suggest to base the 3D RP-RKHS interpolation on UET15($X = 6$) nonadditive energies.

Beyond that, by different C_{2v} scans Fig. 5.4 (b) reveals that for certain cuts through the nonadditive energy landscape one obtains an unphysical short-range behavior with $V_3 \rightarrow -\infty$, which consequently spoils the complete trimer interaction energy and thus

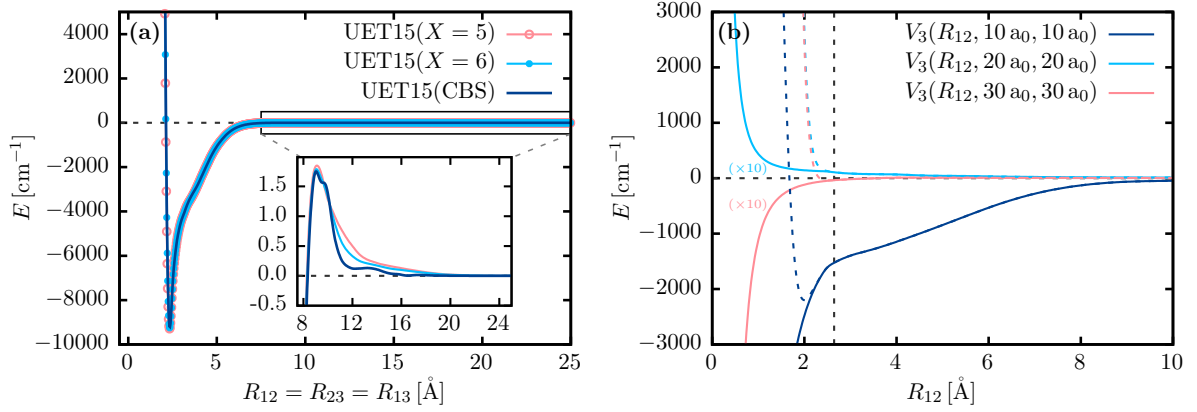


FIGURE 5.4.: **(a)** One-dimensional scan along D_{3h} geometries for the nonadditive energy function V_3 obtained from the 3D RP-RKHS interpolation procedure as described in Sec. 5.1.2. The underlying trimer interaction energies to extract the *ab-initio* V_3 energies were computed at RHF-UCCSD(T)/ECP28MDF/UET15 level of theory with increasing basis set sizes and the CBS values obtained from Eq. (5.29). The oscillatory behavior of the UET15(CBS) curve is due to intersections between the UET15($X = 5$) and UET15($X = 6$) curves. **(b)** C_{2v} scans for the RP-RKHS interpolated V_3 function along the internuclear coordinate R_{12} . For some configurations the nonadditive energy reveals an unphysical behavior in the short-range with $V_3 \rightarrow -\infty$ spoiling the complete trimer interaction energy and thus subsequent scattering calculations (see text for details). This motivates to introduce a short-range correction according to Eqs. (5.36) and (5.37) to render physically correct functions. The resulting V_3^* curves are indicated by dashed lines.

subsequent scattering calculations. This could be due to the attractive nature around equilateral geometries so that the RP-RKHS method “learns” the wrong behavior for short internuclear distances, which are not covered by the training set. Furthermore, in the very short-range the many-body decomposition of Eq. (5.7) would represent V_3 as the difference between two large quantities, which is certainly not a good approximation. To ensure the physically correct short-range behavior one may modify the interpolated V_3 functions as follows [308]

$$V_3^*(R_{12}, R_{23}, R_{13}) = \alpha [h(R_{12}/R_0) + h(R_{23}/R_0) + h(R_{13}/R_0)] + [g(R_{12}/R_0)g(R_{23}/R_0)g(R_{13}/R_0)] V_3(R_{12}, R_{23}, R_{13}) \quad (5.36)$$

where the parameters α and R_0 are *a priori* free parameters and may eventually be adjusted so to match experimental findings. The cutoff functions are defined as

$$h(R_{ij}/R_0) = \left[1 - \tanh(2R_{ij}/R_0) \right]^{12}, \quad (5.37a)$$

$$g(R_{ij}/R_0) = 1 - h(R_{ij}/R_0). \quad (5.37b)$$

Note that the damping function according to Eq. (5.23) only controls the effect of the leading long-range terms V_3^{DDD} and V_3^{DDQ} to the full nonadditive energy. Generic cases of the short-range-corrected nonadditive energy function V_3^* are shown in Fig. 5.4 for $R_0 = 5.0 a_0$ and $\alpha = 0.1$ a.u..

The final trimer PES is constructed according to

$$V_{\text{Rb}_3}^{\text{opt}}(R_{12}, R_{23}, R_{13}) = \sum_{i<j} V_{\text{Rb}_2}^{\text{opt}}(R_{ij}) + V_3^*(R_{12}, R_{23}, R_{13}), \quad (5.38)$$

with the dimer potentials according to Eq. (5.34) obtained at UET17(CBS) level of theory and the short-range corrected nonadditive contribution V_3^* following from an approach according to Eq. (5.26) based on UET15($X = 6$) *ab-initio* calculations. Both parts used the RHF-UCCSD(T)/ECP28MDF method. This, yields the following quartet ground state equilateral triangular equilibrium

$$\mathbf{R}_{\text{eq}}^{\text{opt}} = (5.4067, 5.4067, 5.4067) \text{ \AA} \quad \text{and} \quad V_{\text{Rb}_3}^{\text{opt}}(\mathbf{R}_{\text{eq}}^{\text{opt}}) = -1137.97569 \text{ cm}^{-1}. \quad (5.39)$$

Technical remarks

The discussion of this chapter may be supported by the following technical remarks:

- *The CBS extrapolation for the Rb₂ parts with the UET17 basis set family and for the nonadditive contribution V_3 based on the UET15 basis set series both follow the ansatz given in Eqs. (5.29) and (5.30) and thus avoids an $\exp(-bX)$ -ansatz for the E_{RHF} and E_{singles} part as suggested in Ref. [236]. If this approach were used it would have led to even more overestimated/underestimated spectroscopic constants of Rb₂ (cf. Tab. 5.1) and to even more pronounced oscillations in the long-range part of V_3 as shown in Fig. 5.4*
- *The RP-RKHS interpolation procedures for both the additive parts V_{Rb_2} and the nonadditive part V_3 (in terms of interaction energies) used atomic units for numerical convenience. Thus the resulting data shown in Figs. 5.1 to 5.4 and provided in Tabs. 5.1 and 5.2 were scaled afterwards to use consistent units (\AA and cm^{-1}) throughout this thesis. According to Eq. (5.7) interaction energies were committed to the RP-RKHS method*
- *The calculations of the Rb₃ quartet ground state energies at RHF-UCCSD(T)/ECP28MDF/UET15 level of theory have been performed on the JUSTUS 2 cluster*
- *This chapter uses the notation X when referring to the cardinality of the UET15 and*

UET17 basis sets to clearly distinguish from the RP-RKHS parameter n introduced in Sec. 5.1. The remaining parts of this thesis however use n to label the cardinal number

The RP-RKHS interpolation method as described in this chapter was implemented in PYTHON and FORTRAN [309] and thus globally smooth and physically meaningful PESs can be routinely generated. This allows for interfacing with codes designed for studying ultracold collisions. Preliminary calculations of $\text{Rb}_2 + \text{Rb}$ collisional processes based on the Rb_3 quartet ground-state PES of this work revealed interesting insights into the dynamics of the system. Further investigations will be devoted to these aspects and may be published in the future.

Part III

HIGH-ACCURACY *ab-initio* CALCULATIONS FOR Rb_2^+

6

LIMITATIONS OF COUPLED-CLUSTER APPROXIMATIONS FOR Rb_2^+

The material presented in this chapter has been published in

[324] J. Schnabel, L. Cheng, and A. Köhn, *J. Chem. Phys.* **155**, 124101 (2021).

The following investigations were stimulated by recent experimental findings [111, 114, 120–122, 310] for studying ion-atom collisions in ultracold rubidium quantum gases. These pilot experiments aim at entering the *s*-wave scattering regime which is expected to provide a rich experimental platform for subsequent studies on the quantum level. The physics of ion-atom scattering is based on the corresponding interaction potentials, such as the $X^2\Sigma_g^+$ electronic ground state of Rb_2^+ and the asymptotically degenerate (1) $^2\Sigma_u^+$ state, as illustrated in Fig. 6.1. The characteristic ion-atom interaction length scale is defined by $R^* \propto \sqrt{\mu C_4} \approx 5000 a_0$ [110]. Due to the level of control attained in the ultracold regime, highly accurate potentials (over the full range of R^*) are needed as a starting point for subsequent studies of corresponding properties related to the design and performance of these experiments.

When applying coupled-cluster (CC) methods with perturbative noniterative or approximate iterative treatments of triple excitations to the determination of the cationic dimer potential energy curves (PECs), certain limitations are revealed. It is demonstrated that these CC approaches lead to an unphysical long-range barrier, which seems to be undocumented so far. In particular, it is shown that this spurious feature also occurs for the CCSD(T) method: the “gold standard” of quantum chemistry. By unraveling the origin of this long-range problem, it is shown that it is related to a symmetry instability of the underlying Hartree-Fock mean-field approach leading to asymptotic orbitals representing two +0.5-fold charged ions. This in turn leads to

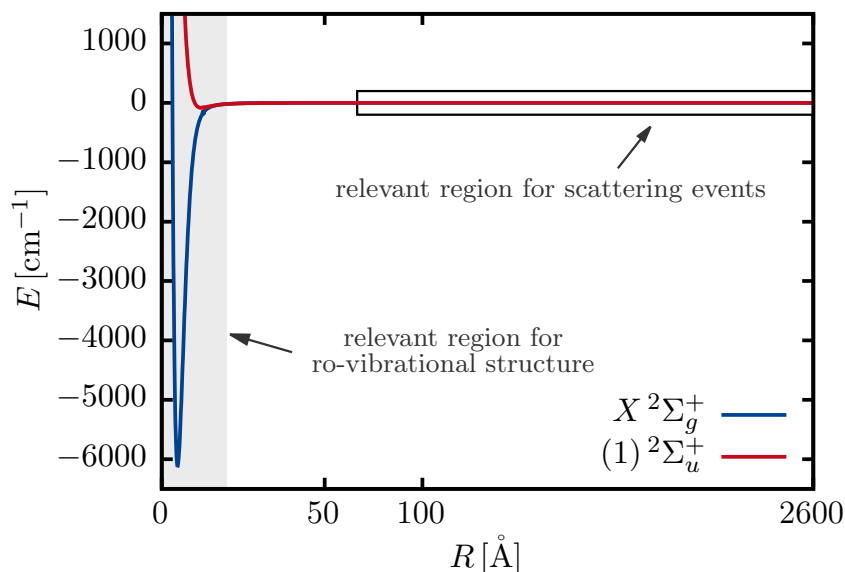


FIGURE 6.1.: Schematic illustration of the $X\ 2\Sigma_g^+$ and $(1)\ 2\Sigma_u^+$ potential energy curves (PECs) of Rb_2^+ over the entire range relevant to study ion-atom scattering physics. The PECs need to be accurate in the binding region to investigate the ro-vibrational structure as well as in the long-range region where the actual scattering events take place. *Freely adapted from J. Schnabel et al., J. Chem. Phys. 155, 124101 (2021).*

wrong leading-order $1/R$ components in the asymptotic region of respective PECs obtained from perturbative coupled-cluster approximations.

6.1 | Computational approach

High-accuracy *ab-initio* calculations of atomic and molecular energies often rely on additivity schemes [236, 238, 311–314]. Here it is assumed that the Hartree-Fock (HF) reference energy and the CCSD(T) correlation contribution, both extrapolated to the complete basis set (CBS) limit, form a good basis to add higher-level correlation contributions (i.e. those beyond CCSD(T) such as CCSDT, CCSDT(Q), etc.), and higher-order relativistic effects on top to finally obtain the total electronic energy to the highest possible accuracy.

The Rb_2^+ system is treated as an effective 17 electron system where only the $4s^2 4p^6 5s^1$ electrons of Rb are explicitly correlated in the CC calculations, while all the remaining electrons are modeled via the small-core scalar-relativistic pseudopotential ECP28MDF from Ref. [250]. In general, results based on a small-core ECP (scECP) description are more accurate as compared to using a lcECP (cf., e.g., the Rb_3 system in Chap. 4), since most of the repulsive interaction of the core electrons is recovered [265]. To exclude

possible errors due to the scECP approach, the HF and CC parts were also investigated using the all-electron spin-free exact two-component theory in its one-electron variant (SFX2C-1e) [315, 316]. The spin-restricted open-shell (ROHF) approach was chosen for the HF calculations and for generating orbitals for the subsequent single-reference CC calculations. The latter used an spin-unrestricted formulation with singles, doubles and perturbative noniterative triple excitations: the ROHF-CCSD(T) method [29, 30, 210, 317] (also often referred to as “RHF-UCCSD(T)”).

The exploration of the problem encountered for the CCSD(T) PEC also involved approximative iterative triples methods as the CCSDT- n ($n=1b,2,3,4$) approaches [211–215] as well as investigating contributions due to higher excitations entering via CCSDT [34–37] and CCSDT(Q) [38–40]. For the latter the CCSDT(Q)/B variant for ROHF reference was used [41].

Beyond that, generating highly accurate ion-atom interaction potentials requires large basis sets which are flexible enough to describe both the entire range defined by R^* and the repulsive short-range region sufficiently accurate. The basis set should moreover show smooth convergence behavior with respect to extrapolation to estimate the CBS limit. This is generally fulfilled by correlation consistent basis sets (cf. Sec. 3.5) and therefore the recently published [240] aug-cc-p(w)CV n Z-PP basis sets ($n = 3, 4, 5$) for use in correlated molecular calculations of alkali metal and alkaline earth atoms, designed for the ECP28MDF pseudopotential, have been used. For all-electron SFX2C-1e based computations, the aug-cc-pwCVTZ-X2C basis set was used.

The ECP-based ROHF-CCSD(T) as well as the SFX2C-1e-ROHF-CCSD(T) calculations were performed using the MOLPRO 2018.2 program package [224, 225, 251]. The CCSDT- n ($n=1b,2,3,4$) and CCSDT results were obtained using the C_{FOUR} program package [317–320], while CCSDT(Q) energies were computed using the MRCC program suite [40, 47, 321, 322].

6.2 | Failure of standard coupled-cluster methods

The following investigations are restricted to the long-range region of the $X\ ^2\Sigma_g^+$ PEC of Rb_2^+ , while it is noted that there is the $(1)\ ^2\Sigma_u^+$ state which becomes degenerate to the former one in the asymptote, as shown in Fig. 6.1.

To avoid numerical errors in the underlying ROHF and CC calculations the corresponding convergence thresholds were tightened *a priori* as discussed in more detail in Appendix F.4. The resulting long-range tails are shown in Fig. 6.2 for the aug-cc-

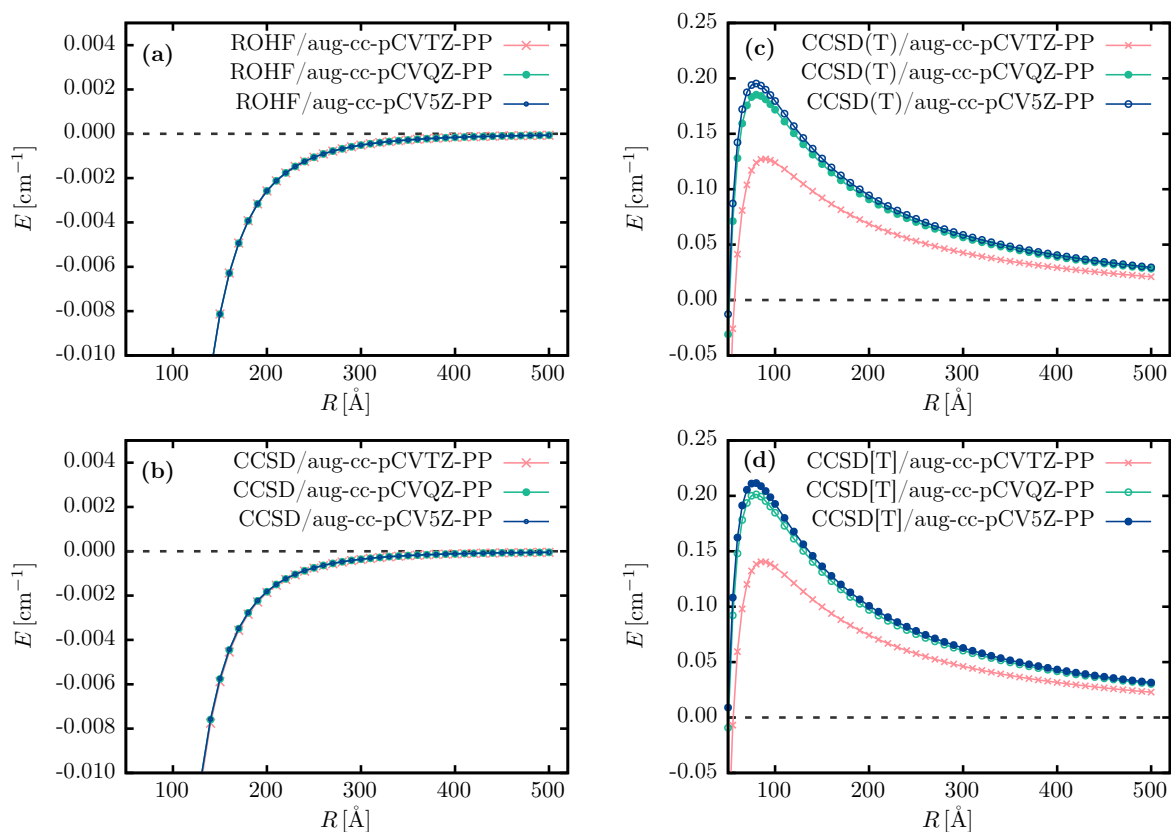


FIGURE 6.2.: Overview of the long-range tails of the $X\ 2\Sigma_g$ PECs of Rb_2^+ for different aug-cc-pCV n Z-PP basis set sizes and calculations based on the ECP28MDF approximation. The ROHF reference energies are shown in (a). Coupled-cluster singles and doubles (CCSD) energies are illustrated in (b). The inclusion of perturbative noniterative triples corrections are shown in (c) for the CCSD(T) approach and in (d) for the CCSD[T] method. These perturbation-theory based methods lead to unphysical repulsive long-range barriers as discussed in more detail in the text. All energies are given as interaction energies with respect to the asymptote (extrapolated limit for $R \rightarrow \infty$). *Freely adapted from J. Schnabel et al., J. Chem. Phys. 155, 124101 (2021).*

pCV n Z-PP basis sets with $n = T, Q, 5$. The ROHF and CCSD contributions show the expected, weakly attractive $\propto -R^{-4}$ [110], asymptotic behavior. However, including perturbative noniterative triples corrections according to Eqs. (3.47), (3.49) and (3.50), produces small repulsive barriers at $R \approx 100 \text{ \AA}$ with $\approx \mathcal{O}(0.15 \text{ cm}^{-1})$ in size. This is illustrated in Figs. 6.2 (c) and (d) for the CCSD(T) and the CCSD[T] method, respectively. The latter approach leads to a slightly more pronounced hump occurring at the same position. This may indicate that the problem is connected with the fourth-order energy correction after Eq. (3.47) and demonstrates that the fifth-order correction that defines CCSD(T), leads to a small but clearly insufficient compensation effect. This is discussed in more detail in Sec. 6.4.

It turns out that the spurious long-range hump can indeed be considered as an inherent problem of the CCSD(T) approximation, since further sources of error can be excluded after thoroughly studying their impact (see Appendix F.4 for more details):

1. The convergence thresholds were tightened to reduce the numerical noise for energies to $\mathcal{O}(2.5 \cdot 10^{-7} \text{ cm}^{-1})$ thus excluding numerical errors
2. A basis set incompleteness error can be already excluded from Fig. 6.2: the hump is independent of the basis set size. In fact the size of the hump even slightly increases with increasing basis set size, thus also excluding basis set superposition errors (BSSEs). This is furthermore demonstrated in the appendix F.4.2 by applying the counterpoise correction scheme.
3. The long-range barrier is independent of the choice of the reference determinant, i.e. spin-restricted open-shell (ROHF) or spin-unrestricted (UHF) as demonstrated by Fig. F.8 yielding to virtually the same result with absolute energy differences $\mathcal{O}(10^{-2} \text{ cm}^{-1})$
4. Both spin-unrestricted [RHF-UCCSD(T)] and partially spin-restricted [RHF-RCCSD(T)] coupled-cluster theory, cf. Refs. [32, 217, 218] and Sec. 3.3.2, lead to the long-range hump with energy differences in the order of $\mathcal{O}(10^{-4} \text{ cm}^{-1})$

Furthermore, the problem is not an artefact due to the scECP approximation, since an all-electron SFX2C-1e-ROHF-CCSD(T) calculation leads to a hump at the same position and with the same order of magnitude. This is shown in Fig. 6.3, where the ECP28MDF pseudopotential is replaced by the X2C Hamiltonian. The long-range barrier is also independent of whether the aug-cc-pCV n Z-PP or the aug-cc-pwCV n Z-PP basis sets from Ref. [240] are used, as demonstrated in Appendix F.4.3. Beyond that, it is important to note that the reported problem is not due to neglecting multireference effects. The quasi-degenerate $X \ ^2\Sigma_g^+$ and $(1) \ ^2\Sigma_u^+$ states of Rb_2^+ are of different symmetry and thus do not mix. Consequently, these states are single reference systems for all internuclear distances and the situation is different as compared to the ground state PEC of LiNa where multireference effects are present and CCSD(T) fails to correctly describe the respective bond cleavage [323]. Finally, it was found that the long-range barrier is universal for X_2^+ systems with $X = \{\text{Li}, \text{Na}, \text{K}, \text{Rb}, \text{Cs}\}$, as shown in Fig. F.10.

Further, it may be investigated if the occurrence of the long-range tail is due to the noniterative approximative nature of the CCSD(T) and CCSD[T] approaches. In

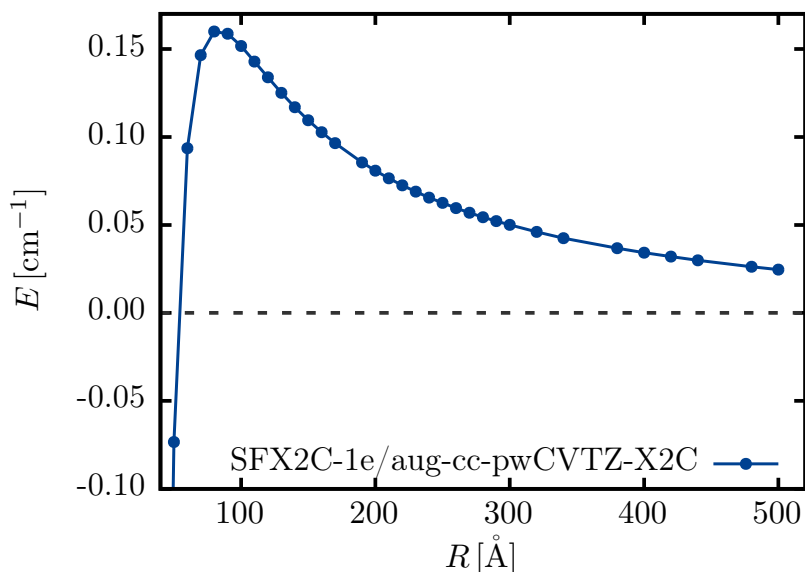


FIGURE 6.3.: All-electron SFX2C-1e $X^2\Sigma_g^+$ PEC of Rb_2^+ based on a ROHF-CCSD(T)/aug-cc-pwCVTZ-X2C approach. are given as interaction energies relative to the asymptote. *Freely adapted from J. Schnabel et al., J. Chem. Phys. 155, 124101 (2021).*

Sec. 3.3.2 a particular class of iterative approximations to CCSDT was introduced: the CCSDT- n methods with $n=1,2,3,4$ [211–215]. Here contributions due to triples excitations conveyed via \hat{T}_3 are not determined perturbatively, rather than by including them into the solution of the coupled-cluster equations according to Eq. (3.41). The singles and doubles residuals are thus equivalent to the one obtained for full CCSDT while the $n=1,2,3$ methods avoid including N_{AO}^8 -scaling terms in the projection onto triply excited determinants. The CCSDT-4 method partially includes such terms and is thus almost as expensive as CCSDT. Figure 6.4 shows the resulting long-range PECs obtained at ECP28MDF/aug-cc-pCVTZ-PP level of theory. The CCSDT-1b, CCSDT-2 and CCSDT-3 methods still show the long-range barrier at the same position ($R \approx 100 \text{ \AA}$) and of the same order of magnitude ($\approx 0.15 \text{ cm}^{-1}$). The size of the hump decreases with increasing number of terms included in the solution of the triples residual equation. However, only if the full Hamiltonian enters via $\langle \Phi_{I_3} | [\hat{H}, \hat{T}_3] | \Phi_0 \rangle$, i.e. for CCSDT-4, the repulsive barrier disappears. This method is already almost as expensive as CCSDT and there is no reason to prefer the former over the latter.

The CCSDT- n ($n=1,2,3$) methods as well as the non-iterative CCSD(T) (or CCSD[T]) approach have the $\langle \Phi_0 | \hat{T}_3^\dagger \hat{f}_N \hat{T}_3 | \Phi_0 \rangle$ term as given in Eq. (3.47) in common. This suggests that this term does not correctly account for interatomic interactions. In fact it only contains the interaction with the Hartree-Fock density of the other atom [324].

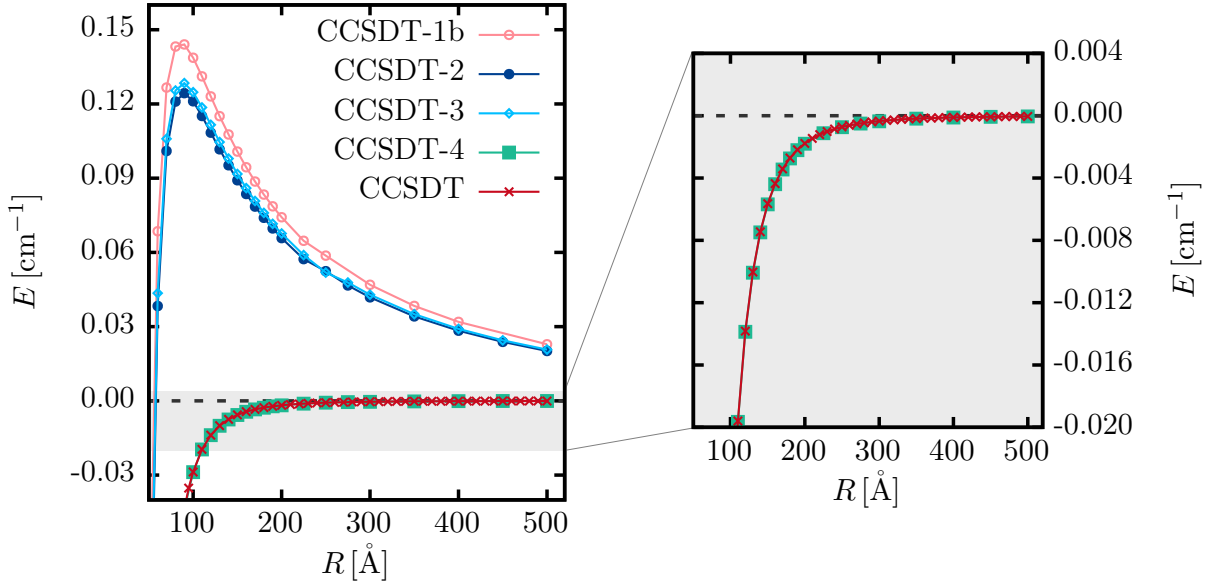


FIGURE 6.4.: Comparison of the long-range tails of the $X^2\Sigma_g^+$ PECs of Rb_2^+ resulting from using different iterative approximations to CCSDT as well as the PEC obtained from a full CCSDT calculation. The hump decreases in size with increasing number of terms included in the triples residual (see text for more details). But only the CCSDT-4 method, which is computationally almost as expensive as CCSDT avoids the barrier. All energies are given as interaction energies relative to the asymptote obtained from computations at ECP28MDF/aug-cc-pCVTZ-PP level of theory.

The perturbative inclusion of even higher excitations such as CCSDT(Q) [325], leads to the same phenomenon. The observed hump is in fact smaller in size but nevertheless entirely spoils the long-range behavior of the PEC. This is reported in Fig. F.11.

6.3 | Symmetry breaking

From a mathematical perspective X_2^+ systems, with $X \in \{\text{Li}, \text{Na}, \text{K}, \text{Rb}, \text{Cs}\}$, are generally characterized by the point group $D_{\infty h}$ (i.e. the computational point group is D_{2h}). This reflects the quantum mechanical indistinguishability of the two limiting cases $\text{Rb} + \text{Rb}^+$ and $\text{Rb}^+ + \text{Rb}$. The correct asymptotes of the Σ_g and Σ_u states, respectively, are thus symmetric and antisymmetric superpositions of both limiting cases and are given by

$$|X^2\Sigma_g^+\rangle = \frac{1}{\sqrt{2}} (|0, +\rangle + |+, 0\rangle), \quad (6.1a)$$

$$|(1)^2\Sigma_u^+\rangle = \frac{1}{\sqrt{2}} (|0, +\rangle - |+, 0\rangle). \quad (6.1b)$$

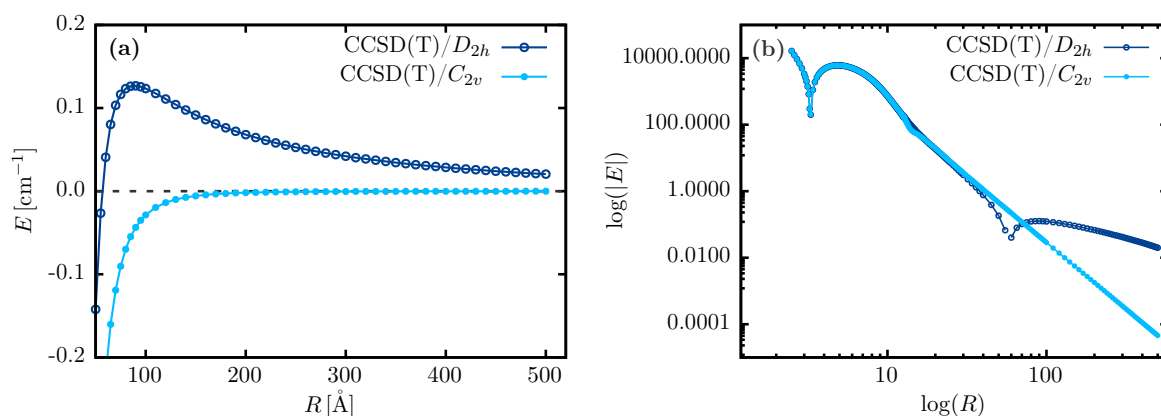


FIGURE 6.5.: **(a)** Comparison of long-range tails of the $X\ 2\Sigma_g^+$ PECs at CCSD(T) level of theory using either symmetry-adapted ($D_{\infty h}$, i.e. computational point group is D_{2h}) or symmetry-broken ($C_{\infty v}$, i.e. computational point group is C_{2v}) ROHF orbitals. Breaking the symmetry of the system removes the unphysical long-range barrier (see text for more details). **(b)** Doubly logarithmic representation of the CCSD(T) PECs. The long-range interaction of the symmetry-broken solution shows the correct weakly attractive R^{-4} behavior while the symmetry-adapted curve reveals a repulsive $1/R$ component causing the unphysical barrier. The tiny deviation of the symmetry-broken solution for $\approx 12 - 20\ \text{\AA}$ is due to a numerical bistability discussed in more detail in connection with Fig. 6.7 (a). Calculations were performed at ECP28MDF/aug-cc-pCVTZ-PP level of theory and energies are given as interaction energies relative to the asymptote. *Freely adapted from J. Schnabel et al., J. Chem. Phys. 155, 124101 (2021).*

The coupled-cluster approach is based on a Hartree-Fock reference, which provides a zeroth-order description of the system. As pointed out in Sec. 3.2.1, the Hartree-Fock method is a mean-field theory and the solution of the nonlinear Roothaan-Hall equations (3.19) involves the iterative self-consistent field (SCF) method. This need to define self-consistent solutions leads to different orbitals for Rb and Rb^+ and thus the solution of the separated fragments is at conflict with the symmetry requirement that the two limiting cases $\text{Rb} + \text{Rb}^+$ and *vice versa* are quantum mechanically indistinguishable. The symmetry-adapted solution converges to the state-averaged orbitals of Rb and Rb^+ and thus all the orbitals are a compromise of the neutral and ionic orbitals. This problem lives on in the Fockian, the effective one-electron potential of the system according to Eq. (3.12). As indicated in the previous section, the Fock operator is crucial for defining perturbative corrections in coupled-cluster theory. Instead of describing the correct superposition it merely contains the compromise solution with half an electron on the left and half an electron on the right nucleus, possibly explaining the repulsive long-range barrier as a consequence of a leading-order repulsive $1/R$ component in the asymptotic region of the respective PECs [324].

If the cause of the problem is indeed connected with a size-consistency error of

symmetry-adapted mean-field solutions, breaking the symmetry of the system should recover the correct long-range behavior. This means that the point group symmetry may be lowered to $C_{\infty v}$ (i.e. the computational point group is C_{2v}) to obtain size-consistent mean-field solutions. Quantum mechanically speaking one projects onto one of the two limiting cases: $|0, +\rangle = \text{Rb} + \text{Rb}^+$ or *vice versa*. This can be tested by carrying out CCSD(T) calculations using symmetry-broken ROHF orbitals. The resulting long-range part of the PEC is shown in Fig. 6.5 (a).

Apparently, reducing the symmetry of the system to $C_{\infty v}$ avoids the long-range barrier and thus proves that it is related to a symmetry instability of the underlying Hartree-Fock mean-field solution. This is further illustrated by the doubly logarithmic representation in Fig. 6.5 (b), which clearly reveals the above mentioned leading-order repulsive $1/R$ component in the long-range tail of the symmetry-adapted CCSD(T) PEC. This wrong repulsive $1/R$ asymptotic behavior is also contained in the SFX2C-1e, CCSDT-n ($n=1,2,3$) and CCSDT(Q) approaches and explains the barriers obtained in Figs. 6.3, 6.4 and F.11. This is in contrast to the PEC of the symmetry-broken solution that reveals the correct leading-order attractive R^{-4} behavior. Moreover, the symmetry-broken solutions coincide with the energy of the isolated fragments in the long-range, while the symmetry-adapted solutions converge, as noted previously, to the state-averaged orbitals of Rb and Rb^+ . This is reflected in the corresponding offsets of $\approx 40 \text{ cm}^{-1}$ for ROHF solutions, $\approx 10 \text{ cm}^{-1}$ for CCSD results and $\approx -2 \text{ cm}^{-1}$ for CCSD(T) PECs, as displayed in Fig. 6.6. In the short-range region the symmetry-broken solutions suddenly collapse to the symmetry-adapted ones. This takes place at $R = R_{\text{CF}} \approx 12.6 \text{ \AA}$ which defines the so-called *Coulson-Fischer point*, where the first derivative shows a discontinuity. For $R \leq R_{\text{CF}}$ the symmetry-broken and symmetry-adapted solutions are degenerate, while for $R > R_{\text{CF}}$ the symmetry-broken curves branch off the symmetry-adapted ones. Deeper understanding of this behavior may be gained by analyzing the differences between the two solutions, as illustrated on the right-hand side of Fig. 6.6. One may first note that due to the different asymptotes of symmetry-adapted and symmetry-broken results, they show a different decay behavior to the equilibrium state. This can be observed from the tiny humps indicated by the respective insets in Fig. 6.6. Due to the repulsive long-range barrier of symmetry-adapted CCSD(T) solutions, this behavior is more pronounced in this case. Moreover, the CCSD and CCSD(T) cases show additional troughs for $R \in (R_{\text{CF}}, 15 \text{ \AA}]$. For CCSD this is a consequence of an intersection between symmetry-broken and symmetry-adapted solutions behind the Coulson-Fischer point. The CCSD(T) trough

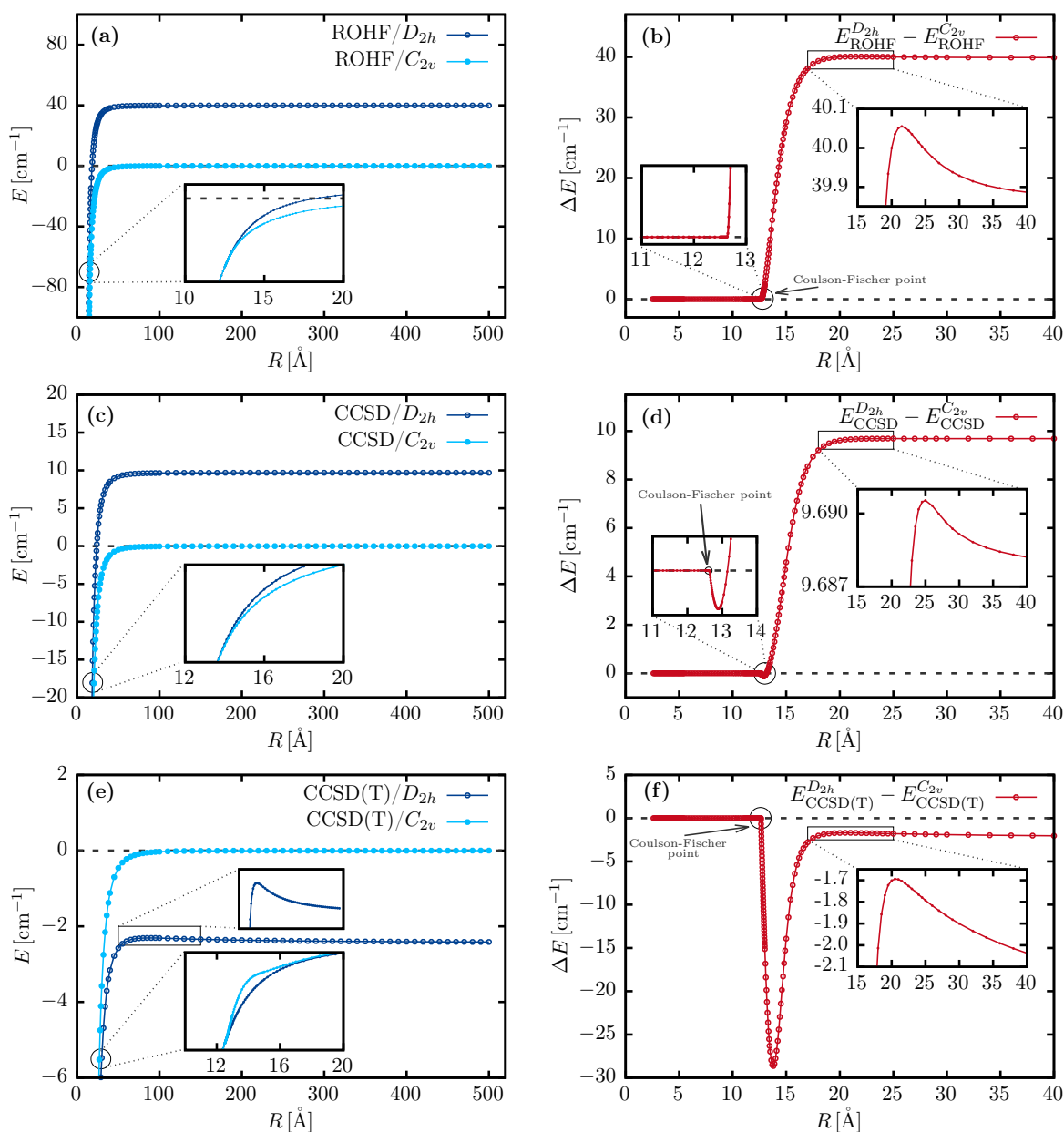


FIGURE 6.6.: Comparison of symmetry-adapted and symmetry-broken $X^2\Sigma_g^+$ PECs of Rb_2^+ . The **upper panel** corresponds to the ROHF case with the PECs shown in (a) and their respective difference illustrated in (b). The symmetry-broken solution collapses to the symmetric one at the Coulson-Fischer point R_{CF} showing a discontinuous first derivative. For $R > R_{\text{CF}}$ the symmetry-broken solution branches off the symmetry-adapted one. The insets shown on the right-hand side in each figure on the right panel indicate the different long-range decay behavior to the equilibrium between symmetry-broken and symmetry-adapted solutions due to their convergence to different asymptotes. The left insets on the right panel display the vicinity of the Coulson-Fischer point. The **middle panel** shows the corresponding situations for the ROHF-CCSD case while the **lower panel** shows the ROHF-CCSD(T) solutions. The calculations were performed at ECP28MDF/aug-cc-pCVTZ-PP level of theory, with energies given relative to the separated isolated fragments limit, i.e. $\text{Rb}+\text{Rb}^+$. *Freely adapted from J. Schnabel et al., J. Chem. Phys. 155, 124101 (2021).*

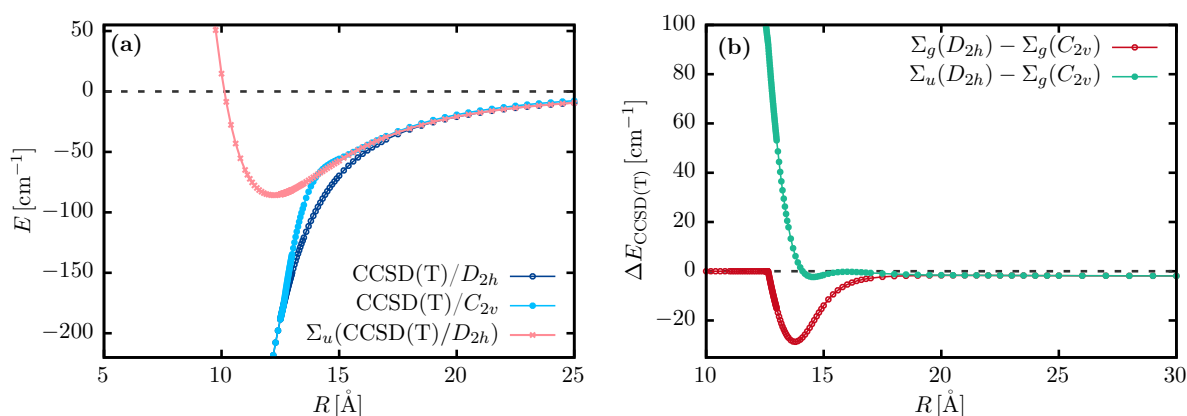


FIGURE 6.7.: Visualization of the numerical bistability for the symmetry-broken Σ_g PEC of Rb_2^+ . The PECs in (a) represent a close-up of Fig. 6.6 (e) and additionally show the Σ_u solution. In the region $R \in (R_{\text{CF}}, 15 \text{ \AA}]$, the symmetry-broken Σ_g solution strongly mixes with the Σ_u state, which falls into the same IRREP for C_{2v} calculations. This is further demonstrated by the corresponding CCSD(T) energy differences, as shown in (b). The calculations are based on the ECP28MDF pseudopotential approach with the aug-cc-pCVTZ-PP basis set. Energies are given relative to the separated isolated fragments $\text{Rb} + \text{Rb}^+$. Freely adapted from J. Schnabel et al., *J. Chem. Phys.* **155**, 124101 (2021).

is significantly more pronounced and results from a hump in the symmetry-broken PEC occurring in the previously mentioned region as shown by the lower inset in Fig. 6.6 (e).

The origin of this tiny barrier can be explained by additionally considering the symmetry-adapted Σ_u solution in this region, which is illustrated in Fig. 6.7. Due to the numerical bistability of the symmetry-broken Σ_g solution it strongly mixes with the Σ_u state, which, for the C_{2v} point group symmetry, falls into the same IRREP as the Σ_g state. This means that for $R \in (R_{\text{CF}}, 15 \text{ \AA}]$ the symmetry-broken solution cannot “decide” between the symmetry-adapted Σ_g and Σ_u curves to which one to collapse. The differences shown in Fig. 6.7 (b) further confirm this behavior. Finally, this also explains the indicated deviation in Fig. 6.5 (b).

In conclusion, the findings reported in this section suggest that the best long-range model may be based on symmetry-broken solutions. The most promising protocol is to use symmetry-broken (T) [and (Q)] corrections in the long-range region and properly merge with symmetry-adapted results in the intermediate range. This approach is discussed in more detail in Chap. 7.

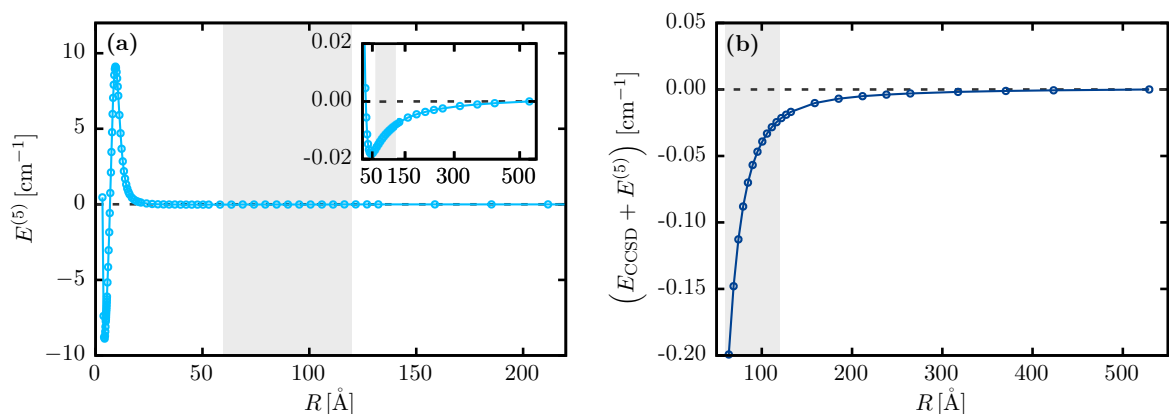


FIGURE 6.8.: **(a)** Illustration of the fifth-order noniterative triples correction $E_{(T)}^{(5)}$ according to Eq. (3.49). The area highlighted in gray marks the region where the long-range barrier usually occurs. The inset demonstrates that $E_{(T)}^{(5)}$ is slightly attractive in this area explaining the tiny compensation effect when closely comparing the CCSD(T) and CCSD[T] long-range tails as shown in Figs. 6.2 (c) and (d). Thus, merely adding $E_{(T)}^{(5)}$ to the CCSD energy, as displayed in **(b)**, does not show the long-range hump. All energies are given relative to the last *ab-initio* point and calculations were performed at ECP28MDF/aug-cc-pCVTZ-PP level of theory.

6.4 | Discussion

The findings discussed so far suggest that the unphysical long-range barrier is connected to a symmetry instability of the underlying mean-field approach and the way it enters perturbative coupled-cluster approximations. Further analysis of the CCSD(T) energy expression according to Eq. (3.50), with the fourth-order correction after Eq. (3.47) and the fifth-order term as given by Eq. (3.49), reveals that the latter contribution does not cause the problems. The $E_{(T)}^{(5)}$ term is shown in Fig. 6.8 (a) with the area where the long-range hump usually occurs highlighted in gray. In this area, $E_{(T)}^{(5)}$ is slightly attractive, thus explaining the above mentioned compensation effect occurring for CCSD(T) as compared to CCSD[T]. Figure 6.8 (b) further demonstrates that adding $E_{(T)}^{(5)}$ to the CCSD energy yields a physically correct long-range tail.

However, formally these findings do not reveal whether the previously discussed mean-field problems are caused by the approximative nature of the energy expression or if they are due to the use of approximate triples amplitudes \hat{T}_3 after Eq. (3.48). The latter can be systematically investigated using a flexible framework for obtaining leading order perturbative triples corrections as shown in Ref. [324]. Herein, it has been demonstrated that the artificial long-range hump of (symmetry-adapted) CCSD(T) PECs originates from the use of \hat{T}_3 amplitudes obtained from perturbative CC singles,

doubles and triples (CCSDT) amplitude equations after Eq. (3.48). The basic idea underlying this “proof” follows the derivation as outlined below [325].

It starts with the formulation of the coupled-cluster equations (3.41) in terms of an energy functional, yielding [326]

$$\mathcal{L} = \langle \Phi_0 | (1 + \hat{\Lambda}) \bar{H} | \Phi_0 \rangle , \quad (6.2)$$

with the similarity transformed Hamiltonian \bar{H} after Eq. (3.42) and the $\hat{\Lambda}$ operator consisting of a set of deexcitation operators with analogous definition to that of the excitation operators of the cluster operator in Eq. (3.38). This allows for an alternative treatment of triples contributions in terms of an external perturbation to the CCSD Lagrangian with fictitious field strength χ , yielding [326–329]

$$\mathcal{L}(\hat{T}_1, \hat{T}_2, \chi \hat{T}_3) = \langle \Phi_0 | (1 + \hat{\Lambda}_{\text{CCSD}}) \bar{H}(\chi) | \Phi_0 \rangle , \quad (6.3)$$

with the CCSD- Λ -operator $\hat{\Lambda}_{\text{CCSD}} = \hat{\Lambda}_{1,\text{CCSD}} + \hat{\Lambda}_{2,\text{CCSD}}$. Triples excitations \hat{T}_3 contribute to \bar{H} in the same way as in the CCSDT method. If exact \hat{T}_3 amplitudes were available a finite field CCSD calculation with $\chi = 1$ would define the exact CCSDT energy. This finite field CCSD calculation uses the CCSDT equation but treats triples excitations as perturbation and as such, the CCSDT energy can be expressed via a Taylor expansion

$$\begin{aligned} E_{\text{CCSDT}} &= \mathcal{L}(\hat{T}_1, \hat{T}_2, \chi \hat{T}_3) \Big|_{\chi=1} , \\ &= \left[\mathcal{L} \Big|_{\chi=0} + \chi \frac{d\mathcal{L}}{d\chi} \Big|_{\chi=0} + \frac{1}{2} \chi^2 \frac{d^2\mathcal{L}}{d\chi^2} \Big|_{\chi=0} + \dots \right] \Big|_{\chi=1} , \\ &= \mathcal{L} \Big|_{\chi=0} + \frac{d\mathcal{L}}{d\chi} \Big|_{\chi=0} + \frac{1}{2} \frac{d^2\mathcal{L}}{d\chi^2} \Big|_{\chi=0} + \dots , \\ &= E_{\text{CCSD}} + \frac{d\mathcal{L}}{d\chi} \Big|_{\chi=0} + \frac{1}{2} \frac{d^2\mathcal{L}}{d\chi^2} \Big|_{\chi=0} + \dots , \end{aligned} \quad (6.4)$$

with the first-order energy correction defined as

$$\begin{aligned} \frac{d\mathcal{L}}{d\chi} \Big|_{\chi=0} &= \left\langle \Phi_0 \left| \hat{\Lambda}_{\text{CCSD}} \frac{\partial \bar{H}(\chi)}{\partial \chi} \right| \Phi_0 \right\rangle \Big|_{\chi=0} , \\ &= \langle \Phi_0 | \hat{\Lambda}_{\text{CCSD}} [\hat{H}, \hat{T}_3] | \Phi_0 \rangle . \end{aligned} \quad (6.5)$$

If leading-order triples amplitudes according to Eq. (3.48) are used then Eq. (6.5) represents the triples contribution of the CCSD(T) $_{\Lambda}$ method [31, 206, 330]. However,

Eq. (6.5) also allows for using \hat{T}_3 amplitudes obtained from the n -th iteration of the solution of the CCSDT amplitude equations with converged CCSD amplitudes adopted as initial guess. This approach leads to a systematic improvement of the \hat{T}_3 amplitudes as compared to those resulting from Eq. (3.48) and thus to an improved triples energy correction through Eq. (6.5). Using triples amplitudes obtained from the $n \geq 3$ rd iteration of CCSDT equations removes the long-range hump as reported in Ref. [324] and finally proves the above statement. However, it should be noted that only from order five on the method reveals the correct R^{-4} asymptotic behavior.

This finding also holds for iterative approximations to CCSDT, i.e. CCSDT- n (with $n=1,2,3$) since the resulting equations for determining triples amplitudes approximately, are formally similar to Eq. (3.48).

7

TOWARDS HIGHLY-ACCURATE Rb_2^+ INTERACTION POTENTIALS

This chapter exploits the findings presented previously in Chap. 6 on how to avoid the long-range barrier occurring for perturbative coupled-cluster approximations for the construction of physical meaningful and highly-accurate Rb_2^+ interaction potentials based on ROHF-CCSD(T) *ab-initio* calculations. The procedure described below is designed such that it may serve as a foundation for constructing as accurate potential energy curves (PECs) as the present computational resources allow.

The following further outlines the underlying physics of ion-atom interactions, including novel experimental techniques aiming to study these interactions on the pure quantum level. The PEC construction procedure is restricted to the CCSD(T) level of theory, but accounts for the correct long-range and exchange-splitting behavior and can be straightforwardly extended to higher-level correlation effects. The finally obtained interaction potentials for the $X\ ^2\Sigma_g^+$ and $(1)\ ^2\Sigma_u^+$ states of Rb_2^+ are used to extract spectroscopic constants and to investigate their ro-vibrational structure. These results extend the available literature data and raise them to an improved level of accuracy.

7.1 | Physical basics and experimental motivation

The investigation of ion-atom interaction potentials has been stimulated by recent experimental progress towards entering the ultracold quantum regime of hybrid ion-atom systems [111, 114, 120–122, 310]. This would mark a milestone for exploring ion-atom collisions, since the cold regime ($T > 1$ mK) is essentially classical, while in the ultracold ($T < 1$ mK) the *s*-wave collision and thus the pure quantum regime

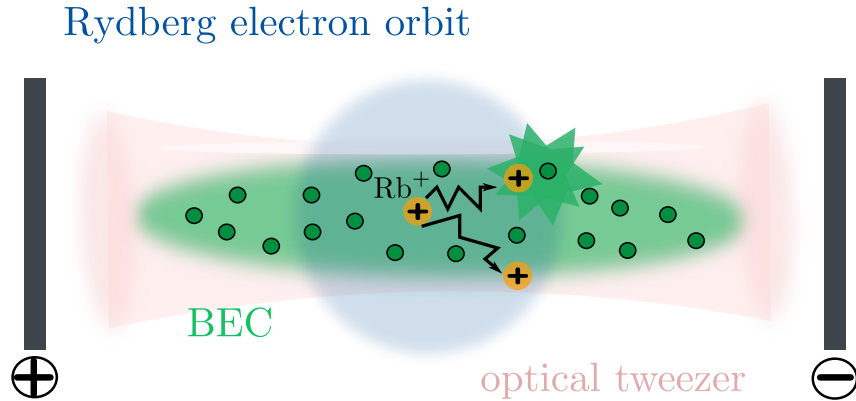


FIGURE 7.1.: Schematic and strongly simplified illustration of the experimental idea to study ion-atom interactions in a Bose-Einstein condensate (green). The BEC is trapped in an optical tweezer (pink) and the ionic impurity is implanted into the BEC through a single Rydberg excitation, where the respective Rydberg electron orbit (blue) exceeds the size of the atomic cloud (principal quantum number $n \sim 200$). The ion is accelerated by an applied electric field leading to diffusive transport through the BEC [122, 123]. Two exemplary trajectories indicate collisions with host gas atoms (green spheres), which is mainly governed by Langevin scattering. This setup further allows for studying three-body recombination processes involving the formation of a weakly bound Rb_2^+ molecule and a second Rb atom carrying away part of the released binding energy [121]. *Inspired by figures from K.S. Kleinbach et al., Phys. Rev. Lett. 120, 193401 (2018) and T. Dieterle et al., Phys. Rev. Lett. 126, 033401 (2021).*

is reached. In Ref. [114] this could be successfully demonstrated for Li_2^+ , where accompanying highly accurate *ab-initio* calculations were used to determine bounds for the ion-atom scattering length. Reaching the *s*-wave collision regime for Rb_2^+ is considerably more difficult due to more stringent temperature requirements because of its large reduced mass. Nevertheless, the respective experimental method uses the same ideas that are based on implanting an ionic impurity into a cigar-shaped Bose-Einstein condensate (BEC) through the controlled creation of an individual Rydberg atom from the atomic ensemble (strong Rydberg blockade grants the creation of a single impurity) [111, 120, 121]. In this way the Rydberg electron is promoted to an orbit with principal quantum number $n \sim 200$ (orbital radius $\approx 4 \mu\text{m}$), exceeding the BEC size (micron-sized) by far. In a subsequent step, the single Rydberg atom is ionized to start the ion-atom interaction between the Rb^+ ion and the ground state host gas atoms. All this is schematically illustrated in Fig. 7.1. This procedure decelerates the produced ion and results in a small initial kinetic energy of $E_{\text{kin}} \approx k_B \times 50 \mu\text{K}$ [121, 122].

The scattering properties depend on the long-range form of the $X \ ^2\Sigma_g^+$ and $(1) \ ^2\Sigma_u^+$

interaction potentials as illustrated in Fig. 6.1. For diatomic ions with a single active electron (i.e. alkali-metal systems such as Rb_2^+) this long-range behavior contains the two contributions

$$V_{\text{LR}}(R) = V_{\text{ind/disp}}(R) \pm V_{\text{exch}}(R), \quad (7.1)$$

where $V_{\text{ind/disp}}(R)$ describes the leading induction and dispersion interactions and V_{exch} is the exchange interaction term. For interactions between an S -state atom and an S -state ion, $V_{\text{ind/disp}}(R)$ is defined as [110]

$$V_{\text{ind/disp}}(R) = -\frac{C_4^{\text{ind}}}{R^4} - \frac{C_6^{\text{ind}}}{R^6} - \frac{C_6^{\text{disp}}}{R^6} + \dots \quad (7.2)$$

The leading term is due to the charge of the ion inducing an electric dipole moment of the atom and thus causing an interaction. The corresponding induction coefficient is given by

$$C_4^{\text{ind}} = \frac{1}{2}q^2\alpha_{\text{d}}, \quad (7.3)$$

where q is the charge of the ion and α_{d} is the static electric dipole polarizability of the neutral atom. The next higher-order long-range induction term is caused by the interaction between the charge of the ion and the induced electric quadrupole moment of the atom, with the respective coefficient

$$C_6^{\text{ind}} = \frac{1}{2}q^2\alpha_{\text{q}}, \quad (7.4)$$

defined by the static electric quadrupole polarizability α_{q} of the atom. The leading-order dispersion term accounts for dynamic interactions due to instantaneous dipole-induced dipole moments of the ion and the atom arising from quantum fluctuations. Higher-order terms accounting for higher-order multipole polarizabilities and higher-order dispersion interactions (dipole-quadrupole, dipole-octupole, quadrupole-quadrupole, etc.) could be further added to Eq. (7.2), but since reaching the s -wave scattering regime for Rb_2^+ is barely possible at all, truncation after the R^{-6} terms is usually sufficient.

The exchange interaction is a consequence of the indistinguishability of the two limiting cases $\text{Rb}^+ + \text{Rb}$ and vice versa; cf. also Eq. (6.1). Thus, it is defined by the energy splitting between the gerade and ungerade states and determines the cross section for resonant charge transfer [331]. For alkali-metal X_2^+ systems, it generally

involves one active electron and if both ion and atom are in a S -state, it is of the form (in atomic units) [119, 125]

$$V_{\text{exch}}(R) = \frac{V_{X^2\Sigma_g^+}(R) - V_{(1)^2\Sigma_u^+}(R)}{2}, \quad (7.5)$$

$$= \frac{1}{2}AR^\alpha e^{-\beta R} \left[1 + \frac{B}{R} + \frac{C}{R^2} + \dots \right], \quad (7.6)$$

where the parameters α , β and B are related by simple expressions to the ionization potential I_{Rb} of the neutral Rb atom. They are defined as

$$\beta = \sqrt{2I_{\text{Rb}}}, \quad \nu = \frac{1}{\beta}, \quad \alpha = (2\nu - 1) \quad \text{and} \quad B = \nu^2 \left(1 - \frac{1}{2}\nu \right). \quad (7.7)$$

The value for the ionization potential I_{Rb} is taken from Ref. [258] and corresponds to experimental results, yielding $I_{\text{Rb}}^{\text{exp}} = 0.15350655 E_{\text{h}}$ (originally $I_{\text{Rb}}^{\text{exp}} = 4.1771281 \pm 0.0000012 \text{ eV}$). The parameter A corresponds to the normalization factor of the asymptotic wavefunction and becomes [125, 332], given the parameters from Eq. (7.7)

$$A = -\frac{\beta^2(2\beta)^{2\nu}e^{-\nu}}{\Gamma(\nu+1)\Gamma(\nu)}, \quad (7.8)$$

where $\Gamma(\cdot)$ denotes the Gamma function as defined in Appendix E.3.1. The second order expansion coefficient C of Eq. (7.7) may be obtained from fit to *ab-initio* data but here it is taken from Ref. [119] with $C = -19.22$.

The leading term of the long-range ion-atom interaction potential according to Eq. (7.2) marks the essential difference to atom-atom scattering events (e.g. for the ground-state of Rb_2 the leading long-range term is $\propto R^{-6}$). By equating the $-C_4/R^4$ -term to the kinetic energy one can define the characteristic interaction length scale R^* as [110]

$$R^* = \sqrt{\frac{2\mu C_4}{\hbar^2}}. \quad (7.9)$$

This length scale is at least an order of magnitude larger as compared to neutral atom-atom ones. The respective energy scale becomes

$$E^* = \frac{\hbar^2}{2\mu(R^*)^2} \propto \frac{1}{2\mu^2 C_4}. \quad (7.10)$$

This characteristic energy scale is at least two orders of magnitude smaller than the one for neutral atom-atom systems, marking one of the reasons why reaching the s -wave

collision regime for ion-atom systems is more challenging as compared to neutral atom systems. Furthermore, this explains the comparatively early onset of s -wave scattering for the Li ion-atom system due to its small reduced mass. For the Rb_2^+ system the s -wave scattering limit is $E^* = k_B \times 79 \text{ nK}$ [111].

Nevertheless, most recent experimental achievements encourage to further work on highly accurate Rb_2^+ interaction potentials. By applying homogeneous electric fields along the long-axis direction of the BEC, the transport of the ion through the atomic cloud could be measured [121, 122]. This is also illustrated in Fig. 7.1. These experiments revealed that a large fraction of the Rb^+ ions undergo three-body recombination processes and enabled to estimate typical binding energies of threshold bound states. Therefore, the experiments may pave the way to probe chemical reaction channels on the quantum level. This so-called state-to-state chemistry will require resolving the quantized molecular energy levels both theoretically and experimentally. This further shows the importance of having accurate *ab-initio* potentials at hand. The *ab-initio* potentials could also help to make more quantitative statements for conditions needed to identify effects beyond Langevin scattering, since current theoretical models for scattering calculations only involve simplified long-range potentials [123].

Finally, the recent development of a high-resolution ion microscope [310] allows for the spatial resolution of Rydberg atoms and marks, among the outlined achievements, a next milestone towards the ultimate goal of studying polaron physics.

7.2 | Computational aspects and prospects

In Sec. 6.1 it was already briefly outlined that high-accuracy quantum-chemical calculations often rely on additivity schemes [236, 238, 311–314]. A systematic way to define such a scheme follows the so-called HEAT (High accuracy Extrapolated Ab-initio Thermochemistry) protocol [313, 333, 334], according to which the total molecular energy E is computed via

$$E = E_{\text{HF}}^{\infty} + \Delta E_{\text{CCSD(T)}}^{\infty} + \Delta E_{\text{HLC}} + \Delta E_{\text{higher-rel}}. \quad (7.11)$$

Herein, E_{HF}^{∞} and $\Delta E_{\text{CCSD(T)}}^{\infty}$ are the contributions of the Hartree-Fock energy and the CCSD(T) correlation energy at the estimated complete basis set (CBS) limit obtained via extrapolation. Correlation effects that account for contributions beyond CCSD(T) are denoted as higher-level correlation effects ΔE_{HLC} and higher-order relativistic effects are labeled by $\Delta E_{\text{higher-rel}}$. In this respect, it should be noted that for systems involving

bond cleavage, CCSD(T) is expected to fail and thus Eq. (7.11) does not represent a proper approach for computing corresponding PECs. However, for the ground state of Rb_2^+ this is unproblematic since it is a single reference system for the entire range of internuclear distances and hence CCSD(T) is expected to work well.

As a natural continuation of Chap. 6, the following discussion is restricted to the construction of high-precision and physically meaningful Rb_2^+ PECs at CCSD(T) level of theory, incorporating the previously acquired insights to avoid the spurious long-range barrier. Thus, symmetry-adapted and symmetry-broken ROHF-CCSD(T) [i.e. RHF-UCCSD(T) in MOLPRO fashion] calculations with the ECP28MDF small-core pseudopotential [250] and the aug-cc-pCV n Z-PP ($n = 3,4,5$) basis sets from Ref. [240] were performed for all Rb_2^+ results presented in this chapter. It should be noted that the same convergence thresholds as outlined in Appendix F.4 are imposed for these calculations. In the spirit of the additivity scheme of Eq (7.11), the construction procedure discussed in Sec. 7.3 can be systematically extended to *ab-initio* calculations accounting for higher-level correlation effects (i.e. CCSDT, CCSDT(Q), etc.) or to those based on the all-electron spin-free exact two component theory in its one-electron variant [i.e., e.g. SFX2C-1e-ROHF-CCSD(T)]. Therefore, it is useful to first benchmark the HEAT protocol according to Eq. (7.11) to reveal both its expected accuracy and its limitations.

This may be achieved by calculations of ionization energies I_{Rb} of atomic Rb as presented in Tab. 7.1, showing the dependence of I_{Rb} on both core-valence correlated basis set variants [aug-cc-p(w)CV n Z-PP] from Ref. [240] with respect to increasing basis set size. As suggested by the E_{HF}^∞ and $E_{\text{CCSD(T)}}^\infty$ terms of the HEAT protocol, it is necessary to estimate the CBS limit values to obtain accurate results. However, due to the small oscillations between the $n = 4$ and $n = 5$ values as obtained from Tab. 7.1, the use of standard extrapolation techniques might cause convergence problems. In this regard, a detailed analysis of the basis set convergence with respect to increasing cardinality was carried out in Appendix F.2. This analysis revealed that the Hartree-Fock reference energy and the singles contribution to the CC correlation energy show an irregular behavior with increasing basis set size, possibly causing the above oscillations. Instead of interpolating these terms using the largest basis set, with n_{max} the largest consistent cardinal number, was found as a reasonable compromise. This yields an ansatz of the form as already defined in Eq. (5.29), with

$$E_{\text{HF}}^\infty \approx E_{\text{HF}}(n = n_{\text{max}}) \quad (7.12)$$

TABLE 7.1.: Dependence of the Rb ionization energy I_{Rb} (in eV) on the aug-cc-p(w)CV n Z-PP basis sets [240] with respect to increasing cardinality (labeled by n) and the impact of higher-level correlation effects as well as higher-order relativistic corrections (see text for details). The correlation energy was extrapolated either according to the conventional two-point n^{-3} formula [238, 239] or by using an approach based on the application of the Riemann- ζ function, as proposed recently in Ref. [304]. Reference energies and singles contributions to the CCSD correlation energy were excluded from the extrapolation procedure (see text for details). The experimental value is $I_{\text{Rb}}^{\text{exp}} = 4.177\,128\,1$ eV [258].

basis set size	ECP calcs.		SFX2C-1e [325]
	aug-cc-pwCV n Z-PP	aug-cc-pCV n Z-PP	ANO-RCC+UET17
$n = 3$	4.157429	4.125985	4.161396
$n = 4$	4.172722	4.159782	4.168993
$n = 5$	4.172448	4.166632	4.171510
$n = 6$	–	–	4.172440
CBS	4.172207	4.174037	4.173717
CBS $_{\zeta}$	4.172165	4.175328	4.173885
$+\Delta E_{\text{T}}^{\text{TQ}}$	0.000108	0.000298	0.000211
$[+\Delta E_{\text{T}}^{\text{TQ}}(\zeta)]$	0.000016	0.000287	0.000157
$+\Delta E_{(\text{Q})}^{\text{TQ}}$ [325]	0.001542	0.001329	0.001319
$[+\Delta E_{(\text{Q})}^{\text{TQ}}(\zeta)]$ [325]	0.001618	0.001370	0.001366
$+\Delta E_{\text{higher-rel}}$	–	–	0.002425
Σ	4.173857	4.175664	4.177672
Σ_{ζ}	4.173799	4.176985	4.177833

and

$$\Delta E_{\text{CCSD(T)}}^{\infty} \approx E_{\text{singles}}(n = n_{\text{max}}) + E_{\text{pair}}^{\infty} + E_{(\text{T})}^{\infty}. \quad (7.13)$$

The pair energy (E_{pair}^{∞}) and the noniterative perturbative triples ($E_{(\text{T})}^{\infty}$) contributions were extrapolated to the CBS limit using either the conventional two-point n^{-3} formula (CBS row), as given in Eq. (5.30) [238, 239], or an approach based on the Riemann- ζ function (CBS $_{\zeta}$), as proposed recently in Ref. [304].

The higher-level correlation contributions ΔE_{HLC} of Eq. (7.11) are computed via

$$\Delta E_{\text{T}}^{\text{TQ}} = E_{\text{CCSDT}}^{\text{TQ}} - E_{\text{CCSD(T)}}^{\text{TQ}}, \quad (7.14a)$$

$$\Delta E_{(Q)}^{\text{TQ}} = E_{\text{CCSDT}(Q)}^{\text{TQ}} - E_{\text{CCSDT}}^{\text{TQ}}, \quad (7.14b)$$

where TQ denotes that the corresponding correlation contribution has been obtained by extrapolating the CCSD(T), CCSDT, and CCSDT(Q) correlation energies with $n = 3$ and $n = 4$ basis-sets using the two-point n^{-3} formula.

The resulting values of 4.173 857 eV for the aug-cc-pwCV n Z-PP basis sets and 4.176 985 eV for the aug-cc-pCV n Z-PP basis sets, as obtained from Tab. 7.1, agree well with the experimental value of $I_{\text{Rb}}^{\text{exp}} = 4.1771281 \pm 0.0000012$ eV [258]. A comparative analysis in Appendix F.1 with the UET17 basis sets as introduced in Chap. 5 finally shows the need of using basis sets, which were explicitly designed for a specific problem to obtain even better agreement with experimental findings. In the present case, it is not surprising that the UET17 basis sets perform better for ionization energies compared to the aug-cc-p(w)CV n Z-PP ones, since the former was constructed from basis sets originally optimized with respect to atomic polarizabilities [250]. Hence, the aug-cc-p(w)CV n Z-PP basis sets may still perform better for Rb_2^+ as they were designed for use in correlated molecular calculations.

Even more accurate results may be obtained by getting rid of the approximate ECP treatment and apply the all-electron spin-free exact two-component theory in its one-electron variant, SFX2C-1e [315, 316], instead. The expected accuracy of this approach is also tested for ionization energies of atomic Rb. However, for SFX2C-1e calculations, the corresponding aug-cc-pwCV n Z-X2C basis sets are only available up to $n = 4$ [240]. Therefore, the calculations corresponding to the third column of Tab. 7.1 used s-, p- and d-type primitive functions of the uncontracted ANO-RCC (23s,19p,11d) set augmented with f-, g-, h-, and i-type functions of the UET17 basis set series, as given in Tab. F.1 to obtain the TZ, QZ, 5Z, and 6Z sets [325]. The primitives of the ANO-RCC set are considerably tighter than the respective exponents of the UET17 basis set. In Appendix F.1 it is shown that the HF energy already reached its CBS limit for the UET17 basis set family and the singles contributions do not reveal the irregular behavior reported above for the aug-cc-p(w)CV n Z-PP basis sets. Thus, the CBS extrapolation was carried out for the total correlation energies using an n^{-3} approach, yielding smooth convergence as shown in Tab. 7.1. The same holds for higher-level correlation effects of SFX2C-1e calculations.

The higher-order relativistic effects $\Delta E_{\text{higher-rel}}$ of Eq. (7.11) are defined relative to the SFX2C-1e calculations and consist of the spin-orbit (SO) correction and the contribution from the Gaunt term, the two-electron picture-change (2e-pc) correction and quantum electrodynamics (QED) effects. The Gaunt term is obtained as the

difference between the spin-orbit X2C Hamiltonian [335–337] with atomic mean-field SO integrals [338] and the SFX2C-1e scheme at the CCSD(T) level. The 2e-pc correction is obtained as the difference between spin-free Dirac-Coulomb (SFDC) and SFX2C-1e CCSD(T) results [325]. It is less straightforward to incorporate $\Delta E_{\text{higher-rel}}$ into ECP calculations. The difficulty is that the ECP already contains a two-component spin-orbit coupled part with corresponding parameters adjusted to valence energies obtained at all-electron multiconfiguration Dirac-Coulomb-Hartree-Fock (DC-HF) level of theory, which includes relativistic effects at a four-component level of theory. Furthermore, one cannot use the difference between SFX2C-1e and higher order relativistic effects and ECP results using TZ or QZ basis sets (which are the largest correlation consistent basis sets available for SFX2C-1e) as the correction to ECP. The quality of these basis sets are not exactly the same as those for ECP calculations, so taking the difference introduces additional errors.

The spin-orbit, Gaunt, and two-electron picture-change corrections obtained at the CCSD(T) level using the uncontracted ANO-RCC basis set amount to 0.000 401 eV, 0.000 066 eV and 0.000 721 eV, respectively. A QED correction of 0.001 237 eV has been taken from Ref. [339]. The final computed value of 4.177 833 eV agrees very well with the experimental value of 4.177 128 eV, although the present agreement to within 0.001 eV seems somewhat fortuitous considering the remaining uncertainty in the treatment of basis-set and HLC effects.

This calculation of the ionization energy is very promising for reaching comparable accuracy for Rb_2^+ interaction potentials, if the HEAT protocol is systematically applied. Thus, it is important to describe a construction procedure for physically meaningful PECs at CCSD(T) level of theory, whereupon one can incorporate higher-order contributions according to Eq. (7.11). In this section, corresponding scECP-based ROHF-CCSD(T) calculations for I_{Rb} were performed using the MOLPRO 2018.2 program package [224, 225, 251]. Higher-level correlation contributions as listed in Tab. 7.1 were obtained using the CFOUR program package [317–320] and the MRCC program suite [40, 47, 321, 322].

7.3 | Construction procedure

The findings of Sec. 6.3 suggest that using both symmetry-broken and symmetry-adapted (T) corrections may be a promising approach to construct well-defined hybrid PECs for the $X\ ^2\Sigma_g^+$ and $(1)\ ^2\Sigma_u^+$ states of Rb_2^+ . Using symmetry-broken solutions for

the description of the respective long-range tails avoids the repulsive barriers and thus renders the entire curve physically meaningful. With this, it remains to properly merge with symmetry-adapted solutions in the intermediate range. The following describes a construction procedure that joins symmetry-broken and symmetry-adapted solutions and further grants a correct exchange splitting interaction between the $X^2\Sigma_g^+$ and $(1)^2\Sigma_u^+$ states.

The hybrid ROHF-CCSD(T) energies for the gerade and ungerade states are defined as

$$E_{\text{CCSD(T)}}^{\text{hybrid}}(R) = E_{\text{ROHF}}^{D_{2h}}(R) + \Delta E_{\text{CCSD}}^{D_{2h}}(R) + \Delta E_{(T)}^{\text{hybrid}}(R), \quad (7.15)$$

where the first two terms denote the ROHF reference energy and the CCSD correlation contribution, respectively, both obtained from symmetry-adapted calculations. The last term in Eq. (7.15) describes the hybrid (T) correction, which may be written as

$$\Delta E_{(T)}^{\text{hybrid}}(R) = \Delta E_{(T)}^{C_{2v}} \Theta(R - R_m) + \left[\Delta E_{(T)}^{D_{2h}}(R) + |\Delta E_s| \right] \Theta(R_m - R), \quad (7.16)$$

with the Heaviside function $\Theta(R)$. This formally represents the use of (T) corrections from symmetry-broken calculations to model the long-range tail [first term in Eq. (7.16)] and the proper merging to symmetry-adapted (T) corrections at some merging point R_m in the intermediate region to describe the remaining part of the PEC [second term in Eq. (7.16)]. At R_m the symmetry-adapted values have to be shifted by the respective energy difference $|\Delta E_s|$ to the symmetry-broken solution to obtain a continuous curve. This construction procedure is also visualized in Fig. 7.2. The small oscillation that occurs for the symmetry-broken (T) curve before it collapses to the symmetry-adapted one is a consequence of the numerical bistability of the symmetry-broken CCSD(T) solution in the region where it cannot “decide” whether to collapse to the symmetry-adapted Σ_g or Σ_u state; cf. Sec. 6.3. Note that the point group labels merely refer to the computational point groups, which are Abelian subgroups of the actual $D_{\infty h}$ and $C_{\infty v}$ continuous groups.

The merging point R_m enters as an additional degree of freedom into the model and might eventually be adjusted so to optimally reproduce certain experimental findings (e.g. spectroscopic constants, scattering lengths or vibrational levels). Since the $X^2\Sigma_u^+$ and $(1)^2\Sigma_u^+$ states are asymptotically degenerate the above construction procedure can be used for both PECs. This implies, as discussed below, that R_m should be chosen identically for both the gerade and the ungerade state. The same choice for R_m is only justified if both states are reasonably well degenerate for a particular merging

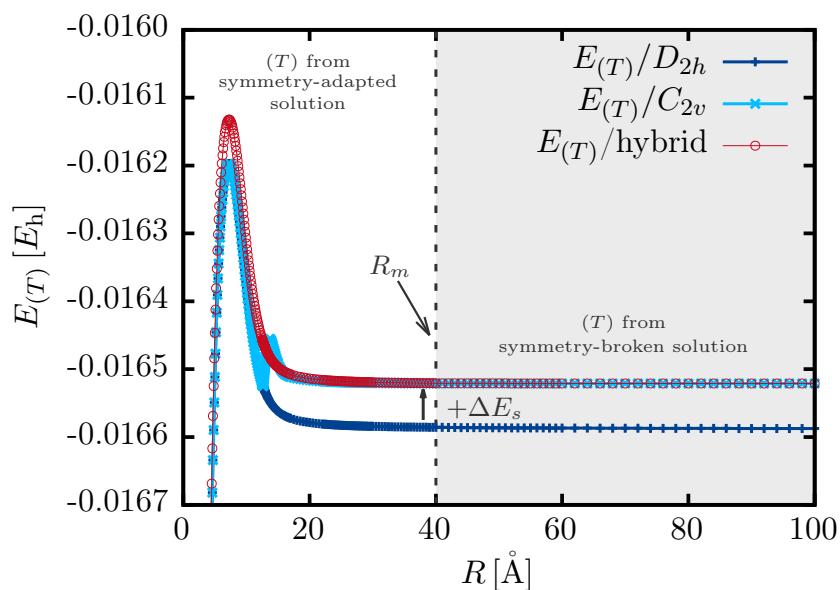


FIGURE 7.2.: Schematic visualization of the hybrid PEC construction procedure according to Eqs. (7.15) and (7.16). As discussed in Sec. 6.3, at the Coulson-Fischer point R_{CF} the symmetry-broken solutions collapse to the symmetry-adapted ones, which also holds for (T) corrections as displayed here. Using symmetry-broken (T) solutions in the long-range (gray area) avoids the repulsive barrier. At some point R_m (dashed vertical line; here chosen to be $R_m = 40.0 \text{ \AA}$) in the intermediate region one has to properly merge with the symmetric solution by shifting it by ΔE_s . This yields a hybrid (T) description. The merging point enters as an additional degree of freedom with the only restriction defined by Eq. (7.17). This example corresponds to calculations of the $X \ ^2\Sigma_g^+$ state at ECP28MDF/aug-cc-pCV5Z-PP level of theory.

point. In the following, it is assumed that this is the case if the difference between the symmetry-adapted ROHF-CCSD(T) absolute energies is $\leq 10^{-8} E_h$. Furthermore, the merging point R_m should be sufficiently far apart from the repulsive long-range barrier occurring at $R \approx 100 \text{ \AA}$ (cf. Fig. 6.2). These two conditions define the restriction

$$27.0 \text{ \AA} \leq R_m < 50.0 \text{ \AA}. \quad (7.17)$$

In the following this value is set, without loss of generality, to $R_m = 40.0 \text{ \AA}$.

The analysis of ionization energies listed in Tab. 7.1 demonstrated the importance of basis set extrapolation to estimate the CBS limit of the aug-cc-pCV n Z-PP basis sets. This importance is also expected for Rb_2^+ , where it was again found best to use an approach based on Eqs. (7.12) and (7.13). An alternative approach with singles contributions included in the n^{-3} two-point extrapolation formula for CCSD(T) correlation energies revealed negligible effects on the dissociation energy D_e and the equilibrium distance R_e of the $X \ ^2\Sigma_g^+$ and $(1) \ ^2\Sigma_u^+$ states. However, due to the observed irregular behavior of

singles contributions that occurred in atomic calculations, as discussed in Appendix F.2, it may be better to also not extrapolate this part in molecular calculations. Furthermore, it was found that using the actually suggested three-point-extrapolation formula [236] according to Eq. (F.1) for the Hartree-Fock energy and the singles contribution yielded rather strong oscillations in the asymptotic region of the corresponding Rb_2^+ PECs. This is in line with the observations from Chap. 5 concerning Rb_2 PECs and the V_3 contribution of Rb_3 based on the UET17 and UET15 basis set series and might be due to the fact that an e^{-bn} -ansatz tends to exaggerate tiny irregularities.

Again, note that consistent CBS values are only obtained if the merging point R_m has been chosen equally for all basis sets used for extrapolation.

Beyond estimating the CBS values, the PECs shall also serve as a solid foundation for studying Rb^+ - Rb scattering events. As outlined in Sec. 7.1 this is determined by the respective long-range form of the interaction potentials and involves the exchange splitting [cf. Eq. (7.1)] between the gerade and ungerade states. Thus, to allow for accurate predictions of scattering properties, it is important to ensure that the *ab-initio* data reproduce the exchange interaction as suggested by Eq. (7.6). This also explains why it is important to choose the same R_m value for both the $X^2\Sigma_g^+$ and the $(1)^2\Sigma_u^+$ state (if it were chosen differently the V_{exch} term would show a discontinuity). The following protocol may be used to incorporate the exchange interaction into the PEC construction procedure:

1. Compute the difference $\Delta(R)$ between the theoretically suggested exchange splitting $V_{\text{exch}}(R)$ of Eq. (7.6) [with corresponding parameters from Eqs. (7.7) and (7.8)] and the one according to Eq. (7.5) resulting from the use of CBS *ab-initio* values $\tilde{V}_{\text{exch}}(R)$, i.e.

$$\Delta(R) = V_{\text{exch}}(R) - \tilde{V}_{\text{exch}}(R). \quad (7.18)$$

2. It is not necessary to account for the correct exchange splitting of Eq. (7.6) over the entire range of internuclear distances, since according to Ref. [332] this theoretical formula is only valid for

$$R\beta \gg 1 \quad \text{and} \quad R\beta^2 \gg 1. \quad (7.19)$$

In the following it is assumed that this means that both products have to be at least one order of magnitude greater than one. Accordingly, this yields a range \mathbb{W} of internuclear distances R , where one has to ensure that the theoretically suggested exchange splitting is correctly reproduced by the respective PECs. This

means that the PECs have to be modified for (note that Eq. (7.6) is given in atomic units)

$$R \in \mathbb{V} = [40.0, \infty) a_0 \approx [21.0, \infty) \text{ \AA}. \quad (7.20)$$

Note that this is independent from the *fixed* chosen merging parameter R_m introduced above to join symmetry-broken and symmetry-adapted (T) corrections. The *ab-initio* long-range parts \tilde{V}_{LR} of the $X \ ^2\Sigma_g^+$ and $(1) \ ^2\Sigma_u^+$ states will show the V_{exch} form of Eq. (7.6) if they are *additionally* modified according to

$$\tilde{V}_{\text{LR}}^{\Sigma_g^+}(R) = \begin{cases} \tilde{V}_{\text{LR}}^{\Sigma_g^+}(R) + \Delta(R_v = 40.0 a_0), & \text{for } R < 40.0 a_0 \\ \tilde{V}_{\text{LR}}^{\Sigma_g^+}(R) + \Delta(R), & \text{for } R \geq 40.0 a_0 \end{cases}, \quad (7.21)$$

and

$$\tilde{V}_{\text{LR}}^{\Sigma_u^+}(R) = \begin{cases} \tilde{V}_{\text{LR}}^{\Sigma_u^+}(R) - \Delta(R_v = 40.0 a_0), & \text{for } R < 40.0 a_0 \\ \tilde{V}_{\text{LR}}^{\Sigma_u^+}(R) - \Delta(R), & \text{for } R \geq 40.0 a_0 \end{cases}, \quad (7.22)$$

where R_v labels the lower bound of the validity interval (7.20). Thus, for $R \in \mathbb{V}$ the long-range tails are continuously shifted via $\Delta(R)$, while for $R \notin \mathbb{V}$ they are constantly shifted to provide a smooth connection.

3. Pass the modified *ab-initio* data (\equiv “hybrid/CBS/mod” level of theory) to the one-dimensional RP-RKHS interpolation method as discussed in Chap. 5. This guarantees the correct reproduction of leading-order induction and dispersion interaction according to Eq. (7.2).

In general, this scheme may be applied to those *ab-initio* data obtained at the highest available level of theory, i.e. for instance the hybrid ROHF-CCSD(T) approach with higher-level correlation effects included.

Figure 7.3 (a) provides an overview of exchange splittings \tilde{V}_{exch} that result from *ab-initio* data with different basis set sizes and compares them with the theory curve (7.6). The splittings for the QZ basis set show a tiny barrier of $\approx 3 \cdot 10^{-3} \text{ cm}^{-1}$ in size, independent if the pure symmetry-adapted solution or the hybrid PEC model of Eq. (7.15) is used. Numerical errors can be excluded since the same convergence thresholds as in Chap. 6 were used (cf. Appendix F.4). It could be shown that the tiny barrier already occurs at the HF level and may thus be attributed to limitations of the aug-cc-pCVQZ-PP basis set in terms of lacking appropriate diffuse functions (e.g. d-aug-QZ). The long-range tail is generally rather sensitive to the augmentation

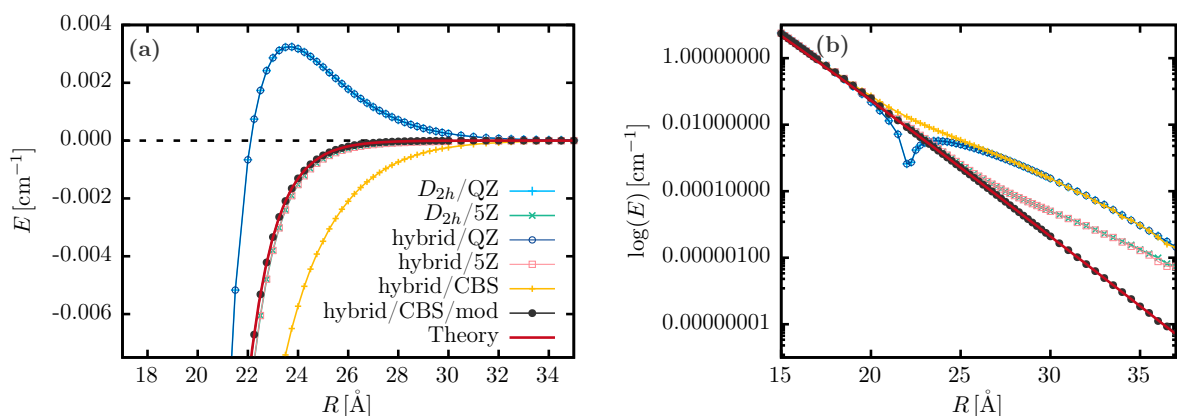


FIGURE 7.3.: Overview on basis set effects on the *ab-initio* exchange splitting \tilde{V}_{exch} according to Eq. (7.5). **(a)** The tiny hump occurring for both symmetry-adapted and hybrid ROHF-CCSD(T) results [Eq. (7.15)] at QZ basis set quality indicates an insufficient description in terms of diffuse functions. The barrier disappears for the 5Z basis set but leads to a large deviation of the exchange splitting at the hybrid/CBS level relative to the theoretical form (red curve). The black dotted line shows the modified hybrid/CBS results (\equiv hybrid/CBS/mod) that follow from modifying the hybrid/CBS *ab-initio* data according to Eqs. (7.21) and (7.22) within the protocol discussed in this regard. **(b)** Logarithmic representation to clarify the deviations.

of the applied basis set and more accurate and reliable answers may be generated if these basis set effects were further studied and properly accounted for by higher augmentations with diffuse functions. The aug-cc-pCV5Z-PP basis set almost coincides with the theory curve and one may thus conclude that it is sufficiently augmented. However, due to the comparatively bad performance of the QZ basis, the CBS result goes off the theory curve. This demonstrates the need to modify these results to correctly reproduce the theory. The deviations of the different approaches relative to the theory curve (7.6) are clarified in the logarithmic representation of Fig. 7.3 (b).

The one-dimensional RP-RKHS interpolation method as discussed in Chap. 5 is used to produce the Rb_2^+ interaction potentials of the $X^2\Sigma_g^+$ and $(1)^2\Sigma_u^+$ states. Corresponding training data are generated subject to the above construction procedure by first transforming the *ab-initio* calculations according to the hybrid model of Eqs. (7.15) and (7.16). The resulting data are then modified to reproduce the correct exchange interaction using Eqs. (7.21) and (7.22). It is important to provide sufficient training data in the region $R \in [20.0, 60.0]$ Å to ensure precise interpolation of the exchange interaction. Beyond that region, the training data should be chosen sparsely to grant extrapolation to the correct long-range form after Eq. (7.2). As shown in Sec. 5.1.1 this is readily incorporated in the RP-RKHS method, provided that experimental or highly

accurate theoretical values for C_4^{ind} , C_6^{ind} , C_6^{disp} , etc. are available. The C_4^{ind} and C_6^{ind} induction coefficients are proportional to the static electric dipole polarizability α_d and the static electric quadrupole polarizability α_q , respectively; cf. Eqs. (7.3) and (7.4). In Ref. [340] it has been suggested to use the measured α_d value from Ref. [341], yielding $C_4^{\text{ind}} = 2.751960345 \cdot 10^6 \text{ cm}^{-1} \text{ \AA}^4$. There are several theoretical works that computed values for static electric multipole polarizabilities. In the following the most recent α_q value based on relativistic coupled-cluster calculations from Ref. [342] is taken, yielding $C_6^{\text{ind}} = 0.156412961 \cdot 10^8 \text{ cm}^{-1} \text{ \AA}^6$. The C_6^{disp} coefficient may be obtained from fitting to *ab-initio* data, which is further discussed in Sec. 7.4. However, as the *s*-wave scattering regime for Rb_2^+ might not be reached at all (cf. Sec. 7.1) it is expected to be sufficient to only include the first two leading-order induction contributions (i.e. C_4^{ind} and C_6^{ind}).

The remaining RP-RKHS parameters are chosen as

$$n_{\text{Rb}_2^+} = 2 \quad \text{and} \quad m_{\text{Rb}_2^+} = 1 \quad \text{and} \quad s_{\text{Rb}_2^+} = 2, \quad (7.23)$$

and $R_a = 20.0 \text{ \AA}$ for the $X^2\Sigma_g^+$ state and $R_a = 85.0 \text{ \AA}$ for the $(1)^2\Sigma_u^+$ state. Furthermore, to provide a physically meaningful short-range description a respective correction of the form given in Eq. (5.31) has been applied.

7.4 | Results

The above construction procedure yields the PECs shown in Fig. 7.4 (a) corresponding to the hybrid ROHF-CCSD(T) approach of Eq. (7.15) at the CBS limit of the aug-cc-pCVnZ-PP basis set with incorporated modification for correct exchange interaction (i.e. hybrid/CBS/mod level of theory). As exemplarily depicted in Fig. 6.1, the ground state is much deeper than the ungerade state, which only shows a very shallow well at about 12 \AA . The choice of the merging point R_m , within the constraints defined by Eq. (7.17), mainly determines the long-range behavior of the respective PECs, while it leaves R_e effectively unchanged and alters D_e by less than 0.5 cm^{-1} . This is even less for the modification introduced by accounting for the theoretically suggested exchange interaction. The free parameter R_m can be viewed as defining the lower bound of the fitting range to extract higher-order induction and dispersion coefficients (C_6^{disp} , etc.) from corresponding *ab-initio* data. This is indicated in Fig. 7.4 (b) in terms of differences between *ab-initio* long-range tails and the theoretical behavior V_{ind} according to Eq. (7.2) with only C_4^{ind} or additionally C_6^{ind} included. Since symmetry-broken and symmetry-adapted (T) solutions converge to different asymptotes (cf. Fig. 7.2), the long-range tail

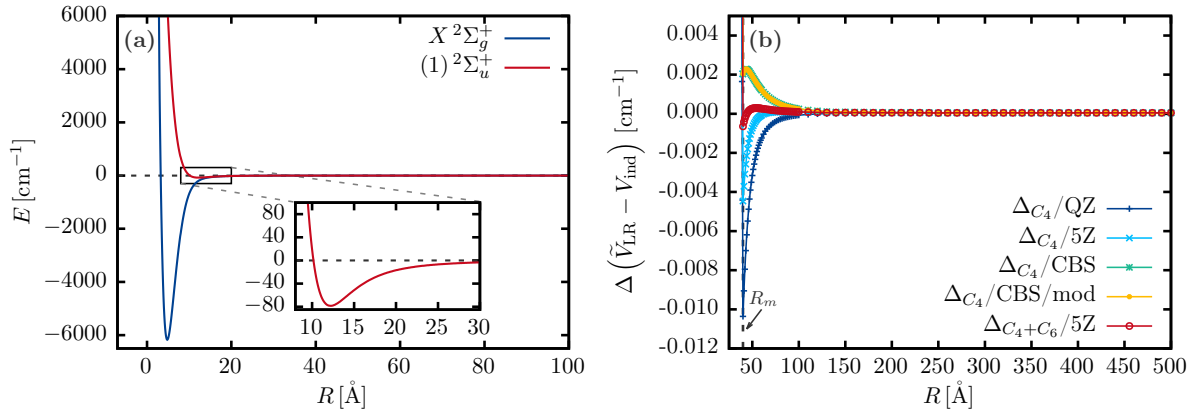


FIGURE 7.4.: **(a)** Potential energy curves of the $X\ 2\Sigma_g^+$ and $(1)\ 2\Sigma_u^+$ states of Rb_2^+ resulting from the construction procedure of Sec. 7.3 with the RP-RKHS interpolation method based on *ab-initio* data at hybrid/CBS/mod level of theory. The inset shows the shallow potential well of the ungerade state. **(b)** Differences between the hybrid ROHF-CCSD(T) *ab-initio* long-range PEC tails \tilde{V}_{LR} obtained according to Eq. (7.15) and $V_{\text{ind}}(R)$ after Eq. (7.2) with only C_4^{ind} included ($\equiv \Delta_{C_4}$) or additionally C_6^{ind} considered ($\equiv \Delta_{C_4+C_6}$) for different basis set sizes. The merging point R_m mainly determines the fitting range to extract long-range C coefficients. Results corresponding to the QZ and 5Z basis sets are more attractive as compared to the theory. The CBS result spoils the long-range description. This explains the values obtained through fitting in Tab. 7.2 and indicates the problems to obtain higher-order induction/dispersion coefficients from fits (see text for details).

and thus the difference with respect to the form after Eq. (7.2) behaves differently left and right to R_m .

The extraction of higher-order induction and dispersion coefficients from fits to *ab-initio* data might improve the PECs obtained from the RP-RKHS method by including these coefficients into the extrapolation form defined by Eq. (7.2). The fit quality may be first tested in terms of fitting approaches that merely involve the leading order $-C_4^{\text{ind}}/R^4$ term and then compare to experimental and theoretical available values of the static electric dipole polarizability α_d through Eq. (7.3). Table 7.2 lists the results as a function of increasing basis set size. First this looks rather promising, since the fitted C_4^{ind} values and thus the thereof extracted static electric dipole polarizabilities α_d are close to experimental values and in accordance with other theoretical works. The theoretical values were either obtained from using simple asymptotic wavefunctions for the valence electron to evaluate multipolar matrix elements [301] or from applying relativistic *ab-initio* methods [250, 342, 344, 345]. However, the differences between asymptotic *ab-initio* energies and $V_{\text{ind}}(R)$ according to Eq. (7.2) with C_4^{ind} or additionally C_6^{ind} included, as shown in Fig. 7.4 (b) reveal certain problems connected with the fitting approach to obtain higher-order induction/dispersion coefficients. The results

TABLE 7.2.: Synopsis of C_4^{ind} coefficients obtained through fitting of corresponding *ab-initio* data at hybrid ROHF-CCSD(T) level of theory after Eq. (7.15) with different basis set sizes. Equation (7.3) connects the induction coefficients to the static electric dipole polarizability α_d and allows for comparison with experimental measurements and theoretical works. The numbers obtained here may be understood with Fig. 7.4 (b) and the discussion in the text.

basis set size	$\alpha_d [\text{\AA}^3]$	$C_4^{\text{ind}} [10^6 \text{ cm}^{-1} \text{\AA}^4]$
$n = 4$	47.69	2.769 278 754
$n = 5$	47.43	2.754 157 578
CBS	47.14	2.737 557 003
CBS/mod	47.14	2.737 535 731
experimental works		
[343]	47.24	2.743 249 772
[341]	47.39	2.751 960 345
theoretical works		
[301] (asymptotic wavefunctions)	47.64	2.766 477 967
[250] (CCSD(T) with DK method)	47.29	2.746 153 296
[344] (relativistic all-order approach)	47.72	2.771 123 605
[342] (relativistic coupled-cluster method)	47.17	2.739 022 661

strongly depend on the fitting range which is mainly determined by R_m . Due to the negative energy differences obtained for the QZ- and 5Z basis set qualities the corresponding results are slightly larger compared to the experimental ones. If the C_6^{ind} contribution is included to the theory curve after Eq. (7.2) the 5Z basis set shows very good agreement. However, extrapolating to the CBS limit spoils this behavior independent of the inclusion of the modification in terms of the exchange interaction. Using the corresponding *ab-initio* energies in the fitting approach with C_4^{ind} and C_6^{ind} fixed to experiment and theory, respectively, would lead to exceedingly large and negative values for C_6^{disp} . This would be in contrast to what has been observed for other alkali dimer cations in Ref. [119]. In line with the observations for the exchange interaction in Fig. 7.3, this also suggests to investigate basis set effects, in particular in regard to augmentation with diffuse functions. So far, it is recommended, if at all, to extract higher-order dispersion and induction coefficients from 5Z results. The obtained values could be used to check the sensitivity of scattering calculations on accounting for such higher-order effects.

Table 7.3 gives an overview of spectroscopic constants for both the $X \ ^2\Sigma_g^+$ and the $(1) \ ^2\Sigma_u^+$ state. The minima of the potentials may be characterized by the dissociation energy D_e (the positive binding energy) and the corresponding equilibrium distance R_e

TABLE 7.3.: Overview on the aug-cc-pCV n Z-PP basis set size dependence of spectroscopic constant of the $X\ ^2\Sigma_g^+$ and $(1)\ ^2\Sigma_u^+$ states of Rb_2^+ extracted from RP-RKHS interpolated PECs based on *ab-initio* data obtained from the hybrid ROHF-CCSD(T) approach of Eq. (7.15). The CBS/mod results contain the modifications entering through accounting for the correct exchange splitting behavior. The potentials minima are characterized by the dissociation energy D_e and the equilibrium distance R_e . The rovibrational ground state ($v = 0, J = 0$) relative to the dissociation asymptote is labeled by D_0 and was calculated using the LEVEL16 code [346]. Experimental and theoretical results are given for comparison. The assignment to the respective constituting isotope $^{85}\text{Rb}_2^+$ or $^{87}\text{Rb}_2^+$ is given in parenthesis.

basis set size	$X\ ^2\Sigma_g^+$			$(1)\ ^2\Sigma_u^+$		
	D_e [cm^{-1}]	D_0 [cm^{-1}]	R_e [\AA]	D_e [cm^{-1}]	D_0 [cm^{-1}]	R_e [\AA]
$n = 4$	6153.2971	–	4.8269	80.3830	–	12.2205
$n = 5$	6163.4805	–	4.8139	79.4019	–	12.2067
CBS	6174.1610	–	4.8000	78.3109	–	12.1906
CBS/mod ($^{87}\text{Rb}_2^+$)	6174.1488	6151.3451	4.8000	78.3231	76.4975	12.1906
CBS/mod ($^{85}\text{Rb}_2^+$)	6174.1488	6151.0786	4.8000	78.3231	76.4764	12.1906
experimental works						
[347, 348]	5888±484	–	–	–	–	–
[349]	–	–	3.94	–	–	–
[350]	6049±807	–	–	–	–	–
[351] ($^{85}\text{Rb}_2^+$)	–	$\geq 6307.5(6)$	–	–	–	–
theoretical works						
[127]	6167	–	4.7943	82	–	12.1340
[352]	5816	–	4.8684	–	–	–
[351] ($^{85}\text{Rb}_2^+$)	–	6200	–	–	–	–

obtained from the RP-RKHS interpolated PECs based on *ab-initio* interaction energies relative to the last *ab-initio* point at $R = 500.0\ \text{\AA}$. The energies of the rovibrational ground states [i.e. $(v, J) = (0, 0)$] are labeled by D_0 and were extracted from calculations using the LEVEL16 code [346]. Here, the quantum numbers v and J denote vibrational and rotational states, respectively.

Due to the discussed basis set effects occurring for the *ab-initio* exchange splittings, merely the extrapolated CBS values are modified according to Eqs. (7.21) and (7.22). For both $X\ ^2\Sigma_g^+$ and $(1)\ ^2\Sigma_u^+$ states this only leads to tiny changes in D_e , while R_e remains unaffected as can be observed from Tab. 7.3. Further one may notice that in the case of the $X\ ^2\Sigma_g^+$ state, increasing the basis set size yields increased potential

well depths and reduced equilibrium distances. For the $(1) \ ^2\Sigma_u^+$ state the situation is reversed with both D_e and R_e decreasing with increasing basis set size. Note that the results presented in this chapter are still based on the first two terms of the pursued HEAT protocol after Eq. (7.11). Preliminary results for the $X \ ^2\Sigma_g^+$ state including higher-level correlation (HLC) effects at CCSDT level of theory according to Eq. (7.14) revealed that D_e is increased by $\approx +2 \text{ cm}^{-1}$ to $D_e \approx 6176 \text{ cm}^{-1}$, while the equilibrium distance slightly elongates by $\approx +0.2 \text{ pm}$.

There are comparatively few experimental data available in the literature to benchmark the accuracy of the presented *ab-initio* results. This might be due to the stringent temperature requirements for the Rb_2^+ system to enter the ultracold regime; cf. Sec. 7.1. Experimental works found in the literature dating back to the 60s to 80s of the last century and have been performed in Rb vapor with densities of $2.69 \cdot 10^{19} \text{ atoms cm}^{-3}$ [347]. This clearly leads to large uncertainties in the measurements, as indicated in Tab. 7.3. Experimental techniques range from associative photoionization [347, 348] to rough estimates based on the analysis of charge exchange cross sections [349] to multiphoton ionization of Rb_2 and subsequent dissociation of dimer ions by one or more additional photons [350]. The most recent experimental work [351] aimed at measuring the ionization potential of $^{85}\text{Rb}_2$ formed via photoassociation of ultracold ^{85}Rb atoms. The molecules were subsequently excited by single-photon UV transitions to states above the ionization threshold. This approach resulted in an upper limit for the ionization energy of $^{85}\text{Rb}_2$ and provided a lower bound for D_0 of $^{85}\text{Rb}_2^+$; as reported in Tab. 7.3 with $D_0 \geq 6307.5 \text{ cm}^{-1}$.

Similarly, the literature barely provides any theoretical works on Rb_2^+ . Results are either based on calculations using an approximated Hamiltonian and a large-core pseudopotential approach [127] or on model potential calculations [352]. The latter treats the molecular ion by one active electron moving in the field of two alkali ions. This is described by the sum of ℓ -independent electron-ion interaction potentials, a core-polarization potential, and a core-core interaction potential. There are only few *ab-initio* calculations; for instance the one accompanying the experimental work in Ref. [351]. Herein, the authors use an approach originally proposed for calculations on Rb_2 based on a non-empirical relativistic large-core pseudopotential and a full-valence configuration-interaction treatment. Spin-orbit effects were accounted for in the valence CI calculations via the CIPSO procedure (configuration interaction with perturbation including spin-orbit coupling). Details on this approach may be found in Ref. [353].

The previously mentioned HLC effects at CCSDT level merely introduce corrections

of $\leq \mathcal{O}(10 \text{ cm}^{-1})$. Since correlation contributions beyond full triples corrections (i.e. CCSDT(Q), CCSDTQ, etc.) are usually even smaller, one may not expect considerable changes in regard to D_e , D_0 and R_e by including all computationally affordable HLC terms so to get from $D_0(\text{CBS}/\text{mod}) = 6151.3451 \text{ cm}^{-1}$ to the lower bound of Ref. [351] with $D_0^{\text{exp}} \geq 6307.5 \text{ cm}^{-1}$. Therefore, if the latter is taken as solid reference, one may first conclude that relativistic effects are rather important. But, the applied ECP28MDF small-core pseudopotential [250] includes a two-component spin-orbit coupled part with corresponding parameters adjusted to valence energies obtained at all-electron multiconfiguration Dirac-Coulomb-Hartree-Fock (DC-HF) level of theory, which includes relativistic effects at a four-component level of theory. Thus, the present approach already accounts for important relativistic effects and it may not be expected that higher-order relativistic contributions relative to SFX2C-1e results (cf. Sec. 7.2) lead to significant changes of $\mathcal{O}(150 \text{ cm}^{-1})$ to reach D_0^{exp} as given in Tab. 7.3. This implies that basis set effects may play the most decisive role, which is also supported by the above observations concerning the exchange interaction in Fig. 7.3 and the fitting approach to obtain induction and dispersion coefficients (cf. Fig. 7.4 and Tab. 7.2). These findings suggested a lack of diffuse functions. Preliminary investigations in Appendix F.7 using the UET17 and UET17(lt) basis sets of Tabs. F.1 and F.2, respectively, as well as the aug-cc-pwCVnZ-PP variants from Ref. [240], confirm this sensitivity on basis set effects. The aug-cc-pwCVnZ-PP series reveals an analogous irregular behavior for D_e with increasing n as observed for ionization energies in Tab. 7.1; with $D_e(n=3) \approx 6164 \text{ cm}^{-1}$, $D_e(n=4) \approx 6255 \text{ cm}^{-1}$ and $D_e(n=5) \approx 6173 \text{ cm}^{-1}$. Thus, estimating proper CBS values might turn out problematic. The equilibrium distance R_e for each n is shortened by $\approx 0.1 \text{ \AA}$ as compared to the respective aug-cc-pCVnZ-PP curves given in Tab. 7.3. In contrast to that, the UET17 and UET17(lt) basis sets behave regularly. The former yields $D_e(\text{UET17}/n=4) \approx 6153 \text{ cm}^{-1}$, $D_e(\text{UET17}/n=5) \approx 6172 \text{ cm}^{-1}$, and $D_e(\text{UET17}/n=6) \approx 6176 \text{ cm}^{-1}$, thus suggesting $D_e(\text{UET17}/\text{CBS}) \approx 6180 \text{ cm}^{-1}$. The UET17(lt) basis set, where the tightest g -, h -, and i -exponents were replaced by diffuse ones, show $D_e(\text{UET17(lt)}/n=4) \approx 6156 \text{ cm}^{-1}$, $D_e(\text{UET17(lt)}/n=5) \approx 6179 \text{ cm}^{-1}$ and $D_e(\text{UET17(lt)}/n=6) \approx 6188 \text{ cm}^{-1}$ from which one can estimate $D_e(\text{UET17(lt)}/\text{CBS}) \approx 6200 \text{ cm}^{-1}$. For both the UET17 and UET17(lt) basis set, R_e is comparable to the values obtained for aug-cc-pCVnZ-PP in Tab. 7.3. On the one hand this demonstrates that basis set effects introduce most significant contributions as compared to missing HLC or higher-order relativistic effects. On the other hand it endorses the importance of augmenting basis sets with diffuse functions. This

augmentation may then have impact on both the exchange splitting and D_e (D_0). Beyond that, it may be worth testing different coupled-cluster methods such as the electron affinity equation-of-motion coupled-cluster (EA-EOM-CC) approach [354]. Recent theoretical investigations on Li_2^+ , Na_2^+ and K_2^+ [129–131] were based on (non-relativistic) EA-EOM-CCSD or EA-EOM-CCSDT computations as well as on EA-EOM-CCSD calculations with scalar relativistic effects included via the Douglas-Kroll-Hess method. The results reported therein, e.g., for the $X^2\Sigma_g^+$ ground state of K_2^+ [131], with all electrons correlated at EA-EOM-CCSDT or EA-EOM-CCSD-DK2 level of theory using ANO-RCC or ANO-RCC+ basis sets, respectively, show deviations of $\approx \pm 200 \text{ cm}^{-1}$ with respect to the experimentally derived value of D_e and up to 0.1 \AA discrepancy for R_e . This is in line with present findings on Rb_2^+ and may support the previous implication that basis set effects are the most subtle part for highly accurate investigations of X_2^+ systems, with $X = \{\text{Li}, \text{Na}, \text{K}, \text{Rb}, \text{Cs}\}$.

Besides, an analysis of the rovibrational term values supported by the $X^2\Sigma_g^+$ and $(1)^2\Sigma_u^+$ RP-RKHS interpolated PECs at hybrid/ROHF-CCSD(T)/CBS/mod level of theory revealed the existence of 282 and 70 vibrational levels, respectively. These calculations were performed using the LEVEL16 program [346] assuming that Rb_2^+ exclusively consists of the ^{87}Rb isotope. To obtain $V(r)$ with the correct long-range behavior, inner-turning points ranging from 3.0 to 640.0 \AA and 8.0 to 640.0 \AA for the gerade and ungerade states, respectively, have to be provided. The corresponding rovibrational structures for $(v, J = 0)$ are shown in Figs. 7.5 (a) and (b). The last bound state for the gerade state was found for $(v'', J'') = (281, 7)$ with $E_b^*[X^2\Sigma_g^+] = -7.3878 \text{ MHz}$ and the one for the ungerade state at $(v', J') = (69, 5)$ with $E_b^*[(1)^2\Sigma_u^+] = -5.1350 \text{ MHz}$. These numbers were obtained by integrating the radial Schrödinger equation from 2.4 to 2500.0 \AA in case of the $X^2\Sigma_g^+$ state and from 5.1 to 2500.0 \AA , respectively for the $(1)^2\Sigma_u^+$ state, using the Numerov-Cooley algorithm as implemented in LEVEL16. This huge integration range is by far larger than for conventional quantum chemistry applications, but is necessary due to the characteristic interaction length scale $R^* \approx 2500 \text{ \AA}$ of Eq. (7.9). This required to set the integration mesh size to $\text{RH} = 0.01$, which is much larger than $\text{RH}_{\text{Lit}} = 0.0005$, as actually suggested according to Ref. [346]. The accuracy of the eigenvalues and eigenfunction obtained, however is largely determined by the size of RH . Hence, the reliability of the obtained threshold bound states should be considered with caution. There are even higher lying threshold bound states expected; their detection would require integration ranges $R > 2500.0 \text{ \AA}$. This is where conventional *ab-initio* codes reach their limits as they are usually designed

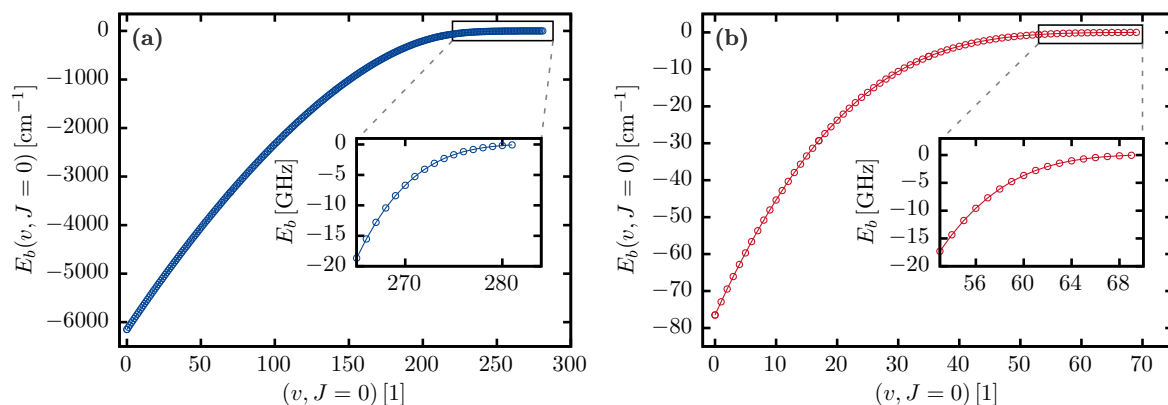


FIGURE 7.5.: Binding energies E_b of vibrational levels v corresponding to the rotational quantum number $J = 0$. The calculations are based on the RP-RKHS interpolated PECs at hybrid/CBS/mod level of theory using the LEVEL16 code assuming that Rb_2^+ exclusively contains the ^{87}Rb isotope. **(a)** Results for the $X^2\Sigma_g^+$ state. It was found that the respective PEC supports 282 vibrational levels. The inset shows a close-up to the threshold bound-states (note that the energy scale is given in GHz for improved visualization of the threshold bound states). **(b)** Results for the $(1)^2\Sigma_u^+$ state. It was found that the respective PEC supports 70 vibrational levels. The inset shows a close-up to the threshold bound-states (note that the energy scale is given in GHz for improved visualization of the threshold bound states).

to accurately predict deeply bound rovibrational states. Furthermore, the calculation of threshold bound states may also be affected by the final PEC depth.

Nevertheless, the deeply bound rovibrational states should be on the same level of accuracy as the corresponding PEC. This means that the total number of rovibrational states and their assignment to the respective eigenenergies depend on the final potential depth obtained at the highest possible level of theory. As indicated in Tab. 7.3 and discussed previously the potential depth, at least for the $X^2\Sigma_g^+$ state, is expected to increase. However, comparing the magnitude of the states resolved so far, to the 41 vibrational levels supported by the $a^3\Sigma_u$ PEC of Rb_2 , with a well-depth of $\approx 241 \text{ cm}^{-1}$ (see Appendix F.3), directly shows the exceedingly large interaction range of Rb_2^+ . Even the $(1)^2\Sigma_u^+$ state of Rb_2^+ supports 70 vibrational levels within a very shallow well depth of $\approx 78 \text{ cm}^{-1}$.

This chapter showed that it is possible to construct physically meaningful interaction potentials for Rb_2^+ based on a hybrid ROHF-CCSD(T) approach to circumvent the occurrence of the repulsive long-range barrier as discussed in Chap. 6. Furthermore, the PECs for the $X^2\Sigma_g^+$ and $(1)^2\Sigma_u^+$ states are designed such that they reproduce the exchange splitting according to Eq. (7.6). This is particularly important for subsequent scattering calculations based on these curves. While the presented approach also

allows to include higher-level correlation contributions and higher-order relativistic effects, it could be demonstrated that basis set effects play the most important role in reaching high accuracy. In this regard, the investigations of the exchange interaction in Fig. 7.3, of the C_4^{ind} coefficients in Tab. 7.2, and of the spectroscopic constants D_e , D_0 and R_e in Tab. 7.3 revealed the need for basis sets augmented with more diffuse functions. This will be thoroughly analyzed for a future publication.

Part IV

CONCLUSION

8

SUMMARY AND OUTLOOK

This thesis was stimulated by two experimental proposals in the field of ultracold quantum gases. On the one hand, the realization of PA processes of isolated ultracold rubidium trimers and on the other hand exploring the prospects towards entering the quantum level for $\text{Rb} + \text{Rb}^+$ ion-atom scattering processes. The presented results may provide some experimental guidance but may also serve as a solid foundation for subsequent theoretical studies. Concerning the latter, this work provides an opportunity to directly interface with research groups studying ultracold collision processes. Beyond that, the present work reveals certain limitations of standard perturbative coupled-cluster methods and extends the theoretical understanding of the inherent Jahn-Teller physics of the Rb_3 system.

The major part of this thesis addressed the investigation of Rb_3 in the context of PA experiments. In doing so, it yielded an extensive overview of available states using a pragmatic multireference configuration-interaction (MRCI) approach with a large-core effective core potential (ECP) and a core-polarization potential (CPP) together with a large uncontracted even-tempered valence basis set. The analysis of special cuts through the potential-energy landscape of both doublet and quartet states gave an idea of the respective topologies and helped to estimate the mutual position as well as the expected density of electronic states. In connection with the topology of the Rb_3 PESs several aspects of the (pseudo) Jahn-Teller effect have been discussed. Furthermore, the consequences of combined Renner-Teller plus PJT interactions for linear geometries were outlined. A survey of SOC effects revealed that they are generally weak, particularly for low-lying states involved in possible PA schemes. By studying equilibrium states further useful information towards the realization of PA processes could be generated. The exploration of selected inner-turning point (ITP) locations on the quartet ground-state PES allowed to identify promising PA candidates. Here major focus was placed on the $1^4E''$ state (formed by the two lowest-lying excited

states 1^4A_2 and 1^4B_2). Investigating the main coupling effects for the first excited quartet state (1^4A_2) including electronic dipole transition strengths at ITP geometries, intersections to nearby doublet and quartet states as well as spin-orbit couplings, confirmed the 1^4A_2 state as a promising candidate for use in PA processes.

Beyond that, the $1^4E''$ state was further analyzed in the framework of JT theory. The potential part of the corresponding JT Hamiltonian including up to fourth-order anharmonicity and vibronic coupling parameters was diagonalized. This yielded an analytically exact representation of the respective JT potential-energy landscape in the two-dimensional branching space spanned by the Q_2 and Q_3 modes. The comparison to conventional analytic forms of the JT manifold revealed that the $1^4E''$ state indeed requires a fourth-order approach to sufficiently reproduce *ab-initio* data.

Furthermore, the excited quartet manifold Q , showing an unusual coupling behavior with quadruple interactions, has been thoroughly investigated. Several 1D and 2D cuts through the subspaces spanned by the (symmetry-adapted) JT coordinates helped in unraveling some aspects of the underlying coupling mechanisms. This was further supported by an one-dimensional analysis of the Q_3 component of respective non-adiabatic coupling matrix elements (NACMEs).

Another achievement of this thesis was to provide an interface to codes designed for studying, among others, $Rb_2 + Rb$ collision processes. In this regard, it was shown how to construct a globally smooth and physically meaningful PES for the quartet ground-state of Rb_3 based on high quality *ab-initio* data using a specifically adapted variant of the kernel ridge regression technique: the RP-RKHS interpolation method. The corresponding implementation is available in PYTHON and FORTRAN [309]. The power of this interpolation was demonstrated in an analysis of the Rb_2 PEC corresponding to the $a^3\Sigma_u$ state. The underlying *ab-initio* data were calculated at ROHF-CCSD(T) level of theory with a small-core ECP and large uncontracted even-tempered basis sets. In order to reach higher accuracy, the additive two-body contributions to the final Rb_3 were modified so that they reproduce the experimentally derived values for D_e and R_e of the $a^3\Sigma_u$ state. Furthermore, the non-additive three-body term was scaled to grant a meaningful short-range behavior of the respective contribution.

A further major topic of this thesis was to obtain highly accurate ion-atom interaction potentials for Rb_2^+ in the spirit of an additive scheme to systematically include results from higher theory levels. In doing so, it could be demonstrated that several coupled-cluster methods with noniterative or approximate iterative treatments of triple excitations can lead to unphysical PECs with a small [$\approx \mathcal{O}(0.1 \text{ cm}^{-1})$] long-range

barrier at around 100 Å. The origin was found to be connected with the need to define self-consistent solutions, which at the same time cannot be both consistent with the separated fragments (different orbitals for Rb^+ and Rb) and with the quantum mechanically imposed symmetry requirement (indistinguishable cases $\text{Rb}^+ + \text{Rb}$ and vice versa). The resulting asymptotic orbitals tend to describe two +0.5-fold charged ions in the long-range limit, thus causing a repulsive coulombic interaction with a leading-order $1/R$ component. This problem lives on in the Fockian and affects the perturbative estimates of the \hat{T}_3 amplitudes finally leading to the repulsive long-range barrier. By breaking the symmetry of the system, it was shown how the unphysical CCSD(T) long-range behavior can be avoided.

This led to a construction procedure for obtaining highly accurate ion-atom interaction potentials representing the final investigations of this work. The presented procedure may straightforwardly be extended to any high-accuracy theory level but in this thesis has been tested for ROHF-CCSD(T). It was demonstrated that using symmetry-broken (T) corrections in the long-range properly merged with symmetry-adapted ones in the intermediate range yield physically meaningful PECs for both the $X\ ^2\Sigma_g^+$ and $(1)\ ^2\Sigma_u^+$ states of Rb_2^+ . The construction procedure further accounts for a correct exchange interaction between the gerade and ungerade states. Accordingly adapted *ab-initio* data were passed to the RP-RKHS interpolation method to obtain smooth PECs allowing for potential later use in scattering calculations. Based on the RP-RKHS interpolated PECs [355] spectroscopic constants were extracted and the rovibrational structure has been analyzed.

Outlook

There are several possible extensions to the work presented in this thesis, some of which have been already indicated at the respective parts. The work on studying the prospects for photoassociating Rb_3 would definitely benefit from using the generated quartet ground state PES for further exploring $\text{Rb}_2 + \text{Rb}$ collision processes. In this regard, one should first verify if the part corresponding to the $a\ ^3\Sigma_u$ PEC of Rb_2 yields the experimentally measured scattering length. If this is the case, subsequent scattering calculations for Rb_3 should provide valuable estimates of expected lifetimes and may open new insights for improved guidance towards the experimental realization of Rb_3 PA processes. In this spirit, future investigations could consider proper diabaticization techniques aiming at the subsequent use of a diabatic PES interpolation ansatz as

presented in Ref. [145]. This approach would include a comprehensive study of SOC effects and may yield coupled PES manifolds of excited states.

Beyond that, one could extend the understanding of the Rb_3 system in terms of the Jahn-Teller effect theory. This may include fitting proper PJT Hamiltonians to *ab-initio* data and analyzing if there is a critical transition from a pure JT to a combined JT plus PJT regime. In this regard, it may be finally necessary to also consider couplings to the totally symmetric breathing mode Q_1 . One could start investigating this effect based on the analytic representation obtained for the $1^4E''$ state in Sec. 4.5. This analytic study could be further extended to fifth- or sixth-order JT Hamiltonians. Furthermore, the understanding of the Q -manifold discussed in Sec. 4.6 could also benefit from considering couplings to the Q_1 mode. Here it is also necessary to set up proper model Hamiltonians that capture the corresponding physics. This could be further improved by extending the study of NACMEs to higher dimensions (i.e. exploring, e.g., the Q_2 - Q_3 subspace) and to also investigate the remaining components (Q_1 and Q_2) of the NACMEs.

Finally, a deeper understanding of the coupling mechanisms for linear configurations of Rb_3 would require an analysis in terms of the Renner-Teller or the combined RT plus PJT effect theory.

Future works related to the study of highly accurate ion-atom interaction potentials of Rb_2^+ may start with using the currently available RP-RKHS PECs of the $X^2\Sigma_g^+$ and $(1)^2\Sigma_u^+$ states in scattering calculations. This might help to make more quantitative statements for conditions needed to identify effects beyond $\text{Rb}+\text{Rb}^+$ Langevin scattering in corresponding experimental setups. From a theoretical or technical point of view it would be interesting to examine the sensitivity of scattering calculations on using higher-level PECs or on including higher-order induction/dispersion coefficients into the description of the long-range tail.

The goal of producing as accurate PECs as available computational resources allow may be further followed to push the PEC construction procedure in its current setup as reported in Chap. 7 to its limits. In this respect, it were interesting to consider both ECP-based calculations and all-electron approaches using the spin-free exact two component theory in its one-electron variant (SFX2C-1e) and include higher-order relativistic effects. However, the most important aspect may be a profound analysis of basis set effects and their impact on the exchange splitting, the long-range form and on spectroscopic constants. In combination with exploring higher-level correlation contributions as well as relativistic effects, this may finally give an estimate

on the achievable accuracy in general. Furthermore, it might be worth to study the performance of alternative CC methods such as the electron affinity equation-of-motion coupled-cluster (EA-EOM-CC) approach. Finally, one could devote some further effort to properly study the rovibrational structure of the gerade and ungerade ground states of Rb_2^+ , especially the exploration concerning the threshold bound-states.

Part V

APPENDIX

A

POINT GROUPS AND SELECTION RULES

This chapter is intended to support the discussion of the Jahn-Teller effect theory in Sec. 2.3 and the analysis of electronic dipole transitions and spin-orbit coupling effects of Rb_3 in Chap. 4. The following group theoretical considerations are thus restricted to the relevant point groups of homonuclear triatomic systems. The interested reader is referred to, e.g., Ref. [356] for in-depth information.

A.1 | The D_{3h} point group

The symmetry properties of equilateral triangular configurations of X_3 systems are described by the D_{3h} point group. The group consists of six irreducible representations (IRREPs) $\Gamma^{(i)}$. Electronic states, i.e. the molecular wavefunction and molecular properties (dipole moment, orbital angular momentum, etc.) in general can be assigned to an IRREP. The behavior of IRREPs under the symmetry operations of the group are summarized in the character table A.1. The character of a symmetry operation is defined as the trace of the corresponding matrix representation. The symmetry operations are: E the identity operation, rotations about the C_3 axis (where $2C_3$ indicates that the rotation is either clockwise or counter-clockwise), three rotations about the C_2 axes, reflection at one horizontal mirror plane σ_h , reflections at three vertical mirror planes σ_v and the rotation-reflection about the alternating S_3 axis (where $2S_3$ again denotes that there is also the inverse operation). The last two columns define to which IRREPs given functions belong. Here x may refer to the μ_x component of the dipole moment and $R_i, i \in \{x, y, z\}$ could represent the orbital angular momentum operator. The product table A.2 defines the resulting IRREP after taking the direct product of any two IRREPs of the point group.

As described in Sec. 4.1 realizing photoassociation (PA) processes requires non-

TABLE A.1.: Character table for the D_{3h} point group.

	E	$2C_3$	$3C_2$	σ_h	$2S_3$	$3\sigma_v$	lin. funct., rot.	quad. funct.
A'_1	1	1	1	1	1	1	–	$x^2 + y^2, z^2$
A'_2	1	1	–1	1	1	–1	R_z	–
E'	2	–1	0	2	–1	0	x, y	$x^2 - y^2, 2xy$
A''_1	1	1	1	–1	–1	–1	–	–
A''_2	1	1	–1	–1	–1	1	z	–
E''	2	–1	0	–2	1	0	R_x, R_y	xy, yz

TABLE A.2.: Product table for the D_{3h} point group.

	A'_1	A'_2	E'	A''_1	A''_2	E''
A'_1	A'_1	A'_2	E'	A''_1	A''_2	E''
A'_2	A'_2	A'_1	E'	A''_2	A''_1	E''
E'	E'	E'	$A'_1 + A'_2 + E'$	E''	E''	$A''_1 + A''_2 + E''$
A''_1	A''_1	A''_2	E''	A'_1	A'_2	E'
A''_2	A''_2	A''_1	E''	A'_2	A'_1	E'
E''	E''	E''	$A''_1 + A''_2 + E''$	E'	E'	$A'_1 + A'_2 + E'$

vanishing electronic dipole transition matrix element between the initial and final states. This involves considering selection rules to identify symmetry-allowed transitions. First, in the case of electronic dipole transitions the total spin of the initial $|i\rangle$ and final $|f\rangle$ states must be the same, i.e.

$$\Delta S = 0. \quad (\text{A.1})$$

Given the dipole operator

$$\hat{\mu} = -q\hat{r}, \quad (\text{A.2})$$

with the electric charge q and the position operator $\hat{r} = (\hat{x}, \hat{y}, \hat{z})^T$, non-vanishing transitions for the components $j \in \{x, y, z\}$ of the dipole operator, have to obey the *necessary* condition

$$\langle i|\hat{\mu}_j|f\rangle \neq 0 \quad \implies \quad \Gamma(|i\rangle) \otimes \Gamma(\hat{\mu}_j) \otimes \Gamma(|f\rangle) = A'_1. \quad (\text{A.3})$$

This shows that finite electronic dipole transition moments may be only obtained if the direct product of the corresponding IRREPs $\Gamma^{(i)}$ yields the totally symmetric IRREP A'_1 of the D_{3h} point group. The IRREPs for the respective components of the dipole operator are obtained from Tab. A.1. Using the product table A.2 the following symmetry-allowed dipole transitions can be identified

$$\hat{\mu}_{x,y} : \langle A'_1 | \hat{\mu}_{x,y} | E' \rangle, \langle A'_2 | \hat{\mu}_{x,y} | E' \rangle, \langle E' | \hat{\mu}_{x,y} | E' \rangle, \\ \langle A''_1 | \hat{\mu}_{x,y} | E'' \rangle, \langle A''_2 | \hat{\mu}_{x,y} | E'' \rangle, \langle E'' | \hat{\mu}_{x,y} | E'' \rangle, \quad (A.4)$$

and

$$\hat{\mu}_z : \langle A'_1 | \hat{\mu}_z | A''_2 \rangle, \langle A'_2 | \hat{\mu}_z | A''_1 \rangle, \langle E' | \hat{\mu}_z | E'' \rangle. \quad (A.5)$$

For homonuclear alkali-metal trimers this only allows for quartet-quartet- and doublet-doublet-couplings due to Eq. (A.1).

When spin-orbit coupling (SOC) effects are considered this additionally allows for

$$\Delta S = 0, \pm 1, \quad (A.6)$$

for the total spin between initial and final states. Thus, this condition allows for doublet-quartet mixing besides the doublet-doublet and quartet-quartet couplings. The *necessary* condition for non-vanishing SOC effects is analogous to Eq. (A.3), i.e. the direct product of initial state, spin-orbit coupling operator (correlating to the function $R_i, i \in \{x, y, z\}$) and final state must yield the totally symmetric IRREP A'_1 . Using the character table A.1 as well as the corresponding product table A.2 one finds the following symmetry-allowed couplings

$$(\hat{L}\hat{S})_{x,y} : \langle A'_1 | (\hat{L}\hat{S})_{x,y} | E'' \rangle, \langle A'_2 | (\hat{L}\hat{S})_{x,y} | E'' \rangle, \langle A''_1 | (\hat{L}\hat{S})_{x,y} | E' \rangle, \\ \langle A''_2 | (\hat{L}\hat{S})_{x,y} | E' \rangle, \langle E' | (\hat{L}\hat{S})_{x,y} | E'' \rangle, \quad (A.7)$$

and

$$(\hat{L}\hat{S})_z : \langle A'_1 | (\hat{L}\hat{S})_z | A'_2 \rangle, \langle E' | (\hat{L}\hat{S})_z | E' \rangle, \langle A''_1 | (\hat{L}\hat{S})_z | A''_2 \rangle, \\ \langle E'' | (\hat{L}\hat{S})_z | E'' \rangle. \quad (A.8)$$

A.2 | The C_{2v} point group

The symmetry properties of isosceles triangular geometries of X_3 systems are described by the C_{2v} point group. The group consists of the four IRREPs A_1, B_1, B_2, A_2 and is

defined by the following symmetry operations: the identity operator E , rotations about the twofold rotation axis C_2 chosen along a preferred direction (here, cf. Fig. 4.3 (a), along the z axis), reflections at the two mirror planes $\sigma_v(xz)$ and $\sigma_v(yz)$ for a choice of the coordinate system according to Fig. 4.3 (a). The character table A.3 summarizes the behavior of the IRREPs with respect to the symmetry operations. Again, the last two

TABLE A.3.: Character table for the C_{2v} point group.

	E	$C_2(z)$	$\sigma_v(xz)$	$\sigma_v(yz)$	lin. funct., rot.	quad. funct.
A_1	1	1	1	1	z	x^2, y^2, z^2
A_2	1	1	-1	-1	R_z	xy
B_1	1	-1	1	-1	x, R_y	xz
B_2	1	-1	-1	1	y, R_x	yz

columns show to which IRREPs given functions (dipole operator, angular momentum operator, etc.) belong to. The product table A.4 defines the IRREP resulting from taking the direct product of any two IRREPs of the C_{2v} point group.

TABLE A.4.: Product table for the C_{2v} point group.

	A_1	A_2	B_1	B_2
A_1	A_1	A_2	B_1	B_2
A_2	A_2	A_1	B_2	B_1
B_1	B_1	B_2	A_1	A_2
B_2	B_2	B_1	A_2	A_1

Since the computational point group of the Rb_3 system for configurations showing at least C_{2v} symmetry is C_{2v} , it is required to also consider the corresponding selection rules for this point group. First, for electronic dipole transitions the total spin of the initial and final states must be the same and thus Eq. (A.1) has to be fulfilled. The *necessary* condition for non-vanishing transitions now becomes

$$\langle i|\hat{\mu}_i|f\rangle \neq 0 \quad \implies \quad \Gamma(|i\rangle) \otimes \Gamma(\hat{\mu}_i) \otimes \Gamma(|f\rangle) = A_1, \quad (\text{A.9})$$

with the totally symmetric IRREP A_1 of the C_{2v} point group. The IRREPs of the components of the dipole operator $\hat{\mu}_i$ are given in the character table A.3 and with

Tab. A.4 the following symmetry-allowed dipole transitions can be identified

$$\hat{\mu}_x : \langle A_1 | \hat{\mu}_x | B_1 \rangle , \langle B_2 | \hat{\mu}_x | A_2 \rangle , \quad (\text{A.10})$$

and

$$\hat{\mu}_y : \langle A_1 | \hat{\mu}_y | B_2 \rangle , \langle B_1 | \hat{\mu}_y | A_2 \rangle , \quad (\text{A.11})$$

and

$$\hat{\mu}_z : \langle A_1 | \hat{\mu}_z | A_1 \rangle , \langle B_1 | \hat{\mu}_z | B_1 \rangle , \langle B_2 | \hat{\mu}_z | B_2 \rangle , \langle A_2 | \hat{\mu}_z | A_2 \rangle . \quad (\text{A.12})$$

The selection rules for spin-orbit couplings are derived analogously to the previous section using Tabs. A.3 and A.4 as well as Eq. (A.9). This yields the following symmetry-allowed spin-orbit couplings

$$(\hat{\mathbf{L}}\hat{\mathbf{S}})_x : \langle A_1 | (\hat{\mathbf{L}}\hat{\mathbf{S}})_x | B_2 \rangle , \langle B_1 | (\hat{\mathbf{L}}\hat{\mathbf{S}})_x | A_2 \rangle , \quad (\text{A.13})$$

and

$$(\hat{\mathbf{L}}\hat{\mathbf{S}})_y : \langle A_1 | (\hat{\mathbf{L}}\hat{\mathbf{S}})_y | B_1 \rangle , \langle B_2 | (\hat{\mathbf{L}}\hat{\mathbf{S}})_y | A_2 \rangle , \quad (\text{A.14})$$

and

$$(\hat{\mathbf{L}}\hat{\mathbf{S}})_z : \langle B_1 | (\hat{\mathbf{L}}\hat{\mathbf{S}})_z | B_2 \rangle , \langle A_1 | (\hat{\mathbf{L}}\hat{\mathbf{S}})_z | A_2 \rangle . \quad (\text{A.15})$$

Again, due to Eq. (A.6) besides quartet-quartet and doublet-doublet couplings also doublet-quartet couplings are allowed.

A.3 | The C_s point group

For non-linear arrangement of X_3 systems the three atoms always define a plane and thus the most general point group to characterize electronic states of triatomic molecules is C_s . The group consists of the symmetric IRREP A' and the antisymmetric one A'' . The only symmetry operations are the identity operator E and reflections at the mirror plane σ_h defined by the three atoms. The behavior of the IRREPs under these symmetry operations is given in the character table A.5. The product table A.6 is trivial and defines the IRREP resulting from taking the direct product.

The corresponding selection rules for electronic dipole transitions and spin-orbit couplings are derived analogously to what was shown in the previous sections.

TABLE A.5.: Character table for the C_s point group.

	E	σ_h	lin. funct., rot.	quad. funct.
A'	1	1	x, y, R_z	x^2, y^2, z^2
A''	1	-1	z, R_x, R_y	xz, yz

TABLE A.6.: Product table for the C_s point group.

	A'	A''
A'	A'	A''
A''	A''	A'

A.4 | Subduction tables

The number of symmetry elements of a given group defines its order. Groups of higher order have certain subgroups. For instance, the point group C_{2v} with order four is a subgroup of D_{3h} with order 12, cf. Tabs. A.1 and A.3. The correlation between the IRREPs of a given group and those of its subgroups is shown in so called correlation or subduction tables. In many cases the correlation between groups is not unique. For example in C_s one has to define which plane from the parent group becomes the sole plane σ_h of the C_s point group.

In this work the doublet and quartet states of Rb_3 are labeled according to the IRREPs of the C_{2v} point group. Moreover, MOLPRO calculations for Rb_3 configurations of $D_{\infty h}$ or D_{3h} symmetry were performed using the C_{2v} point group symmetry. In order to properly discuss (pseudo) Jahn-Teller and/or Renner-Teller coupling effects it is important to obtain the correct assignment of the IRREPs in C_{2v} to those in D_{3h} or $D_{\infty h}$. These mappings, $C_{2v} \rightarrow D_{3h}$ or $C_{2v} \rightarrow D_{\infty h}$, respectively, are obtained from the correlation tables A.7 and A.8. The reduction of $D_{\infty h}$ to D_{2h} and C_{2v} is only shown for the relevant states of this work (i.e. Σ and Π).

The most general point group for investigating X_3 systems is C_s since the three atoms always define a plane. When, for instance, studying the JT APES in the Q_2 - Q_3 branching space, corresponding calculation have to be performed in C_s symmetry. Thus, to obtain global potential energy surfaces for X_3 systems, the computational point group has to be C_s to provide a sufficient set of data points that cover a vast region of all possible configurations. Moreover, a rather technical aspect is that icMRCI

TABLE A.7.: Subduction D_{3h} to C_{2v} .

D_{3h}	$C_{2v} [\sigma_h \rightarrow \sigma_v(xz)]$	$C_{2v} [\sigma_h \rightarrow \sigma_v(xy)]$	$C_{2v} [\sigma_h \rightarrow \sigma_v(yz)]$
A'_1	A_1	A_1	A_1
A'_2	B_1	B_1	B_2
E'	$A_1 + B_1$	$A_1 + B_2$	$A_1 + B_2$
A''_1	A_2	A_2	A_2
A''_2	B_2	B_1	B_1
E''	$A_2 + B_2$	$A_2 + B_1$	$A_2 + B_1$

TABLE A.8.: Subduction $D_{\infty h}$ to D_{2h} to C_{2v} .

$D_{\infty h}$	D_{2h}	$C_{2v} [C_2(z)]$	$C_{2v} [C_2(y)]$	$C_{2v} [C_2(x)]$
Σ_g^+	A_g	A_1	A_1	A_1
Σ_g^-	B_{1g}	A_2	B_2	B_1
Σ_u^+	B_{1u}	A_1	B_1	B_2
Σ_u^-	A_u	A_2	A_2	A_2
Π_g	B_{2g}, B_{3g}	B_1, B_2	A_2, B_1	B_2, A_2
Π_u	B_{2u}, B_{3u}	B_2, B_1	A_1, B_2	B_1, A_1

calculations, as implemented in MOLPRO, mostly show exact degeneracies of, e.g., Jahn-Teller intersections at $Q_2 = Q_3 = 0$, only if the correlating calculations are performed in C_s symmetry. Therefore it is important to know the mapping $C_{2v} \rightarrow C_s$ which is shown in Tab. A.9. This correlation is not unique.

TABLE A.9.: Subduction table for the IRREPs from the C_{2v} to the C_s point group.

C_{2v}	$C_s [\sigma(xz)]$	$C_s [\sigma(yz)]$
A_1	A'	A'
B_1	A'	A''
B_2	A''	A'
A_2	A''	A''

B

NORMAL ORDERING AND WICK'S THEOREM

Normal ordering and Wick's theorem [203] are general mathematical concepts in the framework of second quantization. These concepts originated from quantum field theory where they refer to the vacuum state $|\text{vac}\rangle$. In the context of quantum chemistry the vacuum state is not a good reference. A better choice is the Hartree-Fock reference $|\Phi_0\rangle$ which will be used in the following discussion as the "mean-field vacuum".

As described in Sec. 3.3.2 when formulating coupled-cluster theory in second quantization, all operators can be expressed in terms of strings of fermionic annihilation (a) and creation (a^\dagger) operators that fulfill the anti-commutation relations after Eq. (3.33). The creation and annihilation operators are also used to generate excited determinants from the Hartree-Fock reference $|\Phi_0\rangle$. Therefore, any matrix element of an operator may be written as expectation value with respect to $|\Phi_0\rangle$. Here normal ordering provides a systematic way of bookkeeping for nonzero contributions. A normal ordered string $\{bcde\}$ is defined such that its expectation value vanishes

$$\langle\Phi_0|\{bcde\}|\Phi_0\rangle \stackrel{!}{=} 0, \quad (\text{B.1})$$

where $\{\}$ denotes normal ordering and b, c, d, e are arbitrary operators. Only if the string is empty the expectation value becomes $\langle\Phi_0|\{ \}|\Phi_0\rangle = \langle\Phi_0|\Phi_0\rangle = 1$. Wavefunction-based quantum chemical methods are designed such that the orbital space is splitted into the two subspaces of occupied, labelled with indices i, j, k, \dots , and virtual orbitals, labelled with a, b, c, \dots . With the definition from Eq. (B.1) one can directly deduce in which way two creation and annihilation have to be arranged to be in normal order, i.e. such that action onto $|\Phi_0\rangle$ gives a zero

$$a_i a_j^\dagger \quad \text{or} \quad a_a^\dagger a_i \quad \text{or} \quad a_a^\dagger a_b \quad \text{or} \quad a_i^\dagger a_j^\dagger \quad \text{or} \quad a_a^\dagger a_b^\dagger. \quad (\text{B.2})$$

Using the anti-commutation relations of Eq. (3.33) any string of creation and annihilation operators can be written as a linear combination of normally-ordered strings; mostly containing a reduced number of operators multiplied by Kronecker deltas. These reduced terms may be viewed as arising from so-called *contractions* between operator pairs which are defined as [201]

$$\overline{bc} = bc - \{bc\}. \quad (\text{B.3})$$

This is a systematization of the above indicated anticommutator trick and it can be readily shown, using Eqs. (3.33) and (B.2), that the only nonvanishing contractions between two creation and annihilation operators are

$$\overline{a_a a_b^\dagger} = a_a a_b^\dagger - \underbrace{\{a_a a_b^\dagger\}}_{-a_b^\dagger a_a} = [a_a, a_b^\dagger]_+ = \delta_{ab}, \quad (\text{B.4a})$$

$$\overline{a_i^\dagger a_j} = a_i^\dagger a_j - \underbrace{\{a_i^\dagger a_j\}}_{-a_j a_i^\dagger} = [a_i^\dagger, a_j]_+ = \delta_{ij}. \quad (\text{B.4b})$$

A formal generalization of the above to an arbitrary string of annihilation and creation operators is achieved by Wick's theorem. It states that any string of creation and annihilation operators may be written as a linear combination of normal-ordered strings [201]:

Theorem B.1 (Wick Theorem)—*Let $bcd \cdots xyz$ be an arbitrary string of creation and annihilation operators, then it holds*

$$\begin{aligned} bcd \cdots xyz &= \{bcd \cdots xyz\} + \sum_{1\text{-fold}} \overline{bcd \cdots xyz} + \sum_{2\text{-fold}} \overline{bcde} \cdots xyz + \cdots \\ &\quad + \text{full contractions} \end{aligned} \quad (\text{B.5})$$

This further involves the following rules:

1. Contractions between non-neighboring operators introduce a sign change depending on the number of transpositions:

$$\overline{bcde} = \overline{bcd}e \quad \text{or} \quad \overline{bcde} = -\overline{bdce}$$

2. Only expectation values (with respect to the reference determinant) with full contractions give non-vanishing contributions.

3. Given two normal-ordered strings $\{bcd \dots\}$ and $\{xyz \dots\}$ only contractions between normal-ordered strings need to be evaluated. For instance:

$$\begin{aligned} \{bcd \dots\}\{xyz \dots\} &= \{abc \dots xyz \dots\} + \sum_{1\text{-fold}} \{\overbrace{abc \dots}^{\quad} xyz \dots\} \\ &+ \sum_{2\text{-fold}} \{\overbrace{abc \dots xyz}^{\quad} \dots\} + \dots + \text{full contractions} \end{aligned}$$

This systematically extends to products of several strings.

C

COMPUTATIONAL DETAILS FOR Rb₃

This part of the Appendix supports the discussion of Chap. 4 with a number of technical details ranging from the exponents corresponding to the UET15 basis set to certain aspects of some MOLPRO calculations. It is thus intended to interested readers who may want to use the UET15 basis set or to those who may need some inspiration for selected MOLPRO input files either for reproduction purposes or as a starting point for subsequent calculations.

C.1 | The UET15 basis set family

The construction procedure for the uncontracted even-tempered basis set (UET15) used for investigating the Rb₃ system as shown in Sec. 4.2 yields the exponents listed in Table C.1.

For the proper construction of a high-accuracy quartet ground-state PES as described in Sec. 5.3 the UET15 basis set was extended to allow for systematically increasing the basis set size from UET15($n = 4$) to UET15($n = 6$), with the cardinal number n (note that in Sec. 5.3 the cardinal number was labeled by X). This is required to estimate the complete basis set (CBS) limit for corresponding energies through extrapolation. To this end, first one additional g function was added to the original basis set according to Tab. C.1 and h and i -exponents were subsequently generated using Eq. (4.4). The resulting exponents corresponding to this UET15($n = 4, 5, 6$) basis sets are summarized in Tab. C.2.

TABLE C.1.: Exponents ζ_i of the 15s12p7d5f3g uncontracted even-tempered basis set (UET15) constructed for investigating doublet and quartet states of Rb₃ over an energy range of $\approx 20000 \text{ cm}^{-1}$ using a lcECP+CPP approach.

Exponents				
s	p	d	f	g
240.216 800	46.597 790	1.750 670	2.431 530	2.836 785
105.929 280	17.646 390	0.614 850	0.714 329	0.833 384
46.712 021	6.682 615	0.215 940	0.209 854	0.244 830
20.598 771	2.530 679	0.075 840	0.061 650	
9.083 515	0.958 358	0.026 636	0.018 112	
4.005 591	0.362 926	0.009 355		
1.766 360	0.137 439	0.003 285		
0.778 918	0.052 047			
0.343 482	0.019 710			
0.151 467	0.007 464			
0.066 793	0.002 827			
0.029 454	0.001 070			
0.012 988				
0.005 728				
0.002 526				

TABLE C.2.: Exponents ζ_i of the UET15($n = 4$) [15s12p7d5f4g], UET15($n = 5$) [15s12p7d5f4g3h] and UET15($n = 6$) [15s12p7d5f4g3h2i] basis sets constructed analogously to the ones listed in Tab. C.1. These basis sets have been generated for use in RHF-UCCSD(T)/ECP28MDF calculations as described in Sec. 5.3.

Exponents						
s	p	d	f	g	h	i
240.216 800	46.597 790	1.750 670	2.431 530	2.836 785	3.242 040	3.647 295
105.929 280	17.646 390	0.614 850	0.714 329	0.833 384	0.952 439	1.071 494
46.712 021	6.682 615	0.215 940	0.209 854	0.244 830	0.279 805	
20.598 771	2.530 679	0.075 840	0.061 650	0.071 926		
9.083 515	0.958 358	0.026 636	0.018 112			
4.005 591	0.362 926	0.009 355				
1.766 360	0.137 439	0.003 285				
0.778 918	0.052 047					
0.343 482	0.019 710					
0.151 467	0.007 464					
0.066 793	0.002 827					
0.029 454	0.001 070					
0.012 988						
0.005 728						
0.002 526						

C.2 | Molpro input files for Rb₃ investigations

This section provides selected MOLPRO input files associated with several aspects of the Rb₃ investigations as discussed in Chap. 4. These inputs contain comments to reveal their basic features. Some further experiences on how calculations might be successfully completed are shared in Sec. C.2.6.

C.2.1 | MRCI geometry optimization and frequency calculation

Input C.1 gives an idea on how to perform geometry optimizations using the C_{2v} point group symmetry. This specific example corresponds to the geometry optimization of the quartet ground-state 1⁴B₁.

INPUT C.1: Example input for a MRCI geometry optimization

```

***,Rb3 (1){}^4B_1 quartet ground state geometry optimization

memory,800,m

gprint,orbital,civector,ref;

! lcECP and UET15
basis={
ecp,Rb,36,4,2;
1; 2,1.000000,0.000000;
1; 2,1.106700,65.136000;
2; 2,0.317770,2.987200*1/3; 2,0.303130,2.880100*2/3;
2; 2,0.379960,-1.957400*2/5; 2,0.372770,-1.897200*3/5;
1; 2,0.088950,-0.026739;
2; 2,0.317770,-2.987200*2/3; 2,0.303130,2.880100*2/3;
2; 2,0.379960,1.957400*2/5; 2,0.372770,-1.897200*2/5;
s,Rb,even,15,2.26770917961,0.778918234455;
p,Rb,even,12,2.64064146551,0.223338403475;
d,Rb,even,7,2.84731323465,0.0758400392843;
f,Rb,even,5,3.40393405964,0.209854050117;
g,Rb,2.8367850,0.8333842,0.2448297;
}

!C2v symmetry
symmetry,x,y
geometry={rb,0,0,0,DR;
          rb,0,Rd1,0,0;

```



```

        rb,0,Rd2,0,0
    }
    ! Define a meaningful starting geometry
    DR = (sqrt(3)/2.)*10.037
    Rd1 = 0.5*10.037
    Rd2 = -Rd1

    !CPP card
    {cpp,init,1;
      rb,1,8.67,,0.23;}

    !MCSCF calc to produce reference space and orbitals
    !only B1 symmetry required
    {multi;occ,5,4,2,1;closed;
      wf,3,2,3;state,2;}
    !MRCI only for 14B1
    {ci,maxit=40,nocheck;orbit,ignore_error;occ,5,4,2,1;closed;wf,3,2,3;
      option,nstati=37;}
    ! Geometry optimization by default uses first state
    ! of last computed symmetry
    {optg,displace=symm}

```

The characterization of the obtained extremum as minimum or saddle point, requires to consider the corresponding Hessian (the matrix of second derivatives of the energy with respect to nuclear displacements). Currently, MOLPRO MRCI frequency calculations are only possible without using any symmetry: this is referred to the null card C_1 . As a consequence the electronic states cannot be assigned by their respective IRREPs. Instead, one has to strictly follow the energetic ordering of the computed states for a given geometry. Hence, before one can actually classify the kind of extremum found from the preceding geometry optimization for the state under consideration, one first has to determine the energetic ordering of states corresponding to this geometry. This assignment is trivial for the quartet ground state in its equilibrium geometry since it always corresponds to the first state. The respective frequency calculation of the quartet ground state is given in input [C.2](#).

INPUT C.2: Example input for MRCI frequency calculation

```

***,Rb3 quartet ground state MRCI frequency calc.
! Increasing memory mostly required
memory,5000,m
! Tighten global thresholds often improves convergence
! and ensures accuracy

```

```
gthresh ,energy=1.d-10,oneint=1.d-20,twoint=1.d-20;
gthresh ,prefac=1.d-15,zero=1.d-13

gprint ,orbital ,civector ,ref;

angstrom

basis={
ecp,Rb,36,4,2;
1; 2,1.000000,0.000000;
1; 2,1.106700,65.136000;
2; 2,0.317770,2.987200*1/3; 2,0.303130,2.880100*2/3;
2; 2,0.379960,-1.957400*2/5; 2,0.372770,-1.897200*3/5;
1; 2,0.088950,-0.026739;
2; 2,0.317770,-2.987200*2/3; 2,0.303130,2.880100*2/3;
2; 2,0.379960,1.957400*2/5; 2,0.372770,-1.897200*2/5;
s,Rb,even,15,2.26770917961,0.778918234455;
p,Rb,even,12,2.64064146551,0.223338403475;
d,Rb,even,7,2.84731323465,0.0758400392843;
f,Rb,even,5,3.40393405964,0.209854050117;
g,Rb,2.8367850,0.8333842,0.2448297;
}
! C1-symmetry, using geometry from C2v OPTG
symmetry,nosym
geometry={rb,0,0,0,DR;
          rb,0,Rd1,0,0;
          rb,0,Rd2,0,0;}
Rd1 = 0.5*5.331
Rd2 = -Rd1
DR = sqrt(3)*Rd1

{cpp,init,1;
 rb,1,8.67,,0.23;}
!Reduce state averaging since only quartet ground state required
{multi,maxit=150;occ,12;closed;
 wf,3,1,3;state,5;}
!test for pspace (-1)
{ci,maxit=195,maxiti=900,nocheck;orbit,ignore_error;occ,12;closed;wf
 ,3,1,3;state,1;option,nstati=20;pspace,-1;}
EMRCI = energy(1) !Save desired state to be optimized in variable EMRCI

!Geometry optimization using symmetrical displacement coordinates
!(want to classify C2v extremum)
```

```
!reduce step length for improved convergence
{optg,displace=symm,dstep=0.005,variable=EMRCI}
{freq;variable,EMRCI}
```

A common error for frequency calculations of high-lying excited states is “CI VECTOR FOR STATE X DOES NOT OVERLAP SUFFICIENTLY WITH REFERENCE VECTORS”. In some cases it may help to increase the `nstati` value (as also suggested by the MOLPRO output) or to redefine the `pspace` to avoid this error. Sometimes it is also helpful to change the active space of the preceding MCSCF calculation. Another possibility may be to reduce the number of states in the state-averaged MRCI calculation since it might be the case that not all states are sufficiently described by the space of reference configurations. Furthermore, it is usually advisable to use the `noroot_follow` option, cf. Input C.5 and Sec. C.2.6, which is not documented in the MOLPRO manual.

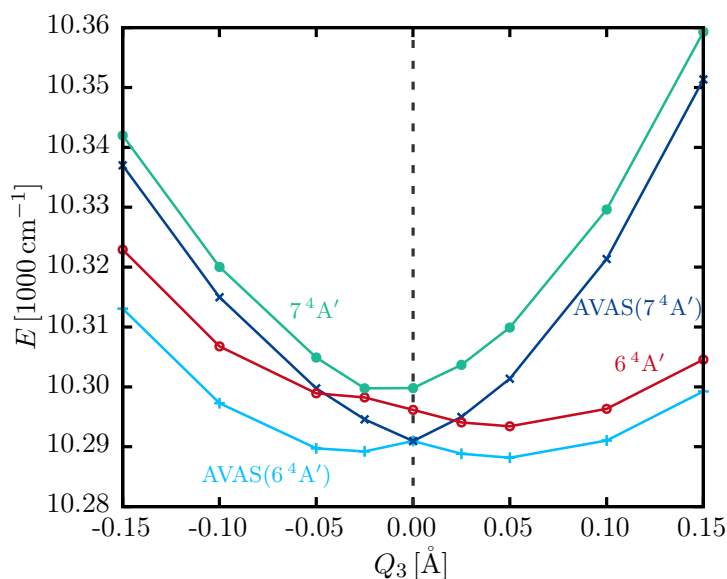


FIGURE C.1.: The $2^4E'$ Jahn-Teller manifold, see Fig. 4.6 (d), along the C_{2v} preserving coordinate Q_3 with $Q_2 = 0.0 \text{ \AA}$ and $Q_1 = 9.1816 \text{ \AA}$; cf. Input C.3. Calculations were performed using C_s symmetry. The light blue and dark blue curves correspond to calculations based on the AVAS scheme to generate an optimal active space. The red and green curves represent calculations based on a 9/3 active orbital space. The failure of producing the degeneracy at $Q_3 = 0.0 \text{ \AA}$ in the latter case illustrates the importance and sensitivity of accurate results on the choice of the active space.

C.2.2 | Obtaining exact degeneracies: A short note

As indicated in the technical remarks of Sec. 4.3.3 (numerical) exact degeneracies, as required by symmetry for JT states, are often not guaranteed when using the MRCI approach as implemented in MOLPRO. This has been also reported in Ref. [94] analyzing the pseudo Jahn-Teller potential-energy-landscape of the $2^2E'$ and $1^2A'_1$ states of K_3 . The following briefly considers this problem for the $2^4E'$ JT manifold of Rb_3 , where the degeneracy occurs between the high-lying excited states 3^4A_1 and 4^4B_1 in C_{2v} nomenclature, respectively between the $6^4A'$ and $7^4A'$ states in C_s nomenclature; see Fig. 4.6 (d). This JT state has been studied previously by Hauser *et al.* in Ref. [96] where it was noted that corresponding orbitals had to be hand-picked to ensure the degeneracy of the $2^4E'$ state at D_{3h} geometries.

Furthermore, it was found that in some cases of this work using the MRCI method as implemented in MOLPRO with C_{2v} symmetry cannot produce (numerical) exact degeneracies. The degeneracy of the $1^4E''$ JT pair at $Q_2 = Q_3 = 0$ occurring between the states $[(1^4B_2, 1^4A_2) \cong (1^4A'', 2^4A'')]$ is reproduced to good accuracy for calculations using C_s symmetry and a 9/3 active orbital space (according to MOLPRO's orbital

ordering: A'/A''). This approach fails for the $2^4E'$ state as shown in Fig. C.1.

This failure in producing exact degeneracies is often due to an insufficiently chosen active space. To find the optimal orbital reference space the AVAS scheme [223] was applied yielding an active space of 12/3. The resulting PECs are shown in Fig. C.1 with the corresponding example input C.3 given below.

INPUT C.3: Producing exact degeneracy using AVAS

```

***,Rb3 2^4Ep state with AVAS for exact degeneracy

memory,1000,m

gthresh,energy=1.d-10,oneint=1.d-20,twoint=1.d-20;
gthresh,prefac=1.d-15,zero=1.d-13

angstrom

gprint,orbital,civector,ref;

! Fix breathing mode to value in equilateral triangular configuration
Q1 = 9.181601330922618

! array of symmetric distortion coordinate Qx
Qxvec=[-0.3,-0.2,-0.1,-0.05,-0.025,0.0,0.025,0.05,0.1,0.2,0.3]

! Scan along symmetric stretch mode
do ii = 1,#Qxvec
Qx=Qxvec(ii)

! Transform to internal coordinates
R13 = (sqrt(6)*(sqrt(2)*Q1 - Qx))/6.
R23 = sqrt(3)*Q1 - 2.0*R13

! Transform to Cartesian coordinates
xb = 0.5*R23
xc = -xb
DR = sqrt(R13**2 - (R23/2.)**2)

basis={
ecp,Rb,36,4,2;
1; 2,1.000000,0.000000;
1; 2,1.106700,65.136000;
2; 2,0.317770,2.987200*1/3; 2,0.303130,2.880100*2/3;

```

```
2; 2,0.379960,-1.957400*2/5; 2,0.372770,-1.897200*3/5;
1; 2,0.088950,-0.026739;
2; 2,0.317770,-2.987200*2/3; 2,0.303130,2.880100*2/3;
2; 2,0.379960,1.957400*2/5; 2,0.372770,-1.897200*2/5;
s,Rb,even,15,2.26770917961,0.778918234455;
p,Rb,even,12,2.64064146551,0.223338403475;
d,Rb,even,7,2.84731323465,0.0758400392843;
f,Rb,even,5,3.40393405964,0.209854050117;
g,Rb,2.8367850,0.8333842,0.2448297;
}
```

```
! Cs symmetry
```

```
symmetry,y
geometry={rb,0,0,0,DR;
          rb,0,xb,0,0;
          rb,0,xc,0,0}
```

```
{cpp,init,1;
  rb,1,8.67,,0.23;}
```

```
! AVAS to generate proper active space
```

```
{rhft,maxit=120;occ,3,0;wf,3,1,3;
  avas,basis=def2-tzvp,thr=0.1;
  center,1,1s,1p;
  center,2,1s,1p;
  center,3,1s,1p;
  orbital,2100.2;
}
```

```
! CASSCF starting with previously generated orbitals
```

```
{multi,maxit=120;start,2100.2;
  wf,3,1,3;state,9;}
```

```
! 24Ep = 34A1+44B1 = 64Ap+74Ap
```

```
! energetically well separated from higher lying states of Ap symmetry
```

```
! ==> sufficient to set number of states to 7
```

```
{ci,maxit=195,maxiti=1000,nocheck;orbit,ignore_error;wf,3,1,3;state,7;
  option,nstati=20;save,3103.2}
```

```
! Define variables to save results in table
```

```
R(ii) = Qx
E1(ii) = energy(6)
E2(ii) = energy(7)
```

```
end do
! Print results to table
table ,R,E1,E2
```

Besides, it should be noted that the 2 ⁴E' JT pair has to be treated with “extra” caution as the extrema on the lower PES sheet occur close to the central COIN and are nearly symmetrically lifted when lowering the symmetry to C_{2v}; see Tab. D.1 and Fig. C.1. Hence, it requires further detailed investigations to finally characterize the topology of this potential-energy landscape: analyze if it is of tricorn topology or a Mexican-hat-like surface.

C.2.3 | Spin-orbit calculation with the ECP-LS technique

A generic input file that shows how to compute the spin-orbit matrix by using the ECP-LS technique with the large-core ECP is given in input C.4. The calculation uses the C_{2v} point group symmetry and corresponds to the investigation of the size of SOC effects at the equilibrium geometry of the first excited quartet state 1 ⁴A₂. The heat-map representation was shown in Fig. 4.9.

INPUT C.4: Example input for SO calculation

```
***,Rb3 SO coupling

memory ,800,m

gprint ,orbital ,civector;

ANGSTROM

! Geometry of the 1^4A_2 state
DR=3.310
re=5.700
xb = 0.5*re
xc = -0.5*re

! lcECP and UET15 definition
basis={
ecp,Rb,36,4,2;
1; 2,1.000000,0.000000;
1; 2,1.106700,65.136000;
2; 2,0.317770,2.987200*1/3; 2,0.303130,2.880100*2/3;
```

```

2; 2,0.379960,-1.957400*2/5; 2,0.372770,-1.897200*3/5;
1; 2,0.088950,-0.026739;
2; 2,0.317770,-2.987200*2/3; 2,0.303130,2.880100*2/3;
2; 2,0.379960,1.957400*2/5; 2,0.372770,-1.897200*2/5;
s,Rb,even,15,2.26770917961,0.778918234455;
p,Rb,even,12,2.64064146551,0.223338403475;
d,Rb,even,7,2.84731323465,0.0758400392843;
f,Rb,even,5,3.40393405964,0.209854050117;
g,Rb,2.8367850,0.8333842,0.2448297;
}

```

```
!Using C2v point group symmetry
```

```
symmetry,x,y
```

```
geometry={rb,0,0,0,DR;
          rb,0,xb,0,0;
          rb,0,xc,0,0}
```

```
{cpp,init,1;
```

```
rb,1,8.67,,0.23;}
```

```
{multi;occ,5,4,2,1;closed;
```

```
wf,3,1,1;state,5;wf,3,2,1;state,4;wf,3,3,1;state,2;wf,3,4,1;
```

```
wf,3,1,3;state,4;wf,3,2,3;state,5;wf,3,3,3;state,3;wf,3,4,3;state,3;}
```

```
{ci,nocheck;orbit,ignore_error;occ,5,4,2,1;closed;wf,3,1,1;state,5;
option,nstati=50;save,3101.2}
```

```
{ci,nocheck;orbit,ignore_error;occ,5,4,2,1;closed;wf,3,2,1;state,4;
option,nstati=50;save,3102.2}
```

```
{ci,nocheck;orbit,ignore_error;occ,5,4,2,1;closed;wf,3,3,1;state,2;
option,nstati=50;save,3103.2}
```

```
{ci,nocheck;orbit,ignore_error;occ,5,4,2,1;closed;wf,3,4,1;option,nstati
=50;save,3104.2}
```

```
{ci,nocheck;orbit,ignore_error;occ,5,4,2,1;closed;wf,3,1,3;state,4;
option,nstati=37;save,4101.2}
```

```
{ci,nocheck;orbit,ignore_error;occ,5,4,2,1;closed;wf,3,2,3;state,5;
option,nstati=37;save,4102.2}
```

```
{ci,nocheck;orbit,ignore_error;occ,5,4,2,1;closed;wf,3,3,3;state,3;
option,nstati=37;save,4103.2}
```

```
{ci,nocheck;orbit,ignore_error;occ,5,4,2,1;closed;wf,3,4,3;state,3;
option,nstati=37;save,4104.2}
```

```
! SO-calculation
```

```
! Each SO matrix element is calculated individually (wigner=0)
```

```
! Individual matrix elements and contributions of internal and
```

```
! external configuration classes are printed (matel=1)
{ci;hlsmat,ecp,3101.2,3102.2,3103.2,3104.2,4101.2,4102.2,4103.2,4104.2;
  print,hls=0,vls=0;option,wigner=0,matel=1;}
```

C.2.4 | A Q_3 scan including spin-orbit coupling

The Input C.5 generally shows how to perform PES scans with spin-orbit coupling included using the ECP-LS technique with the large-core ECP. This corresponds to the upper left inset of Fig. 4.11 (a) but can be easily adapted to produce cuts along different directions in the configuration space. These calculations may be required as a starting point for subsequent diabaticization approaches and diabatic PES interpolation approaches (potential collaboration with W. Eisfeld, University Bielefeld).

INPUT C.5: Example input of a Q_3 scan including SOC

```
***,Rb3 Q3 scan for 14Epp JT state including SOC

memory,1000,m

gthresh,energy=1.d-12,oneint=1.d-20,twoint=1.d-20;
gthresh,prefac=1.d-15,zero=1.d-13

angstrom

gprint,orbital,civector,ref;

! breathing mode fixed to 14A2 Minimum
Q1 = 8.33463
! symmetric distortion coordinate Qx
Qxvec=[-0.005,-0.0025,0.0,0.0025,0.005]

do ii = 1,#Qxvec
  Qx=Qxvec(ii)

R13 = (sqrt(6)*(sqrt(2)*Q1 - Qx))/6.
R12 = R13
R23 = sqrt(3)*Q1 - R12 - R13
xb = 0.5*R23
xc = -xb
DR = sqrt(R13**2 - (R23/2.)**2)

basis={
```

```
ecp,Rb,36,4,2;
1; 2,1.000000,0.000000;
1; 2,1.106700,65.136000;
2; 2,0.317770,2.987200*1/3; 2,0.303130,2.880100*2/3;
2; 2,0.379960,-1.957400*2/5; 2,0.372770,-1.897200*3/5;
1; 2,0.088950,-0.026739;
2; 2,0.317770,-2.987200*2/3; 2,0.303130,2.880100*2/3;
2; 2,0.379960,1.957400*2/5; 2,0.372770,-1.897200*2/5;
s,Rb,even,15,2.26770917961,0.778918234455;
p,Rb,even,12,2.64064146551,0.223338403475;
d,Rb,even,7,2.84731323465,0.0758400392843;
f,Rb,even,5,3.40393405964,0.209854050117;
g,Rb,2.8367850,0.8333842,0.2448297;
}
! Cs symmetry
symmetry,y
geometry={rb,0,0,0,DR;
          rb,0,xb,0,0;
          rb,0,xc,0,0}

{cpp,init,1;
 rb,1,8.67,,0.23;}

{multi,maxit=120;occ,9,3;closed;wf,3,1,1;state,9;wf,3,2,1;state,3;
 wf,3,1,3;state,9;wf,3,2,3;state,6;}
! noroot_follow option to ensure convergence of all high-lying
! quartet and doublet states
{ci,noroot_follow,maxit=195,maxiti=2000,nocheck;orbit,ignore_error;occ
 ,9,3;closed;wf,3,1,1;state,9;option,nstati=50;pspace,-1;save,3101.2}
{ci,noroot_follow,maxit=195,maxiti=2000,nocheck;orbit,ignore_error;occ
 ,9,3;closed;wf,3,2,1;state,3;option,nstati=50;pspace,-1;save,3102.2}
{ci,noroot_follow,maxit=195,maxiti=2000,nocheck;orbit,ignore_error;occ
 ,9,3;closed;wf,3,1,3;state,9;option,nstati=20;save,4101.2}
{ci,noroot_follow,maxit=195,maxiti=2000,nocheck;orbit,ignore_error;occ
 ,9,3;closed;wf,3,2,3;state,6;option,nstati=20;save,4102.2}
! Compute SO matrix
{ci;hlsmat,ecp,3101.2,3102.2,4101.2,4102.2;print,hls=0,vls=0;option,
 wigner=0,matel=1;}

end do
```

As mentioned previously, the use of the `noroot_follow` option works as a convenient patch to avoid the common error message “CI VECTOR FOR STATE X DOES NOT

OVERLAP SUFFICIENTLY WITH REFERENCE VECTORS". For the above setup this occurs on a quite regular basis as soon as high-lying doublet and/or quartet states are involved.

C.2.5 | Non-adiabatic coupling matrix elements

Non-adiabatic coupling matrix elements (NACMEs), as shown for the NaF example in Fig. 2.1 and for the investigations concerning the Q -manifold of Rb₃ in Fig. 4.16, are computed using the DDR procedure of MOLPRO. An example input for corresponding calculations may follow the structure shown in input C.6.

INPUT C.6: Example input for calculating NACMEs along a Q_3 scan

```

***,Rb3 non-adiabatic coupling

memory,1000,m

gthresh,energy=1.d-10,oneint=1.d-20,twoint=1.d-20;
gthresh,prefac=1.d-15,zero=1.d-13

angstrom

gprint,orbital,civector,ref;

! Reference geometry
Q1 = 10.5
Qx = -1.5

R13 = (sqrt(6)*(sqrt(2)*Q1 - Qx))/6.
R23 = sqrt(3)*Q1 - 2.0*R13

xb = 0.5*R23
xc = -xb
DR = sqrt(R13**2 - (R23/2. )**2)

! lcECP and UET15
basis={
ecp,Rb,36,4,2;
1; 2,1.000000,0.000000;
1; 2,1.106700,65.136000;
2; 2,0.317770,2.987200*1/3; 2,0.303130,2.880100*2/3;
2; 2,0.379960,-1.957400*2/5; 2,0.372770,-1.897200*3/5;
1; 2,0.088950,-0.026739;

```

```
2; 2,0.317770,-2.987200*2/3; 2,0.303130,2.880100*2/3;
2; 2,0.379960,1.957400*2/5; 2,0.372770,-1.897200*2/5;
s,Rb,even,15,2.26770917961,0.778918234455;
p,Rb,even,12,2.64064146551,0.223338403475;
d,Rb,even,7,2.84731323465,0.0758400392843;
f,Rb,even,5,3.40393405964,0.209854050117;
g,Rb,2.8367850,0.8333842,0.2448297;
}
symmetry,y
! noorient should always be used for diabatization
orient,noorient
geometry={rb,0,0,0,DR;
          rb,0,xb,0,0;
          rb,0,xc,0,0}
{cpp,init,1;
 rb,1,8.67,,0.23;}

{multi;maxiter,120;occ,9,3;closed;
 wf,3,1,3;state,5;orbital,2140.2}

! Scan along symmetric stretch mode
Qxvec=[-1.25,-1.2,-1.15,-1.1,...,1.1,1.15,1.2,1.25]

! Fixed displacement for each Qx
DQx = 0.001

! Loop over geometries
do ii=1,#Qxvec

Qx=Qxvec(ii)

R13 = (sqrt(6)*(sqrt(2)*Q1 - Qx))/6.
R23 = sqrt(3)*Q1 - 2.0*R13
xb = 0.5*R23
xc = -xb
DR = sqrt(R13**2 - (R23/2.)**2)

! Don't use extra symmetries
{multi;maxiter,120;occ,9,3;closed;wf,3,1,3;state,5;orbital,2140.2;
 noextra}
! MRCI at Qx, store orbitals at 6000.2 and (transition) densities to
8000.2
```

```
{ci,noroot_follow,nocheck,maxit=195,maxiti=1000;orbit,ignore_error;occ
,9,3;closed;wf,3,1,3;state,5;option,nstati=25;save,6000.2;dm,8000.2}

E1(ii)=energy(2)
E2(ii)=energy(3)
E3(ii)=energy(4)
E4(ii)=energy(5)

! Increment bond distance by DRa
Qxnew = Qx+DQx

R13 = (sqrt(6)*(sqrt(2)*Q1 - Qxnew))/6.
R23 = sqrt(3)*Q1 - 2.0*R13
xb = 0.5*R23
xc = -xb
DR = sqrt(R13**2 - (R23/2. )**2)

! generate diabatic orbitals by maximizing the
! overlap with the orbitals at the reference geometry
{multi;maxiter,120;occ,9,3;closed;wf,3,1,3;state,5;start,2140.2;orbital
,2141.2;diab,2140.2;noextra}
! MRCI at positively displaced geometry. Save orbitals to 6001.2
{ci,noroot_follow,nocheck,maxit=195,maxiti=1000;orbit,ignore_error;occ
,9,3;closed;wf,3,1,3;state,5;option,nstati=25;save,6001.2;}
! Compute overlap and transition density <R|R+DR>
! save transition density to record 8100.2
{ci;trans,6000.2,6001.2;dm,8100.2}

! Repeat at Rap-DRa
Qxnew2 = Qx-DQx

R13 = (sqrt(6)*(sqrt(2)*Q1 - Qxnew2))/6.
R23 = sqrt(3)*Q1 - 2.0*R13
xb = 0.5*R23
xc = -xb
DR = sqrt(R13**2 - (R23/2. )**2)

! generate diabatic orbitals by maximizing the
! overlap with the orbitals at the reference geometry
{multi;maxiter,120;occ,9,3;closed;wf,3,1,3;state,5;start,2140.2;orbital
,2142.2;diab,2140.2;noextra}
! MRCI at negatively displaced geometry. Save orbitals to 6002.2
```

```
{ci,noroot_follow,nocheck,maxit=195,maxiti=1000;orbit,ignore_error;occ
,9,3;closed;wf,3,1,3;state,5;option,nstati=25;save,6002.2;}
! Compute overlap and transition density <R|R-DR>
! save transition density to record 8200.2
{ci;trans,6000.2,6002.2;dm,8200.2}

! Compute NACMEs using 3-point formula
{ddr,2*DQx
orbital,2140.2,2141.2,2142.2;
density,8000.2,8100.2,8200.2;
states,2.1,3.1}
nacme2_3(ii)=nacme

{ddr,2*DQx
orbital,2140.2,2141.2,2142.2;
density,8000.2,8100.2,8200.2;
states,2.1,4.1}
nacme2_4(ii)=nacme

{ddr,2*DQx
orbital,2140.2,2141.2,2142.2;
density,8000.2,8100.2,8200.2;
states,2.1,5.1}
nacme2_5(ii)=nacme

{ddr,2*DQx
orbital,2140.2,2141.2,2142.2;
density,8000.2,8100.2,8200.2;
states,3.1,4.1}
nacme3_4(ii)=nacme

{ddr,2*DQx
orbital,2140.2,2141.2,2142.2;
density,8000.2,8100.2,8200.2;
states,3.1,5.1}
nacme3_5(ii)=nacme

{ddr,2*DQx
orbital,2140.2,2141.2,2142.2;
density,8000.2,8100.2,8200.2;
states,4.1,5.1}
nacme4_5(ii)=nacme
```

```
end do

table ,Qxvec ,E1 ,E2 ,E3 ,E4
title ,MRCI energies

table ,Qxvec ,nacme2_3 ,nacme2_4 ,nacme2_5 ,nacme3_4 ,nacme3_5 ,nacme4_5
title ,Non-adiabatic couplings for Rb3 quartets
```

C.2.6 | Experiences for running calculations successfully

The input files given above use a number of options both for the calculations in general and exclusively for the corresponding MRCI parts. The latter might cause most of potential problems. The following comments may provide some hints how to successfully run corresponding calculations by explaining why certain options were used, how they might be adjusted for related calculations and what have to be accounted for when using them:

- The `nocheck` and `orbit,ignore_error` options were originally used for PES scans including all states under consideration corresponding to a given IRREP. In these cases low-lying doublet and quartet states usually converge reliably while energetically high-lying excited states may cause convergence problems. To prevent the calculation from stopping and to use converged orbitals from the previous geometry for calculating the present ones, these options were included for efficiency reasons. Subsequently, the resulting outputs as well as the corresponding PECs have to be carefully analyzed to identify and remove non-converged states. For geometry optimizations and frequency calculations these options should be removed.
- Tighten the global thresholds `oneint`, `twoint` and `prefac` allow for a denser grid of available one- and two-electron integrals which often leads to improved convergence to the cost of increased computation time.
- If the space of reference configuration was chosen properly, increasing or decreasing the number defined by the `nstati` option may often help to accomplish the calculation.
- In some cases the MRCI program breaks with the error message “Internal expansion vectors linearly dependent”. To this end it is often helpful to redefine the primary configuration space using the `pspace` option

- The `noroot_follow` option is not documented in the MOLPRO manual, even though it represents an effective patch to converge MRCI calculations that involve all doublet and quartet states under consideration; cf. Input C.5. In particular, this often avoids that the MRCI program breaks with the error “CI VECTOR FOR STATE X DOES NOT OVERLAP SUFFICIENTLY WITH REFERENCE VECTORS”

As soon as energetically high-lying states and/or cases with a large number of states belonging to the same IRREP (i.e. in particular in C_s symmetry) are considered, the MRCI program might run into some problems while the preceding CASSCF calculation usually converges rapidly and reliably. In some cases this might be due to the fact that the reference space is incomplete to properly describe the states under consideration. In these cases it may help to redefine the active space by including more orbitals in the reference wavefunction or using the AVAS protocol to generate a suitable active space automatically. In other cases it might suffice to increase the number of states which are to be calculated or increase/decrease the number defined by the `nstat` option. In many cases it is sufficient to use the `noroot_follow` option.

D

FACTS AND FIGURES FOR THE Rb₃ SYSTEM

This part of the Appendix provides more details in terms of numbers and additional figures concerning the investigations of the Rb₃ system and thus supports the findings presented in Chaps. 4 and 5.

D.1 | Extended overview of Rb₃ states

In addition to Sec. 4.3 where only identified global (or local) minima of doublet and quartet states of Rb₃ were discussed, a more detailed overview is given in the following. Therefore, all extremal points found for the doublet and quartet manifolds up to the $5s + 2 \cdot 5p$ asymptote are shown in Fig. D.1. The corresponding numbers and classifications of the extrema are listed in Tabs. D.1 and D.3 for triangular configurations and in Tabs. D.2 and D.4 for linear geometries. Due to the discussed numerical difficulties of frequency calculations at MRCI level of theory (see Appendix C.2) there occurred some convergence problems for a few high-lying and/or close-in-energy states. In Tabs. D.1 and D.3 as well as in Tabs. D.2 and D.4 these states are labeled with »true classification failed«. So far it is only ensured that they represent extremal points on the corresponding PESs but they could still turn out as minimum or saddle points and require further investigation.

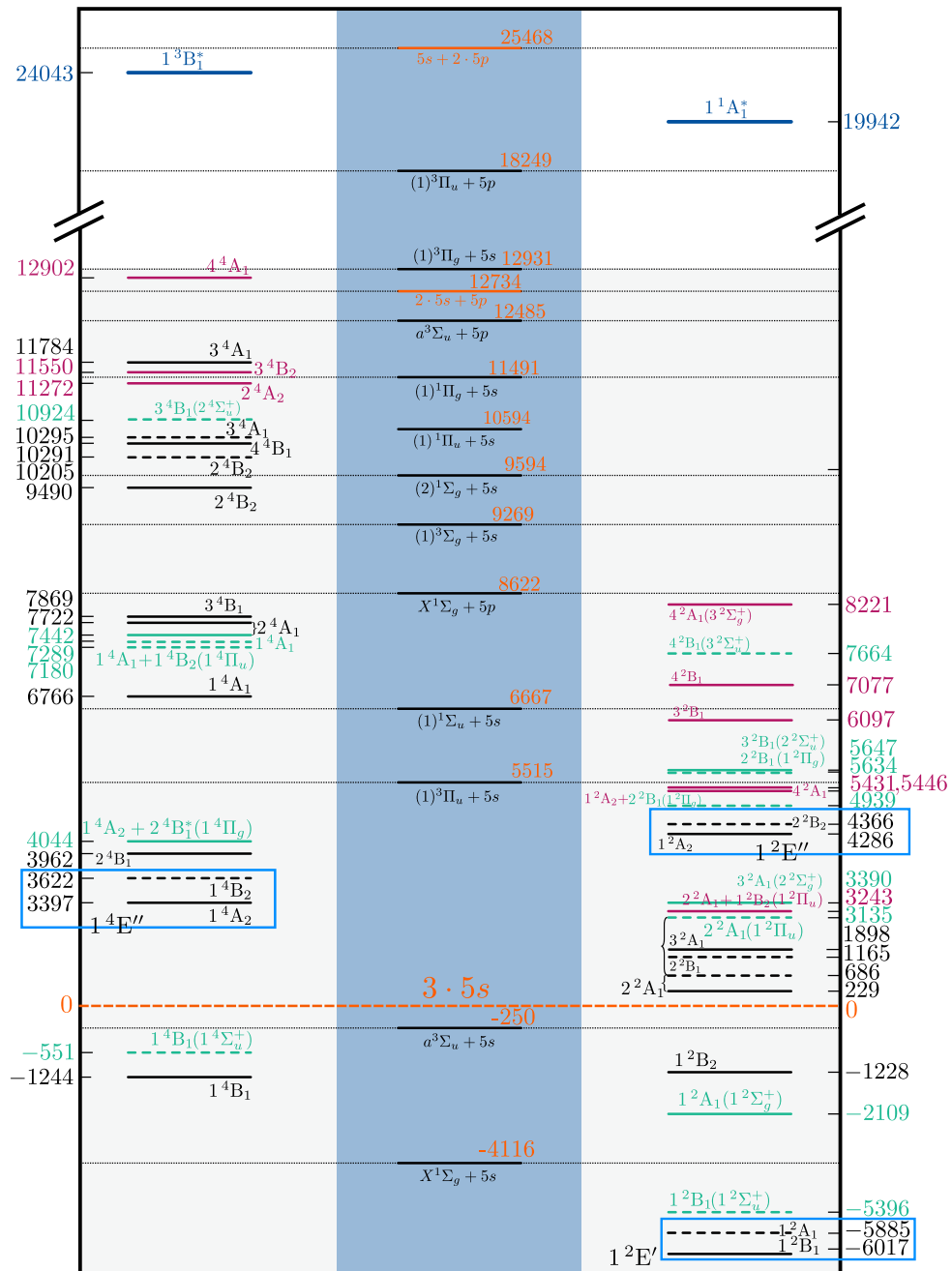


FIGURE D.1.: Overview of the energy levels of all doublet and quartet states of Rb₃ listed in Tabs. D.1 to D.5 optimized at MRCI(lcECP+CPP)/UET15 level of theory. Black levels correspond to triangular minima while green levels refer to linear minima. Levels given in bordeaux correspond to states (linear or triangular) for which the true three-dimensional classification in terms of harmonic frequency calculations failed. First-order saddle points are marked by dashed lines (both for linear and triangular geometries). For degenerate components of a linear Π state (e.g. $1^4A_2 + 2^4B_1^*$) the asterisks denotes that this state corresponds to a first-order saddle point (bending instability due to combined Renner-Teller and pseudo Jahn-Teller effect). Examples for Jahn-Teller pairs are highlighted by light blue boxes. A complete overview of states that undergo JT distortions was given in Tab. 4.3. *Freely adapted from J. Schnabel et al., Phys. Rev. A* **103**, 022820 (2021).

TABLE D.1.: Synopsis of extremal points found for **triangular** (C_{2v} and D_{3h}) configurations of **quartet** states of Rb_3 computed at MRCI(lcECP+CPP)/UET15 level of theory. Geometries are given in terms of the internal coordinates (perimetric coordinates) introduced in Fig. 4.3 and energies (E_{rel}) are given relative to the $3 \cdot \text{Rb}$ asymptote. The states are labeled according to the C_{2v} IRREPs with the corresponding assignment to the D_{3h} IRREPs given in parenthesis. The listed numbers complement the findings of the energy-level diagram of Fig. D.1.

State (D_{3h})	R_{12}, R_{23}, R_{13} [\AA] (R_1, R_2, R_3)	Geometry	E_{rel} [cm^{-1}]	Classification
1^4B_1 ($1^4\text{A}'_2$)	5.311, 5.311, 5.311 (2.656, 2.656, 2.656)	D_{3h}	-1244	Minimum
1^4A_2 ($1^4\text{E}''$)	4.368, 5.700, 4.368 (1.518, 2.850, 2.850)	C_{2v}	3397	Minimum
1^4B_2 ($1^4\text{E}''$)	4.913, 4.146, 4.913 (2.840, 2.073, 2.073)	C_{2v}	3622	First-order saddle point imag. freq. asymmetric stretch mode
2^4B_1 ($1^4\text{E}'$)	4.442, 8.179, 4.442 (0.352, 4.090, 4.090)	C_{2v}	3962	Minimum
1^4A_1 upper ($1^4\text{E}'$)	4.993, 8.076, 4.993 (0.955, 4.038, 4.038)	C_{2v}	6766	Minimum
2^4A_1 ($1^4\text{A}'_1$)	5.325, 5.325, 5.325 (2.663, 2.663, 2.663)	D_{3h}	7722	Minimum
3^4B_1 ($2^4\text{A}'_2$)	5.084, 5.084, 5.084 (2.542, 2.542, 2.542)	D_{3h}	7869	Minimum
2^4B_2 ($2^4\text{E}''$)	4.443, 6.217, 4.443 (1.335, 3.109, 3.109)	C_{2v}	9490	Minimum
2^4B_2 upper ($2^4\text{E}''$)	5.476, 4.207, 5.476 (3.373, 2.104, 2.104)	C_{2v}	10205	First-order saddle point imag. freq. symmetric stretch mode
4^4B_1 ($2^4\text{E}'$)	5.283, 5.337, 5.283 (2.615, 2.669, 2.669)	C_{2v}	10291	Minimum
3^4A_1 lower ($2^4\text{E}'$)	5.318, 5.279, 5.318 (2.679, 2.640, 2.640)	C_{2v}	10295	First-order saddle point imag. freq. asymmetric stretch mode
2^4A_2 ($2^4\text{E}''$)	4.924, 4.874, 4.924 (2.487, 2.437, 2.437)	C_{2v}	11272	Local C_{2v} extremum, true classification failed
3^4B_2 ($1^4\text{A}''_2$)	4.619, 4.619, 4.619 (2.310, 2.310, 2.310)	D_{3h}	11550	Local C_{2v} extremum, true classification failed
3^4A_1 upper ($2^4\text{E}'$)	4.687, 7.226, 4.687 (1.074, 3.613, 3.613)	C_{2v}	11784	Minimum
4^4A_1 ($3^4\text{E}'$)	4.862, 6.126, 4.862 (1.799, 3.063, 3.063)	C_{2v}	12902	Local C_{2v} extremum, true classification failed

TABLE D.2.: Synopsis of extremal points found for **linear** ($D_{\infty h}$) geometries of **quartet** states of Rb₃ computed at MRCI(lcECP+CPP)/UET15 level of theory. Geometries are given in terms of the internal coordinates (perimetric coordinates) introduced in Fig. 4.3 and energies (E_{rel}) are given relative to the 3 · Rb asymptote. The states are labeled according to the C_{2v} IRREPs with the corresponding assignment to the $D_{\infty h}$ IRREPs given in parenthesis. The listed numbers complement the findings of the energy-level diagram of Fig. D.1.

State ($D_{\infty h}$)	R_{12}, R_{23}, R_{13} [Å] (R_1, R_2, R_3)	E_{rel} [cm ⁻¹]	Classification
1 ⁴ B ₁ (1 ⁴ Σ _u ⁺)	5.916, 11.831, 5.916 (0.000, 5.916, 5.916)	-551	First-order saddle point
1 ⁴ A ₂ + 2 ⁴ B ₁ (1 ⁴ Π _g)	4.435, 8.869, 4.435 (0.000, 4.435, 4.435)	4044	Renner-Teller pair with 2 ⁴ B ₁ turning out as saddle point
1 ⁴ A ₁ + 1 ⁴ B ₂ (1 ⁴ Π _u)	4.581, 9.162, 4.581 (0.000, 4.581, 4.581)	7180	Both first-order saddle points due to PJT interaction with 2 ⁴ A ₁
1 ⁴ A ₁ (1 ⁴ Π _u → 1 ⁴ Σ _g ⁺) ^a	5.248, 10.495, 5.248 (0.000, 5.248, 5.248)	7289	First-order saddle point
2 ⁴ A ₁ (1 ⁴ Σ _g ⁺ → 1 ⁴ Π _u) ^a	4.937, 9.874, 4.937 (0.000, 4.937, 4.937)	7442	Minimum
3 ⁴ B ₁ (2 ⁴ Σ _u ⁺)	4.660, 9.319, 4.660 (0.000, 4.660, 4.660)	10924	First-order saddle point

^a As a consequence of a combined pseudo Jahn-Teller and Renner-Teller interaction two A₁ (B₁) states, one of them arising from a Π state, can mix and thus interchange for greater displacements along $D_{\infty h}$ geometries; cf. Fig. 4.7 (b).

TABLE D.3.: Synopsis of extremal points found for **triangular** (C_{2v} and D_{3h}) configurations of **doublet** states of Rb_3 computed at MRCI(lcECP+CPP)/UET15 level of theory. Geometries are given in terms of the internal coordinates (perimetric coordinates) introduced in Fig. 4.3 and energies (E_{rel}) are given relative to the $3 \cdot \text{Rb}$ asymptote. The states are labeled according to the C_{2v} IRREPs with the corresponding assignment to the D_{3h} IRREPs given in parenthesis. The listed numbers complement the findings of the energy-level diagram of Fig. D.1.

State (D_{3h})	R_{12}, R_{23}, R_{13} [\AA] (R_1, R_2, R_3)	Geometry	E_{rel} [cm^{-1}]	Classification
1^2B_1 ($1^2E'$)	4.379, 5.393, 4.379 (1.682, 2.697, 2.697)	C_{2v}	-6017	Minimum
1^2A_1 ($1^2E'$)	4.863, 4.197, 4.863 (2.765, 2.096, 2.096)	C_{2v}	-5885	First-order saddle point imag. freq. asymmetric stretch mode
1^2B_2 ($1^2A_2'$)	4.276, 4.285, 4.276 (2.134, 2.143, 2.143)	C_{2v}	-1228	Minimum
2^2A_1 lower ($2^2E'$)	4.398, 6.073, 4.398 (1.361, 3.037, 3.037)	C_{2v}	229	Minimum
2^2A_1 upper ($2^2E'$)	5.170, 4.206, 5.170 (3.067, 2.103, 3.067)	C_{2v}	686	First-order saddle point imag. freq. asymmetric stretch mode
2^2B_1 ($2^2E'$)	4.825, 4.825, 4.825 (2.413, 2.413, 2.413)	D_{3h}	1165	First-order saddle point imag. freq. symmetric stretch mode
3^2A_1 ($1^2A_1'$)	4.557, 4.557, 4.557 (2.279, 2.279, 2.279)	D_{3h}	1898	Minimum
1^2A_2 ($1^2E''$)	4.337, 5.132, 4.337 (1.771, 2.566, 2.566)	C_{2v}	4286	Minimum
2^2B_2 ($1^2E''$)	4.742, 4.208, 4.742 (2.638, 2.104, 2.104)	C_{2v}	4366	First-order saddle point imag. freq. asymmetric stretch mode
4^2A_1 lower ($2^2A_1'$)	4.603, 5.414, 4.603 (1.896, 2.707, 2.707)	C_{2v}	5431	Local C_{2v} extremum, true classification failed
4^2A_1 upper ($2^2A_1'$)	5.138, 4.350, 5.138 (2.963, 2.175, 2.175)	C_{2v}	5446	Local C_{2v} extremum, true classification failed
3^2B_1 ($3^2E'$)	4.921, 4.893, 4.921 (2.475, 2.447, 2.447)	C_{2v}	6097	Local C_{2v} extremum, true classification failed
4^2B_1 ($1^2A_2'$)	5.215, 5.215, 5.215 (2.608, 2.608, 2.608)	D_{3h}	7077	Local C_{2v} extremum, true classification failed

TABLE D.4.: Synopsis of extremal points found for **linear** ($D_{\infty h}$) geometries of Rb₃ **doublet** states computed at MRCI(lcECP+CPP)/UET15 level of theory. Geometries are given in terms of the internal coordinates (perimetric coordinates) introduced in Fig. 4.3 and energies (E_{rel}) are given relative to the 3 · Rb asymptote. The states are labeled according to the C_{2v} IRREPs with the corresponding assignment to the $D_{\infty h}$ IRREPs given in parenthesis. The listed numbers complement the findings of the energy-level diagram of Fig. D.1.

State ($D_{\infty h}$)	R_{12}, R_{23}, R_{13} [Å] (R_1, R_2, R_3)	E_{rel} [cm ⁻¹]	Classification
1^2B_1 ($1^2\Sigma_u^+$)	4.357, 8.714, 4.357 (0.000, 4.357, 4.357)	-5396	First-order saddle point
1^2A_1 ($1^2\Sigma_g^+$)	4.795, 9.590, 4.795 (0.000, 4.795, 4.795)	-2109	Minimum
2^2A_1 ($1^2\Pi_u \rightarrow 2^2\Sigma_g^+$) ^a	4.755, 9.510, 4.755 (0.000, 4.755, 4.755)	3135	First-order saddle point
$2^2A_1 + 1^2B_2$ ($1^2\Pi_u$)	4.213, 8.426, 4.213 (0.000, 4.213, 4.213)	3243	True classification failed
3^2A_1 ($2^2\Sigma_g^+ \rightarrow 1^2\Pi_u$) ^a	4.440, 8.880, 4.440 (0.000, 4.440, 4.440)	3390	Minimum
$1^2A_2 + 2^2B_1$ ($1^2\Pi_g$)	4.358, 8.716, 4.358 (0.000, 4.358, 4.358)	4939	2^2B_1 first-order saddle point, 1^2A_2 classification failed
2^2B_1 ($1^2\Pi_g \rightarrow 2^2\Sigma_u^+$) ^a	5.014, 10.028, 5.014 (0.000, 5.014, 5.014)	5634	First-order saddle point
3^2B_1 ($2^2\Sigma_u^+ \rightarrow 1^2\Pi_g$) ^a	4.930, 9.860, 4.930 (0.000, 4.930, 4.930)	5647	Minimum
4^2B_1 ($3^2\Sigma_u^+$)	4.961, 9.922, 4.961 (0.000, 4.961, 4.961)	7664	First-order saddle point
4^2A_1 ($3^2\Sigma_g^+$)	5.197, 10.394, 5.197 (0.000, 5.197, 5.197)	8221	True classification failed

^a As a consequence of a combined pseudo Jahn-Teller and Renner-Teller interaction two A_1 (B_1) states, one of them arising from a Π state, can mix and thus interchange for greater displacements along $D_{\infty h}$ geometries; cf. Fig. 4.7 (a).

TABLE D.5.: Synopsis of extremal points found for both singlet and triplet state of Rb₃⁺ in triangular and linear geometry, respectively, computed at MRCI(lcECP+CPP)/UET15 level of theory. Geometries are given in terms of the internal coordinates (perimetric coordinates) introduced in Fig. 4.3 and energies (E_{rel}) are given relative to the 3 · Rb asymptote. The states are labeled according to the C_{2v} IRREPs with the corresponding assignment to the $D_{3h}/D_{\infty h}$ IRREPs given in parenthesis. The listed numbers complement the findings of the energy-level diagram of Fig. D.1.

State ($D_{3h}/D_{\infty h}$)	R_{12}, R_{23}, R_{13} [Å] (R_1, R_2, R_3)	Geometry	E_{rel} [cm ⁻¹]	Classification
1^1A_1 ($^1A'_1$)	4.610, 4.610, 4.610 (2.305, 2.305, 2.305)	D_{3h}	19942	Minimum
1^3B_1 ($^3\Sigma_u^+$)	4.875, 9.749, 4.875 (0.000, 4.875, 4.875)	$D_{\infty h}$	24043	Minimum

D.2 | More information on spin-orbit coupling effects of Rb₃

In Sec. 4.3.5 it was mentioned that the typical magnitude of spin-orbit coupling strengths amounts to 20 to 70 cm⁻¹ while corresponding spin-orbit-induced energy shifts and zero-field splittings are much smaller. The Tabs. D.6 to D.9 give explicit values to endorse these findings.

TABLE D.6.: Synopsis of spin-orbit coupling (SOC) effects calculated at MRCI(lcECP+CPP)/UET15 level of theory using the ECP-LS technique. The results refer to the extremal points listed in Tab. D.1 for the **quartet** states of Rb₃ in **triangular configurations** (i.e. D_{3h} or C_{2v}). SOC leads to a splitting into two degenerate levels: Kramers pairs. Energies are given as the difference between SO results E and the corresponding unperturbed energy E_0

State (geom.)	$E - E_0$ [cm ⁻¹]	Splitting [cm ⁻¹]	dominant couplings	strength [cm ⁻¹]
1 ⁴ B ₁ (D_{3h})	-0.158	0.0837	1 ⁴ B ₂	21.35
	-0.0743		1 ⁴ A ₂	14.24
1 ⁴ A ₂ (C_{2v})	-0.228	0.3907	1 ⁴ A ₁	30.83
	-0.618		1 ⁴ B ₁	29.95
1 ⁴ B ₂ (C_{2v})	0.361	0.8121	1 ⁴ B ₁	42.82
	-0.451		1 ⁴ A ₁	21.96
2 ⁴ B ₁ (C_{2v})	4.389	35.239	1 ⁴ A ₂	38.58
	39.628		1 ⁴ A ₂	44.55
1 ⁴ A ₁ (C_{2v}) upper	-0.696	2.506	2 ⁴ A ₂	38.63
	-3.202		1 ⁴ B ₂	35.31
2 ⁴ A ₁ (D_{3h})	-1.819	17.391	2 ⁴ A ₂	46.17
	-19.210		3 ⁴ B ₁	48.67
3 ⁴ B ₁ (D_{3h})	9.387	45.782	2 ⁴ B ₂	50.64
	55.169		2 ⁴ A ₁	52.57
2 ⁴ B ₂ (C_{2v})	0.715	0.356	2 ⁴ B ₁	63.54
	0.359		1 ⁴ A ₂	26.45
4 ⁴ B ₁ (C_{2v})	-19.171	45.262	3 ⁴ A ₁	39.82
	-64.433		3 ⁴ A ₁	45.98
3 ⁴ A ₁ (C_{2v}) lower	-23.718	45.764	3 ⁴ A ₂	48.29
	-69.482		4 ⁴ B ₁	46.00
2 ⁴ A ₂ (C_{2v})	2.963	5.078	2 ⁴ A ₁	53.33
	8.041		3 ⁴ B ₁	32.66
3 ⁴ A ₁ (C_{2v}) upper	-3.066	2.974	3 ⁴ A ₂	27.68
	-0.0921		3 ⁴ B ₁	20.50

TABLE D.7.: Synopsis of spin-orbit coupling (SOC) effects calculated at MRCI(lcECP+CPP)/UET15 level of theory using the ECP-LS technique. The results refer to the extremal points (in the C_{2v} subspace) shown in Tab. D.2 for the **quartet** states of Rb₃ in **linear configurations** (i.e. D_{∞h}). SOC leads to a splitting into two degenerate levels: Kramers pairs. Energies are given as the difference between SO results E and the corresponding unperturbed energy E_0

State (geom.)	$E - E_0$ [cm ⁻¹]	Splitting [cm ⁻¹]	dominant couplings	strength [cm ⁻¹]
2 ⁴ B ₁ (D _{∞h})	-76.982	35.239	1 ⁴ A ₂	46.12
	-41.743		1 ⁴ A ₂	53.25
1 ⁴ A ₂ (D _{∞h})	-164.998	34.357	2 ⁴ B ₁	46.12
	-199.354		2 ⁴ B ₁	53.25
1 ⁴ B ₂ (D _{∞h})	-19.333	78.225	1 ⁴ B ₁	36.74
	58.892		1 ⁴ A ₁	38.87
2 ⁴ A ₁ (D _{∞h})	-0.854	0.722	2 ⁴ A ₂	67.14
	-0.132		2 ⁴ A ₂	22.38

TABLE D.8.: Synopsis of spin-orbit coupling (SOC) effects calculated at MRCI(lcECP+CPP)/UET15 level of theory using the ECP-LS technique. The results refer to the extremal points (in the C_{2v} subspace) listed in Tab. D.3 for the **doublet** states of Rb₃ in **triangular configurations** (i.e. D_{3h} or C_{2v}). SOC leads to a rising or lowering of the energy level representing the degenerate Kramers pair. Energies are given as the difference between SO results E and the corresponding unperturbed energies E_0 .

State (geom.)	$E - E_0$ [cm ⁻¹]	dominant couplings	strength [cm ⁻¹]
1 ² B ₁ (C _{2v})	-0.4450	1 ² B ₂	33.16
1 ² A ₁ (C _{2v})	-0.588	1 ² B ₂	36.01
1 ² B ₂ (C _{2v})	0.9964	1 ² A ₁	49.07
2 ² A ₁ (C _{2v}) upper	0.9760	2 ² B ₂	41.21
3 ² A ₁ (D _{3h})	-1.1198	1 ² A ₂	38.59
1 ² A ₂ (C _{2v})	0.3728	2 ² A ₁	41.66
2 ² B ₂ (C _{2v})	0.064 43	2 ² A ₁	44.48
4 ² A ₁ (C _{2v}) lower	0.2481	2 ² B ₁	32.86
4 ² A ₁ (C _{2v}) upper	0.6338	2 ² B ₁	33.36

TABLE D.9.: Synopsis of spin-orbit coupling (SOC) effects calculated at MRCI(lcECP+CPP)/UET15 level of theory using the ECP-LS technique. The results refer to the extremal points (in the C_{2v} subspace) shown in Tab. D.4 for the **doublet** states of Rb₃ in **linear configurations** (i.e. $D_{\infty h}$). SOC leads to a rising or lowering of the energy level representing the degenerate Kramers pair. Energies are given as the difference between SO results E and the corresponding unperturbed energies E_0 .

State (geom.)	$E - E_0$ [cm ⁻¹]	dominant couplings	strength [cm ⁻¹]
1 ² B ₁ ($D_{\infty h}$)	-0.1687	1 ⁴ B ₂	25.54
1 ² A ₁ ($D_{\infty h}$)	-0.2102	2 ⁴ A ₂	31.93
2 ² A ₁ ($D_{\infty h}$)	-3.1113	1 ² A ₂	39.28
1 ² B ₂ ($D_{\infty h}$)	-73.9239	2 ² A ₁	75.16
3 ² A ₁ ($D_{\infty h}$)	67.8894	1 ² B ₂	69.11
1 ² A ₂ ($D_{\infty h}$)	-34.2703	3 ² A ₁	44.09
3 ² B ₁ ($D_{\infty h}$)	-0.6701	2 ² B ₂	39.75
4 ² B ₁ ($D_{\infty h}$)	7.3173	1 ⁴ B ₂	27.99
4 ² A ₁ ($D_{\infty h}$)	-0.038 12	3 ⁴ A ₂	23.64

D.3 | Brief glimpse of 2D ITP surfaces

When exploring the configuration space in Sec. 4.4.1 it was mentioned that the inner turning points (ITPs) are actually 2D surfaces in the full 3D configuration space. Furthermore, the corresponding analysis of electronic dipole transition strengths between the quartet ground state 1^4B_1 and the first excited quartet state 1^4A_2 revealed that there are no considerable changes in C_s direction (starting from a C_{2v} configuration). These findings are illustrated in Fig. D.2 which may further provide a notion of the topology of the full 2D ITP surface.

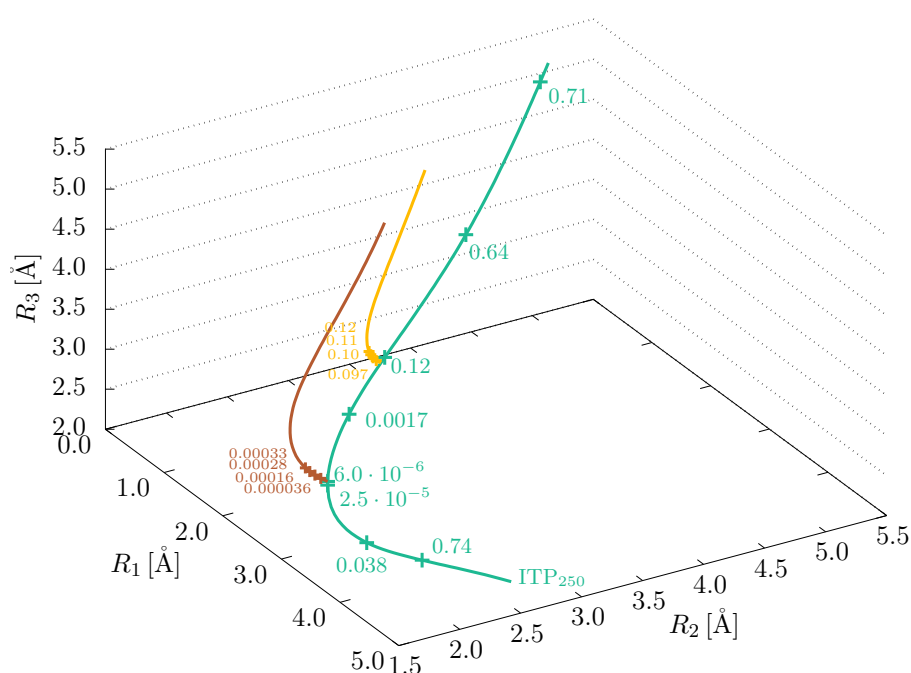


FIGURE D.2.: Supplementary to the discussion of ITPs along with Fig. 4.10 to indicate its actual 2D nature by showing ITP position in C_s direction. The ITPs shown here correspond to the ITP_{250} case, i.e. to the Rb_2+Rb dissociation scenario. The green curve represents the ITP_{250} line in the two-dimensional subspace of C_{2v} configurations as shown in Fig. 4.10. Brown and yellow lines represent ITP scans in C_s direction. The yellow curve starts at a C_{2v} conformation close to the equilibrium geometry of the first excited quartet state 1^4A_2 . The brown curve starts at a geometry close to an equilateral triangle. Values for the electronic dipole transition strengths (in units of $[D^2]$) between the quartet ground state 1^4B_1 and the first excited quartet state 1^4A_2 are given at selected geometries of C_{2v} or C_s symmetry.

D.4 | Supplementary to the $1 E''$ Jahn-Teller pair

In Jahn-Teller (JT) theory it is convenient to define a stabilization energy E_s of the global minima on the lower PES branch E_- from the central COIN as well as a localization energy E_{loc} defining the barrier height in the tricorner potential. These quantities were also introduced in Sec. 4.4.2 in regard to the discussion of the $1^4 E''$ JT potential-energy landscape. In case of the JT stabilization energy one may think of two reasonable definition which are illustrated in Fig. D.3 together with the respective definition of the localization energy.

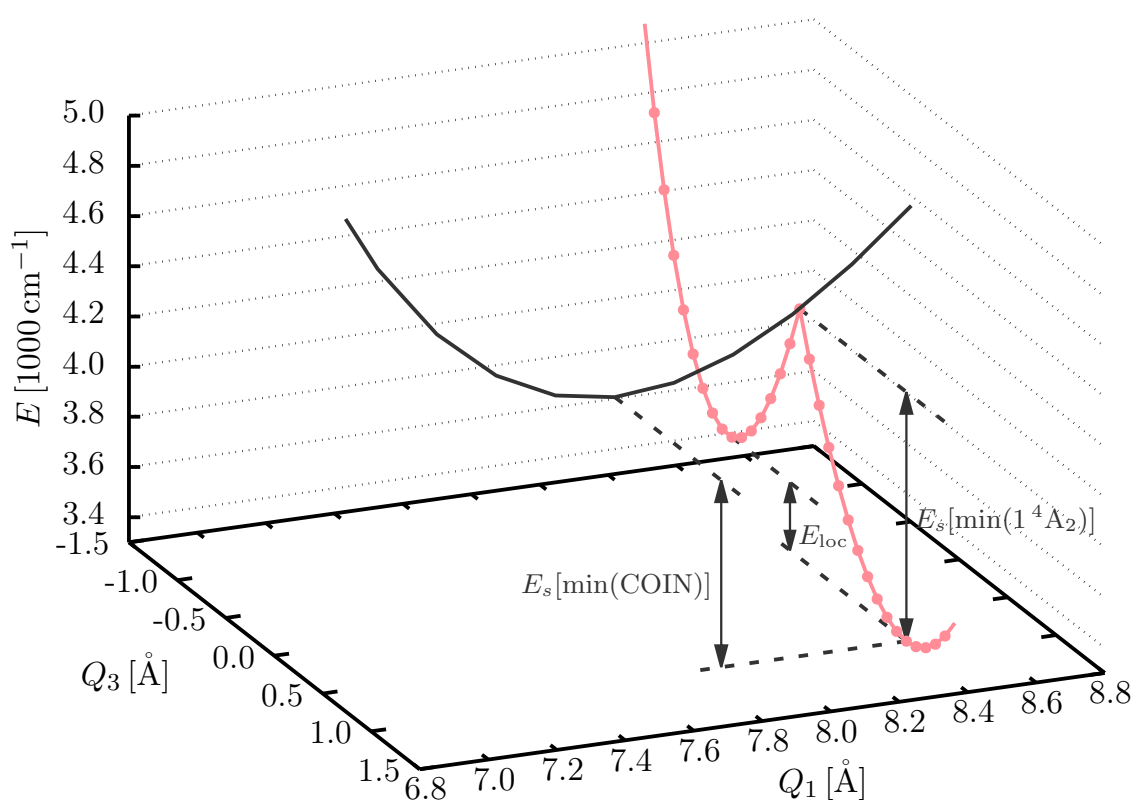


FIGURE D.3.: Cut through the lower PES branch E_- of the $1^4 E''$ JT pair in the $D_{3h}-C_{2v}$ subspace of Q_1 and Q_3 with $Q_1 = 8.335 \text{ \AA}$ adjusted to the position of the $1^4 A_2$ minimum (pink line) as shown in Fig. 4.11 (a). The black line represents the one-dimensional conical intersection seam as indicated in Fig. 4.11 (b). This cut was chosen to illustrate the JT stabilization energy E_s as well as the localization energy E_{loc} . Freely adapted from J. Schnabel et al., *Phys. Rev. A* **103**, 022820 (2021).

D.5 | Supplementary to the analytic Jahn-Teller analysis of the $1^4E''$ state

The analysis of the analytic JT model for the $1^4E''$ manifold derived in Sec. 4.5 was mainly concerned with the respective lower PES branch E_- . A comparison of the corresponding upper branch E_+ obtained analytically with *ab-initio* results is shown in Fig. D.4. The upper surface is a paraboloid of revolution about the center at $Q_2 = Q_3 = 0$ as suggested by JT theory. However, due to intersections with higher-lying states the topology of E_+ starts to deviate from this paraboloid shape for $|Q_2|, |Q_3| \geq 1.5$. It is thus useful to restrict the area wherein the fit quality is evaluated in terms of the RMSD to $Q_2, Q_3 \in [-1.3, 1.3] \text{ \AA}$ as indicated by the dashed squares in Fig. D.4. This was referred to as “restr.,2” in Sec. 4.5.

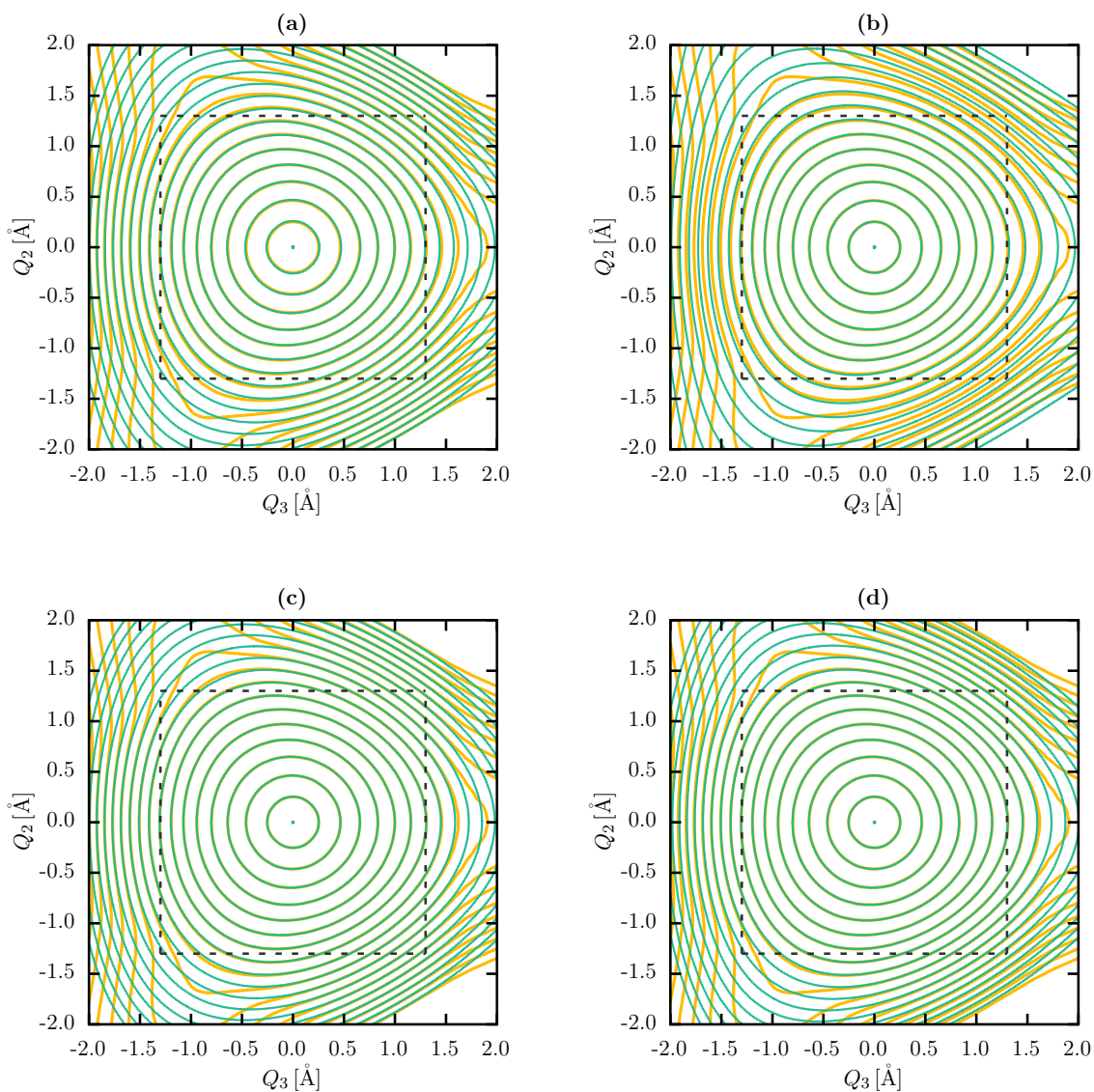


FIGURE D.4.: Comparison of the $1^4E''$ upper JT-APES E_+ (light green crosses) obtained analytically at different JT model levels with the corresponding *ab-initio* data (yellow solid lines). The third order JT expansion after Eq. (4.11) is shown in the upper panel, where in (a) the cubic vibronic coupling parameter V_{3e} is neglected. In (b) this parameter is included. The lower panel corresponds to the case where the potential part of the JT Hamiltonian is expanded up to the fourth order. The “simplified” JT4 model according to Eq. (4.22) is shown in (c) while the “complete” fourth order PES after Eq. (4.17) is shown in (d). In each figure the dashed squares indicate the area within which the restricted RMSD values $\text{RMSD}_{\text{restr},2}$ are calculated. The zero of energy is chosen to coincide with the 1^4A_2 minimum; the global minimum on E_- . The contour lines are given equidistantly with respective energy differences of 500 cm^{-1} covering a range from $E_s[\min(1^4A_2)] = 991 \text{ cm}^{-1}$ to 10000 cm^{-1} . All *ab-initio* data were computed at MRCI(lcECP+CPP)/UET15 level of theory.

D.6 | Spin-orbit coupling effects in the Q -manifold

The effect of spin-orbit coupling on the potential-energy landscape of the Q manifold of quadruple interactions (cf. Sec. 4.6) is shown in Fig. D.5 for a one-dimensional scan along the symmetric distortion coordinate Q_3 . As expected from the relativistic $E \otimes E$ JTE outlined in Sec. 2.3.2, SOC removes the central symmetry-required COIN with an energy splitting of $\Delta \approx \mathcal{O}(10 \text{ cm}^{-1})$ between the corresponding Kramers pairs of the upper and lower PES branches. The additional C_{2v} COINs that are due to interactions with the remaining states are lifted as well. This is in accordance with what has been shown in Refs. [280–282]: the dimension of a COIN seam in the presence of SOC is $N_{\text{int}} - 3$ dimensional (if C_s symmetry can be imposed); with N_{int} the number of internal degrees of freedom. This means that there is merely one COIN point in the full 3D configuration space.

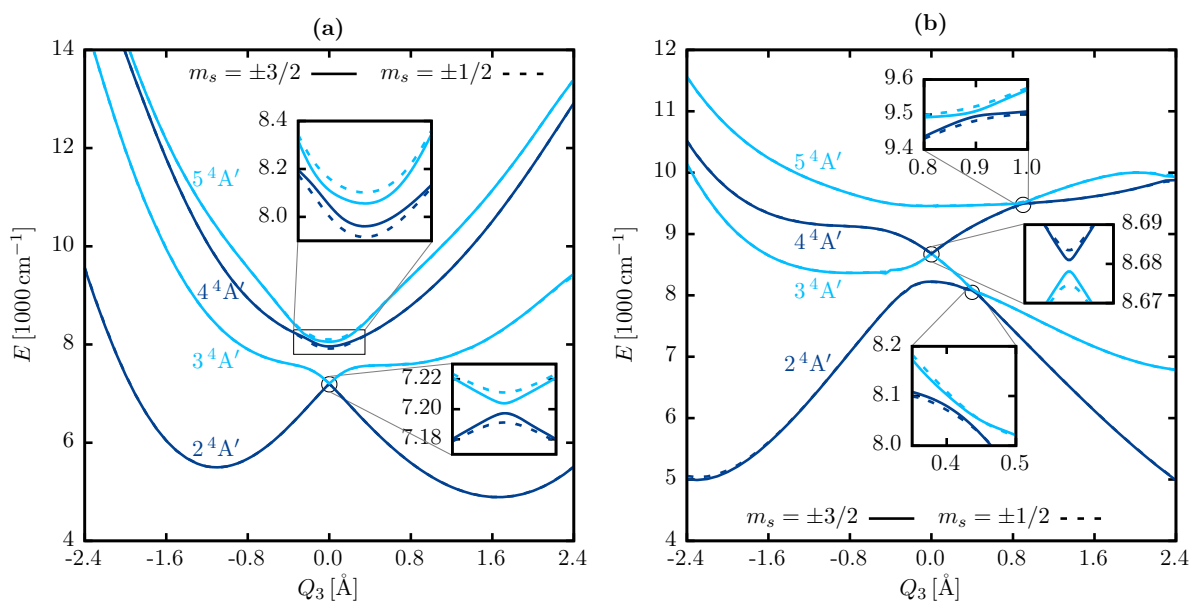


FIGURE D.5.: One-dimensional cuts through the Q -manifold along the C_{2v} preserving symmetric distortion coordinate Q_3 as shown in Fig. 4.16 but including SOC. (a) Cut left to the triple COIN [cf. Fig. 4.15] at $Q_1 \approx 8.451 \text{ \AA}$ and $Q_2 = 0.0 \text{ \AA}$; i.e. the D_{3h} minimum of the $1^4E'$ state as shown in Fig. 4.15 and reported in Tab. 4.3. A cut right to the triple COIN at $Q_1 = 10.5 \text{ \AA}$ and $Q_2 = 0.0 \text{ \AA}$ is illustrated in (b). Spin-orbit coupling removes both the central symmetry-required COINs and the additional C_{2v} ones. Calculations were performed at MRCI(lcECP+CPP)/UET15 level of theory using the ECP-LS technique to account for SOC effects. Energies are given relative to the $3 \cdot \text{Rb}$ asymptote.

D.7 | Nonadditive three-body energy for the quartet ground state of Rb_3

In Sec. 5.3 it was outlined that for the Rb_3 quartet ground state the many-body decomposition according to Eq. (5.7) is valid since the nonadditive contribution V_3 is not overwhelmingly larger than the additive one. This is demonstrated in Fig. D.6 by an one-dimensional scan along equilateral triangular geometries (D_{3h}). This also indicates that nonadditive forces are most important around the equilibrium position of the trimer where they yield a significant contribution to the total trimer equilibrium energy. The short- and long-range behavior is dominated by the additive contribution. However, for scattering calculations it is important to also properly account for the nonadditive effects in these regions.

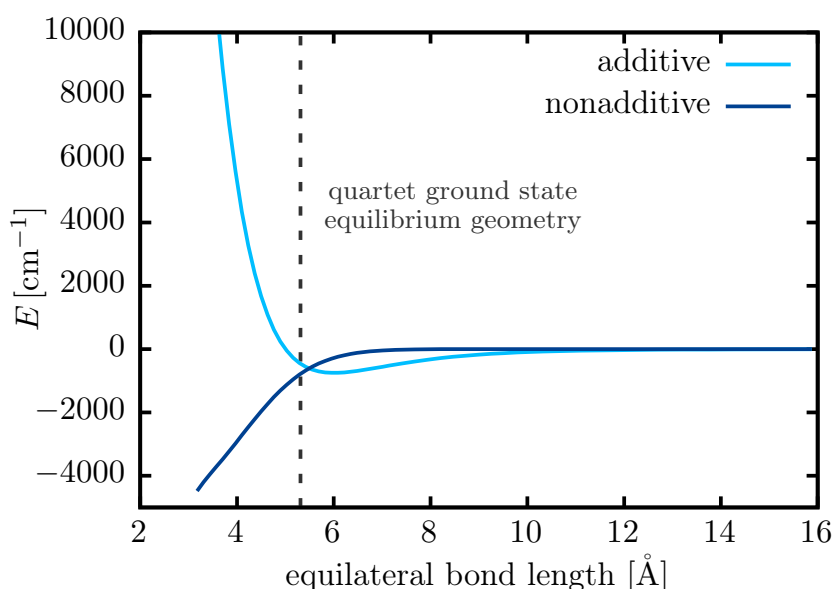


FIGURE D.6.: Comparison of additive (light blue line) and nonadditive (dark blue line) contributions to the trimer interaction energy of the quartet ground-state potential of Rb_3 for a cut along D_{3h} configurations. Calculations were performed at MRCI(lcECP+CPP)/UET15 level of theory. The behavior is qualitatively the same for calculations using a RHF-UCCSD(T)/ECP28MDF/UET15 approach.

E

MATHEMATICAL DETAILS ON KERNEL RIDGE REGRESSION AND RKHS THEORY

This part of the Appendix is intended to provide some mathematical background for the RP-RKHS interpolation method as described in Chap. 5. This includes a discussion from the statistical learning theory perspective as well as highlighting important definitions and theorems. Furthermore, this chapter gives a brief introduction into regularization and gives expressions of special functions.

E.1 | General descriptions and derivation of the reproducing kernel

The RP-RKHS interpolation method presented in Sec. 5.1 corresponds to the class of kernel ridge regression techniques. The latter combines three approaches from machine learning theory in one method. First, the goal of regression, as for any machine learning approach, is to learn a mapping from inputs x to outputs y . A formalization may be to assume $y_i = f(x_i, \beta_i)$ for some unknown function f assigning a certain weight β_i to each input. The goal of learning is to determine the weights for a given labeled training set and to be subsequently able to make predictions on novel inputs [286]. A famous representative is *linear regression* in which the target function f is assumed to be a linear combination of the inputs and may in general (multiple regression model) become

$$\mathbf{y} = \mathbf{X} \cdot \boldsymbol{\beta} + \boldsymbol{\varepsilon}, \quad (\text{E.1})$$

with coefficients (weights) β_i and a noise vector $\boldsymbol{\varepsilon}$ between the linear predictions and the true response. A standard approach to obtain the unknown β_i is the *least squares*

method which minimizes the squared L_2 norm ($\|\cdot\|^2$) of the residual ε

$$\beta^* = \min_{\beta} \|\mathbf{y} - \mathbf{X}\beta\|^2, \quad (\text{E.2})$$

where β^* is the solution vector. In typical data prediction applications the matrix \mathbf{X} may become ill-conditioned, i.e. close to singular and thus the least-squares estimate becomes highly sensitive to random errors in the observed targets. This can also result in effects such as overfitting where some coefficients β_i become large in size [286]. One way to circumvent this problem is *ridge regression* which imposes a penalty on the size of the coefficients. In general, this is described in terms of inverse problem theory and leads to the concept of regularization. The penalty can generally assume many forms while in the case of ridge regression the particular form of Tikhonov regularization (see Appendix E.2 for more details) is imposed. This is a L_2 norm penalty and the coefficients β_i follow from

$$\beta^* = \min_{\beta} \left(\|\mathbf{y} - \mathbf{X}\beta\|^2 + \lambda \|\beta\|^2 \right), \quad (\text{E.3})$$

with the regularization parameter $\lambda \geq 0$.

The kernel ridge regression approach now combines ridge regression with the *kernel trick*. In simple words this means that instead of transforming to a high-dimensional so-called feature space \mathcal{F} , which is often required to unravel the structure of data or to enable linear learning approaches to learn nonlinear functions, a kernel function accomplishes the same result in the original input space \mathcal{X} . Thus, a kernel function only implicitly performs the transformation. The kernel function may be also viewed as measuring the similarity between a pair of input data to learn a corresponding weight for it. Therefrom the method learns how to predict data that are not included in the (input) training data set.

The mathematical stage of kernel ridge regression is the reproducing kernel Hilbert space (RKHS) theory which generalizes any kernelized model. A RKHS is a subspace of a Hilbert space and is formally defined as [285]

Definition E.1. Let \mathcal{H}_k be a Hilbert space of real functions f defined on an index set \mathcal{X} ; then \mathcal{H}_k is called a reproducing kernel Hilbert space (RKHS) endowed with an inner product $\langle \cdot, \cdot \rangle_{\mathcal{H}_k}$ (and norm $\|f\| = \sqrt{\langle f, f \rangle_{\mathcal{H}_k}}$) if there exists a function $k : \mathcal{X} \times \mathcal{X} \rightarrow \mathbb{R}$ with the following properties:

1. For every $x, k(x, x')$ as a function of x' belongs to \mathcal{H}_k

2. k has the *reproducing property*

$$\langle f(\cdot), k(\cdot, \mathbf{x}) \rangle_{\mathcal{H}_k} = f(\mathbf{x}) \quad (\text{E.4})$$

or similarly one may write

$$k(\mathbf{x}, \mathbf{x}') = \langle k(\mathbf{x}, \cdot), k(\mathbf{x}', \cdot) \rangle_{\mathcal{H}_k}. \quad (\text{E.5})$$

Due to the reproducing property, k is denoted as the reproducing kernel (r.k.) function further coming with the following properties [357]

Theorem E.1—Let $k : \mathcal{X} \times \mathcal{X} \rightarrow \mathbb{R}$ be the kernel function of the RKHS \mathcal{H}_k , then k satisfies the following properties

1. k is symmetric: $k(x, x') = k(x', x)$ for any $x, x' \in \mathcal{X}$.
2. k is positive semi-definite: For any $(x_1, x_2, \dots, x_n)^T \in \mathcal{X}^n$ and $(\alpha_1, \alpha_2, \dots, \alpha_n)^T \in \mathbb{R}^n$, it is always $\sum_{i,j=1}^n \alpha_i \alpha_j k(x_i, x_j) \geq 0$.

Here the RKHS uniquely determines k , and vice versa as stated by the theorem below [285, 357]

Theorem E.2 (Moore-Aronszajn theorem [283])—Let \mathcal{X} be an index set. Then for every symmetric, positive semi-definite function $k(\cdot, \cdot)$ on $\mathcal{X} \times \mathcal{X}$ there exists a unique RKHS, and vice versa.

This theorem can be also viewed as establishing the correspondence between kernels and reproducing kernel Hilbert spaces. An approximate idea on how to think of kernel functions might follow from the analogy that in the Hilbert space L_2 the δ -function is the representer of evaluation, i.e. $f(\mathbf{x}) = \int f(\mathbf{x}') \delta(\mathbf{x} - \mathbf{x}') d\mathbf{x}'$. Kernels are the analogue of δ -functions within the smoother RKHS. However, note that $\delta(\mathbf{x}) \notin L_2$ which is in contrast to a RKHS where the kernel function k is the representer of evaluation and itself in the RKHS [285].

The concept of RKHS theory is particularly important in the field of statistical learning theory. This is due to the *representer theorem* which provides solutions to function estimation problems in the form of weighted linear combinations of kernel functions. Hence, given a finite data sample, seeking a proper kernel function is much easier to justify than a search within the unrestricted (in general infinite-dimensional) Hilbert space [357].

Theorem E.3 (Representer theorem according to Schölkopf and Smola [287])—Let \mathcal{X} be a nonempty set and k a kernel on $\mathcal{X} \times \mathcal{X}$. Given a training set $(x_1, y_1), \dots, (x_N, y_N) \in \mathcal{X} \times \mathbb{R}$, a strictly monotonically increasing real-valued function g on $[0, \infty)$ and an arbitrary cost function $L : (\mathcal{X} \times \mathbb{R}^2)^m \rightarrow \mathbb{R} \cup \{\infty\}$, and a class of functions

$$\mathcal{F} = \{f \in \mathbb{R}^{\mathcal{X}} \mid f(\cdot) = \sum_{i=1}^{\infty} \beta_i k(\cdot, z_i), \beta_i \in \mathbb{R}, z_i \in \mathcal{X}, \|f\| < \infty\},$$

where $\|\cdot\|$ is the norm in the RKHS \mathcal{H}_k associated with k , i.e. for any $z_i \in \mathcal{X}$ and $\beta_i \in \mathbb{R}$ ($i \in \mathbb{N}$),

$$\left\| \sum_{i=1}^{\infty} \beta_i k(\cdot, z_i) \right\|^2 = \sum_{i,j=1}^{\infty} \beta_i \beta_j k(z_i, z_j).$$

Then any $f \in \mathcal{F}$ minimizing the regularized cost functional

$$L[(x_1, y_1, f(x_1)), \dots, (x_N, y_N, f(x_N))] + g(\|f\|)$$

admits a finite-dimensional representation of the form

$$f(\cdot) = \sum_{i=1}^N \alpha_i k(\cdot, x_i). \quad (\text{E.6})$$

In the example shown in Sec. 5.1 the cost (sometimes called loss-) function L was chosen to be the squared error loss while the representer theorem also holds for other convex loss functions [286].

Another powerful property of RKHS theory is that in general a P -dimensional RKHS \mathcal{H} can be written as a direct product

$$\mathcal{H} = \mathcal{H}_1 \otimes \mathcal{H}_2 \otimes \dots \otimes \mathcal{H}_P \quad (\text{E.7})$$

in terms of one-dimensional RKHSs $\mathcal{H}_i, i \in \{1, \dots, P\}$ corresponding to P independent coordinates x_i . Thus, the correlating P -dimensional reproducing kernel $K(\mathbf{x}, \mathbf{x}')$ can be constructed via [291, 293]

$$K(\mathbf{x}, \mathbf{x}') = \prod_{i=1}^P k_i(x_i, x'_i), \quad (\text{E.8})$$

where k_i are the r.k.'s. associated with the one-dimensional RKHSs \mathcal{H}_i .

These theoretical fundamentals of RKHSs can be used to derive the one-dimensional reciprocal power (RP) reproducing kernel (r.k.) $q_1^{n,m}(x, x')$ according to Eq. (5.5) on which the construction procedures of the high-accuracy Rb₃ quartet ground state PES

and the Rb_2^+ PECs in Chap. 5 and Chap. 7, respectively, were based. In the following one may assume that the PES $V(x)$ as a function of the internal coordinate x belongs to a RKHS \mathcal{H}_q . By definition \mathcal{H}_q is endowed with a reproducing kernel function q and comes with the *reproducing property* [cf. Eq. (E.4)]

$$V(x) = \langle V(x'), q(x', x) \rangle' \quad (\text{E.9})$$

with the prime indicating that the inner product is taken over the coordinate x' . In general, the $3N - 6$ internal coordinates of an N -atomic molecule are either distancelike (e.g. bond lengths) or anglelike (e.g. bond angles). It is assumed that x is distancelike, thus belonging to the semi-infinite interval $[0, \infty)$ and $V(x)$ is a smooth function of order $n \geq 2$. Since PESs are usually asymptotically constant, $V(x)$ shall further obey

$$\lim_{x \rightarrow \infty} \frac{d^k V(x)}{dx^k} = 0, \quad k = 0, 1, \dots, n-1. \quad (\text{E.10})$$

Furthermore, Ho and Rabitz [291, 293] introduced the inner product between any two functions $V_1(x)$ and $V_2(x)$ defined in the interval $[0, \infty)$ to be of the form

$$\langle V_1(x), V_2(x) \rangle = \int_0^\infty \left[\frac{x^n V_1^{(n)}(x)}{\Gamma(n+1)} \right] \left[\frac{x^n V_2^{(n)}(x)}{\Gamma(n+1)} \right] \frac{dx}{w(x)}, \quad (\text{E.11})$$

with $V^{(n)}(x) \equiv d^n V(x)/dx^n$ and $\Gamma(n+1)$ is the Gamma function, see Sec. E.3. The weight factor $w(x) \geq 0$ is chosen such that it renders the correct asymptotic x -dependence of the PES, i.e.

$$w(x) = x^{-m}, \quad m \geq 1. \quad (\text{E.12})$$

The corresponding r.k. $q(x, x')$ may then be obtained using Eq. (E.9), yielding

$$V(x) = \int_0^\infty \left[\frac{x'^n}{n!} \frac{d^n q(x, x')}{dx'^n} \right] \left[\frac{x'^n}{n!} \frac{d^n V(x')}{dx'^n} \right] \frac{dx'}{w(x')}. \quad (\text{E.13})$$

Comparing this expression with the Taylor formula with exact remainder

$$f(x) = n(-1)^n \begin{cases} \int_0^\infty (x' - x)^{n-1} \left[\frac{1}{n!} \frac{d^n f(x')}{dx'^n} \right] dx', & \text{if } x' \geq x \\ 0, & \text{if } x' < x \end{cases} \quad (\text{E.14})$$

and using the asymptotic constancy Eq. (E.10) one can derive [291, 293]

$$q(x, x') = \begin{cases} n^2 \int_0^\infty (x'' - x)^{n-1} (x'' - x')^{n-1} x''^{-2n} w(x'') dx'', & x'' \geq x, x' \\ 0, & \text{else} \end{cases}. \quad (\text{E.15})$$

In general the last integral cannot be computed analytically. However, for the special choice of the weight factor according to Eq. (E.12) the integral assumes an analytically closed form and the expression for the 1D RP-r.k. after Eq. (5.5) follows.

E.2 | Tikhonov regularization

As indicated above employing regularization techniques is essential to avoid ill-conditioning of linear systems of the form

$$\mathbf{A} \cdot \mathbf{x} = \mathbf{b}, \quad (\text{E.16})$$

which are basically at the heart of all regression approaches. In the machine learning context ill-conditioning can arise for many reasons. On the one hand for a large number of data points or if they are densely clustered the matrix \mathbf{A} (e.g. the kernel matrix, cf. Sec. 5.1) may become rank deficient. On the other hand it can happen that the linear system Eq. (E.16) may not even have a solution if it effectively becomes overdetermined [291]. Furthermore, the target data (\mathbf{b}) may be rather noisy such that solving the linear system again becomes ill-posed. Finally, numerical errors may amplify small singular values which might cause destabilization of the solution of the full system. Hence, one needs a trade-off between data interpolation (exact reproduction of input data) and penalizing the function complexity. An important method to circumvent these problems is the Tikhonov method [284, 285, 288–292] which is used for the regularization of least squares approaches to minimize

$$\mathbf{x}_\lambda = \min_{\mathbf{x}} \left(\|\mathbf{A} \cdot \mathbf{x} - \mathbf{b}\|^2 + \|\mathbf{R} \cdot \mathbf{x}\|^2 \right), \quad (\text{E.17})$$

with the Tikhonov matrix \mathbf{R} to give preference to solutions showing desired properties. For the special choice $\mathbf{R} = \lambda \mathbb{1}$ one obtains the ridge regression method according to Eq. (E.3) giving preference to solutions with smaller norms. The essence of obtaining a regularized (approximate) solution is to filter out destabilizing high frequency components corresponding to small singular values. This can be seen from the singular value decomposition (SVD) of a real square ($n \times n$) matrix \mathbf{A} [358]

$$\mathbf{A} = \mathbf{U} \mathbf{\Sigma} \mathbf{V}^T = \sum_{i=1}^n \sigma_i \mathbf{u}_i \mathbf{v}_i^T, \quad (\text{E.18})$$

with \mathbf{U} and \mathbf{V} orthogonal matrices and $\mathbf{\Sigma} = \text{diag}(\sigma_1, \dots, \sigma_n)$, where σ_i are the singular values. The left and right singular vectors \mathbf{u}_i and \mathbf{v}_i are the orthonormal columns of the matrices \mathbf{U} and \mathbf{V} . With that, the exact least squares solution of Eq. (E.2), or equivalently Eq. (E.16), is given by

$$\mathbf{x}_0 = \mathbf{A}^+ \cdot \mathbf{b} = \sum_{i=1}^n \frac{\mathbf{u}_i^T \mathbf{b}}{\sigma_i} \mathbf{v}_i, \quad (\text{E.19})$$

with the pseudoinverse \mathbf{A}^+ . This form clearly reveals that if \mathbf{b} is perturbed by errors, then the solution is very likely to be dominated by errors that are reinforced by small singular values σ_i

In contrast, the regularized solution of Eq. (E.17) expressed in terms of the SVD with $\mathbf{R} = \lambda \mathbf{1}$ yields [358]

$$\mathbf{x}_\lambda = \sum_{i=1}^n \frac{\sigma_i^2}{\sigma_i^2 + \lambda^2} \frac{\mathbf{u}_i^\top \mathbf{b}}{\sigma_i} \mathbf{v}_i. \quad (\text{E.20})$$

This immediately reveals the role of the regularization parameter λ that dampens or filters out the high frequency components of the solution corresponding to singular values smaller than λ .

The conditioning of a matrix \mathbf{A} is measured by the so-called condition number $\kappa(\mathbf{A})$, which is defined as [290]

$$\kappa(\mathbf{A}) = \|\mathbf{A}^{-1}\| \|\mathbf{A}\|. \quad (\text{E.21})$$

If $\|\cdot\|$ is the L_2 norm, this can be written in terms of the SVD, yielding

$$\kappa(\mathbf{A}) = \frac{\sigma_{\max}}{\sigma_{\min}}, \quad (\text{E.22})$$

with σ_{\max} and σ_{\min} being the maximal and minimal singular values of \mathbf{A} . A problem is said to be ill-conditioned or ill-posed if $\kappa(\mathbf{A})$ is large.

E.3 | Special functions of mathematical physics

The one-dimensional reciprocal-power reproducing kernel as derived in the previous section and applied in Chap. 5 depends on certain special functions. Some of these function reappear in the constrained RP-RKHS method as applied for the diatomic PECs in Sec. 5.1.1. The corresponding definitions are given in the following.

E.3.1 | The Gamma function

The Gamma function is the Euler integral of second kind which is defined as [359]

$$\Gamma(y) = \int_0^\infty x^{y-1} e^{-x} dx. \quad (\text{E.23})$$

This is convergent for $y > 0$. It allows to extent the definition of the factorial to any number x , even if $x \in \mathbb{C}$.

For $x \neq 0, -1, -2, \dots$ it may be also defined via

$$\Gamma(x) = \lim_{x \rightarrow \infty} \frac{n^x \cdot n!}{x(x+1)(x+2) \cdots (x+n)}. \quad (\text{E.24})$$

Among others, the Gamma function comes with the properties

$$\Gamma(x+1) = x\Gamma(x), \quad (\text{E.25a})$$

$$\Gamma(n+1) = n!, \quad \text{for } n \in \mathbb{N}_0. \quad (\text{E.25b})$$

The latter property allows for a generalization of the factorial to any number.

E.3.2 | The Pochhammer symbol

The (rising) *Pochhammer symbol* $(p)_n$ is defined as [360]

$$(p)_n = p(p+1) \cdots (p+n-1) \quad (\text{E.26})$$

$$= \frac{\Gamma(p+n)}{\Gamma(p)} \quad (\text{E.27})$$

for $n \geq 0$. It satisfies

$$(-x)_n = (-1)^n (x-n+1)_n \quad (\text{E.28})$$

and a ratio of Pochhammer symbols is given in closed form by

$$\frac{(x)_n}{(x)_m} = \begin{cases} (x+m)_{n-m} & \text{if } n \geq m \\ \frac{1}{(x+n)_{m-n}} & \text{if } n \leq m. \end{cases} \quad (\text{E.29})$$

E.3.3 | The Gaussian hypergeometric function

The Gaussian hypergeometric function is defined for $|z| < 1$ by the power series [361]

$${}_2F_1(a, b; c; z) = \sum_{n=0}^{\infty} \frac{(a)_n (b)_n}{(c)_n} \frac{z^n}{n!}, \quad (\text{E.30})$$

with the previously defined Pochhammer symbol $(\cdot)_n$. If c is a non-negative integer the power series has the convergence radius $\varrho = 1$ and defines a holomorphic function in z . In the one-dimensional reciprocal-power reproducing kernel $q_1^{n,m}(x, x')$ according to Eq. (5.5) the Gaussian hypergeometric function assumes the form

$${}_2F_1(*) = {}_2F_1\left(-n+1, m+1; n+m+1; \frac{x_{\leq}}{x_{>}}\right). \quad (\text{E.31})$$

The series of Eq. (E.30) terminates if one of the parameter arguments of the hypergeometric function is a nonpositive integer. In this case the function reduces to a polynomial. In general

$${}_2F_1(-m, b; c; z) = \sum_{n=0}^m (-1)^n \binom{m}{n} \frac{(b)_n}{(c)_n} z^n. \quad (\text{E.32})$$

In the case of the reproducing kernel $q^{n,m}(x_<, x_>)$ this is a finite sum of inverse powers $x_>^{-(m+k+1)}$, $k = 0, \dots, (n - 1)$.

E.3.4 | The Beta function

The beta function, also called the Euler integral of the first kind, is a special function that is closely related to the Gamma function (Euler integral of second kind). It is defined by the integral [359]

$$B(x, y) = \int_0^1 t^{x-1} (1-t)^{y-1} dt, \quad (\text{E.33})$$

with $x, y \in \mathbb{C}$ such that $\text{Re}(x) > 0$, and $\text{Re}(y) > 0$. The beta function is symmetric, i.e.

$$B(x, y) = B(y, x) \quad (\text{E.34})$$

for all inputs x and y . A key property of the beta function is its close relationship to the gamma function

$$B(x, y) = \frac{\Gamma(x)\Gamma(y)}{\Gamma(x+y)}. \quad (\text{E.35})$$

F

COMPUTATIONAL DETAILS FOR Rb₂ AND Rb₂⁺

This part of the Appendix supports the investigations of Chaps. 5, 6 and 7 related to Rb₂ and Rb₂⁺ calculations with technical details. Furthermore, it is intended to those readers who may want to use the uncontracted even-tempered UET17 or UET17(lt) basis set series constructed for high-accuracy calculations of Rb₂ and Rb₂⁺

F.1 | The UET17 basis set family

F.1.1 | Exponents and construction

The UET17 basis set series were used in Chap. 5 in the context of the construction of a highly accurate Rb₃ quartet ground state PES to perform *ab-initio* calculations for the additive two-body contributions defined by the Rb₂ potential of the $a^3\Sigma_u$ state. Furthermore, the calculation of ionization energies of atomic Rb at SFX2C-1e level of theory in Chap. 7 was based on the UET17 basis sets.

The corresponding construction procedure proceeded analogously to the one described in Sec. 4.2 for the UET15 basis set given in Tab. C.1. The exponents were derived starting from the valence basis set accompanying the small-core pseudopotential ECP28MDF [250] by first changing the corresponding tightest d exponent to 1.75067 as suggested by Soldán [100]. Subsequently, a $(2s,2p,2d,2f)$ set of diffuse functions was added. Within this resulting span of functions new exponents were calculated in an even-tempered manner, while exponents of higher ℓ -quantum number were generated according to Eq. (4.4) [see Sec. 4.2 and references therein for more details]. This yielded an uncontracted even-tempered basis set family of up to $n = 6$ quality: $[17s14p9d7f6g5h4i] \equiv \text{UET17}(n = 6)$. This also defines the basis sets of $n = 4, 5$ quality

TABLE F.1.: Exponents of the UET17($n = 4$) [17s14p9d7f6g], UET17($n = 5$) [17s14p9d7f6g5h] and UET17($n = 6$) [17s14p9d7f6g5h4i] uncontracted even-tempered basis set. The construction proceeded analogously to the UET15 basis set given in Tab. C.1. Thus, the resulting span of functions (i.e. first and last exponent) for s -, p -, d -, and f -exponents is the same for both basis sets but more exponents within this range were generated in an even-tempered manner for the UET17 family. The UET17 basis set has been used in Chap. 5 in the context of the construction of a high-accuracy Rb₃ quartet ground state PES and in Chap. 7 on the route towards highly accurate Rb₂⁺ interaction potentials.

s	p	d	f	g	h	i
240.216 800	46.597 790	1.750 670	2.431 530	2.836 785	3.242 040	3.647 295
117.344 959	20.489 637	0.798 689	1.074 547	1.253 639	1.432 730	1.611 820
57.322 550	9.009 552	0.364 377	0.474 866	0.554 011	0.633 155	0.712 300
28.001 840	3.961 614	0.166 236	0.209 854	0.244 830	0.279 805	0.314 781
13.678 788	1.741 972	0.075 840	0.092 739	0.108 196	0.123 652	
6.682 034	0.765 967	0.034 599	0.040 984	0.047 814		
3.264 147	0.336 805	0.015 785	0.018 112			
1.594 523	0.148 098	0.007 201				
0.778 918	0.065 120	0.003 285				
0.380 498	0.028 634					
0.185 872	0.012 591					
0.090 798	0.005 536					
0.044 354	0.002 434					
0.021 667	0.001 070					
0.010 584						
0.005 170						
0.002 526						

by neglecting the respective higher functions. Due to the inherent systematically increasing cardinality this basis set family can be also used to estimate complete basis set (CBS) limit values through proper extrapolation approaches. The corresponding exponents are listed in Tab. F.1.

The selection of higher ℓ -exponents generated by application of Eq. (4.4) is not unique. By comparing the exponents in Fig. F.1 corresponding to the UET17 basis sets with the ones of the correlation-consistent basis sets [aug-cc-p(w)CV n Z-PP] designed recently [240] one may note that the g , h and i functions of the UET17 basis set could be too tight. Therefore, a second (less tight) basis set series [UET17(lt)] has been constructed where the tightest g , h and i exponents were replaced by additional diffuse ones. The resulting span of functions is listed in Tab. F.2.

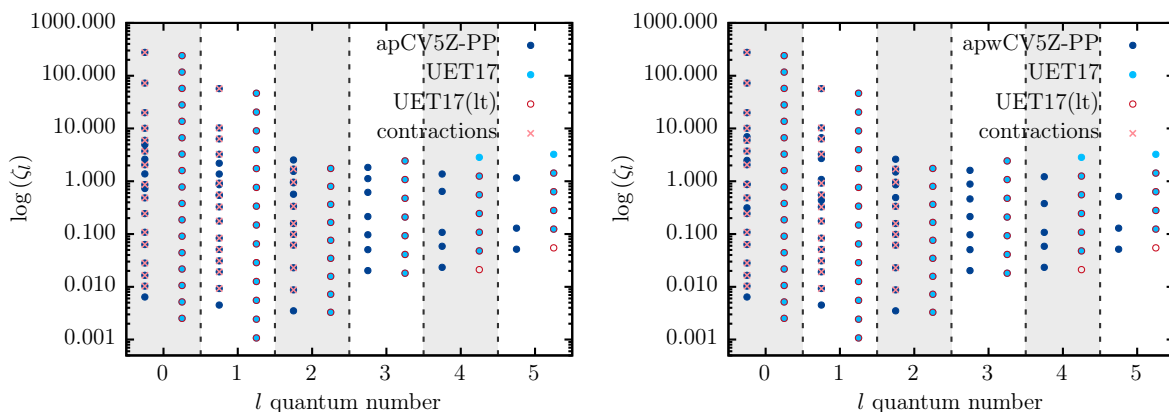


FIGURE F.1.: Comparison of exponents corresponding to the correlation consistent basis sets aug-cc-p(w)CV5Z [240] and the exponents of the UET17($n = 5$) basis set (see text for details on the construction procedure) as listed in Tab. F.1. Exponents which are contracted in the literature basis sets are marked with additional crosses. **Left:** aug-cc-pcV5Z-PP basis set. **Right:** aug-cc-pwCV5Z-PP basis set.

F.1.2 | Extrapolation behavior for ionization energies of Rb

The possibility to systematically increase the cardinality of the UET17 basis sets allows for estimating the CBS limit through proper basis set extrapolation techniques. The respective ansatz used for calculations of the ionization energies of atomic Rb based on the aug-cc-p(w)CV n Z-PP basis sets was outlined in Eqs. (7.12) and (7.13). The Hartree-Fock reference energy and the singles contribution to the CC correlation energy were chosen not to be extrapolated whereas the pair energy E_{pair} and noniterative perturbative triples $E_{(T)}$ contributions were extrapolated according to the conventional two-point n^{-3} formula [238, 239] or by applying an approach based on the Riemann- ζ function [304]. In order to compare the results obtained with the aug-cc-p(w)CV n Z-PP basis sets and the UET17 [UET17(lt)] basis set series consistently, the same CBS extrapolation approach was chosen for the latter ones. This yield the results shown in Tab. F.3 (the respective values from Tab. 7.1 are listed as well). As already mentioned in Sec. 7.2 the supposedly higher accuracy obtained for the UET17 [UET17(lt)] basis set families may be due to the fact that the underlying basis set coming with the ECP28MDF pseudopotential was originally optimized with respect to atomic polarizabilities [250]. In contrast, the aug-cc-p(w)CV n Z-PP were designed for use in correlated molecular calculations [240]. Moreover, the UET17 [UET17(lt)] basis sets are available up to $n = 6$ quality such that the respective two-point extrapolation approach might reach higher accuracy. A comparison of both basis set families for molecular calculations is given in Sec. F.7 in terms of preliminary investigations of the $X^2\Sigma_g^+$ interaction potential of

TABLE F.2.: Exponents of the less tight UET17(lt) variant of the [17s14p9d7f6g5h4i] basis set. Here the tightest exponents in the sequence corresponding to the g , h and i angular momentum quantum numbers, generated from Eq. (4.4), were replaced by additional diffuse ones. This basis set was used only for testing and comparison purposes in Appendix F.2.

s	p	d	f	g	h	i
240.216 800	46.597 790	1.750 670	2.431 530	1.253 639	1.432 730	1.611 820
117.344 959	20.489 637	0.798 689	1.074 547	0.554 011	0.633 155	0.712 300
57.322 550	9.009 552	0.364 377	0.474 866	0.244 830	0.279 805	0.314 781
28.001 840	3.961 614	0.166 236	0.209 854	0.108 196	0.123 652	0.139 109
13.678 788	1.741 972	0.075 840	0.092 739	0.047 814	0.054 645	
6.682 034	0.765 967	0.034 599	0.040 984	0.021 130		
3.264 147	0.336 805	0.015 785	0.018 112			
1.594 523	0.148 098	0.007 201				
0.778 918	0.065 120	0.003 285				
0.380 498	0.028 634					
0.185 872	0.012 591					
0.090 798	0.005 536					
0.044 354	0.002 434					
0.021 667	0.001 070					
0.010 584						
0.005 170						
0.002 526						

Rb₂⁺ with respect to the dissociation energy D_e .

Beyond that, for atomic calculations the design of the UET17 [UET17(lt)] basis sets yields essentially the same Hartree-Fock energies for both Rb and Rb⁺ independent of the cardinal number n , i.e. the CBS limit for the reference energy is already reached. This is shown in Figs. F.2 (a) and F.3 (a), respectively. The remaining contributions to the total CCSD(T) energy do not show the irregular behavior that occurs for the aug-cc-p(w)CV n Z-PP basis sets (cf. Sec. F.2), as further demonstrated by Figs. F.2 and F.3. This has been already indicated in Sec. 7.2 regarding the CBS extrapolation ansatz applied for the correlation contributions of SFX2C-1e calculations. Since all corresponding terms show smooth convergence behavior, the two-point n^{-3} formula can be also applied to the total correlation energy.

TABLE F.3.: Comparison of Rb ionization energies E_{IP} (in eV) calculated with the correlation-consistent aug-cc-p(w)CV n Z-PP [240] and the UET17 and UET17(lt) basis sets given in Tabs. F.1 and F.2, respectively. The correlation energy is extrapolated either according to the conventional two-point n^{-3} formula [238, 239] or by using a novel approach based on the application of the Riemann- ζ function [304]. Reference energies and singles contributions to the correlation energy are excluded from the extrapolation procedure (see text for details). The experimental value is $E_{\text{IP}}^{\text{exp.}} = 4.177128$ eV [258].

basis set size	aug-cc-pwCV n Z-PP	aug-cc-pCV n Z-PP	UET17	UET17(lt)
$n = 3$	4.157 429	4.125 985	–	–
$n = 4$	4.172 722	4.159 782	4.171 369	4.171 330
$n = 5$	4.172 448	4.166 632	4.173 862	4.173 786
$n = 6$	–	–	4.174 761	4.174 680
CBS	4.172 207	4.174 037	4.176 005	4.175 917
CBS $_{\zeta}$	4.172 165	4.175 328	4.176 169	4.176 080

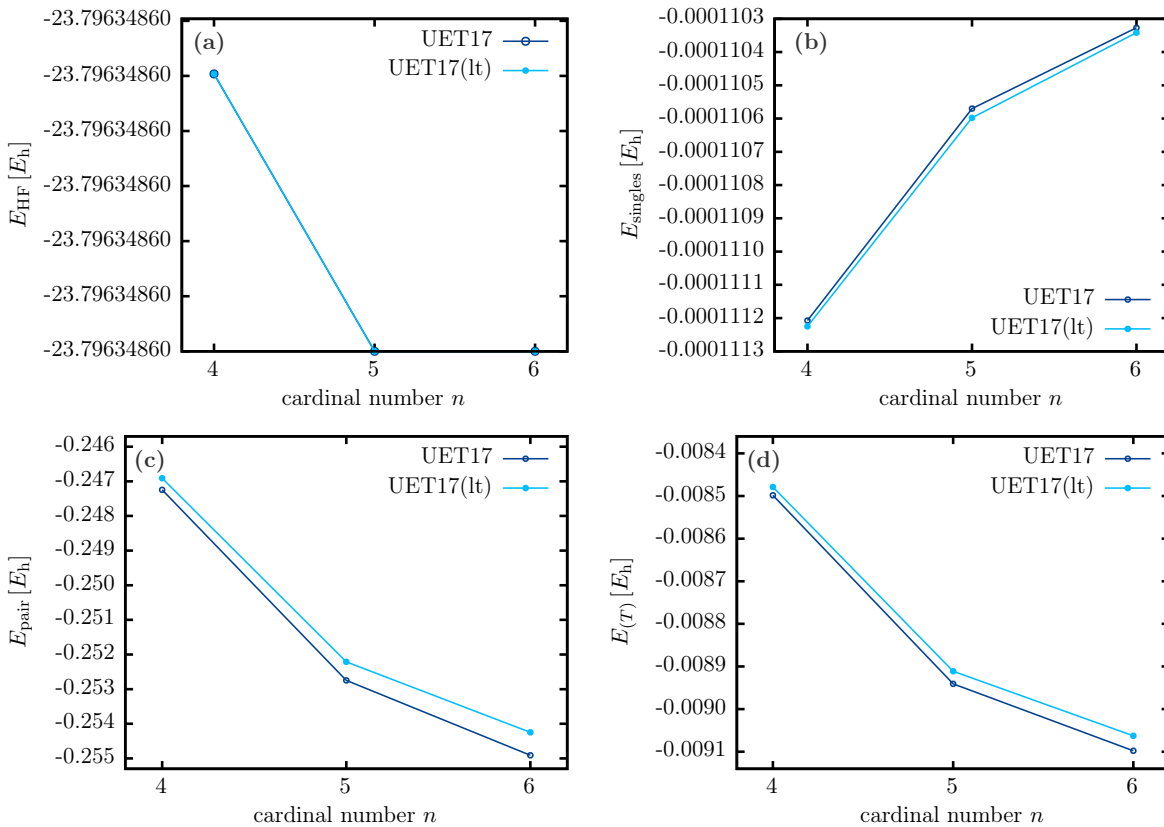


FIGURE F.2.: Reference energy and individual energy contributions to the CCSD(T) correlation energy (cf. Eqs. (7.12) and (7.13)) of the **Rb atom** as a function of the cardinal number n of the UET17 and UET17(lt) basis set families. The Hartree-Fock energy (E_{HF}) is essentially independent of the basis set size while the individual correlation contributions show smooth convergence behavior.

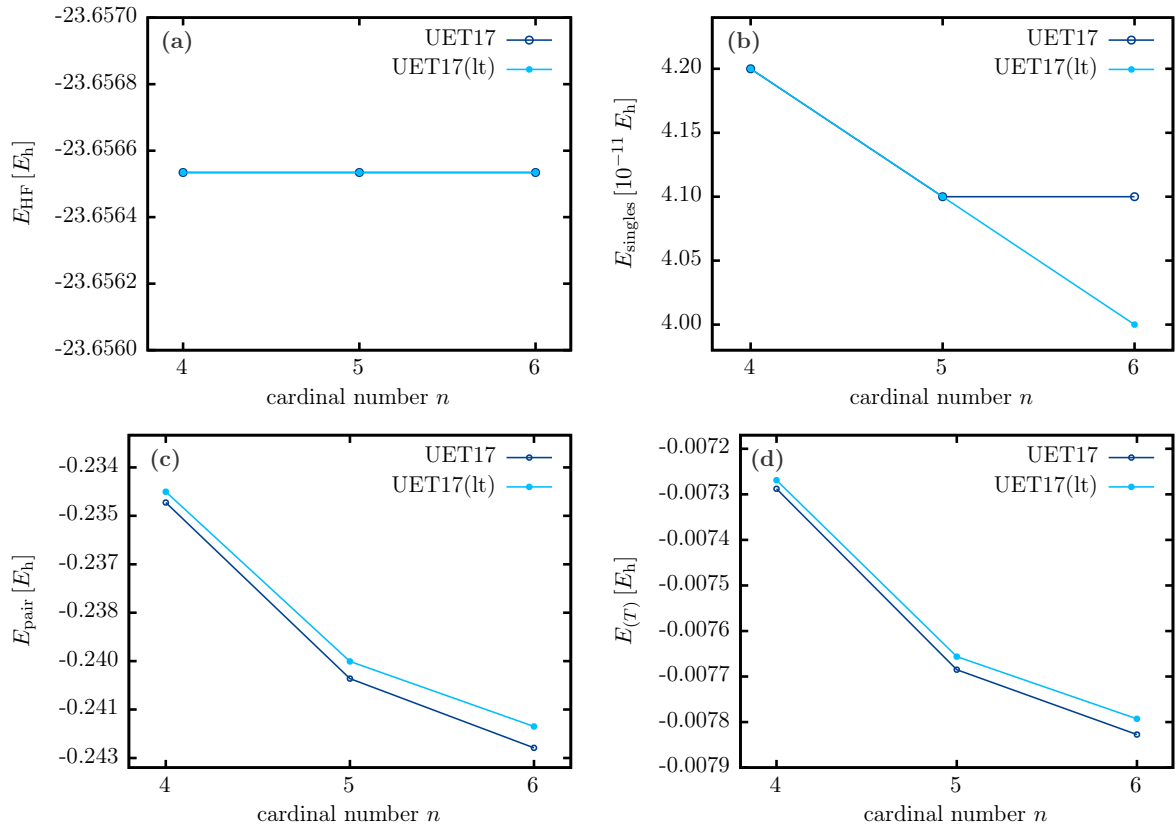


FIGURE F.3.: Reference energy and individual energy contributions to the CCSD(T) correlation energy (cf. Eqs. (7.12) and (7.13)) of the Rb^+ cation as a function of the cardinal number n of the UET17 and UET17(lt) basis set families. The Hartree-Fock energy (E_{HF}) is essentially independent of the basis set size while the individual correlation contributions show smooth convergence behavior.

F.2 | Basis set extrapolation problems for the aug-cc-p(w)CV_nZ-PP family

In Tabs. 7.1 or F.3 the oscillatory behavior between the $n = 4$ and $n = 5$ values of the ionization energies obtained with the aug-cc-p(w)CV_nZ-PP basis sets was attributed to the irregular behavior of the Hartree-Fock and singles energy contributions with respect to increasing basis set size; cf. Sec. 7.2. A detailed view onto the reference energy and each contribution of Eq. (7.13) is shown in Figs. F.4 and F.5 for Rb and Rb⁺, respectively. Indeed, the occurring irregularities in E_{HF} and E_{singles} clearly spoil the application of proper CBS extrapolation approaches. Usually, both contributions are extrapolated according to the three-point formula [236]

$$E_{\text{HF,singles}}(n) = E_{\text{HF,singles}}^{\infty} + ae^{-bn}. \quad (\text{F.1})$$

However, the observed irregular behavior renders this approach meaningless, thus motivating the compromise procedure of Eqs. (7.12) and (7.13).

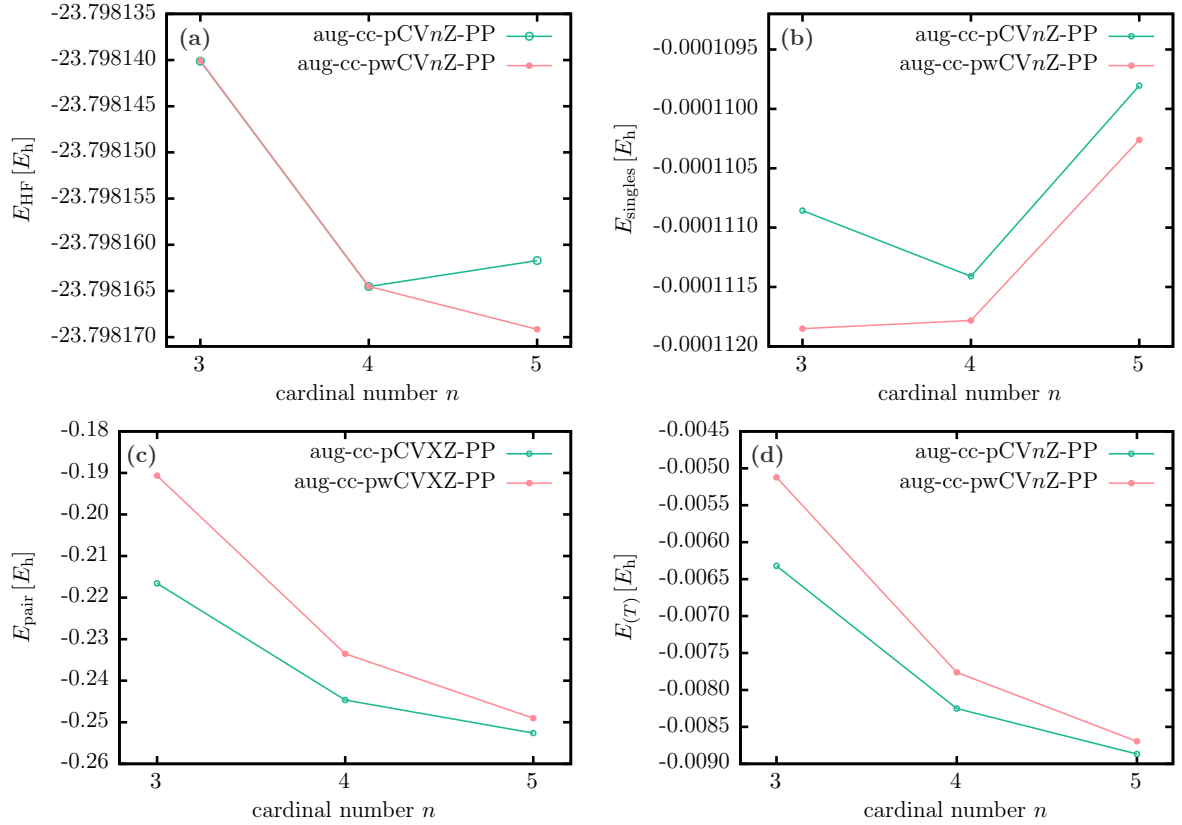


FIGURE F.4.: Reference energy and individual energy contributions to the CCSD(T) correlation energy (cf. Eqs. (7.12) and (7.13)) of the **Rb** atom as a function of the cardinal number n corresponding to the aug-cc-p(w)CV n Z-PP basis sets [240]. The irregularities occurring in the Hartree-Fock (E_{HF}) and singles (E_{singles}) energies render the extrapolation ansatz according to Eq. (F.1) meaningless and cause the oscillatory behavior between the $n = 4$ and $n = 5$ values in Tabs. 7.1 and F.3.

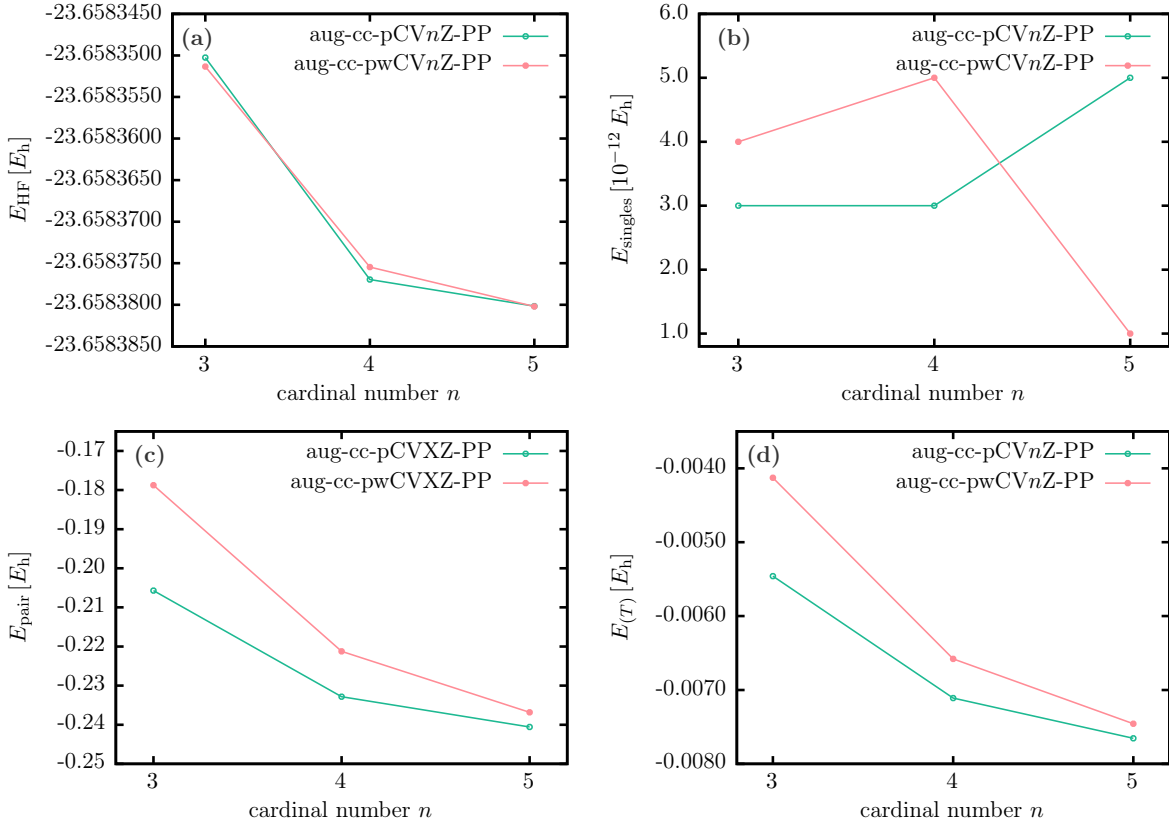


FIGURE F.5.: Reference energy and individual energy contributions to the CCSD(T) correlation energy (cf. Eqs. (7.12) and (7.13)) of the Rb^+ cation as a function of the cardinal number n corresponding to the aug-cc-p(w)CV n Z-PP basis sets [240]. The irregularities occurring in the Hartree-Fock (E_{HF}) and singles (E_{singles}) energies render the extrapolation ansatz according to Eq. (F.1) meaningless and cause the oscillatory behavior between the $n = 4$ and $n = 5$ values in Tabs. 7.1 and F.3.

F.3 | Vibrational levels for the $a\ ^3\Sigma_u$ state of Rb₂

To reveal the quality of the Rb₂ $a\ ^3\Sigma_u$ potentials obtained from the RP-RKHS interpolation procedure as described in Sec. 5.2, one may investigate the resulting rovibrational structure and compare it to experimental data. It appears useful to analyze the RP-RKHS potentials based on RHF-UCCSD(T)/ECP28MDF/UET17(CBS) *ab-initio* data within an approach merely accounting for the short-range correction after Eq. (5.31) [\equiv approach 1] and the approach where *ab-initio* energies and internuclear distances are additionally scaled and shifted to match the experimental results for D_e and R_e from Ref. [305] (\equiv approach 2). The rovibrational energy levels (v, J) were calculated using the LEVEL16 program by R.J. Le Roy [346] assuming ⁸⁷Rb isotopes. In this way 41 vibrational levels were found which is in accordance with experimental findings in Ref. [259]. The corresponding binding energies $E_b(v)$ for $J = 0$ are summarized in Tab. F.4.

TABLE F.4.: Synopsis of calculated (approach 1,2) and experimental values of vibrational energy levels v with rotational quantum number $J = 0$ of the $a^3\Sigma_u$ state of Rb_2 . The rovibrational structure was obtained from using the LEVEL16 program [346] assuming ^{87}Rb isotopes.

$(v, J = 0)$	$E_b(\text{approach 1}) [\text{cm}^{-1}]$	$E_b(\text{approach 2}) [\text{cm}^{-1}]$	$E_b(\text{expt.}) [\text{cm}^{-1}]$ [259]
0	-235.6557	-234.8823	-234.7647
1	-222.6526	-221.9008	-221.6479
2	-210.0011	-209.2708	-208.8991
3	-197.7046	-196.9960	-196.5190
4	-185.7648	-185.0779	-184.5097
5	-174.1836	-173.5184	-172.8743
6	-162.9636	-162.3200	-161.6125
7	-152.1071	-151.4852	-150.7262
8	-141.6168	-141.0167	-140.2174
9	-131.4947	-130.9165	-130.0894
10	-121.7430	-121.1868	-120.3413
11	-112.3641	-111.8299	-110.9756
12	-103.3603	-102.8481	-102.0104
13	-94.3873	-94.2440	-93.3495
14	-86.4885	-86.0203	-85.1920
15	-78.6100	-78.1796	-77.3857
16	-71.1487	-70.7247	-69.9456
17	-64.0603	-63.6585	-62.9201
18	-57.3633	-56.9838	-56.2678
19	-51.0605	-50.7032	-50.0150
20	-45.1541	-44.8193	-44.1586
21	-39.6462	-39.3338	-
22	-34.5375	-34.2476	-33.6279
23	-29.8270	-29.5594	-28.9486
24	-25.5115	-25.2661	-24.6503
25	-21.5854	-21.362	-20.7647
26	-18.0410	-17.8393	-17.2351
27	-14.8688	-14.6883	-14.1013
28	-12.0578	-11.8981	-11.3249
29	-9.5961	-9.4565	-8.8950
30	-7.4706	-7.3504	-
31	-5.6671	-5.5655	-5.0539
32	-4.1700	-4.0860	-
33	-2.9612	-2.8939	-2.5735
34	-2.0185	-1.9665	-1.6694
35	-1.3115	-1.2730	-
36	-0.7973	-0.7694	-0.2781
37	-0.4287	-0.4092	-0.2634
38	-0.1852	-0.1736	-0.0963
39	-0.0550	-0.0500	-0.0217
40	-0.0074	-0.0062	-

F.4 | Excluding possible sources of error for the Rb₂⁺ long-range barrier

In Sec. 6.2 it was claimed that the unphysical repulsive long-range barrier of the X²Σ_g⁺ PEC of Rb₂⁺ occurring for perturbative noniterative and approximate iterative coupled-cluster methods is independent on several sources of error. The investigations presented in the following will support this statement.

F.4.1 | Numerical errors

First, convergence problems due to numerical errors were excluded by significantly tightening several thresholds of the underlying computations:

1. MOLPRO

- The convergence threshold for the density matrix (square sum of the density matrix element changes) of the RHF reference calculation was set to `accu=14`
- The convergence thresholds for the energy and the coupled-cluster amplitudes (square sum of the amplitudes) were set to `thrden=1.d-12` and `thrvar=1.d-16`

2. CFOUR

- `SCF_CONV=11`, i.e. HF-SCF equations are considered converged if maximum change in density matrix elements is less than 10⁻¹¹
- `CC_CONV=11`, i.e. coupled cluster amplitude equations are considered to be converged when the maximum of all (absolute) changes in the amplitudes is less than 10⁻¹¹.

F.4.2 | Basis set superposition errors

The long-range barrier is further not caused by a basis set insufficiency as already concluded from Fig. 6.2 which revealed that the hump is independent of the basis set size and even slightly increases with increasing basis set size. Moreover, the basis set superposition error (BSSE) in small systems (such as Rb₂⁺) is more conveniently suppressed by using rather large basis sets (to which at least the aug-cc-pCV5Z-PP basis set belongs to). Nevertheless, applying the counterpoise correction (cpc) scheme to correct for BSSEs is shown in Fig. F.6 (a). This clearly demonstrates that BSSEs do

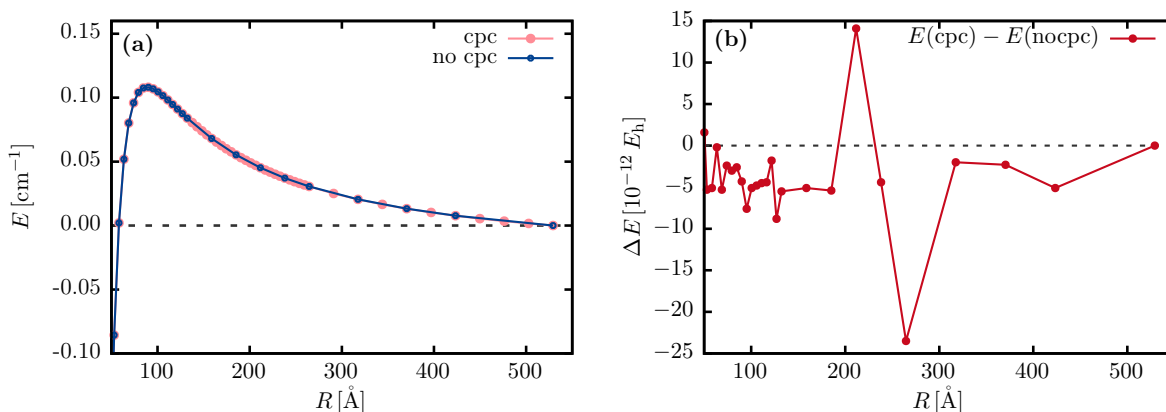


FIGURE F.6.: Analysis of basis set superposition errors (BSSEs) at RHF-UCCSD(T)/ECP28MDF/aug-cc-pCVTZ-PP level of theory by applying the counterpoise correction (cpc) scheme. The long-range tails of the $X^2\Sigma_g^+$ PECs of Rb_2^+ with cpc and without cpc are shown in (a). The presence of the long-range barrier in both cases shows that the problem is not caused by BSSEs. The respective energy differences shown in (b) reveals that accounting for BSSEs has only very small effects in the long-range region. *Freely adapted from J. Schnabel et al., J. Chem. Phys. 155, 124101 (2021).*

not cause the long-range barrier. Figure F.6 furthermore indicates that accounting for BSSEs or not is only a very small effect in the long-range region.

F.4.3 | aug-cc-pCVTZ-PP versus aug-cc-pwCVTZ-PP

In line with the previous discussion on basis set insufficiencies, Fig. F.7 shows that the long-range barrier occurs for both the aug-cc-pCV n Z-PP version and the aug-cc-pwCV n Z-PP variant of the recently published correlation consistent basis sets [240]. Figure F.7 further reveals, exemplarily for $n = 3$, that the weighted core-valence version leads to a slightly more pronounced hump and to an increase of the potentials depth of $\approx 60 \text{ cm}^{-1}$ as compared to the aug-cc-pCVTZ-PP basis set. Furthermore, the equilibrium distance of the PEC corresponding to the aug-cc-pwCVTZ-PP basis set is reduced by 0.1 \AA relative to the curve resulting from the aug-cc-pCVTZ-PP basis set.

F.4.4 | Choice of the reference determinant

The Rb_2^+ system allows for choosing either a spin-restricted open shell (ROHF) or a spin-unrestricted (UHF) approach for the reference determinant. The resulting Hartree-Fock PECs are shown in Fig. F.8 (a) and their corresponding energy difference (in terms of absolute energies) is illustrated in Fig. F.8 (b). The energy difference is in the order of $\mathcal{O}(10^{-5} \text{ cm}^{-1})$. Independent on the choice of the reference wavefunction the

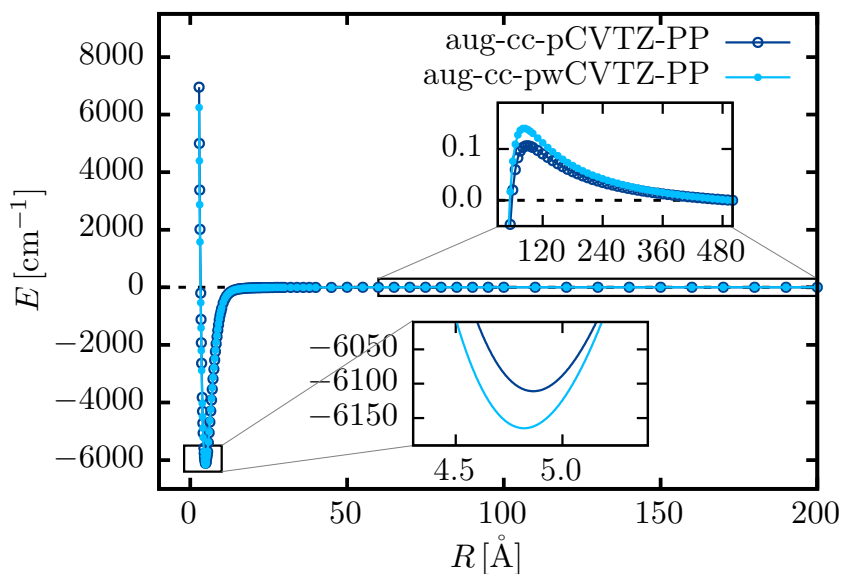


FIGURE F.7.: Comparison of the ground-state $X^2\Sigma_g^+$ potential energy curves obtained at ROHF-CCSD(T)/ECP28MDF level of theory using either the aug-cc-pCVTZ-PP (dark blue) basis set or the aug-cc-pwCVTZ-PP (light blue) basis set. The energies are given as interaction energies relative to the last *ab-initio* point.

subsequent ROHF-CCSD(T) and UHF-CCSD(T) calculations both reveal the long-range barrier; at the same position and of the same order of magnitude. This is shown in Fig. F.8 (c). The resulting energy difference between both approaches, as depicted in Fig. F.8 (d), demonstrates that the choice of the reference has only a minor effect to the CCSD(T) energy.

F.4.5 | Spin-restricted versus spin-unrestricted coupled-cluster

Besides, the choice of the reference wavefunction there is another degree of freedom concerning the spin adaption: spin-unrestricted [RHF-UCCSD(T)] or partially spin-restricted [RHF-RCCSD(T)] coupled-cluster theory. The resulting long-range tails of the $X^2\Sigma_g^+$ PECs of Rb_2^+ are shown in Fig. F.9 (a). The long-range barrier occurs for both approaches, at the same position and of the same order of magnitude. This is further illustrated by the corresponding energy differences (with respect to interaction energies) in Fig. F.9 (b).

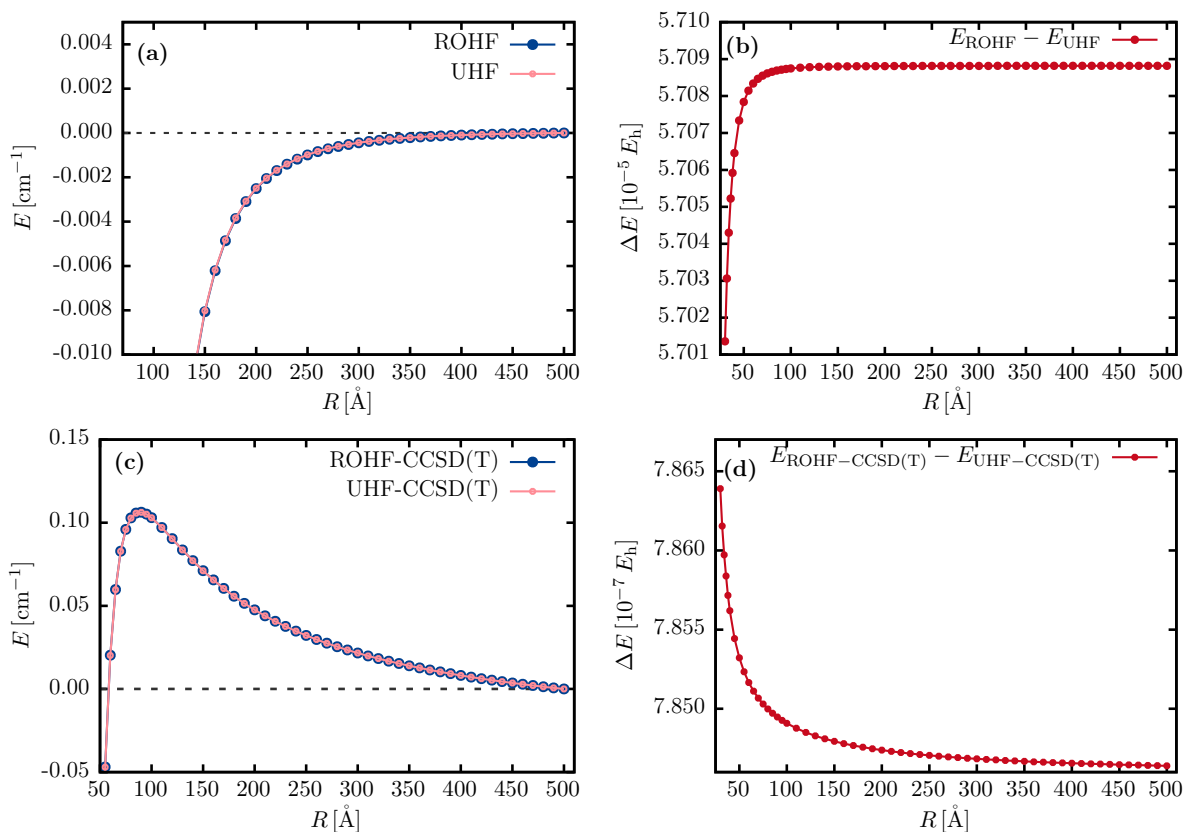


FIGURE F.8.: Overview on the effect of the choice of the reference determinant on the long-range tails of the $X^2\Sigma_g^+$ PECs of Rb_2^+ . The ROHF and UHF PECs are shown in (a). Their respective energy differences (absolute energies) are illustrated in (b). ROHF calculations were performed using the MOLPRO program package while UHF results were generated using CFOUR. The impact of the reference wavefunctions on the subsequent ROHF-CCSD(T) or UHF-CCSD(T) PECs, respectively are shown in (c). The long-range barrier is still present, at the same position with the same order of magnitude. The corresponding energy differences in (d) show that the choice of the reference wavefunction does not matter much in the long-range. ROHF-CCSD(T) results were obtained using MOLPRO and UHF-CCSD(T) energies using CFOUR. For both cases, the calculations were performed at ECP28MDF/aug-cc-pCVTZ-PP level of theory with energies given relative to the last *ab-initio* value. *Freely adapted from J. Schnabel et al., J. Chem. Phys.* **155**, 124101 (2021).

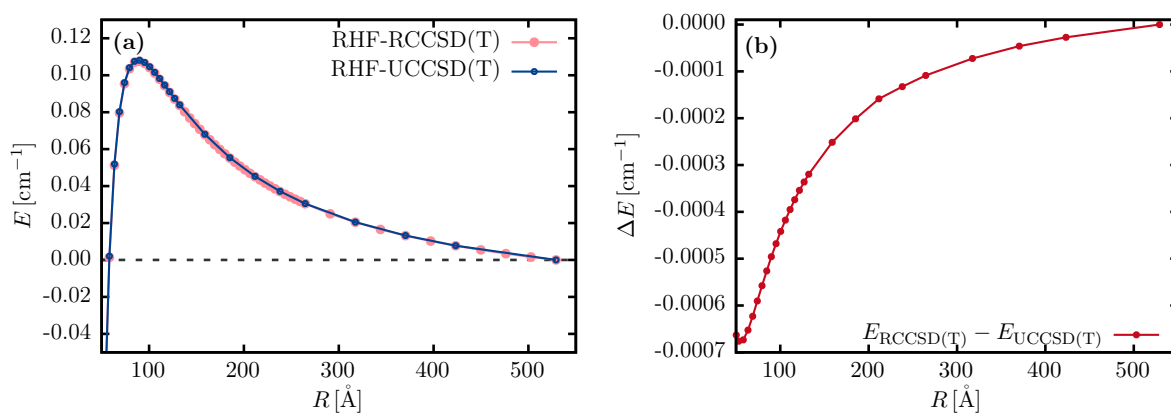


FIGURE F.9.: Comparison of using a spin-unrestricted [RHF-UCCSD(T)] or a partially spin-restricted [RHF-RCCSD(T)] coupled-cluster approach for the calculation of the long-range tails of the $X, ^2\Sigma_g^+$ PECs of Rb_2^+ . The PECs are shown in (a) with the long-range hump occurring for both cases, at the same position with the same order of magnitude. The differences of the respective interaction energies are shown in (b). The calculations were performed at ECP28MDF/aug-cc-pCVTZ-PP level of theory. *Freely adapted from J. Schnabel et al., J. Chem. Phys. 155, 124101 (2021).*

F.5 | Universality of the long-range barrier for alkali-metal dimer cations

The unphysical long-range barrier which is thoroughly investigated for Rb_2^+ in Chap. 6 turns out to be universal for X_2^+ systems with $X = \{\text{Li}, \text{Na}, \text{K}, \text{Rb}, \text{Cs}\}$. An overview on the respective long-range tails of the $X^2\Sigma_g^+$ PECs is given in Fig. F.10. Moreover, this shows that the problem is not connected with the pseudopotential approach, since no ECP has been used for both Li and Na.

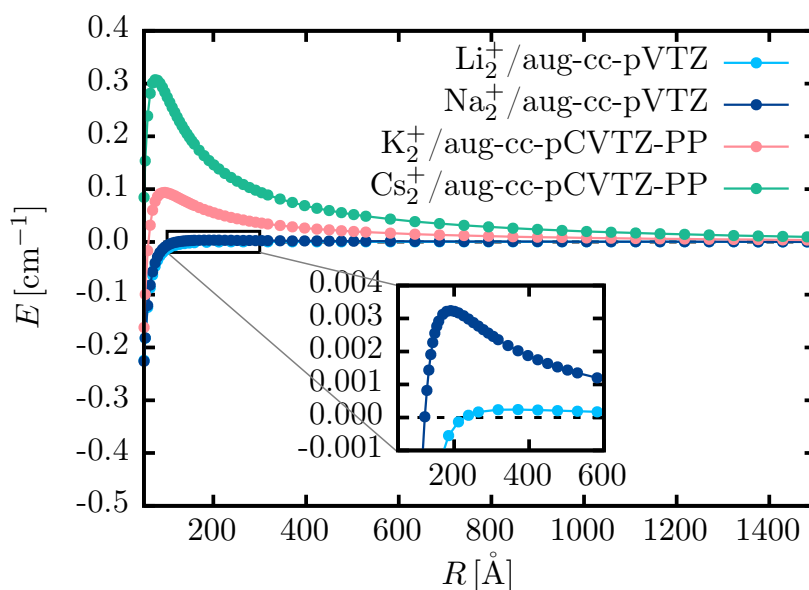


FIGURE F.10.: Overview on the long-range tails of the $X^2\Sigma_g^+$ PECs of several X_2^+ systems with $X = \{\text{Li}, \text{Na}, \text{K}, \text{Rb}, \text{Cs}\}$. No ECP has been used for Li and Na while the ECP10MDF has been applied for K and the ECP46MDF for Cs [250]. All energies are given relative to the respective last *ab-initio* point. Freely adapted from J. Schnabel et al., *J. Chem. Phys.* **155**, 124101 (2021).

F.6 | The CCSDT(Q)-PEC for Rb₂⁺

As discussed in Chap. 6 the long-range barrier is related to a symmetry instability of the underlying Hartree-Fock mean-field solution. Furthermore, it was demonstrated that the problem originates from the use of leading-order \hat{T}_3 amplitudes obtained from approximate CCSDT amplitude equations. This is a general problem which is not only restricted to the CCSD(T) method but occurs whenever iterative or noniterative approximations to the respective complete treatment are introduced. This is shown exemplarily in Fig. F.11 for the ROHF-CCSDT(Q) PEC [325] of the $X^2\Sigma_g^+$ state of Rb₂⁺. More specifically, the CCSDT(Q)/B variant for ROHF reference wavefunctions was used [41]. The hump is smaller in size, as the contributions of connected quadruples are generally smaller than those of connected triples. Nevertheless, despite its smallness the artificial barrier completely spoils the long-range behavior of the potential [324].

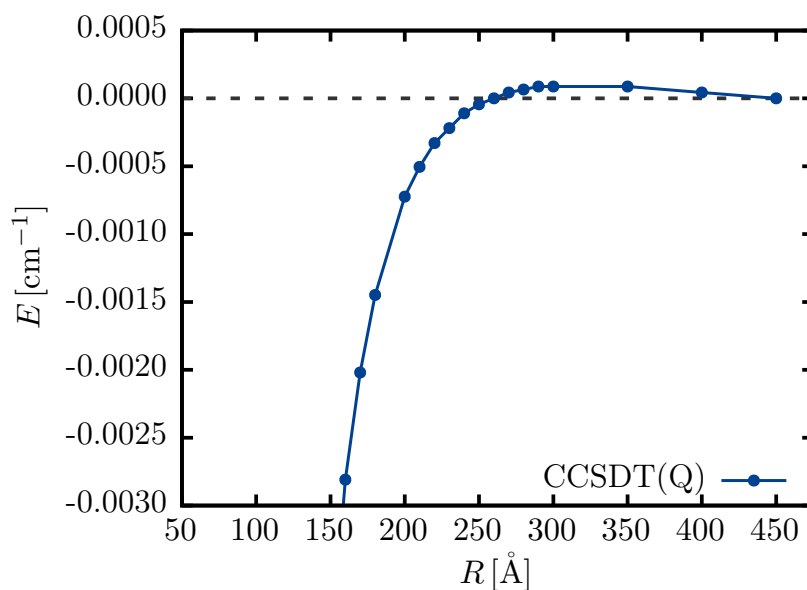


FIGURE F.11.: The long-range tail of the ROHF-CCSDT(Q) PEC of the $X^2\Sigma_g^+$ state of Rb₂⁺. The energies are given relative to the last *ab-initio* point and were obtained using the MRCC program suite [40, 47, 321, 322] at ECP28MDF/aug-cc-pwCVTZ-PP level of theory. The hump moved to larger internuclear distances R compared to the ROHF-CCSD(T) approach and to the iterative approximations to CCSDT (CCSDT- n with $n=1b,2,3$). *Freely adapted from J. Schnabel et al., J. Chem. Phys. 155, 124101 (2021).*

F.7 | Basis set effects on the $X^2\Sigma_g^+$ interaction potential of Rb_2^+

The investigations in Chap. 7 revealed that basis set effects play the most important role for obtaining high-accuracy results concerning both the exchange interaction according to Eq. (7.6) and spectroscopic constants such as D_e , D_0 and R_e . It was already shown in Sec. F.4.3 that the aug-cc-pCVTZ-PP and aug-cc-pwCVTZ-PP basis sets show significant differences concerning D_e and R_e . Preliminary investigations at ROHF-CCSD(T)/ECP28MDF level of theory using the UET17 and UET17(lt) basis sets according to Tabs. F.1 and F.2, respectively, as well as the aug-cc-pwCV n Z-PP series, give the minima shown in Fig. F.12. The energies are given as interaction energies with respect to the respective last *ab-initio* point at $R = 500 \text{ \AA}$ and can thus be used to obtain first estimates on corresponding dissociation energies D_e and equilibrium distances R_e . A discussion of all these effects can be found in the main text in Sec. 7.4.

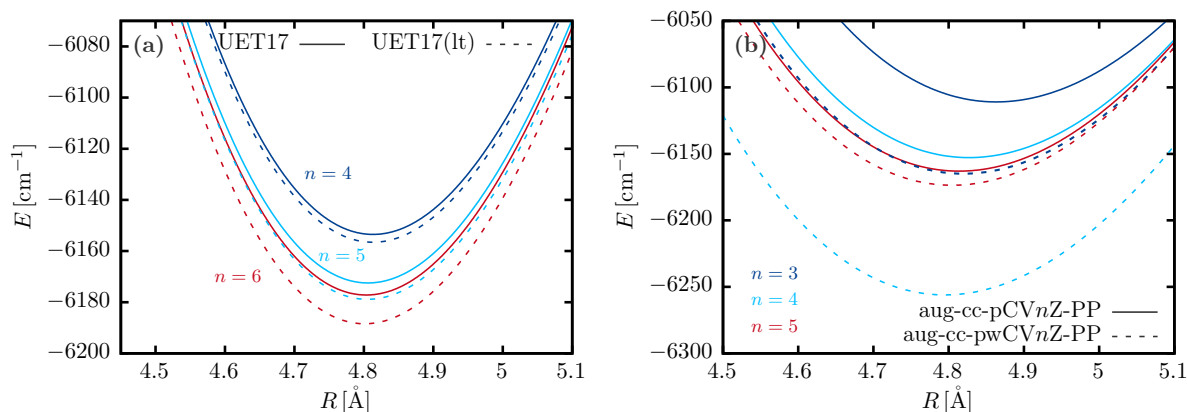


FIGURE F.12.: Comparison of the minima of the $X^2\Sigma_g^+$ ion-atom interaction potential obtained at ROHF-CCSD(T)/ECP28MDF level of theory using different basis sets. All energies are given as interaction energies with respect to the respective last *ab-initio* point at $R = 500 \text{ \AA}$ and can thus be used to obtain first estimates on corresponding dissociation energies D_e and equilibrium distances R_e . The results for the UET17 (solid lines) and UET17(lt) [dashed lines] basis sets according to Tabs. F.1 and F.2, respectively, are shown in (a). The basis set size is labeled by the cardinal number n . The minima for calculations with the aug-cc-pCV n Z-PP (solid lines) and aug-cc-pwCV n Z-PP (dashed lines) basis sets of Ref. [240] are shown in (b). The latter shows an irregular behavior for D_e with respect to increasing basis set size.

BIBLIOGRAPHY

- [1] W. D. Phillips, *Rev. Mod. Phys.* **70**, 721 (1998) (cited on page 1).
- [2] S. Chu, *Rev. Mod. Phys.* **70**, 685 (1998) (cited on page 1).
- [3] C. N. Cohen-Tannoudji, *Rev. Mod. Phys.* **70**, 707 (1998) (cited on page 1).
- [4] W. Ketterle, *Rev. Mod. Phys.* **74**, 1131 (2002) (cited on page 1).
- [5] E. A. Cornell and C. E. Wieman, *Rev. Mod. Phys.* **74**, 875 (2002) (cited on page 1).
- [6] E. L. Raab, M. Prentiss, A. Cable, S. Chu, and D. E. Pritchard, *Phys. Rev. Lett.* **59**, 2631 (1987) (cited on page 1).
- [7] N. Masuhara, J. M. Doyle, J. C. Sandberg, D. Kleppner, T. J. Greytak, H. F. Hess, and G. P. Kochanski, *Phys. Rev. Lett.* **61**, 935 (1988) (cited on page 1).
- [8] J. M. Hutson and P. Soldán, *Int. Rev. Phys. Chem.* **25**, 497 (2006) (cited on page 1).
- [9] D. A. Steck, *Rubidium 87 D Line Data*, available online at <http://steck.us/alkalidata> (revision 2.2.2, 9 July 2021) (cited on page 1).
- [10] G. Quéméner and P. S. Julienne, *Chem. Rev.* **112**, 4949 (2012) (cited on pages 1, 2, 4).
- [11] N. Balakrishnan, *J. Chem. Phys.* **145**, 150901 (2016) (cited on pages 1, 2, 81).
- [12] R. V. Krems, *Phys. Chem. Chem. Phys.* **10**, 4079 (2008) (cited on pages 1, 2, 81).
- [13] O. Dulieu and C. Gabbanini, *Rep. Prog. Phys.* **72**, 086401 (2009) (cited on pages 1, 2, 80).
- [14] M. T. Bell and T. P. Softley, *Mol. Phys.* **107**, 99 (2009) (cited on page 1).
- [15] J. Bohn, A. Rey, and J. Ye, *Science* **357**, 1002 (2017) (cited on pages 1, 2, 81).
- [16] J. Doyle, B. Friedrich, R. V. Krems, and F. Masnou-Seeuws, *Eur. Phys. J. D* **31**, 149 (2004) (cited on pages 1, 2, 81).
- [17] L. D. Carr, D. DeMille, R. V. Krems, and J. Ye, *New J. Phys.* **11**, 055049 (2009) (cited on pages 1, 2).
- [18] M. Tomza, *New J. Phys.* (2021) (cited on page 1).

- [19] E. A. Burt, R. W. Ghrist, C. J. Myatt, M. J. Holland, E. A. Cornell, and C. E. Wieman, *Phys. Rev. Lett.* **79**, 337 (1997) (cited on page 2).
- [20] D. M. Stamper-Kurn, M. R. Andrews, A. P. Chikkatur, S. Inouye, H.-J. Miesner, J. Stenger, and W. Ketterle, *Phys. Rev. Lett.* **80**, 2027 (cited on page 2).
- [21] C. H. Greene, P. Giannakeas, and J. Pérez-Ríos, *Rev. Mod. Phys.* **89**, 035006 (2017) (cited on pages 2, 3).
- [22] W. C. Stwalley and H. Wang, *J. Mol. Spectrosc.* **195**, 194 (1999) (cited on pages 2, 80).
- [23] K. M. Jones, E. Tiesinga, P. D. Lett, and P. S. Julienne, *Rev. Mod. Phys.* **78**, 483 (2006) (cited on pages 2, 80–82).
- [24] J. Ulmanis, J. Deiglmayr, M. Repp, R. Wester, and M. Weidemüller, *Chem. Rev.* **112**, 4890 (2012) (cited on pages 2, 80, 81).
- [25] T. Köhler, K. Góral, and P. S. Julienne, *Rev. Mod. Phys.* **78**, 1311 (2006) (cited on page 2).
- [26] C. Chin, R. Grimm, P. Julienne, and E. Tiesinga, *Rev. Mod. Phys.* **82**, 1225 (2010) (cited on page 2).
- [27] R. J. Bartlett and M. Musiał, *Rev. Mod. Phys.* **79**, 291 (2007) (cited on pages 2, 57, 58, 60).
- [28] M. Urban, J. Noga, S. J. Cole, and R. J. Bartlett, *J. Chem. Phys.* **83**, 4041 (1985) (cited on pages 2, 61, 62).
- [29] R. Krishnan, T. Gary W., P. John A., and H.-G. Martin, *Chem. Phys. Lett.* **157**, 479 (1989) (cited on pages 2, 60–62, 155).
- [30] B. Rodney J., W. J.D., K. S.A., and N. J., *Chem. Phys. Lett.* **165**, 513 (1990) (cited on pages 2, 61, 62, 155).
- [31] J. F. Stanton, *Chem. Phys. Lett.* **281**, 130 (1997) (cited on pages 2, 61, 62, 165).
- [32] J. D. Watts, J. Gauss, and R. J. Bartlett, *J. Chem. Phys.* **98**, 8718 (1993) (cited on pages 2, 61–63, 157).
- [33] K. Raghavachari, *Chem. Phys. Lett.* **589**, SPECIAL NOBEL ISSUE, 35 (2013) (cited on pages 2, 61).
- [34] J. Noga and R. J. Bartlett, *J. Chem. Phys.* **86**, 7041 (1987) (cited on pages 2, 60, 155).

- [35] J. Noga and R. J. Bartlett, *J. Chem. Phys.* **89**, 3401 (1988) (cited on pages 2, 60, 155).
- [36] G. E. Scuseria and H. F. Schaefer, *Chem. Phys. Lett.* **152**, 382 (1988) (cited on pages 2, 60, 155).
- [37] J. D. Watts and R. J. Bartlett, *J. Chem. Phys.* **93**, 6104 (1990) (cited on pages 2, 60, 155).
- [38] K. Stanislaw A. and B. Rodney J., *Chem. Phys. Lett.* **158**, 550 (1989) (cited on pages 2, 63, 155).
- [39] Y. J. Bomble, J. F. Stanton, M. Kállay, and J. Gauss, *J. Chem. Phys.* **123**, 054101 (2005) (cited on pages 2, 63, 155).
- [40] M. Kállay and J. Gauss, *J. Chem. Phys.* **123**, 214105 (2005) (cited on pages 2, 63, 155, 175, 278).
- [41] M. Kállay and J. Gauss, *J. Chem. Phys.* **129**, 144101 (2008) (cited on pages 2, 63, 155, 278).
- [42] S. A. Kucharski and R. J. Bartlett, *Theor. Chim. Acta* **80**, 387 (1991) (cited on pages 2, 60).
- [43] N. Oliphant and L. Adamowicz, *J. Chem. Phys.* **95**, 6645 (1991) (cited on pages 2, 60).
- [44] S. A. Kucharski and R. J. Bartlett, *J. Chem. Phys.* **97**, 4282 (1992) (cited on pages 2, 60).
- [45] D. A. Matthews and J. F. Stanton, *J. Chem. Phys.* **142**, 064108 (2015) (cited on pages 2, 60).
- [46] J. Olsen, *J. Chem. Phys.* **113**, 7140 (2000) (cited on pages 2, 60).
- [47] M. Kállay and P. R. Surján, *J. Chem. Phys.* **115**, 2945 (2001) (cited on pages 2, 60, 155, 175, 278).
- [48] S. Hirata, *J. Phys. Chem. A* **107**, 9887 (2003) (cited on pages 2, 60).
- [49] P. G. Szalay, T. Müller, G. Gidofalvi, H. Lischka, and R. Shepard, *Chem. Rev.* **112**, 108 (2012) (cited on pages 2, 65, 68, 72).
- [50] H. Lischka, D. Nachtigallová, A. J. A. Aquino, P. G. Szalay, F. Plasser, F. B. C. Machado, and M. Barbatti, *Chem. Rev.* **118**, 7293 (2018) (cited on pages 2, 64, 67, 68, 72).

- [51] A. Köhn, M. Hanauer, L. A. Mück, T.-C. Jagau, and J. Gauss, *WIREs Comput. Mol. Sci.* **3**, 176 (2013) (cited on pages 2, 64).
- [52] J. F. Stanton and R. J. Bartlett, *J. Chem. Phys.* **98**, 7029 (1993) (cited on page 2).
- [53] K. Kowalski and P. Piecuch, *J. Chem. Phys.* **115**, 643 (2001) (cited on page 2).
- [54] S. A. Kucharski, M. Włoch, M. Musiał, and R. J. Bartlett, *J. Chem. Phys.* **115**, 8263 (2001) (cited on page 2).
- [55] Y. J. Bomble, K. W. Sattelmeyer, J. F. Stanton, and J. Gauss, *J. Chem. Phys.* **121**, 5236 (2004) (cited on page 2).
- [56] M. Kállay and J. Gauss, *J. Chem. Phys.* **121**, 9257 (2004) (cited on page 2).
- [57] M. Dolg, "Effective Core Potentials", in *Modern methods and algorithms of quantum chemistry*, edited by J. Grotendorst (NIC-Directors, Jülich, 2000), pages 507–540 (cited on pages 2, 75, 84).
- [58] M. Dolg and X. Cao, *Chem. Rev.* **112**, 403 (2012) (cited on pages 2, 75, 83, 84).
- [59] M. Aymar and O. Dulieu, *J. Chem. Phys.* **122**, 204302 (2005) (cited on page 3).
- [60] J. Aldegunde, B. A. Rivington, P. S. Żuchowski, and J. M. Hutson, *Phys. Rev. A* **78**, 033434 (2008) (cited on page 3).
- [61] J. Aldegunde and J. M. Hutson, *Phys. Rev. A* **79**, 013401 (2009) (cited on page 3).
- [62] R. Kosloff, *J. Chem. Phys.* **92**, 2087 (1988) (cited on page 3).
- [63] O. Dulieu and P. S. Julienne, *J. Chem. Phys.* **103**, 60 (1995) (cited on page 3).
- [64] D. T. Colbert and W. H. Miller, *J. Chem. Phys.* **96**, 1982 (1992) (cited on page 3).
- [65] S. H. Yuwono, I. Magoulas, and P. Piecuch, *Sci. Adv.* **6** (2020) 10.1126/sciadv.aay4058 (cited on page 3).
- [66] F. Ferlaino, A. Zenesini, M. Berninger, B. Huang, H.-C. Nägerl, and R. Grimm, *Few-Body Syst.* **51**, 113 (2011) (cited on page 3).
- [67] J. P. D’Incao and B. D. Esry, *Phys. Rev. A* **72**, 032710 (2005) (cited on page 3).
- [68] J. P. D’Incao and B. D. Esry, *Phys. Rev. A* **73**, 030703 (2006) (cited on page 3).
- [69] Y. Wang, J. P. D’Incao, and C. H. Greene, *Phys. Rev. Lett.* **106**, 233201 (2011) (cited on page 3).
- [70] J. Wang, J. P. D’Incao, B. D. Esry, and C. H. Greene, *Phys. Rev. Lett.* **108**, 263001 (2012) (cited on pages 3, 82, 109).

- [71] Y. Wang, J. P. D’Incao, and B. D. Esry, “Chapter 1 - Ultracold Few-Body Systems”, in *Advances in atomic, molecular, and optical physics*, Vol. 62, edited by E. Arimondo, P. R. Berman, and C. C. Lin (Academic Press, 2013), pages 1–115 (cited on page 3).
- [72] C. E. Klauss, X. Xie, C. Lopez-Abadia, J. P. D’Incao, Z. Hadzibabic, D. S. Jin, and E. A. Cornell, *Phys. Rev. Lett.* **119**, 143401 (2017) (cited on page 3).
- [73] G. Delacrétaz, E. R. Grant, R. L. Whetten, L. Wöste, and J. W. Zwanziger, *Phys. Rev. Lett.* **56**, 2598 (1986) (cited on page 3).
- [74] W. E. Ernst and S. Rakowsky, *Ber. Bunsenges. Phys. Chem.* **99**, 441 (1995) (cited on page 3).
- [75] D. T. Vituccio, O. Golonzka, and W. E. Ernst, *J. Mol. Spectrosc.* **184**, 237 (1997) (cited on page 3).
- [76] J. Nagl, G. Auböck, A. W. Hauser, O. Allard, C. Callegari, and W. E. Ernst, *J. Chem. Phys.* **128**, 154320 (2008) (cited on pages 3, 103).
- [77] J. Nagl, G. Auböck, A. W. Hauser, O. Allard, C. Callegari, and W. E. Ernst, *Phys. Rev. Lett.* **100**, 063001 (2008) (cited on page 3).
- [78] A. W. Hauser and W. E. Ernst, *Phys. Chem. Chem. Phys.* **13**, 18762 (2011) (cited on pages 3, 102, 103).
- [79] C. Giese, F. Stienkemeier, M. Mudrich, A. W. Hauser, and W. E. Ernst, *Phys. Chem. Chem. Phys.* **13**, 18769 (2011) (cited on pages 3, 103).
- [80] W. H. Gerber and E. Schumacher, *J. Chem. Phys.* **69**, 1692 (1978) (cited on pages 4, 28, 92).
- [81] J. L. Martins, R. Car, and J. Buttet, *J. Chem. Phys.* **78**, 5646 (1983) (cited on pages 4, 28, 92).
- [82] R. G. Sadygov and D. R. Yarkony, *J. Chem. Phys.* **110**, 3639 (1999) (cited on pages 4, 28, 92).
- [83] D. A. Brue, X. Li, and G. A. Parker, *J. Chem. Phys.* **123**, 091101 (2005) (cited on pages 4, 28, 92, 96).
- [84] T. C. Thompson, G. Izmirlian, S. J. Lemon, D. G. Truhlar, and C. A. Mead, *J. Chem. Phys.* **82**, 5597 (1985) (cited on pages 4, 28, 92).
- [85] R. Martin and E. Davidson, *Mol. Phys.* **35**, 1713 (1978) (cited on pages 4, 28).
- [86] F. Cocchini, T. H. Upton, and W. Andreoni, *J. Chem. Phys.* **88**, 6068 (1988) (cited on pages 4, 28, 38–41, 92, 93, 95, 96, 111, 123, 124).

- [87] J. Schön and H. Köppel, *Chem. Phys. Lett.* **231**, 55 (1994) (cited on pages 4, 28, 37, 38, 92, 123).
- [88] R. Meiswinkel and H. Köppel, *Chem. Phys.* **144**, 117 (1990) (cited on pages 4, 28, 38–40, 92, 96, 123).
- [89] M. Mayer, L. S. Cederbaum, and H. Köppel, *J. Chem. Phys.* **104**, 8932 (1996) (cited on pages 4, 28, 38, 92, 123).
- [90] J. Schön and H. Köppel, *J. Phys. Chem. A* **103**, 8579 (1999) (cited on pages 4, 28, 38, 92, 123).
- [91] Bâldea, I. and Köppel, H., *Eur. Phys. J. D* **30**, 209 (2004) (cited on pages 4, 28, 38, 40, 92, 96, 123, 131).
- [92] A. W. Hauser, C. Callegari, P. Soldán, and W. E. Ernst, *J. Chem. Phys.* **129**, 044307 (2008) (cited on pages 4, 28, 92, 95).
- [93] A. W. Hauser, J. V. Pototschnig, and W. E. Ernst, *Chem. Phys.* **460**, 2 (2015) (cited on pages 4, 28, 92, 123).
- [94] S. Mukherjee and S. Adhikari, *Chem. Phys.* **440**, 106 (2014) (cited on pages 4, 16–18, 28, 92, 127, 220).
- [95] A. W. Hauser, C. Callegari, P. Soldán, and W. E. Ernst, *Chem. Phys.* **375**, 73 (2010) (cited on pages 4, 28, 31, 33, 34, 92, 95, 102, 115, 116, 123).
- [96] A. W. Hauser, G. Auböck, C. Callegari, and W. E. Ernst, *J. Chem. Phys.* **132**, 164310 (2010) (cited on pages 4, 28, 33, 34, 36, 92, 95, 102, 103, 106, 113, 115, 123, 220).
- [97] G. Auböck, J. Nagl, C. Callegari, and W. E. Ernst, *J. Chem. Phys.* **129**, 114501 (2008) (cited on pages 4, 28, 34–36, 92).
- [98] A. W. Hauser, C. Callegari, and W. E. Ernst, “Level-Structure and Magnetic Properties from One-Electron Atoms to Clusters with Delocalized Electronic Orbitals: Shell Models for Alkali Trimers”, in *Advances in the Theory of Atomic and Molecular Systems: Dynamics, Spectroscopy, Clusters, and Nanostructures*, edited by P. Piecuch, J. Maruani, G. Delgado-Barrio, and S. Wilson (Springer Netherlands, Dordrecht, 2009), pages 201–215 (cited on page 4).
- [99] A. W. Hauser, “The electronic structure of alkali trimers in their doublet and quartet manifolds: shell models and quantum chemistry calculations”, PhD thesis (Technische Universität Graz, 2009) (cited on pages 4, 95, 132).

-
- [100] P. Soldán, *J. Chem. Phys.* **132**, 234308 (2010) (cited on pages 4, 84, 85, 92, 96, 97, 99, 135, 138–140, 144, 146, 147, 261).
- [101] P. Soldán, M. T. Cvitaš, J. M. Hutson, P. Honvault, and J.-M. Launay, *Phys. Rev. Lett.* **89**, 153201 (2002) (cited on page 4).
- [102] P. Soldán, M. T. Cvitaš, and J. M. Hutson, *Phys. Rev. A* **67**, 054702 (2003) (cited on pages 4, 144, 146).
- [103] G. Quémener, P. Honvault, J.-M. Launay, P. Soldán, D. E. Potter, and J. M. Hutson, *Phys. Rev. A* **71**, 032722 (2005) (cited on pages 4, 135, 138, 139).
- [104] M. T. Cvitaš, P. Soldán, J. M. Hutson, P. Honvault, and J.-M. Launay, *Phys. Rev. Lett.* **94**, 033201 (2005) (cited on pages 4, 96).
- [105] M. T. Cvitaš, P. Soldán, and J. M. Hutson, *Mol. Phys.* **104**, 23 (2006) (cited on pages 4, 135, 138–140).
- [106] M. T. Cvitaš, P. Soldán, J. M. Hutson, P. Honvault, and J.-M. Launay, *J. Chem. Phys.* **127**, 074302 (2007) (cited on pages 4, 96).
- [107] J. M. Hutson and P. Soldán, *Int. Rev. Phys. Chem.* **26**, 1 (2007) (cited on pages 4, 110, 135, 138, 146).
- [108] M. Lepers and O. Dulieu, *Eur. Phys. J. D* **65**, 113 (2011) (cited on page 4).
- [109] J. Péres-Ríos, M. Lepers, and O. Dulieu, *Phys. Rev. Lett.* **115**, 073201 (2015) (cited on pages 4, 82, 109).
- [110] M. Tomza, K. Jachymski, R. Gerritsma, A. Negretti, T. Calarco, Z. Idziaszek, and P. S. Julienne, *Rev. Mod. Phys.* **91**, 035001 (2019) (cited on pages 5, 153, 156, 169, 170).
- [111] K. Kleinbach, F. Engel, T. Dieterle, R. Löw, T. Pfau, and F. Meinert, *Phys. Rev. Lett.* **120**, 193401 (2018) (cited on pages 5, 153, 167, 168, 171).
- [112] R. Côté and A. Dalgarno, *Phys. Rev. A* **62**, 012709 (2000) (cited on page 5).
- [113] Z. Idziaszek, T. Calarco, P. S. Julienne, and A. Simoni, *Phys. Rev. A* **79**, 010702 (2009) (cited on page 5).
- [114] T. Schmid, C. Veit, N. Zuber, R. Löw, T. Pfau, M. Tarana, and M. Tomza, *Phys. Rev. Lett.* **120**, 153401 (2018) (cited on pages 5, 6, 153, 167, 168).
- [115] K. Jachymski, M. Krych, P. S. Julienne, and Z. Idziaszek, *Phys. Rev. Lett.* **110**, 213202 (2013) (cited on pages 5, 6).

- [116] W. Casteels, J. Tempere, and J. T. Devreese, *J. Low Temp. Phys.* **162**, 266 (2011) (cited on page 5).
- [117] G. E. Astrakharchik, L. A. P. Ardila, R. Schmidt, K. Jachymski, and A. Negretti, *Commun. Phys.* **4**, 94 (2021) (cited on page 5).
- [118] U. Bissbort, D. Cocks, A. Negretti, Z. Idziaszek, T. Calarco, F. Schmidt-Kaler, W. Hofstetter, and R. Gerritsma, *Phys. Rev. Lett.* **111**, 080501 (2013) (cited on page 5).
- [119] R. Côté, “Chapter Two - Ultracold Hybrid Atom–Ion Systems”, in *Advances in atomic, molecular, and optical physics*, Vol. 65, edited by E. Arimondo, C. C. Lin, and S. F. Yelin (Academic Press, 2016), pages 67–126 (cited on pages 5, 170, 183).
- [120] F. Engel, T. Dieterle, T. Schmid, C. Tomschitz, C. Veit, N. Zuber, R. Löw, T. Pfau, and F. Meinert, *Phys. Rev. Lett.* **121**, 193401 (2018) (cited on pages 5, 153, 167, 168).
- [121] T. Dieterle, M. Berngruber, C. Hölzl, R. Löw, K. Jachymski, T. Pfau, and F. Meinert, *Phys. Rev. A* **102**, 041301 (2020) (cited on pages 5, 153, 167, 168, 171).
- [122] T. Dieterle, M. Berngruber, C. Hölzl, R. Löw, K. Jachymski, T. Pfau, and F. Meinert, *Phys. Rev. Lett.* **126**, 033401 (2021) (cited on pages 5, 153, 167, 168, 171).
- [123] K. Jachymski and F. Meinert, *Appl. Sci.* **10** (2020) 10.3390/app10072371 (cited on pages 5, 6, 168, 171).
- [124] K. Jachymski, M. Krych, P. S. Julienne, and Z. Idziaszek, *Phys. Rev. A* **90**, 042705 (2014) (cited on page 6).
- [125] S. Magnier, S. Rousseau, A. Allouche, G. Hadinger, and M. Aubert-Frécon, *Chem. Phys.* **246**, 57 (1999) (cited on pages 6, 170).
- [126] S. Magnier and M. Aubert-Frécon, *J. Quant. Spectrosc. Ra.* **78**, 217 (2003) (cited on page 6).
- [127] A. Jraij, A. Allouche, M. Korek, and M. Aubert-Frécon, *Chem. Phys.* **290**, 129 (2003) (cited on pages 6, 184, 185).
- [128] H. Berriche, *Int. J. Quant. Chem.* **113**, 2405 (2013) (cited on page 6).
- [129] M. Musiał, M. Medrek, and S. A. Kucharski, *Mol. Phys.* **113**, 2943 (2015) (cited on pages 6, 187).
- [130] A. Bewicz, M. Musiał, and S. A. Kucharski, *Mol. Phys.* **115**, 2649 (2017) (cited on pages 6, 187).

- [131] P. Skupin, M. Musiał, and S. A. Kucharski, *J. Phys. Chem. A* **121**, 1480 (2017) (cited on pages 6, 187).
- [132] M. Born and R. Oppenheimer, *Ann. Physik* **389**, 457 (1927) (cited on page 12).
- [133] I. Levine, *Quantum chemistry*, Pearson advanced chemistry series (Pearson, 2014) (cited on page 12).
- [134] H.-J. Werner and A. Köhn, *Lecture notes in advanced methods in quantum chemistry*, 2020 (cited on pages 12, 46).
- [135] M. Baer, “The Electronic Non-Adiabatic Coupling Term in Molecular Systems: A Theoretical Approach”, in *The Role of Degenerate States in Chemistry* (John Wiley & Sons, Ltd, 2002), pages 39–142 (cited on pages 12, 16–18).
- [136] J. von Neumann and E. P. Wigner, *Z. Physik* **30**, 467 (1929) (cited on pages 14, 20).
- [137] E. Teller, *J. Phys. Chem.* **41**, 109 (1937) (cited on pages 14, 20).
- [138] G. Herzberg and H. C. Longuet-Higgins, *Discuss. Faraday Soc.* **35**, 77 (1963) (cited on pages 14, 23).
- [139] H. C. Longuet-Higgins, *Proc. R. Soc. Lond. A* **344**, 147 (1975) (cited on pages 14, 20, 21).
- [140] F. Jensen, *Introduction to Computational Chemistry* (John Wiley & Sons Ltd, 1999) (cited on pages 16, 47–49, 51, 52, 60, 64, 68, 72–74).
- [141] H. G. A. Hellmann, *Z. Phys.* **85**, 180 (1933) (cited on pages 17, 26).
- [142] R. P. Feynman, *Phys. Rev.* **56**, 340 (1939) (cited on pages 17, 26).
- [143] M. Born and V. Fock, *Z. Phys.* **51**, 165 (1928) (cited on page 17).
- [144] D. Simah, B. Hartke, and H.-J. Werner, *J. Chem. Phys.* **111**, 4523 (1999) (cited on page 18).
- [145] D. M. G. Williams and W. Einfeld, *J. Chem. Phys.* **149**, 204106 (2018) (cited on pages 18, 196).
- [146] M. V. Berry and M. Wilkinson, *Proc. R. Soc. Lond. A* **392**, 15 (1984) (cited on pages 19, 21, 23).
- [147] M. V. Berry, “Aspects of Degeneracy”, in *Chaotic Behaviour in Quantum Systems: Theory and Applications*, Vol. 120, edited by G. Casati, NATO ASI Series B. Physics (Plenum Press, 1985), pages 123–140 (cited on pages 19–21).

- [148] H. Cartarius, "Exceptional points in atomic spectra and Bose-Einstein condensates", PhD thesis (University of Stuttgart, 2008) (cited on page 19).
- [149] M. S. Child, "Early Perspectives on Geometric Phase", in *The Role of Degenerate States in Chemistry* (John Wiley & Sons, Ltd, 2002), pages 1–38 (cited on page 20).
- [150] M. V. Berry, *Proc. R. Soc. Lond. A* **392**, 45 (1984) (cited on pages 21, 23).
- [151] D. R. Yarkony, *Acc. Chem. Res.* **31**, 511 (1998) (cited on page 23).
- [152] C. M. R. Rocha and A. J. C. Varandas, *J. Chem. Phys.* **144**, 064309 (2016) (cited on pages 23, 28, 38, 39, 92, 96).
- [153] M. Desouter-Lecomte, C. Galloy, J. C. Lorquet, and M. V. Pires, *J. Chem. Phys.* **71**, 3661 (1979) (cited on pages 23, 24).
- [154] B. J. Whitaker, *Science* **334**, 187 (2011) (cited on page 23).
- [155] H. C. Longuet-Higgins, *Adv. Spectrosc.* **2**, 429 (1961) (cited on pages 23, 29).
- [156] D. R. Yarkony, *Rev. Mod. Phys.* **68**, 985 (1996) (cited on page 23).
- [157] Y. Aharonov and D. Bohm, *Phys. Rev.* **115**, 485 (1959) (cited on page 23).
- [158] C. A. Mead, *J. Chem. Phys.* **70**, 2276 (1979) (cited on page 23).
- [159] C. Alden Mead, *Chem. Phys.* **49**, 23 (1980) (cited on page 23).
- [160] H. A. Jahn, E. Teller, and F. G. Donnan, *Proc. R. Soc.* **161**, 220 (1937) (cited on pages 24, 26).
- [161] I. B. Bersuker, *Chem. Rev.* **101**, 1067 (2001) (cited on pages 24, 26, 27, 31–33, 36–38, 44, 92, 122, 123, 131).
- [162] H. Köppel, W. Domcke, and L. S. Cederbaum, *J. Chem. Phys.* **74**, 2945 (1981) (cited on page 24).
- [163] Y. Liu, I. B. Bersuker, W. Zou, and J. E. Boggs, *Chem. Phys.* **376**, 30 (2010) (cited on pages 24, 37, 42–44, 97).
- [164] A. Varandas, *Chem. Phys. Lett.* **487**, 139 (2010) (cited on pages 25–27, 36, 92).
- [165] E. Wigner, *Nachr. Ges. Wiss. Göttingen*, 133 (1930) (cited on pages 25, 26).
- [166] P. García-Fernández, I. B. Bersuker, J. A. Aramburu, M. T. Barriuso, and M. Moreno, *Phys. Rev. B* **71**, 184117 (2005) (cited on pages 25, 31, 38, 115).
- [167] A. Viel and W. Einfeld, *J. Chem. Phys.* **120**, 4603 (2004) (cited on pages 28–30).
- [168] M. S. Child and H. C. Longuet-Higgins, *Phil. Trans. Roy. Soc. London A* **254**, 259 (1961) (cited on pages 29, 38).

- [169] B. P. Thapaliya, M. B. Dawadi, C. Ziegler, and D. S. Perry, *Chem. Phys.* **460**, 31 (2015) (cited on page 30).
- [170] H. Koizumi and I. B. Bersuker, *Phys. Rev. Lett.* **83**, 3009 (1999) (cited on pages 32, 37).
- [171] T. A. Barckholtz and T. A. Miller, *Int. Rev. in Phys. Chem.* **17**, 435 (1998) (cited on pages 33, 34, 111, 113).
- [172] W. Domcke, S. Mishra, and L. V. Poluyanov, *Chem. Phys.* **322**, 405 (2006) (cited on pages 33, 34, 111).
- [173] L. V. Poluyanov and W. Domcke, *Chem. Phys.* **352**, 125 (2008) (cited on pages 33, 34, 111).
- [174] J. Schön and H. Köppel, *J. Chem. Phys.* **108**, 1503 (1998) (cited on pages 33, 34, 111).
- [175] H. Koizumi and S. Sugano, *J. Chem. Phys.* **102**, 4472 (1995) (cited on pages 33, 111).
- [176] R. Meiswinkel and H. Köppel, *Chem. Phys.* **129**, 463 (1989) (cited on page 36).
- [177] H. C. Longuet-Higgins, U. Öpik, M. H. L. Pryce, and R. A. Sack, *Proc. R. Soc. London Ser. A* **244**, 1 (1958) (cited on page 36).
- [178] H. von Busch, V. Dev, H.-A. Eckel, S. Kasahara, J. Wang, W. Demtröder, P. Sebald, and W. Meyer, *Phys. Rev. Lett.* **81**, 4584 (1998) (cited on pages 36, 37).
- [179] R. Requist, F. Tandetzky, and E. K. U. Gross, *Phys. Rev. A* **93**, 042108 (2016) (cited on pages 36, 37).
- [180] J. Schön and H. Köppel, *J. Chem. Phys.* **103**, 9292 (1995) (cited on pages 37, 40).
- [181] U. Öpik and M. H. L. Pryce, *Proc. R. Soc. London Ser. A* **238**, 425 (1957) (cited on page 37).
- [182] I. B. Bersuker, *Chem. Rev.* **113**, 1351 (2013) (cited on pages 37, 42–44, 93, 131).
- [183] I. B. Bersuker, *Chem. Rev.* **121**, 1463 (2021) (cited on pages 37, 92, 131).
- [184] W. Eisfeld and A. Viel, *J. Chem. Phys.* **122**, 204317 (2005) (cited on pages 38, 40).
- [185] G. Herzberg and E. Teller, *Z. Phys. Chem.* **21B**, 410 (1933) (cited on page 41).
- [186] R. Renner, *Z. Phys.* **92**, 172 (1934) (cited on page 41).
- [187] P. Garcia-Fernandez, I. B. Bersuker, and J. E. Boggs, *J. Phys. Chem. A* **111**, 10409 (2007) (cited on page 42).

- [188] H. Kayi, I. B. Bersuker, and J. E. Boggs, *J. Mol. Struct.* **1023**, 108 (2012) (cited on pages 42, 44).
- [189] P. Garcia-Fernandez and I. B. Bersuker, *Int. J. Quantum Chem.* **112**, 3025 (2012) (cited on pages 42, 44).
- [190] I. B. Bersuker, N. N. Gorinchoi, and V. Z. Polinger, *Theor. Chim. Acta* **66**, 161 (1984) (cited on page 42).
- [191] A. Szabo and N. S. Ostlund, *Modern Quantum Chemistry: Introduction to Advanced Electronic Structure Theory* (Dover Publications, Inc., 1996) (cited on pages 45, 46, 48–52, 55, 56, 69, 72).
- [192] J. C. Slater, *Phys. Rev.* **34**, 1293 (1929) (cited on page 46).
- [193] D. R. Hartree, *Math. Proc. Camb. Philos. Soc.* **24**, 89 (1928) (cited on page 46).
- [194] V. Fock, *Z. Phys.* **61**, 126 (1930) (cited on page 46).
- [195] C. C. J. Roothaan, *Rev. Mod. Phys.* **23**, 69 (1951) (cited on pages 48, 50).
- [196] G. G. Hall and J. E. Lennard-Jones, *Proc. R. Soc. London Ser. A* **205**, 541 (1951) (cited on pages 48, 50).
- [197] M. Dornbach, “Analytical energy gradients for open-shell local second-order Møller-Plesset perturbation theory and applications to large molecules”, PhD thesis (University of Stuttgart, 2018) (cited on page 52).
- [198] C. C. J. Roothaan, *Rev. Mod. Phys.* **32**, 179 (1960) (cited on page 52).
- [199] D. P. Tew, W. Klopper, and T. Helgaker, *J. Comput. Chem.* **28**, 1307 (2007) (cited on pages 53, 73).
- [200] C. Hättig, W. Klopper, A. Köhn, and D. P. Tew, *Chem. Rev.* **112**, 4 (2012) (cited on pages 53, 73).
- [201] T. D. Crawford and H. F. Schaefer III, “An Introduction to Coupled Cluster Theory for Computational Chemists”, in *Reviews in computational chemistry*, Vol. 14, edited by K. B. Lipkowitz and D. B. Boyd (John Wiley & Sons, Ltd, 2000), pages 33–136 (cited on pages 56–63, 210).
- [202] F. Schwabl, *Quantenmechanik für Fortgeschrittene* (Springer-Verlag Berlin Heidelberg, 2008) (cited on page 57).
- [203] G. C. Wick, *Phys. Rev.* **80**, 268 (1950) (cited on pages 58, 209).
- [204] J. Čížek, *J. Chem. Phys.* **45**, 4256 (1966) (cited on page 58).

- [205] J. Čížek, "On the Use of the Cluster Expansion and the Technique of Diagrams in Calculations of Correlation Effects in Atoms and Molecules", in *Advances in chemical physics*, Vol. 14, edited by R. LeFevbre and C. Moser (John Wiley & Sons, Ltd, 1969), pages 35–89 (cited on page 58).
- [206] S. A. Kucharski and R. J. Bartlett, *J. Chem. Phys.* **108**, 5243 (1998) (cited on pages 59, 165).
- [207] G. D. Purvis and R. J. Bartlett, *J. Chem. Phys.* **76**, 1910 (1982) (cited on page 60).
- [208] G. E. Scuseria, A. C. Scheiner, T. J. Lee, J. E. Rice, and H. F. Schaefer, *J. Chem. Phys.* **86**, 2881 (1987) (cited on page 60).
- [209] J. F. Stanton, J. Gauss, J. D. Watts, and R. J. Bartlett, *J. Chem. Phys.* **94**, 4334 (1991) (cited on page 60).
- [210] C. Hampel, K. A. Peterson, and H.-J. Werner, *Chem. Phys. Lett.* **190**, 1 (1992) (cited on pages 60, 155).
- [211] Y. S. Lee and R. J. Bartlett, *J. Chem. Phys.* **80**, 4371 (1984) (cited on pages 61, 155, 158).
- [212] Y. S. Lee, S. A. Kucharski, and R. J. Bartlett, *J. Chem. Phys.* **81**, 5906 (1984) (cited on pages 61, 155, 158).
- [213] N. Jozef, B. Rodney J., and M. Urban, *Chem. Phys. Lett.* **134**, 126 (1987) (cited on pages 61, 155, 158).
- [214] T. Gary W., N. Jozef, and B. Rodney J., *Chem. Phys. Lett.* **145**, 548 (1988) (cited on pages 61, 155, 158).
- [215] Y. He, Z. He, and D. Cremer, *Theor. Chem. Acc.* **105**, 182 (2001) (cited on pages 61, 155, 158).
- [216] J. F. Stanton, W. N. Lipscomb, D. H. Magers, and R. J. Bartlett, *J. Chem. Phys.* **90**, 1077 (1989) (cited on page 62).
- [217] P. J. Knowles, C. Hampel, and H. Werner, *J. Chem. Phys.* **99**, 5219 (1993) (cited on pages 63, 157).
- [218] P. J. Knowles, C. Hampel, and H.-J. Werner, *J. Chem. Phys.* **112**, 3106 (2000) (cited on pages 63, 157).
- [219] H. Werner and P. J. Knowles, *J. Chem. Phys.* **82**, 5053 (1985) (cited on pages 64, 65).

- [220] P. J. Knowles and H.-J. Werner, *Chem. Phys. Lett.* **115**, 259 (1985) (cited on pages 64, 65).
- [221] D. A. Kreplin, P. J. Knowles, and H.-J. Werner, *J. Chem. Phys.* **150**, 194106 (2019) (cited on pages 64–66).
- [222] H. Werner and W. Meyer, *J. Chem. Phys.* **73**, 2342 (1980) (cited on pages 64, 65).
- [223] E. R. Sayfutyarova, Q. Sun, G. K.-L. Chan, and G. Knizia, *J. Chem. Theory Comput.* **13**, 4063 (2017) (cited on pages 64, 103, 221).
- [224] H.-J. Werner, P. J. Knowles, G. Knizia, F. R. Manby, and M. Schütz, *WIREs Comput. Mol. Sci.* **2**, 242 (2012) (cited on pages 65, 68, 84, 155, 175).
- [225] H.-J. Werner, P. J. Knowles, F. R. Manby, J. A. Black, K. Doll, A. Heßelmann, D. Kats, A. Köhn, T. Korona, D. A. Kreplin, Q. Ma, T. F. Miller, A. Mitrushchenkov, K. A. Peterson, I. Polyak, G. Rauhut, and M. Sibaev, *J. Chem. Phys.* **152**, 144107 (2020) (cited on pages 65, 68, 84, 132, 155, 175).
- [226] H. Werner and W. Meyer, *J. Chem. Phys.* **74**, 5794 (1981) (cited on page 65).
- [227] D. A. Kreplin, P. J. Knowles, and H.-J. Werner, *J. Chem. Phys.* **152**, 074102 (2020) (cited on page 66).
- [228] H. Werner and P. J. Knowles, *J. Chem. Phys.* **89**, 5803 (1988) (cited on pages 67–70, 84).
- [229] P. J. Knowles and H.-J. Werner, *Chem. Phys. Lett.* **145**, 514 (1988) (cited on pages 67, 68, 70, 84).
- [230] E. R. Davidson, *J. Comput. Phys.* **17**, 87 (1975) (cited on pages 67, 70).
- [231] P. J. Knowles and H.-J. Werner, *Theor. Chim. Acta* **84**, 95 (1992) (cited on pages 68, 71, 84).
- [232] J. G. Hill, *Int. J. Quantum Chem.* **113**, 21 (2013) (cited on pages 73–75).
- [233] E. Clementi and D. Davis, *J. Comput. Phys.* **1**, 223 (1966) (cited on page 73).
- [234] T. H. Dunning, *J. Chem. Phys.* **90**, 1007 (1989) (cited on page 74).
- [235] H. Trygve, K. Wim, and T. David P., *Mol. Phys.* **106**, 2107 (2008) (cited on page 74).
- [236] D. Feller, *J. Chem. Phys.* **98**, 7059 (1993) (cited on pages 74, 149, 154, 171, 178, 267).

- [237] D. Feller, K. A. Peterson, and J. Grant Hill, *J. Chem. Phys.* **135**, 044102 (2011) (cited on page 74).
- [238] T. Helgaker, W. Klopper, H. Koch, and J. Noga, *J. Chem. Phys.* **106**, 9639 (1997) (cited on pages 74, 143, 154, 171, 173, 263, 265).
- [239] A. Halkier, T. Helgaker, P. Jørgensen, W. Klopper, H. Koch, J. Olsen, and A. K. Wilson, *Chem. Phys. Lett.* **286**, 243 (1998) (cited on pages 74, 143, 173, 263, 265).
- [240] J. G. Hill and K. A. Peterson, *J. Chem. Phys.* **147**, 244106 (2017) (cited on pages 75, 155, 157, 172–174, 186, 262, 263, 265, 268, 269, 273, 279).
- [241] G. A. Petersson, S. Zhong, J. A. Montgomery, and M. J. Frisch, *J. Chem. Phys.* **118**, 1101 (2003) (cited on page 75).
- [242] I. Cherkes, S. Klaiman, and N. Moiseyev, *Int. J. Quantum Chem.* **109**, 2996 (2009) (cited on page 75).
- [243] M. Marinescu and H. R. Sadeghpour, *Phys. Rev. A* **59**, 390 (1999) (cited on page 81).
- [244] T. Kampschulte and J. Hecker Denschlag, *New. J. Phys.* **20**, 123015 (2018) (cited on page 82).
- [245] J. Schnabel, T. Kampschulte, S. Rupp, J. Hecker Denschlag, and A. Köhn, *Phys. Rev. A* **103**, 022820 (2021) (cited on pages 82, 88, 90, 95, 99, 105, 108, 113).
- [246] T. Secker, J.-L. Li, P. M. A. Mestrom, and S. J. J. M. F. Kokkelmans, *Phys. Rev. A* **103**, 022825 (2021) (cited on page 82).
- [247] T. Secker, J.-L. Li, P. M. A. Mestrom, and S. J. J. M. F. Kokkelmans, *Phys. Rev. A* **103**, 032817 (2021) (cited on page 82).
- [248] J.-L. Li, personal communication, May 19, 2021 (cited on page 82).
- [249] H. Silberbach, P. Schwerdtfeger, H. Stoll, and H. Preuss, *J. Phys. B: At. Mol. Phys.* **19**, 501 (1986) (cited on pages 83, 85).
- [250] I. S. Lim, P. Schwerdtfeger, B. Metz, and H. Stoll, *J. Chem. Phys.* **122**, 104103 (2005) (cited on pages 83, 84, 99, 142, 154, 172, 174, 182, 183, 186, 261, 263, 277).
- [251] H.-J. Werner, P. J. Knowles, G. Knizia, F. R. Manby, M. Schütz, et al., *Molpro, version 2018.2, a package of ab initio programs*, see <http://www.molpro.net>, Cardiff, UK, 2018 (cited on pages 84, 155, 175).

- [252] H.-J. Werner, P. J. Knowles, G. Knizia, F. R. Manby, M. Schütz, et al., *Molpro, version 2019.2, a package of ab initio programs*, see <http://www.molpro.net>, Cardiff, UK, 2019 (cited on pages 84, 104, 125).
- [253] H.-J. Werner, P. J. Knowles, G. Knizia, F. R. Manby, M. Schütz, et al., *Molpro, version 2020.1, a package of ab initio programs*, see <http://www.molpro.net>, Cardiff, UK, 2020 (cited on pages 84, 132).
- [254] A. W. Hauser, G. Auböck, C. Callegari, and W. E. Ernst, *J. Chem. Phys.* **132**, 164310 (2010) (cited on page 85).
- [255] D. P. Tew and W. Klopper, *J. Chem. Phys.* **125**, 094302 (2006) (cited on page 85).
- [256] S. Huzinaga and B. Miguel, *Chem. Phys. Lett.* **175**, 289 (1990) (cited on page 85).
- [257] S. Huzinaga and M. Klobukowski, *Chem. Phys. Lett.* **212**, 260 (1993) (cited on page 85).
- [258] P. J. Linstrom and W. G. Mallard, *NIST Chemistry WebBook, NIST Standard Reference Database Number 69*, data retrieved <https://doi.org/10.18434/T4D303>, 2019 (cited on pages 86, 170, 173, 174, 265).
- [259] C. Strauss, T. Takekoshi, F. Lang, K. Winkler, R. Grimm, J. Hecker Denschlag, and E. Tiemann, *Phys. Rev. A* **82**, 052514 (2010) (cited on pages 86, 140, 141, 270, 271).
- [260] H. Salami, T. Bergeman, B. Beser, J. Bai, E. H. Ahmed, S. Kotochigova, A. M. Lyyra, J. Huennekens, C. Lisdat, A. V. Stoliarov, O. Dulieu, P. Crozet, and A. J. Ross, *Phys. Rev. A* **80**, 022515 (2009) (cited on page 86).
- [261] B. Drews, M. Deiß, J. Wolf, E. Tiemann, and J. Hecker Denschlag, *Phys. Rev. A* **95**, 062507 (2017) (cited on page 86).
- [262] C. Amiot and J. Verges, *Mol. Phys.* **61**, 51 (1987) (cited on page 86).
- [263] C. Amiot, *J. Chem. Phys.* **93**, 8591 (1990) (cited on page 86).
- [264] C. Amiot, *Mol. Phys.* **58**, 667 (1986) (cited on page 86).
- [265] G.-H. Jeung, *J. Mol. Spectrosc.* **182**, 113 (1997) (cited on pages 88, 154).
- [266] R. Guérout, P. Soldán, M. Aymar, J. Deiglmayr, and O. Dulieu, *Int. J. Quant. Chem.* **109**, 3387 (2009) (cited on page 88).
- [267] T. Leininger, A. Nicklass, W. Küchle, H. Stoll, M. Dolg, and A. Bergner, *Chem. Phys. Lett.* **255**, 274 (1996) (cited on page 88).

- [268] B. R. Johnson, *J. Chem. Phys.* **73**, 5051 (1980) (cited on page 89).
- [269] H. Suno, B. D. Esry, C. H. Greene, and J. P. Burke, *Phys. Rev. A* **65**, 042725 (2002) (cited on page 89).
- [270] J. Wang, J. P. D’Incao, and C. H. Greene, *Phys. Rev. A* **84**, 052721 (2011) (cited on page 89).
- [271] A. S. Coolidge and H. M. James, *Phys. Rev.* **51**, 855 (1937) (cited on page 89).
- [272] C. L. Pekeris, *Phys. Rev.* **112**, 1649 (1958) (cited on page 89).
- [273] C. L. Pekeris, *Phys. Rev.* **115**, 1216 (1959) (cited on page 89).
- [274] C. L. Pekeris, B. Schiff, and H. Lifson, *Phys. Rev.* **126**, 1057 (1962) (cited on page 89).
- [275] C. L. Pekeris, *Phys. Rev.* **127**, 509 (1962) (cited on page 89).
- [276] Y. Accad, C. L. Pekeris, and B. Schiff, *Phys. Rev. A* **4**, 516 (1971) (cited on page 89).
- [277] B. Schiff, C. L. Pekeris, and Y. Accad, *Phys. Rev. A* **4**, 885 (1971) (cited on page 89).
- [278] E. R. Davidson, *J. Am. Chem. Soc.* **99** (2), 397 (1977) (cited on page 90).
- [279] J. Wolf, M. Deiß, A. Krüchow, E. Tiemann, B. P. Ruzic, Y. Wang, J. P. D’Incao, P. S. Julienne, and J. H. Denschlag, *Science* **358**, 921 (2017) (cited on page 99).
- [280] S. Matsika and D. R. Yarkony, *J. Chem. Phys.* **115**, 2038 (2001) (cited on pages 132, 248).
- [281] S. Matsika and D. R. Yarkony, *J. Chem. Phys.* **115**, 5066 (2001) (cited on pages 132, 248).
- [282] S. Matsika and D. R. Yarkony, *J. Chem. Phys.* **116**, 2825 (2002) (cited on pages 132, 248).
- [283] N. Aronszajn, *Trans. Amer. Math. Soc.* **68**, 337 (1950) (cited on pages 133, 253).
- [284] T. Hastie, R. Tibshirani, and J. Frieman, *The Elements of Statistical Learning*, 2nd edition, Springer Series in Statistics (Springer, New York, NY, 2009) (cited on pages 133, 134, 256).
- [285] C. E. Rasmussen and C. K. I. Williams, “Relationships between GPs and Other Methods”, in *Gaussian Processes for Machine Learning* (The MIT Press, 2006) Chap. 6, pages 129–150 (cited on pages 133, 134, 252, 253, 256).

- [286] K. A. Murphy, *Machine Learning: A probabilistic view* (The MIT Press, 2012) (cited on pages 133, 135, 251, 252, 254).
- [287] B. Schölkopf, R. Herbrich, A. J. Smola, and R. Williamson, *A Generalized Representer Theorem*, see <https://citeseerx.ist.psu.edu/viewdoc/summary?doi=10.1.1.42.8617>, 2000 (cited on pages 133, 254).
- [288] A. N. Tikhonov, V. Y. Arsenin, and F. John, *Solutions of ill-posed problems* (Winston/Wiley, Washington, D.C., 1977) (cited on pages 134, 256).
- [289] B. M., D. M. C., and P. E. R., *Inverse Problems* **1**, 301 (1985) (cited on pages 134, 256).
- [290] B. M., D. M. C., and E. R. Pike, *Inverse Problems* **4**, 573 (1988) (cited on pages 134, 256, 257).
- [291] T. Ho and H. Rabitz, *J. Chem. Phys.* **104**, 2584 (1996) (cited on pages 134, 135, 141, 254–256).
- [292] O. T. Unke and M. Meuwly, *J. Chem. Inf. Model.* **57**, 1923 (2017) (cited on pages 134, 256).
- [293] T. Hollebeek, T.-S. Ho, and H. Rabitz, *Annu. Rev. Phys. Chem.* **50**, 537 (1999) (cited on pages 135, 254, 255).
- [294] T.-S. Ho and H. Rabitz, *J. Chem. Phys.* **113**, 3960 (2000) (cited on pages 135, 136, 141).
- [295] T.-S. Ho, H. Rabitz, and G. Scoles, *J. Chem. Phys.* **112**, 6218 (2000) (cited on page 135).
- [296] J. Higgins, T. Hollebeek, J. Reho, T.-S. Ho, K. K. Lehmann, H. Rabitz, G. Scoles, and M. Gutowski, *J. Chem. Phys.* **112**, 5751 (2000) (cited on pages 135, 138).
- [297] A. Simoni, J.-M. Launay, and P. Soldán, *Phys. Rev. A* **79**, 032701 (2009) (cited on page 135).
- [298] B. M. Axilrod and E. Teller, *J. Chem. Phys.* **11**, 299 (1943) (cited on page 139).
- [299] B. R. J., *J. Phys. B* **3**, 751 (1970) (cited on page 139).
- [300] J. Mitroy and M. W. J. Bromley, *Phys. Rev. A* **68**, 052714 (2003) (cited on pages 140, 146).
- [301] S. H. Patil and K. T. Tang, *J. Chem. Phys.* **106**, 2298 (1997) (cited on pages 140, 146, 182, 183).

- [302] W. L. Bade, *J. Chem. Phys.* **28**, 282 (1958) (cited on page 140).
- [303] P. Soldán and J. M. Hutson, *J. Chem. Phys.* **112**, 4415 (2000) (cited on pages 141, 144).
- [304] B. Lesiuk Michał and Jeziorski, *J. Chem. Theory Comput.* **15**, 5398 (2019) (cited on pages 143, 173, 263, 265).
- [305] Y. Guan, X. Han, J. Yang, Z. Zhou, X. Dai, E. H. Ahmed, A. M. Lyyra, S. Magnier, V. S. Ivanov, A. S. Skublov, and V. B. Sovkov, *J. Chem. Phys.* **139**, 144303 (2013) (cited on pages 143, 144, 270).
- [306] J. A. Lau, J. P. Toennies, and K. T. Tang, *J. Chem. Phys.* **145**, 194308 (2016) (cited on page 145).
- [307] J. B. Bauer and J. P. Toennies, *J. Chem. Phys.* **150**, 144310 (2019) (cited on page 145).
- [308] The explicit form of the cutoff functions has been proposed by José P. D’Incao (JILA, University of Colorado) in several inspiring discussions on the prospects of performing scattering calculations based on the respective Rb₃ quartet ground state potential energy surface. (cited on page 148).
- [309] J. Schnabel and A. Köhn, *RP-RKHS-based interpolation to generate rubidium dimer and trimer potential energy surfaces*, version v1.0, see <https://doi.org/10.5281/zenodo.5379475>, 2021 (cited on pages 150, 194).
- [310] C. Veit, N. Zuber, O. A. Herrera-Sancho, V. S. V. Anasuri, T. Schmid, F. Meinert, R. Löw, and T. Pfau, *Phys. Rev. X* **11**, 011036 (2021) (cited on pages 153, 167, 171).
- [311] D. Feller, K. A. Peterson, and D. A. Dixon, *J. Chem. Phys.* **129**, 204105 (2008) (cited on pages 154, 171).
- [312] J. M. L. Martin and G. de Oliveira, *J. Chem. Phys.* **111**, 1843 (1999) (cited on pages 154, 171).
- [313] A. Tajti, P. G. Szalay, A. G. Császár, M. Kállay, J. Gauss, E. F. Valeev, B. A. Flowers, J. Vázquez, and J. F. Stanton, *J. Chem. Phys.* **121**, 11599 (2004) (cited on pages 154, 171).
- [314] M. S. Schuurman, S. R. Muir, W. D. Allen, and H. F. Schaefer III, *J. Chem. Phys.* **120**, 11586 (2004) (cited on pages 154, 171).
- [315] K. G. Dyall, *J. Chem. Phys.* **115**, 9136 (2001) (cited on pages 155, 174).

- [316] W. Liu and D. Peng, *J. Chem. Phys.* **131**, 1 (2009) (cited on pages 155, 174).
- [317] J. D. Watts, J. Gauss, and R. J. Bartlett, *Chem. Phys. Lett.* **200**, 1 (1992) (cited on pages 155, 175).
- [318] J. F. Stanton, J. Gauss, L. Cheng, M. E. Harding, D. A. Matthews, and P. G. Szalay, *CFOUR, Coupled-Cluster techniques for Computational Chemistry, a quantum-chemical program package*, With contributions from A.A. Auer, A. Asthana, R.J. Bartlett, U. Benedikt, C. Berger, D.E. Bernholdt, S. Blaschke, Y. J. Bomble, S. Burger, O. Christiansen, D. Datta, F. Engel, R. Faber, J. Greiner, M. Heckert, O. Heun, M. Hilgenberg, C. Huber, T.-C. Jagau, D. Jonsson, J. Jusélius, T. Kirsch, K. Klein, G.M. Kopper, W.J. Lauderdale, F. Lipparini, J. Liu, T. Metzroth, L.A. Mück, D.P. O'Neill, T. Nottoli, D.R. Price, E. Prochnow, C. Puzzarini, K. Ruud, F. Schiffmann, W. Schwalbach, C. Simmons, S. Stopkowicz, A. Tajti, J. Vázquez, F. Wang, J.D. Watts and the integral packages MOLECULE (J. Almlöf and P.R. Taylor), PROPS (P.R. Taylor), ABACUS (T. Helgaker, H.J. Aa. Jensen, P. Jørgensen, and J. Olsen), and ECP routines by A. V. Mitin and C. van Wüllen. For the current version, see <http://www.cfour.de>. (cited on pages 155, 175).
- [319] D. A. Matthews, L. Cheng, M. E. Harding, F. Lipparini, S. Stopkowicz, T.-C. Jagau, P. G. Szalay, J. Gauss, and J. F. Stanton, *J. Chem. Phys.* **152**, 214108 (2020) (cited on pages 155, 175).
- [320] L. Cheng and J. Gauss, *J. Chem. Phys.* **135**, 084114 (2011) (cited on pages 155, 175).
- [321] M. Kállay, P. R. Nagy, Z. Rolik, D. Mester, G. S. J. Csontos, J. Csóka, B. P. Szabó, L. Gyevi-Nagy, I. Ladjánszki, L. Szegedy, B. Ladóczki, K. Petrov, M. Farkas, P. D. Mezei, and B. Hégyely, *MRCC, a quantum chemical program suite*, see www.mrcc.hu, 2019 (cited on pages 155, 175, 278).
- [322] M. Kállay, P. R. Nagy, D. Mester, Z. Rolik, G. Samu, J. Csontos, J. Csóka, P. B. Szabó, L. Gyevi-Nagy, B. Hégyely, I. Ladjánszki, L. Szegedy, B. Ladóczki, K. Petrov, M. Farkas, P. D. Mezei, and Á. Ganyecz, *J. Chem. Phys.* **152**, 074107 (2020) (cited on pages 155, 175, 278).
- [323] D. A. Fedorov, A. Derevianko, and S. A. Varganov, *J. Chem. Phys.* **140**, 184315 (2014) (cited on page 157).
- [324] J. Schnabel, L. Cheng, and A. Köhn, *J. Chem. Phys.* **155**, 124101 (2021) (cited on pages 158, 160, 164, 166, 278).

- [325] These investigations and calculations have been designed and performed by Lan Cheng (Department of Chemistry, The John Hopkins University, Baltimore, Maryland 21218, United States). Numbers and figures are printed with respective permission. (cited on pages 159, 165, 173–175, 278).
- [326] J. Arponen, *Ann. Phys.* **151**, 311 (1983) (cited on page 165).
- [327] L. Adamowicz and R. J. Bartlett, *Int. J. Quantum Chem. Symp.* **26**, 245 (1984) (cited on page 165).
- [328] A. C. Scheiner, G. E. Scuseria, J. E. Rice, T. J. Lee, and H. F. Schaefer III, *J. Chem. Phys.* **87**, 5361 (1987) (cited on page 165).
- [329] T. Helgaker and P. Jørgensen, *Adv. Quant. Chem.* **19**, 188 (1988) (cited on page 165).
- [330] T. D. Crawford and J. F. Stanton, *Int. J. Quantum Chem.* **70**, 601 (1998) (cited on page 165).
- [331] J. N. Bardsley, T. Holstein, B. R. Junker, and S. Sinha, *Phys. Rev. A* **11**, 1911 (1975) (cited on page 169).
- [332] B. M. Smirnov, *Phys.-Usp.* **44**, 221 (2001) (cited on pages 170, 178).
- [333] Y. J. Bomble, J. Vázquez, M. Kállay, C. Michauk, P. G. Szalay, A. G. Császár, J. Gauss, and J. F. Stanton, *J. Chem. Phys.* **125**, 064108 (2006) (cited on page 171).
- [334] M. E. Harding, J. Vázquez, B. Ruscic, A. K. Wilson, J. Gauss, and J. F. Stanton, *J. Chem. Phys.* **128**, 114111 (2008) (cited on page 171).
- [335] K. G. Dyall, *J. Chem. Phys.* **106**, 9618 (1997) (cited on page 175).
- [336] W. Kutzelnigg and W. Liu, *J. Chem. Phys.* **123**, 241102 (2005) (cited on page 175).
- [337] M. Iliaš and T. Saue, *J. Chem. Phys.* **126**, 64102 (2007) (cited on page 175).
- [338] J. Liu and L. Cheng, *J. Chem. Phys.* **148**, 144108 (2018) (cited on page 175).
- [339] K. Koziol and G. A. Aucar, *J. Chem. Phys.* **148**, 134101 (2018) (cited on page 175).
- [340] P. Schwerdtfeger and J. K. Nagle, *Mol. Phys.* **117**, 1200 (2019) (cited on page 181).
- [341] M. D. Gregoire, I. Hromada, W. F. Holmgren, R. Trubko, and A. D. Cronin, *Phys. Rev. A* **92**, 052513 (2015) (cited on pages 181, 183).
- [342] J. Kaur, D. K. Nandy, B. Arora, and B. K. Sahoo, *Phys. Rev. A* **91**, 012705 (2015) (cited on pages 181–183).

- [343] W. F. Holmgren, M. C. Reville, V. P. A. Lonij, and A. D. Cronin, *Phys. Rev. A* **81**, 053607 (2010) (cited on page 183).
- [344] M. S. Safronova and U. I. Safronova, *Phys. Rev. A* **83**, 052508 (2011) (cited on pages 182, 183).
- [345] A. Derevianko, W. R. Johnson, M. S. Safronova, and J. F. Babb, *Phys. Rev. Lett.* **82**, 3589 (1999) (cited on page 182).
- [346] R. J. Le Roy, *J. Quant. Spectrosc. Radiat. Transfer* **186**, 167 (2017) (cited on pages 184, 187, 270, 271).
- [347] Y. Lee and B. H. Mahan, *J. Chem. Phys.* **42**, 2893 (1965) (cited on pages 184, 185).
- [348] M. Shafi, C. L. Beckel, and R. Engelke, *J. Mol. Spectrosc.* **42**, 578 (1972) (cited on pages 184, 185).
- [349] R. E. Olson, *Phys. Rev.* **187**, 153 (1969) (cited on pages 184, 185).
- [350] G. S. Wagner and N. R. Isenor, *Can. J. Phys.* **63**, 976 (1985) (cited on pages 184, 185).
- [351] M. A. Bellos, R. Carollo, J. Banerjee, M. Ascoli, A.-R. Allouche, E. E. Eyler, P. L. Gould, and W. C. Stwalley, *Phys. Rev. A* **87**, 012508 (2013) (cited on pages 184–186).
- [352] M. Aymar, S. Azizi, and O. Dulieu, *J. Phys. B: At. Mol. Opt. Phys.* **36**, 4799 (2003) (cited on pages 184, 185).
- [353] A.-R. Allouche and M. Aubert-Frécon, *J. Chem. Phys.* **136**, 114302 (2012) (cited on page 185).
- [354] M. Nooijen and R. J. Bartlett, *J. Chem. Phys.* **102**, 3629 (1995) (cited on page 187).
- [355] J. Schnabel and A. Köhn, *A RP-RKHS-based ion-atom interaction potential generator for the rubidium dimer cation*, version v1.0, see <https://doi.org/10.5281/zenodo.5380311>, 2021 (cited on page 195).
- [356] D. Bishop, *Group Theory and Chemistry*, Dover books on physics and chemistry (Dover, 1993) (cited on page 201).
- [357] K. Anjyo and J. Lewis, *J. Math-for-Ind.* **3A**, 63 (2011) (cited on page 253).
- [358] P. C. Hansen, *SIAM J. Sci. Stat. Comput.* **11**, 503 (1990) (cited on pages 256, 257).
- [359] I. N. Bronštein, K. A. Semendjajew, G. Musiol, and H. Mühlig, *Taschenbuch der Mathematik* (Wissenschaftlicher Verlag Harri Deutsch GmbH, 2008) (cited on pages 257, 259).

- [360] M. Abramowitz and I. A. Stegun, *Handbook of Mathematical Functions* (Dover Publications, 1972) (cited on page 258).
- [361] *Hypergeometric function*. *Encyclopedia of Mathematics*. http://encyclopediaofmath.org/index.php?title=Hypergeometric_function&oldid=47298, Accessed: 2021-08-12 (cited on page 258).

Erklärung über die Eigenständigkeit der Dissertation

Ich versichere, dass ich die vorliegende Arbeit mit dem Titel *Theoretical Investigations for Photoassociation and Ion-Atom Scattering Experiments in Ultracold Rubidium Gases* selbständig verfasst und keine anderen als die angegebenen Quellen und Hilfsmittel benutzt habe; aus fremden Quellen entnommene Passagen und Gedanken sind als solche kenntlich gemacht.

Declaration of Authorship

I hereby certify that the dissertation entitled *Theoretical Investigations for Photoassociation and Ion-Atom Scattering Experiments in Ultracold Rubidium Gases* is entirely my own work except where otherwise indicated. Passages and ideas from other sources have been clearly indicated.

Name/ Name: Jan Schnabel

Unterschrift/ Signature: _____

Datum/ Date: